NASA/CR—2003-212370

Design and Test of Fan/Nacelle Models Quiet High-Speed Fan

Donald Weir
Honeywell Engines & Systems, Phoenix, Arizona

July 2003

The NASA STI Program Office . . . in Profile

Since its founding, NASA has been dedicated to the advancement of aeronautics and space science. The NASA Scientific and Technical Information (STI) Program Office plays a key part in helping NASA maintain this important role.

The NASA STI Program Office is operated by Langley Research Center, the Lead Center for NASA's scientific and technical information. The NASA STI Program Office provides access to the NASA STI Database, the largest collection of aeronautical and space science STI in the world. The Program Office is also NASA's institutional mechanism for disseminating the results of its research and development activities. These results are published by NASA in the NASA STI Report Series, which includes the following report types:

- TECHNICAL PUBLICATION. Reports of completed research or a major significant phase of research that present the results of NASA programs and include extensive data or theoretical analysis. Includes compilations of significant scientific and technical data and information deemed to be of continuing reference value. NASA's counterpart of peer-reviewed formal professional papers but has less stringent limitations on manuscript length and extent of graphic presentations.

- TECHNICAL MEMORANDUM. Scientific and technical findings that are preliminary or of specialized interest, e.g., quick release reports, working papers, and bibliographies that contain minimal annotation. Does not contain extensive analysis.

- CONTRACTOR REPORT. Scientific and technical findings by NASA-sponsored contractors and grantees.

- CONFERENCE PUBLICATION. Collected papers from scientific and technical conferences, symposia, seminars, or other meetings sponsored or cosponsored by NASA.

- SPECIAL PUBLICATION. Scientific, technical, or historical information from NASA programs, projects, and missions, often concerned with subjects having substantial public interest.

- TECHNICAL TRANSLATION. English-language translations of foreign scientific and technical material pertinent to NASA's mission.

Specialized services that complement the STI Program Office's diverse offerings include creating custom thesauri, building customized databases, organizing and publishing research results . . . even providing videos.

For more information about the NASA STI Program Office, see the following:

- Access the NASA STI Program Home Page at ***http://www.sti.nasa.gov***

- E-mail your question via the Internet to help@sti.nasa.gov

- Fax your question to the NASA Access Help Desk at 301–621–0134

- Telephone the NASA Access Help Desk at 301–621–0390

- Write to:
  NASA Access Help Desk
  NASA Center for AeroSpace Information
  7121 Standard Drive
  Hanover, MD 21076

NASA/CR—2003-212370

Design and Test of Fan/Nacelle Models Quiet High-Speed Fan

Donald Weir
Honeywell Engines & Systems, Phoenix, Arizona

Prepared under Contract NAS3–27752

National Aeronautics and
Space Administration

Glenn Research Center

July 2003

Available from

NASA Center for Aerospace Information
7121 Standard Drive
Hanover, MD 21076

National Technical Information Service
5285 Port Royal Road
Springfield, VA 22100

Available electronically at http://gltrs.grc.nasa.gov

TABLE OF CONTENTS

TABLE OF CONTENTS (CONT)

TABLE OF CONTENTS (CONT)

LIST OF FIGURES

Page

LIST OF FIGURES (CONT)

Page

LIST OF FIGURES (CONT)

Page

LIST OF FIGURES (CONT)

Page

LIST OF FIGURES (CONT)

Page

LIST OF FIGURES (CONT)

Page

LIST OF FIGURES (CONT)

Page

LIST OF FIGURES (CONT)

Page

LIST OF FIGURES (CONT)

Page

LIST OF TABLES

NAS3-27752, NASA AST AOI 14
DESIGN AND TEST OF FAN/NACELLE MODELS
QUIET HIGH-SPEED FAN
FINAL REPORT

1. SUMMARY

The Quiet High-Speed Fan program is a cooperative effort between Honeywell Engines & Systems (formerly AlliedSignal Engines & Systems) and the NASA Glenn Research Center. Engines & Systems has designed an advanced high-speed fan that will be tested on the Ultra High Bypass Propulsion Simulator in the NASA Glenn 9 x 15 foot wind tunnel, currently scheduled for the second quarter of 2000. An Engines & Systems modern fan design will be used as a baseline. A nacelle model is provided that is characteristic of a typical, modern regional aircraft nacelle and meets all of the program test objectives.

2. INTRODUCTION AND BACKGROUND

2.1 Quiet High-Speed Fan (QHSF) Program

The QHSF program is a cooperative effort between Engines & Systems and the NASA Glenn Research Center. Engines & Systems has designed an advanced high-speed fan that will be tested on the Ultra-High Bypass (UHB) Propulsion Simulator in the NASA Glenn 9 x 15 foot wind tunnel, currently scheduled for the first quarter of 2000. The QHSF is an advanced single-stage fan designed for a 5 to 20K pound thrust turbofan regional airline application. Advanced aerodynamic, mechanical, aeroelastic, and computational fluid dynamic (CFD) tools have been used to meet aggressive performance goals while attempting to achieve at least a 6 dB reduction in fan noise at a critical takeoff noise condition. Two fans have been built for evaluation at NASA: a baseline and the advanced Engines & Systems design. A nacelle model has been provided that is characteristic of a typical, modern regional aircraft nacelle and meets all of the program test objectives. Figure 2-1 shows the rotor design for the QHSF.

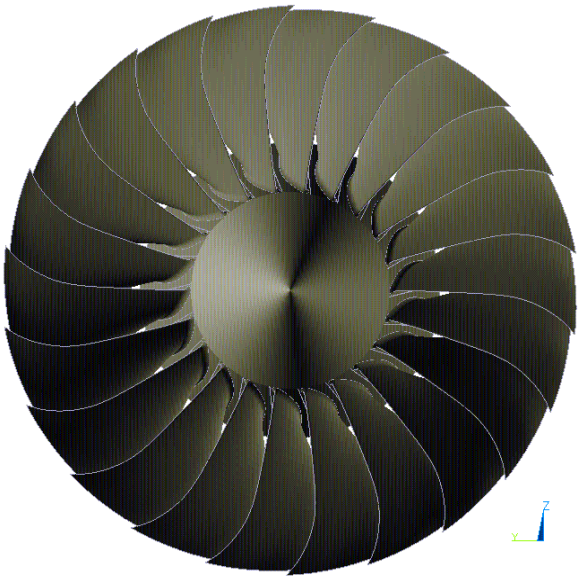

Figure 2-1. The QHSF Has an Advanced Damperless Fan Design With Forward-Swept Blades.

2.2 Baseline Fan

The baseline consists of a damperless, low-aspect- ratio, moderately aft swept rotor and full-span aft swept composite stator vanes. The geared fan configuration allows the fan to run at a tip speed optimized for best performance, stall margin, and noise.

The baseline fan was the subject of considerable acoustic evaluation early in the design phase. Blade and vane counts, rotor/stator spacing, and stator vane sweep were selected to minimize the

noise signature within the fan design constraints. Fan rig spinning-mode measurements were made to verify the design constraints and provide acoustic treatment design criteria. The acoustic effort was concluded with a full-scale engine acoustic test that verified the acoustic design goals, including the acoustic treatment, were met.

Installed performance of the baseline fan was a critical issue. Measuring fan component performance accurately during flight was required. The engine nacelle and inlet section of the flight test engine were custom tailored and instrumented for flow measurement. The engine front frame was also instrumented so fan performance could be measured without impacting fan or engine performance. The fan performance measured in flight at appropriate Reynolds numbers during the extensive flight test program agreed very well with rig and engine data acquired on the ground using conventional fluid metering techniques. The experience gained on this program was used on the Quiet High-Speed Fan program.

2.3 Historical Background

The presence of a shock at the inlet of the fan rotor in a turbofan engine can result in acoustic phenomena that represents substantial noise sources. For example, Multiple Pure Tone (MPT) noise results when the pressure disturbances from the inlet shock moves upstream out of the rotor blade passage. One approach to reducing these shock-related noise sources is to eliminate the formation of the inlet shock in the fan by tailoring the rotor blade shape. The introduction of sweep in the fan rotor blade can reduce the relative velocity component normal to the blade to subsonic values, much as a swept wing on an aircraft can produce subsonic velocities normal to the wing leading edge, even when the resultant velocity is supersonic.

This noise minimization technique was applied by Engines & Systems (formerly AVCO Lycoming) and Bolt, Beranek and Newman, Inc. (BBN) to the design of the QF-12 quiet high-speed fan, as part of a NASA-sponsored program performed between 1974 and 1977 (ref. 1). The fan rotor featured a compound forward-and-aft sweep to eliminate the leading edge shock. However, although shock-induced MPT noise was reduced, the aerodynamic performance of the fan did not meet design goals. The reasons for the performance deficiencies were not determined, but the source was found localized in the rotor. Figure 2-2 shows a summary of the results of the acoustic evaluation of the QF-12.

The ability to accurately predict, during the fan rotor design, the speed range over which the MPT noise will occur can provide a valuable tool for acoustically tailoring the design of the rotor to minimize the effect of this noise source.

2.4 Methods and Technical Approach

The Work Breakdown Structure (WBS) for the Engines & Systems program is presented in Figure 2-3. The methods and technical approach for each WBS element is presented below.

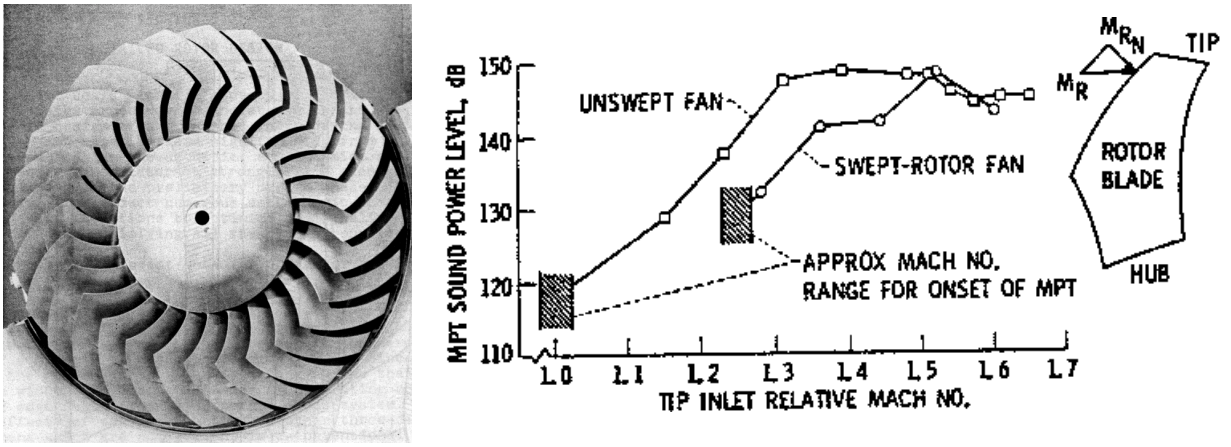

Figure 2-2. The QF-12 Fan Demonstrated the Feasibility of Using Blade Leading Edge Sweep to Reduce Fan Noise.

2.4.1 Aerodynamic and Mechanical Design (AA)

The Quiet High-Speed Fan is an advanced single-stage fan designed for a 5 to 20K pound-thrust turbofan regional airline application. Typical customer requirements in this market specify a medium to high bypass ratio (BPR = 4 to 8) turbofan, based on thrust, thrust specific fuel consumption, and nacelle drag trades. This BPR range requires a transonic fan with an overall design point pressure ratio of 1.6 to 1.8, high specific flow, excellent efficiency and operability across its range of operation, and light weight. The fan must also be a robust design capable of meeting stringent foreign object damage criteria, and must meet increasingly stringent acoustic requirements. For the fan to have adequate stall margin in the fan pressure ratio range of interest (1.6 to 1.8), the rotor corrected tip speed must be in the range of 1350 to 1500 ft/sec and rotor tip relative Mach numbers from 1.3 to 1.5.

The rotor design incorporates damperless, low-aspect-ratio (wide chord), forward-swept rotor blades with low hub/tip radius ratio and high annular specific flow. The stator system incorporates highly 3-D airfoils with leading edge sweep and tangential lean. The advanced swept rotor and acoustically optimum stator system results in a compact fan module package to minimize weight, nacelle drag, and cost while meeting the aggressive acoustic goals.

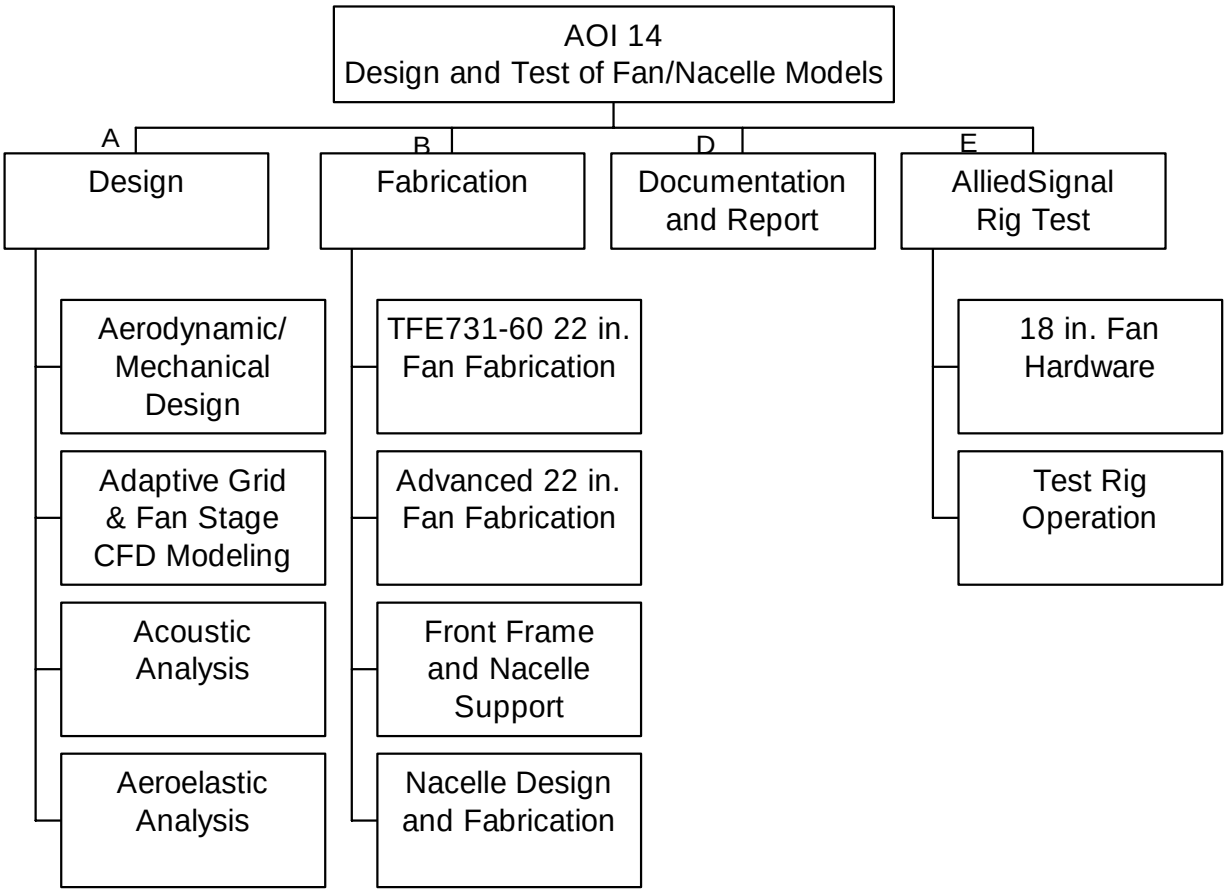

Figure 2-3. The WBS Is structured to Mirror the Elements of the Statement of Work for the Quiet High-Speed Fan.

Engines & Systems' axial fan/compressor aerodynamic and mechanical design system is an integrated system of 2-D and 3-D steady-state aerodynamic and mechanical design/analysis methods, including 2-D streamline curvature, 3-D inviscid flow analysis, 3-D viscous flow analysis, and 3-D mechanical analysis. During the design process, Design of Experiments (DOE) methods were used to help guide aerodynamic and mechanical design iterations.

2.4.2 Adaptive Grid and Fan Stage CFD Modeling (AB)

Two CFD investigations were performed, the first to study those flowfield characteristics that have the potential to impact the acoustic performance of the fan, and the second to study the aerodynamic performance of the fan stage, including blade-row interaction effects. In the first investigation, the DAWES and RAMPANT CFD codes were used to provide different means of achieving the necessary computational grid resolution to produce accurate predictions of acoustically relevant flow structures.

The 3-D viscous steady-flow DAWES program was used in the evaluation of several candidate rotor designs featuring various noise reduction concepts. The DAWES program was used to

estimate the onset of multiple-pure-tone (MPT), or "buzzsaw", noise based on predictions of inlet shock position relative to rotor-tip speed.

In addition to the DAWES analysis, the 3-D viscous, steady-flow RAMPANT program was applied to predict rotor inlet shock position. RAMPANT uses an unstructured, adaptive grid, that can more accurately and efficiently resolve complex geometric and flowfield details than the structured, non-adaptive, sheared H-grid employed by the DAWES program. By selectively adapting the RAMPANT grid, the program attempted to more accurately resolve inlet shock position, which assisted in calibrating the accuracy of the DAWES program predictions. An initial application of the RAMPANT program to the baseline fan rotor was first performed to validate the program's capability to resolve inlet shock structure with grid adaptation, and to compare the DAWES results with RAMPANT for a case having test data available.

The DAWES and RAMPANT analyses also provided predictions of the rotor-wake configuration that were used to estimate the trace speed of the rotor wake on the stator leading edge. By employing lean and sweep in the stator design, it was possible to maintain subsonic trace speeds, and therefore minimize the acoustic effects of rotor wake passing.

In the second CFD investigation, aerodynamic performance and blade-row interaction effects for the complete quiet high-speed fan stage were predicted by performing a 3-D viscous, steady-flow stage analysis with Adamczyk's average-passage program. Application of the program for the quiet high-speed fan stage analysis expanded Engines & Systems' experience base with the program to include an advanced, highly 3-D fan design incorporating noise reduction features. Calibration of the program for this fan stage analysis will be possible with available test data.

2.4.3 Acoustic Analysis (AC)

Two types of acoustic analyses were conducted on the advanced design. First, an assessment of the impact of the blade sweep on the onset of multiple pure tone noise (buzzsaw) was made. Second, an analysis of the fan design to minimize rotor stator interaction tones was completed.

The buzzsaw noise assessment was made in conjunction with the CFD activity. The CFD model of the rotor was evaluated at supersonic tip speeds near the expected onset of the buzzsaw noise. The corrected speed corresponding to the onset was determined. This value then defines the maximum cutback thrust level for operation without buzzsaw noise.

The candidate designs of the advanced fan were evaluated with the BBN/V072 code to assess the noise improvement in the subsonic tip speed regime. Comparisons with the baseline results will quantify the expected benefit to be measured during the rig test.

2.4.4 Aeroelastic analysis (AD)

To ensure flutter-free operation of the fan, attempts were made to evaluate the operating map from choke to stall at several speed conditions using one or more of the computer codes UNSFLO, FREPS, and TURBO-AE to determine that the aerodynamic damping coefficient

remains positive. This analysis was completed at the important airfoil radii with the 3-D steady flowfield computed from the DAWES program.

UNSFLO is a 2-D coupled Euler / Navier-Stokes unsteady aerodynamics code developed at MIT and modified to include blade motion by Engines & Systems. FREPS was developed by NASA Glenn and integrates structural finite-element results with a 2-D inviscid Potential flow solver to predict the vibratory response of airfoils. TURBO-AE is under development at NASA Glenn and integrates the NASA/Mississippi State University 3-D viscous code TURBO with structural finite-element results to predict the vibratory response of a fully 3-D airfoil.

2.4.5 Fan Design and Fabrication (BA, BB, and BC)

The fan rotor blades were machined out of titanium bar stock. The fan disk was machined out of a pancake forging of high strength steel. The fan stator assembly consists of composite vanes and aluminum hub and shroud rings. The vanes were formed with a stainless steel mold, pre-impregnated graphic epoxy tape cut into flat patterns, and a temperature-controlled hydraulic press in Engines & Systems' composite development fabrication shop. The hub and shroud rings were fabricated using a lathe and an EDM used to cut the slots for the composite vanes. The vanes were locked into place using an assembly fixture and Room Temperature Vulcanizing (RTV) rubber. The front frame was cast using the “Quick Cast” technique. Stereolithography segments of the frame were produced using a special resin and glued together into a 360-degree assembly. This assembly was used to make an aluminum investment casting. The casting was then machined and instrumented.

2.4.6 Nacelle Design and Fabrication (BD)

Micro Craft, Inc. provided design services to Engines & Systems for the quiet high-speed fan nacelle model. Engines & Systems fabricated, instrumented, and assembled the nacelle model for delivery to NASA Glenn.

The nacelle accommodates a fan diameter of approximately 22 inches. The Engines & Systems fan/stator/strut assembly was integrated with the drive rig fan balance and nacelle balance. Core flow was passively simulated by an annular passage from the struts exhausting internal to the nacelle. An instrumentation section was provided that mates the flight inlet to the fan housing. Static pressure taps and boundary layer rakes in this section facilitate mass flow measurements. Provisions were made for later installation of acoustic treatment with hard-wall liners provided for the first test.

Micro Craft employed 3-D computer aided design (CAD) and finite-element analysis (FEA) tools in the design of the nacelle. Detail drawings were made of all model parts. Engines & Systems and its vendors fabricated all nacelle parts.

2.4.7 Documentation (D)

In addition to this final report and normal progress reporting requirements, two additional reports were generated during this program.

Engines & Systems Report 21-9591, NAS3-27752, NASA AST – AOI 14, Design and Test of Fan/Nacelle Models, Quiet High-Speed Fan Design Report, March 31, 1997.
Engines & Systems Report 21-9931, Design and Test of Fan/Nacelle Models, Quiet High-Speed Fan, CFD Modeling Subtask Final Report, November 30, 1998.

2.4.8 Engines & Systems Rig Test (E)

Engines & Systems designed and fabricated a set of QHSF rotor blades and stator vanes for testing in the Engines & Systems 18-inch fan rig in Phoenix, AZ. The blades and vanes were fabricated with the same process used for the 22-inch rig parts. A test was conducted to provide fan performance and limited acoustic data.

3. AERODYNAMIC AND MECHANICAL DESIGN

A summary of the QHSF design results are presented in the following sections. A complete description of the design process is presented in Reference 2.

3.1 Design objectives

The QHSF stage design included objectives from the acoustic, aerodynamic, mechanical, and aeroelastic disciplines. Acoustic objectives included a 6 dB reduction in effective perceived noise (EPNdB) at takeoff relative to the baseline. The intent of the design was focused on obtaining noise reductions through the use of unconventional design techniques: control the rotor wake impinging on the stator LE, reduce rotor normal inlet relative Mach number, and control shocks within blade passage. Aerodynamic objectives were to obtain baseline performance (or better) with a forward-swept rotor and acoustically matched vanes. Mechanical and aeroelastic objectives were to obtain Engines & Systems and NASA criteria for stress and burst margins, proper positioning of mode/harmonic crossings to minimize high vibratory strains, and provide sufficient flutter margin throughout the operating region.

The aerodynamic design criteria are shown in Table 3-1. The mechanical criteria are shown in Table 3-2 and Figure 3-1.

Table 3-1. Specific Aerodynamic Design Criteria.

Fan Aero Design Point (100% N_{1C})

	22 in. DIA
Wcorr, lbm/s	98.9
Wc/A, lbm/s/ft^2	42.7
Utcorr, ft/s	1474
Bypass ratio	3.8
P/P, overall	1.82
Eff ad, overall	≥0.895
Stall margin (N_{1C}=C)	15%
Hub/Tip ratio	0.35
Rotor blade count	22
Stator vane count	52

Table 3-2. Specific Mechanical Design Criteria.

- Airfoil and Attachment LCF Life > 10^5 cycles
  - Peak Stress in Attachment and Airfoil
- HCF Life > 10^7 Cycles
  - Frequency, Excitation (Inlet Distortion Harmonics, Speed @Resonance)
- Bird-Ingestion Capability
  - Bird Weight, LE Thickness
- Flutter Margin Exceeds Baseline
  - Reduced Frequency, Twist/Flex, and Incidence
- Blade Weight Equal to Or Less Than Baseline

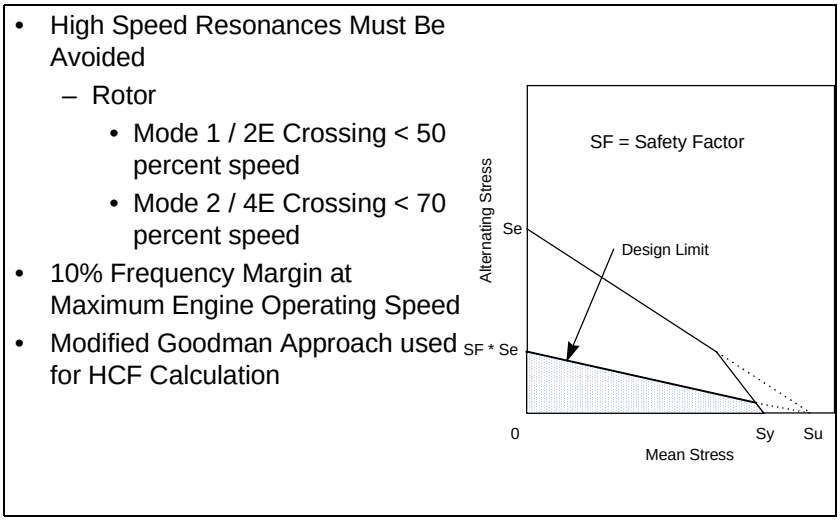

Figure 3-1. Mechanical Criteria for High-Cycle Fatigue.

3.2 Rotor Geometry

The final QHSF design configuration was chosen based on an extensive design study presented in Reference 2. It is the result of a series of four Design of Experiments (DOE) analyses that evaluated acoustic, aerodynamic, mechanical, and aeroelastic attributes. Final blade geometry span-wise distributions are shown in Figure 3-2 through 3.2-6. Tabular geometry data of the blade is included in Reference 2. Values in the figures represent the NASA rig rotor design (22-inch diameter at the rotor leading edge tip). The incidence was calculated using CFD at the design point. The large incidence increase at the tip was due to the end wall modeling of the boundary layer at the rotor inlet.

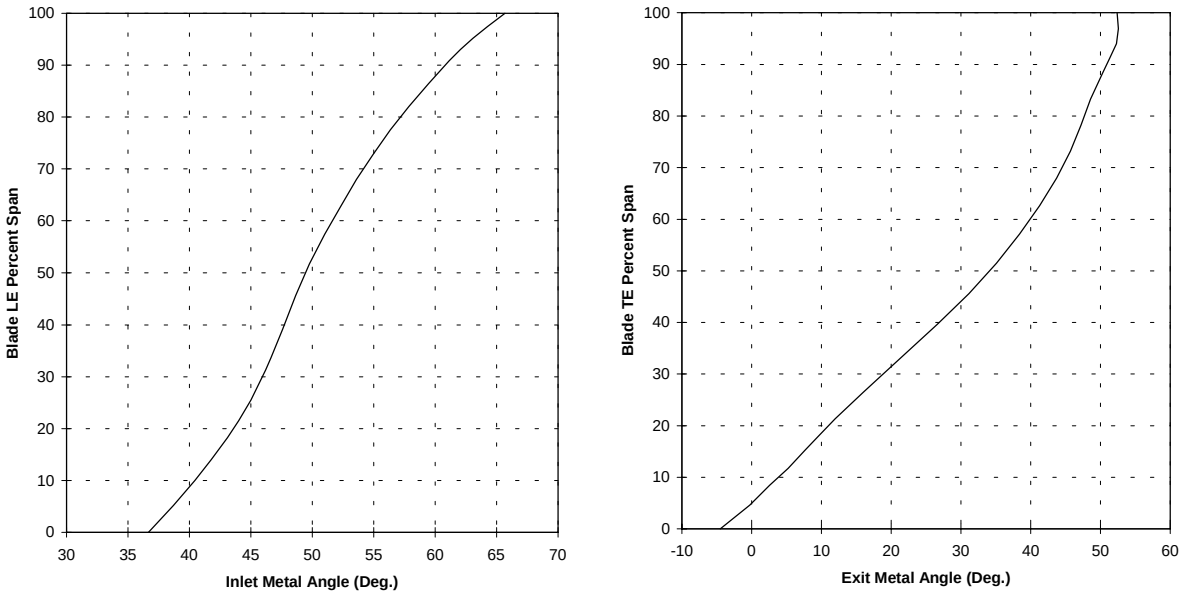

Figure 3-2. Blade Inlet and Exit Metal Angle.

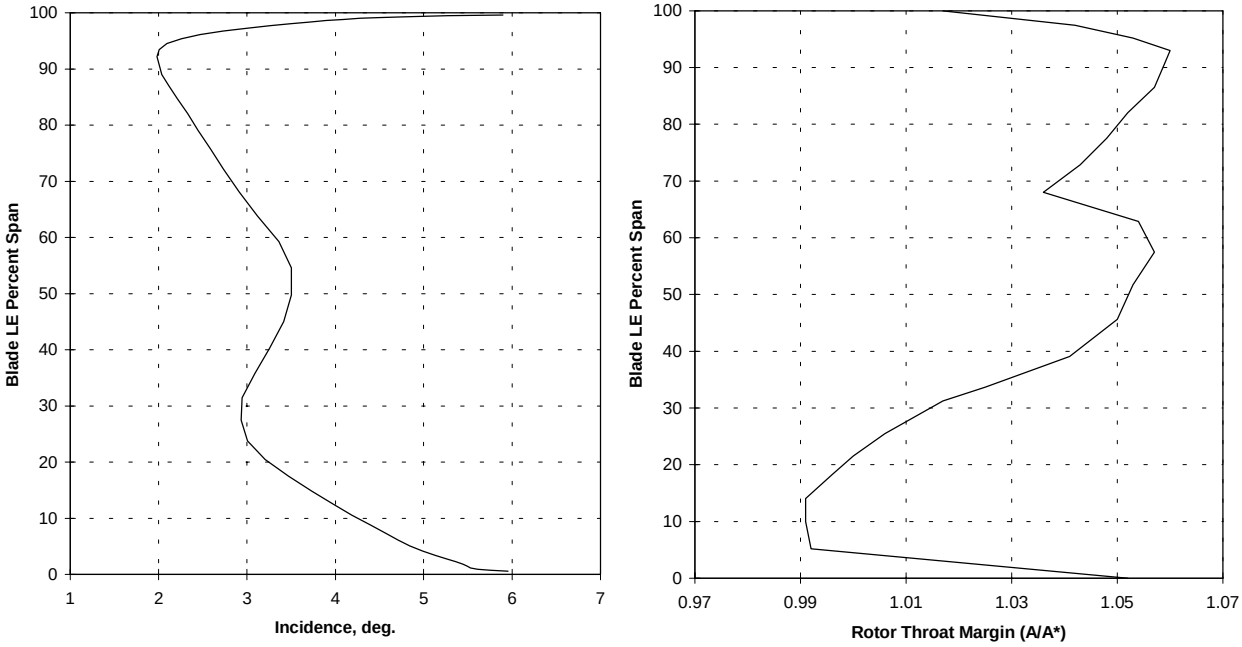

Figure 3-3. Blade Incidence and Throat Margin.

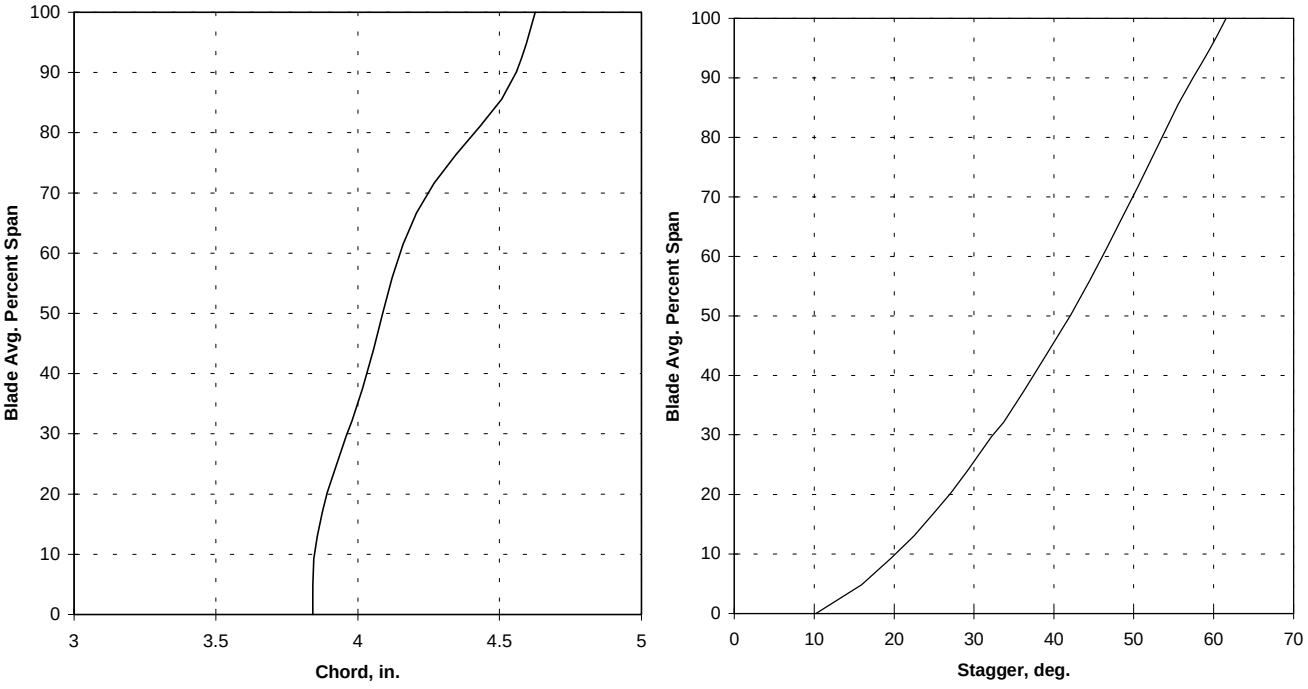

Figure 3-4. Blade Chord and Stagger Angle.

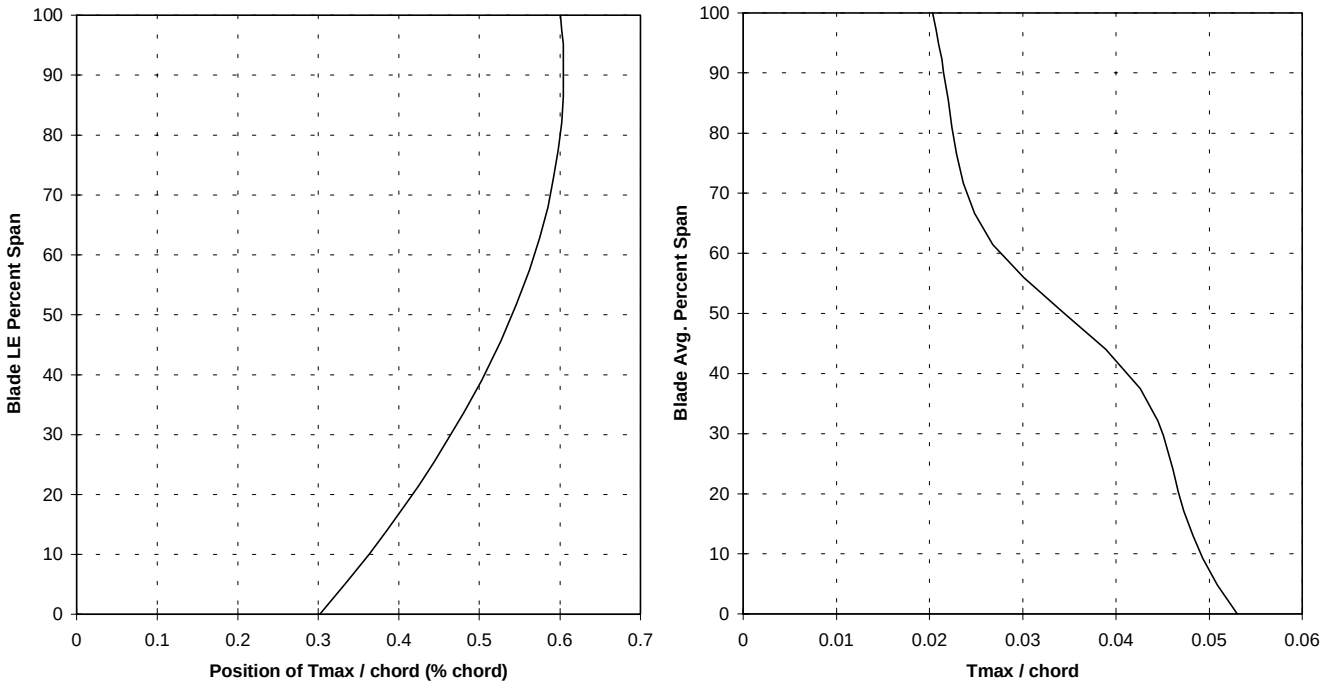

Figure 3-5. Blade Position of Maximum Thickness and Maximum Thickness/Chord Ratio.

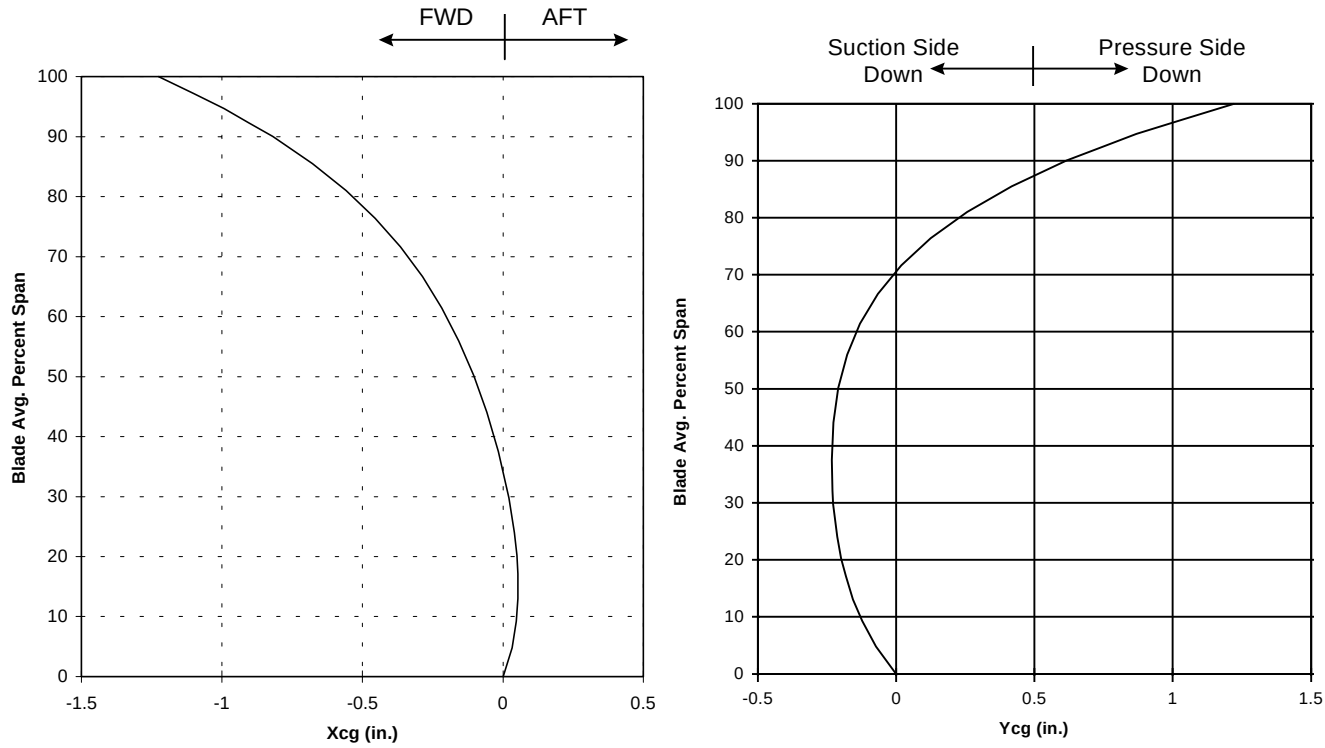

Figure 3-6. Blade CG Stacking.

3.3 Rotor Mechanical

A fully 3-D finite element model was constructed of the entire rig scale (22-inch diameter) fan rotor, including the airfoil, blade attachment, and disk. The complete model is shown in Figure 3-7. The airfoil and blade attachment were modeled separately and connected via an Engines & Systems multi-point constraint equation technique. Due to cyclic symmetry, the disk model consisted of a single, slotted wedge.

For computational efficiency, the disk and attachment were modeled as linear substructures. Blade-to-disk interaction at the dovetail was modeled using 3-D contact surface elements. The blade material was chosen to be Ti-6Al-4V STOA with the following nominal properties:

Property	75F	250F
Modulus, Mpsi	17.5	17.1
Weight Density, lb/in3	0.161	0.161
0.2% Yield Strength, ksi	137.7	111.4
Ultimate Strength, ksi	146.2	127.3

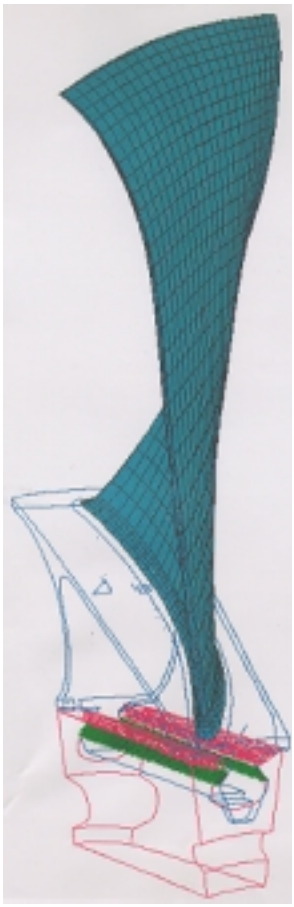

Figure 3-7. A Complete QHSF Rotor Blade Model Was Used for the Structural Analysis.

A physical speed of 15,444 rpm was applied to the rotor along the X-axis. The cut wedge faces were coupled together cylindrically to enforce cyclic symmetry. Axial (thrust) and tangential (torque) loads were reacted on the forward annular face representing the disk bolt flange. A uniform metal temperature of 75F was applied to the platform/attachment and 85F was applied to the disk to simulate operating conditions. Suction and pressure-side static pressure and metal temperatures corresponding to the aerodynamic design point distributions were mapped to the corresponding element faces on the airfoil.

As constructed, the airfoil model represented the at-speed, design point geometry ("hot" shape). The first phase of the static analysis is to calculate the manufactured shape ("cold"), that will, under design point conditions of speed, temperature, and pressure, deflect the blade into the desired "hot" shape. This is done using an iterative procedure within ANSYS where the maximum error between the deflected cold geometry and the desired hot geometry is reduced to less than 0.001 inch. Figure 3-8 shows the maximum principal stress distribution on the pressure and suction sides of the airfoil.

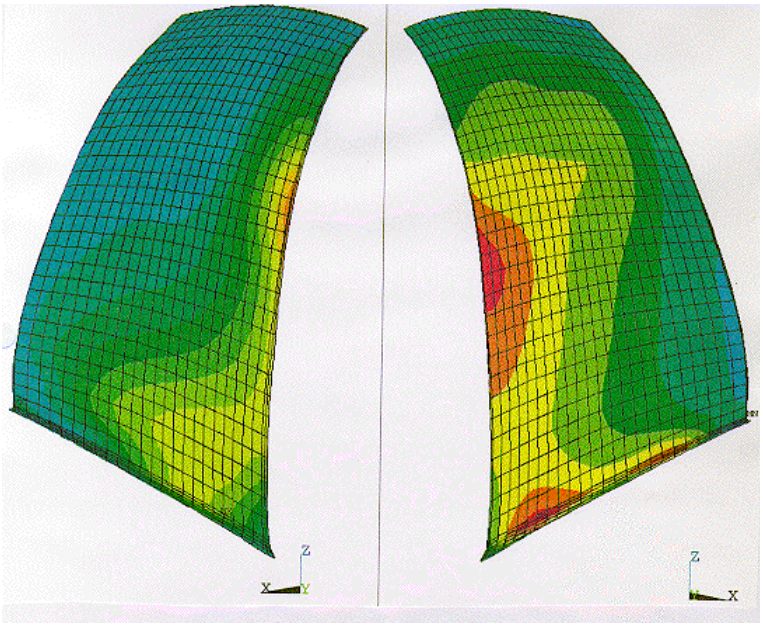

Figure 3-8. The Maximum Stresses on the QHSF Rotor Blade Occur at the Leading Edge.

Figure 3-9 shows the vector sum (scalar) displacement of the airfoil. The maximum airfoil deflection is predicted to be 0.376 inch. Radial displacements (positive outward from center) are shown in Figure 3-10. A maximum radial deflection of 0.051 inch occurs at the leading-edge.

Modal analysis was performed on the QHSF blade using the same model as was used for the static analysis. The effect of the disk was ignored based on the relative rigidity of the disk combined with past experience with similar designs.

All nodes on the contact faces of the blade dovetail were fixed in the three translational degrees-of -freedom (DOF). To define the Campbell diagram, two analyses were performed. The first analysis was done assuming uniform room temperature, with no pressure loading, and no rotational speed. The second analysis assumed design point metal temperatures, static pressures, and a rotational speed of 15,444 rpm. Natural frequencies for the first five modes are tabulated below. Also included are the frequencies for the fixed-root condition (attachment effects neglected) under identical conditions.

	Mode				
Conditions	1	2	3	4	5
Room temp., 0 rpm	172	520	879	1136	1521
Design point temp, 15,444 rpm	349	704	984	1485	1568
Fixed-Root, 0 rpm	177	599	879	1333	1556
Fixed Root, 15,444 rpm	373	791	1020	1600	1682

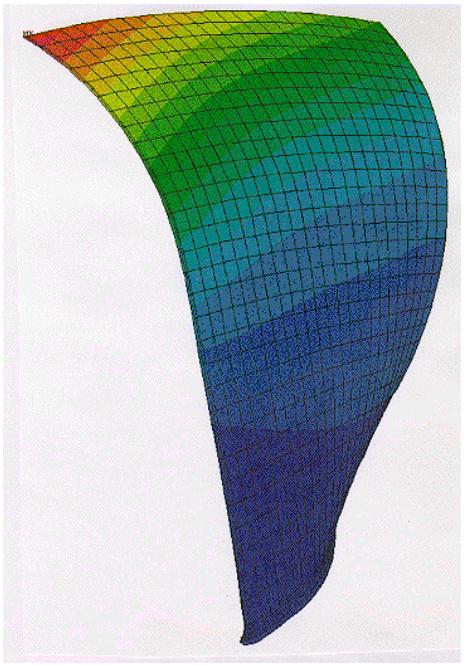

Figure 3-9. A Maximum Deflection Of 0.376 In. Is Seen at the QHSF Rotor Blade Tip.

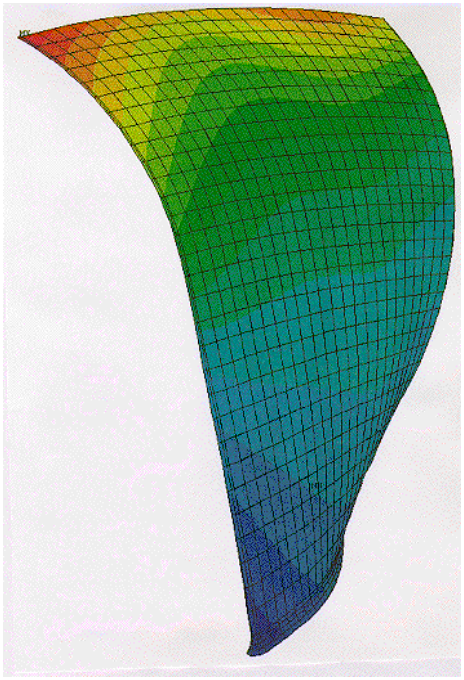

Figure 3-10. The Maximum Radial Deflection of the QHSF Rotor Blade Tip Is Only 0.051 In.

The resulting Campbell diagrams are shown in Figure 3-11 along with the first six excitation orders. Vertical lines highlight the design speed of 15,444 rpm as well as the maximum test speed of 110 percent. Design speed frequency margin with respect to the nearest excitation order for the first five modes is tabulated below.

	Mode/Engine Order				
Conditions	1/2E	2/3E	3/4E	4/6E	5/6E
ADP temp, 15,444 rpm	58%	15%	5%	6%	2%

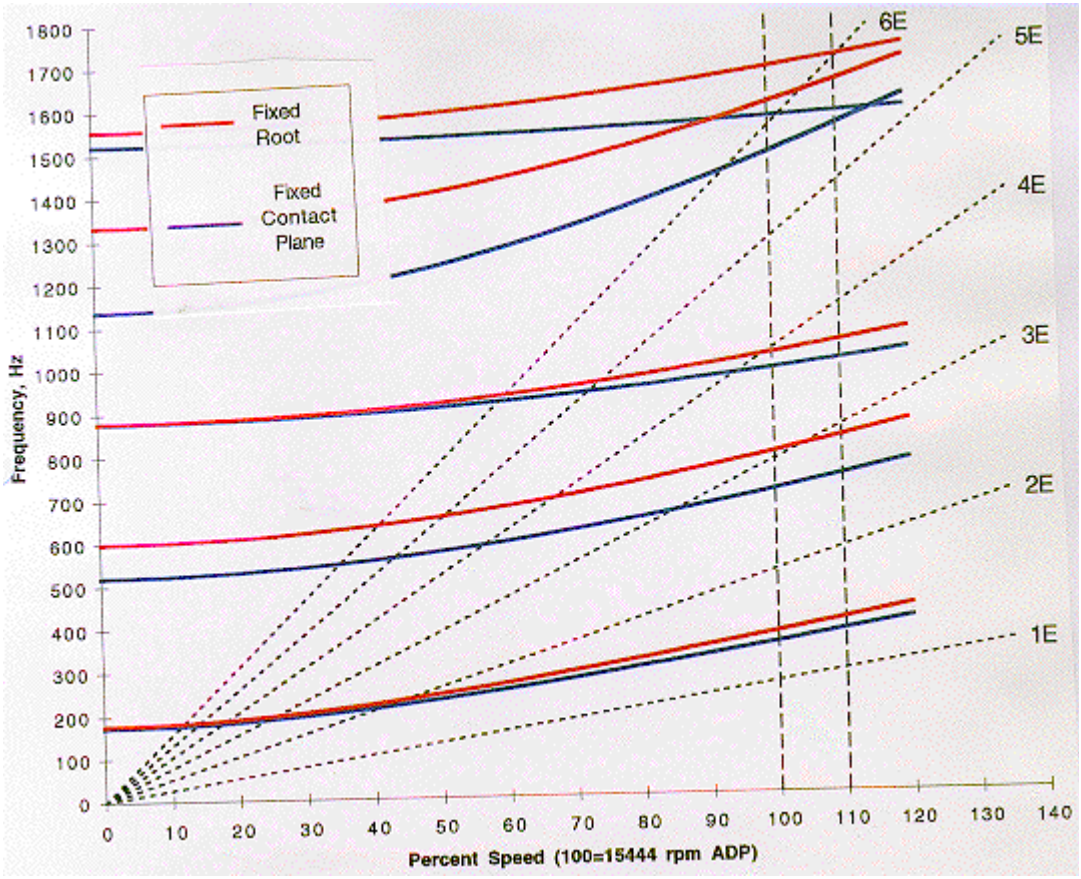

Figure 3-11. The Campbell Diagram for the QHSF Rotor Blade Shows the 3E Mode Crossing in the Fan Operating Range.

As the Campbell diagrams illustrate, a significant frequency shift was experienced for Modes 2 and 4 after adding the attachment to the model. The shift in Mode 2 frequency of 11 percent is especially relevant as it moved the 3E crossing to within the operating range.

Engines & Systems criteria for flutter is based on reduced frequency (fc/V), where f is the blade natural frequency, c is the chord at 75 percent span, and V is the design-point relative velocity at 75 percent span. The twist-to-flex ratio is used to characterize the mode as being flexure-dominate (small ratio) or torsion-dominant (large ratio). Generally accepted limits for fc/V are:

Bending Mode: fc/V >= 0.33
Torsion Mode: fc/V >= 1.60

The reduced frequency flutter parameter calculations are tabulated below.

	Parameter				Twist/Flex	
Mode	F, Hz	C, in.	V, ft/sec	fc/V	75%	95%
1	349	4.31	1435	0.6	.45	.37
2	704	4.31	1435	1.1	4.8	1.1
3	984	4.31	1435	1.6	1.3	1.8
4	1485	4.31	1435	2.3	1.2	.62
5	1568	4.31	1435	2.5	.82	.42

As can be seen in the above table, Mode 1 is predominantly flexure, thus its reduced frequency of 0.6 exceeds the standard criteria. Modes 2 and 3 both display significant torsional activity hence the standard criteria of 1.6 should apply. Mode 2 appears to be moderately aggressive, due in part to the frequency shift associated with the attachment.

A preliminary foreign-object-damage assessment performed on the QHSF blade indicated leading-edge thickness parameters to be well within Engines & Systems experience. This analysis is comparative in nature and considers only spanwise geometric characteristics, leading edge thickness distribution, blade count, metal angles, bird weight, as well as other parameters. The computed damage tolerance factors are compared with a data base consisting of very successful, marginal, and poor designs. This analysis however, can not account for the high degree of forward sweep and tangential lean built into the QHSF.

A more accurate prediction of ingestion damage was obtained using the NOSAPM code developed for the Air Force Wright Aeronautical Laboratories (ref. 3). NOSAPM can perform an inelastic, transient, impact response analysis on the rotating blade, and predict with good success the resulting permanent deformations of the airfoil. A key characteristic of the code is a loading model that allows an interactive determination of the pressure distribution on the impacted blade based on the blade's instantaneous deflected shape. With simple user input defining the geometry and initial conditions, i.e., rotor rpm, bird weight and trajectory, etc., the program solves for the blade transient response.

Figure 3-12 shows the impact model in detail. Since the impact analysis is nonlinear, the model was constructed using the "cold" geometry as described above. The shaded region represents the predefined set of impacted elements centered upon the designated impact radius.

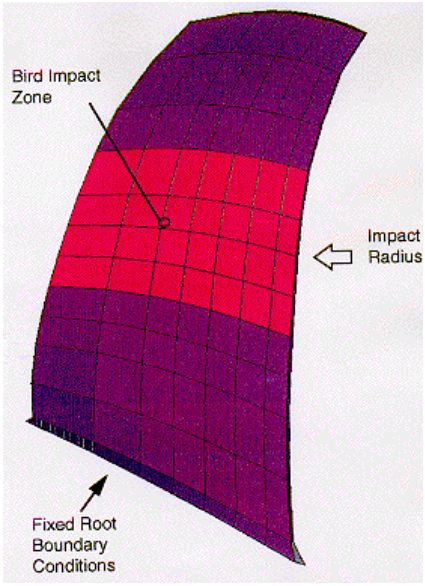

Figure 3-12. NOSAPM Impact Model for the QHSF Rotor Blade.

As certification requirements vary with the inlet area of the fan, this analysis was performed at baseline fan scale. The bird weight, impact radius, as well as the rotor rotational speed were chosen to match conditions defined for a FAA certification test of the baseline fan. These conditions were defined as follows:

Rotor Speed	88.8%
Bird Weight	1.5 pounds
Aircraft Forward Speed	138 knots
Impact Radius	56% span

Transient response of the blade due to the bird impact was determined. The maximum displacement of approximately 3.1 inches occurs at the tip trailing edge. Figure 3-13 shows the permanent deformation contours overlaid on the undeformed blade. Damage appears to be localized to the leading edge tip; the maximum deformation is 0.36 inch. The remainder of the blade appears to have been unaffected by the impact.

An identical analysis performed on the baseline blade revealed contrasting results. Instead of localized deformation like the QHSF, the baseline blade exhibited an overall gross torsional deformation (restagger).

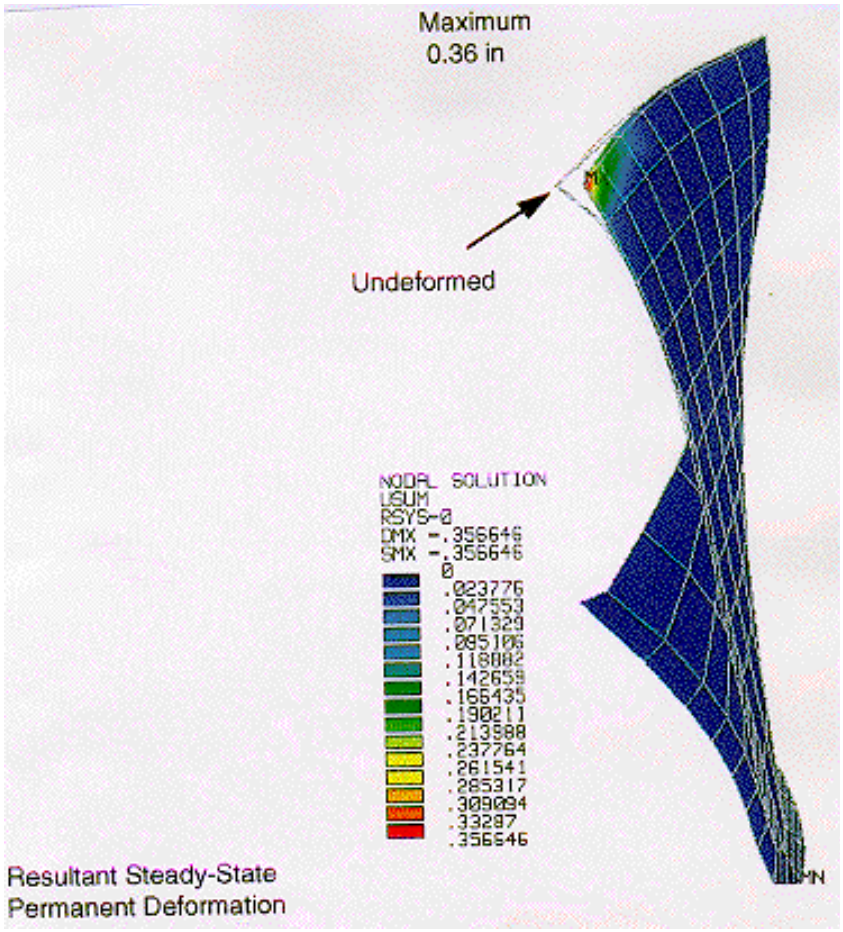

Figure 3-13. Bird Impact Damage for the QHSF Rotor Blade Is Predicted To Be Limited to the Blade Tip.

3.4 Disk Mechanical

Figure 3-14 shows the layout of the disk with undercuts and the preliminary torque sleeve mounted on the NASA balance. A 3-D finite element model of the disk was built and coupled with the 3-D blade and attachment models for stress analysis. The stresses in the disk and the attachment were minimized by repositioning the blade foot print on the attachment in the tangential direction. Figure 3-15 shows the maximum principal stresses in the disk at design speed for final rotor airfoil loads.

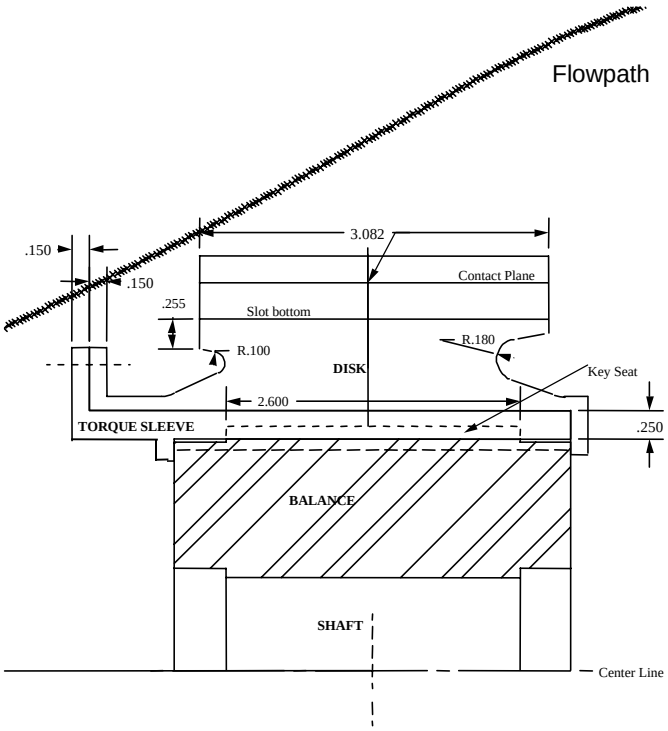

Figure 3-14. QHSF Disk Layout With Torque Sleeve Mounted on NASA Balance.

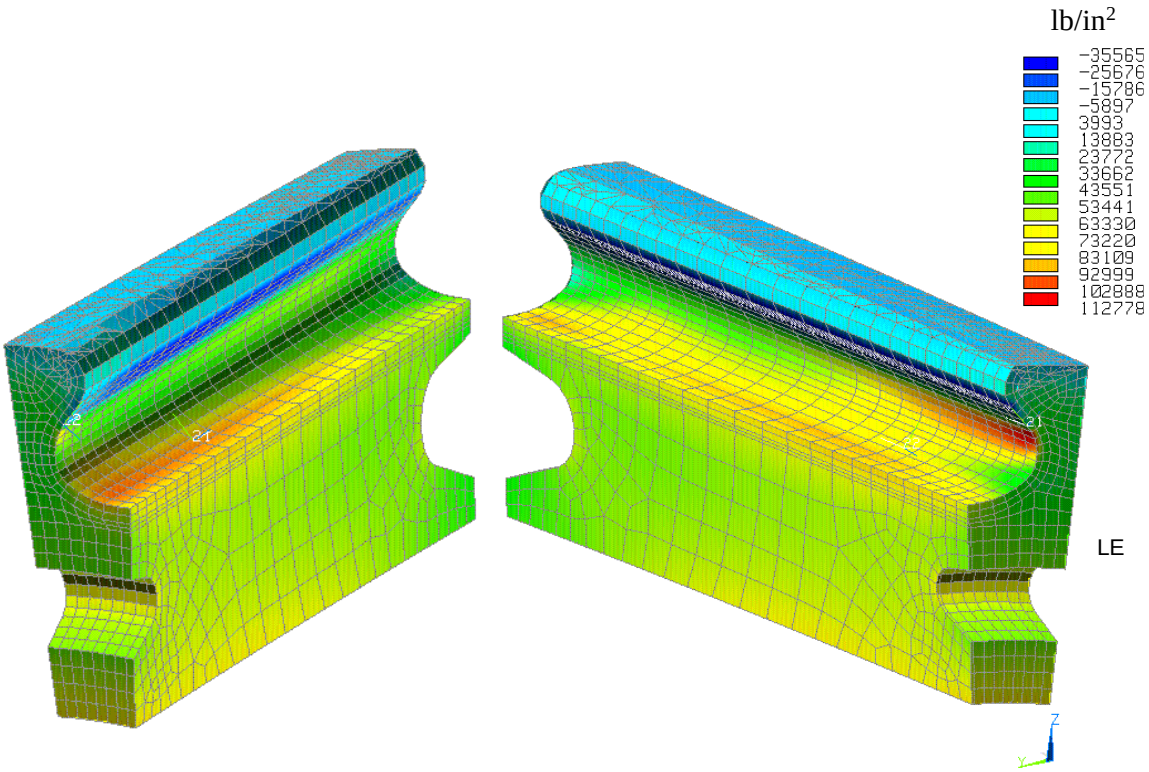

Figure 3-15. Maximum Principal Stresses in the Disk at Design Speed With the QHSF Airfoil Loads Are Shown.

3.5 Rotor Aerodynamic

The design concentrated on achieving a close performance match relative to the baseline such that the acoustic benefits of the forward-swept technology could be easily deduced from the test data. DAWES analyses at the aerodynamic design point showed only a slight shift in speedline characteristics relative to the baseline. At the design efficiency goal, the flow was 0.3 percent lower than the design goal, while the pressure ratio was 1.3 percent higher. At the design flow goal, the efficiency was 0.2 point lower while the pressure ratio was 0.3 percent lower. However, analyses completed from choke to stall showed slightly higher peak efficiency than the baseline and approximately one point higher as the rotor was throttled up from peak efficiency to stall. Spanwise distributions of pressure ratio, temperature ratio, efficiency, deviation, omega-bar, and D-factor are shown in Figure s 3-16 through 3-18, respectively. As previously mentioned, an endwall total pressure loss was being modeled at the rotor leading edge and the effect is evident in the figures.

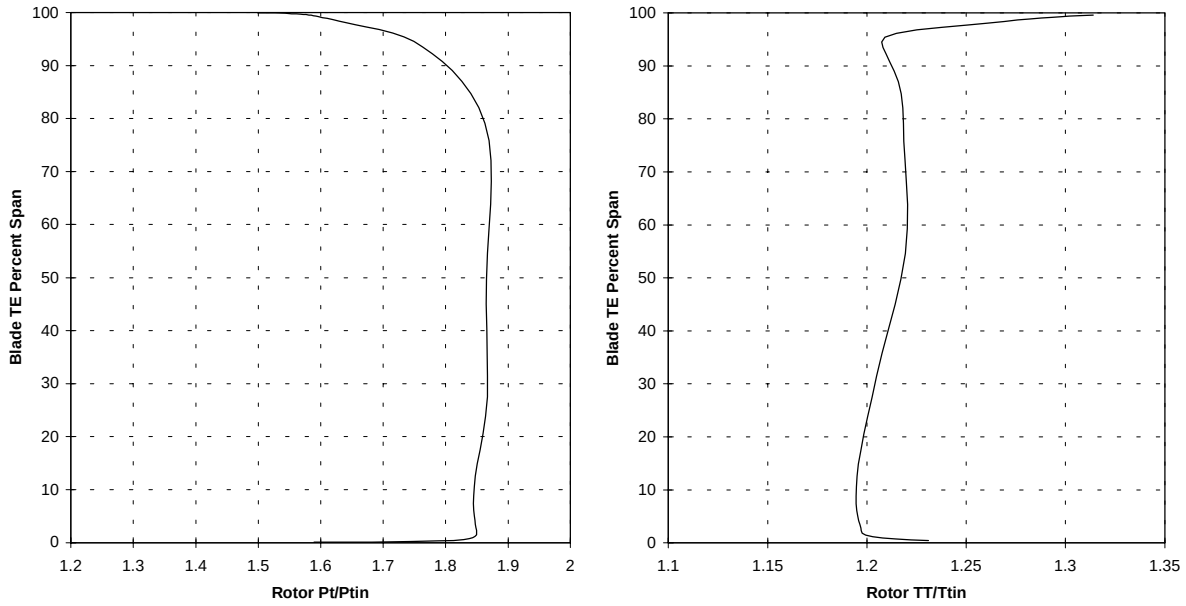

Figure 3-16. DAWES Calculated Rotor Pressure Ratio and Temperature Ratio at the Aerodynamic Design Point.

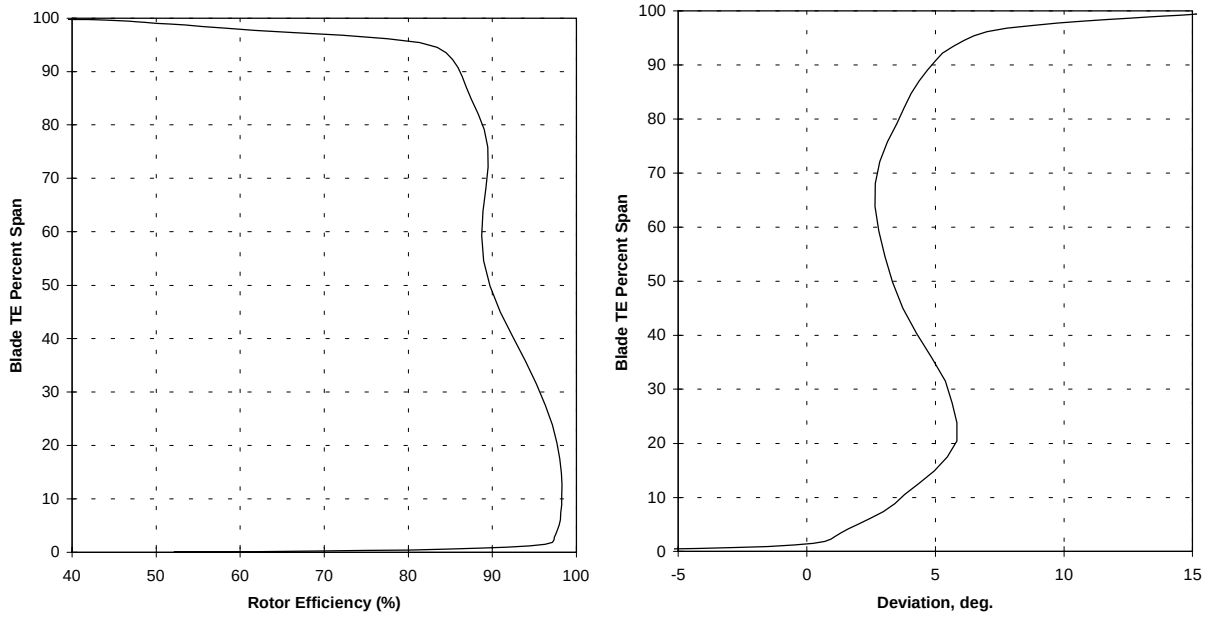

Figure 3-17. DAWES Calculated Rotor Efficiency and Deviation at the Aerodynamic Design Point.

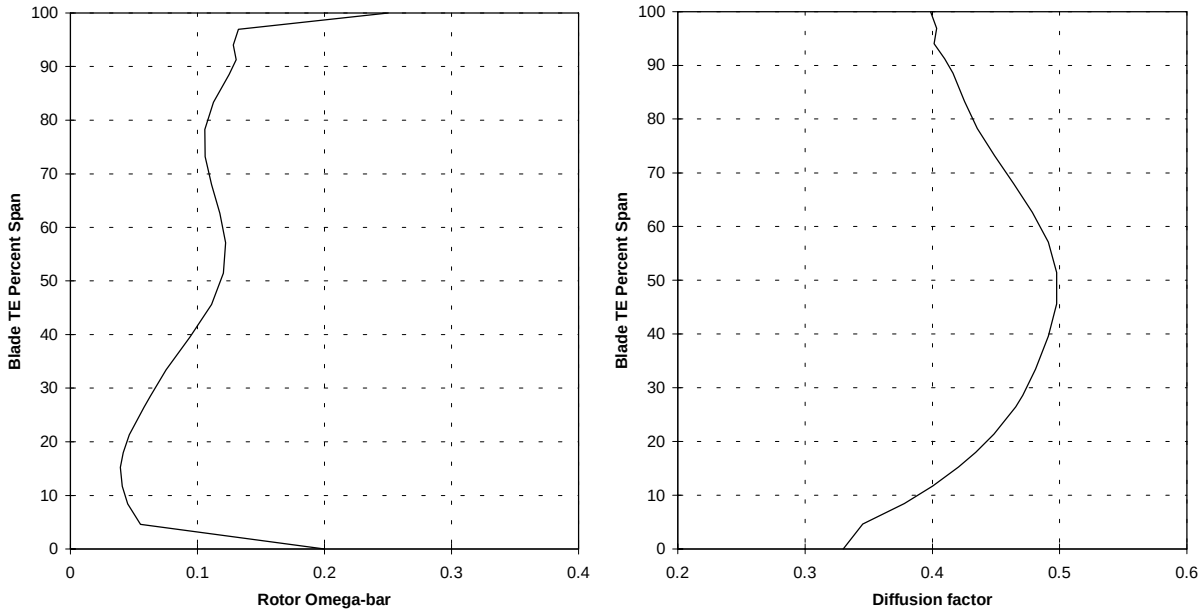

Figure 3-18. Rotor Omega-Bar and D-Factor at the Aerodynamic Design Point.

The increase in omega-bar near mid-span was due to an increase in shock loss as the blade effective sweep approached zero degrees. Effective sweep is the oblique shock angle as the inlet flow enters the blade passage. The oblique shock angle is a function of stream surface angle, blade lean angle, station lean angle (blade sweep), and relative flow angle. When the shock angle is considered a shock surface, both the blade leading edge and the impingement point on the suction surface of the adjacent blade (across the passage) must be accounted. Figures 3-19 and 3-20 show the difference in the effective sweep calculation (in terms of normal inlet relative Mach number) between leading edge only and a simple average calculation of the leading edge and the suction surface impingement point. The figures also show an inherent difference between the forward-swept QHSF and the aft -wept baseline in that the shock surface will always reduce the benefit of a forward-swept blade, while it will always increase the benefit of an aft swept blade. Although the QHSF design had significant benefits near the tip, it was slightly worse than the baseline near the mid-span.

A rotor-only predicted map for the QHSF is shown in Figure 3-21 and Figure 3-22. DAWES analyses were completed at the points indicated. Relative to test data of the baseline rotor, flow and work agreed very well but the efficiency would be adjusted higher by approximately 1.5 points.

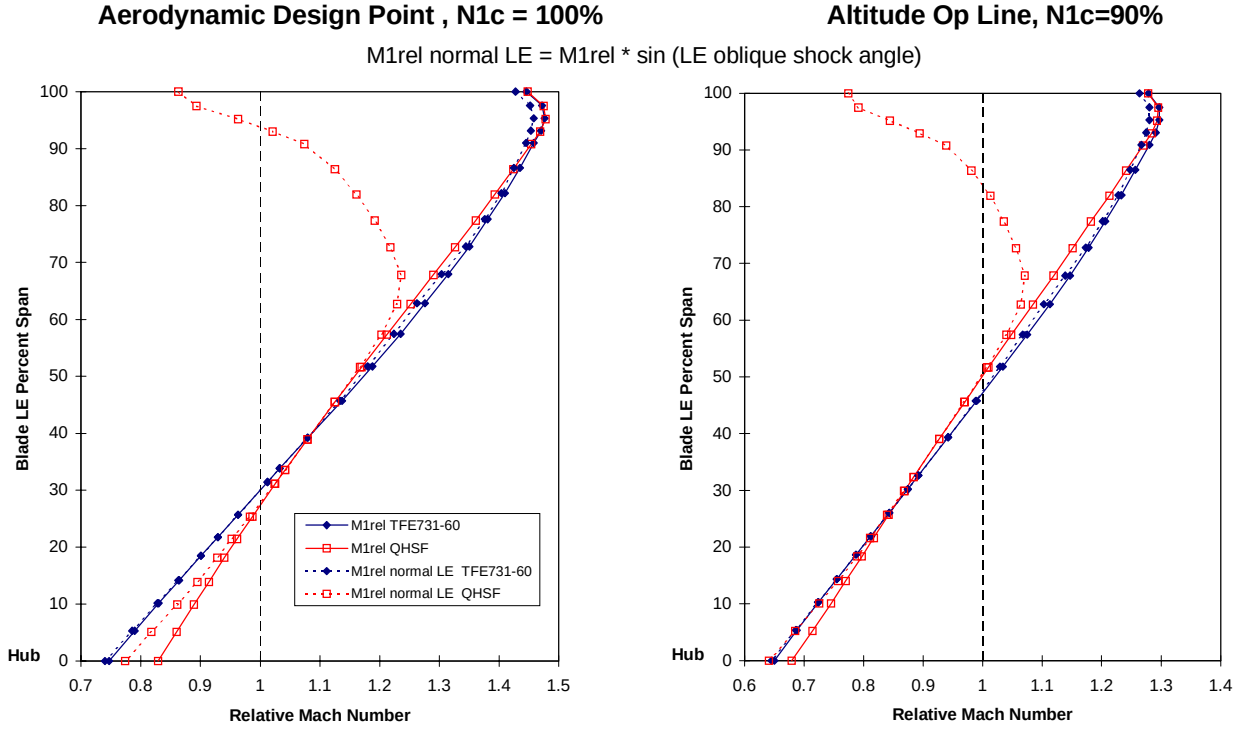

Figure 3-19. Effect of Blade Leading Edge Effective Sweep on Inlet Relative Normal Mach Number at 90 And 100% N1c.

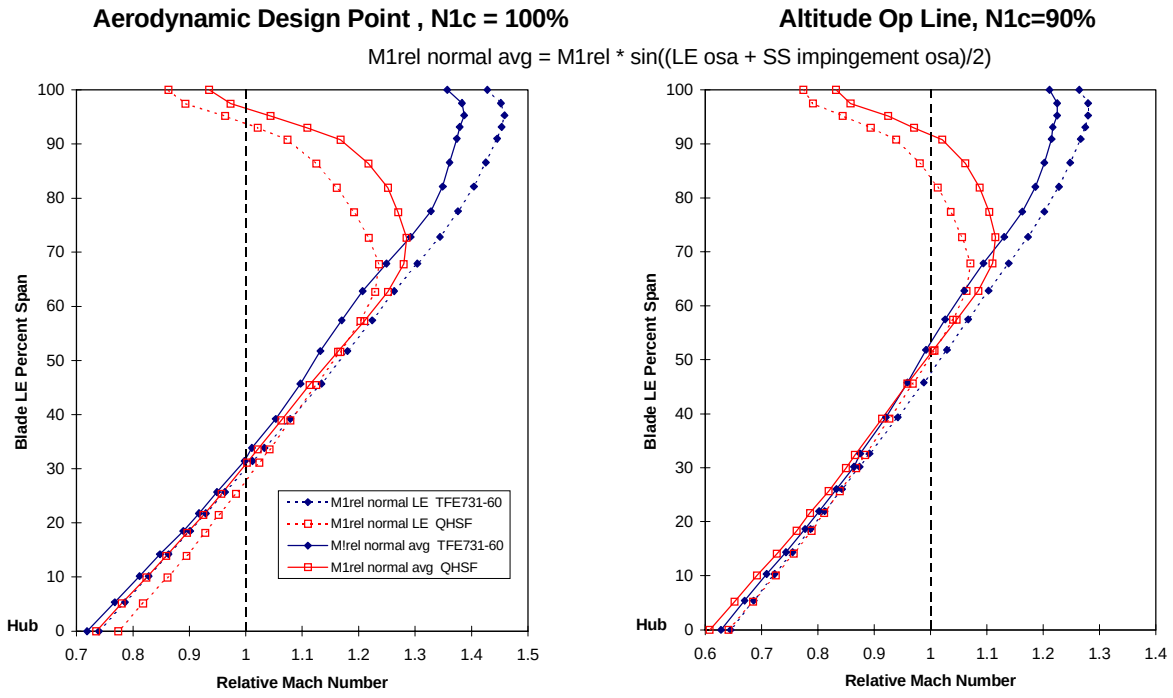

Figure 3-20. Effect of the Combination of Blade Leading Edge and Suction Surface Impingement Effective Sweep on Inlet Relative Normal Mach Number at 90 and 100% N1c.

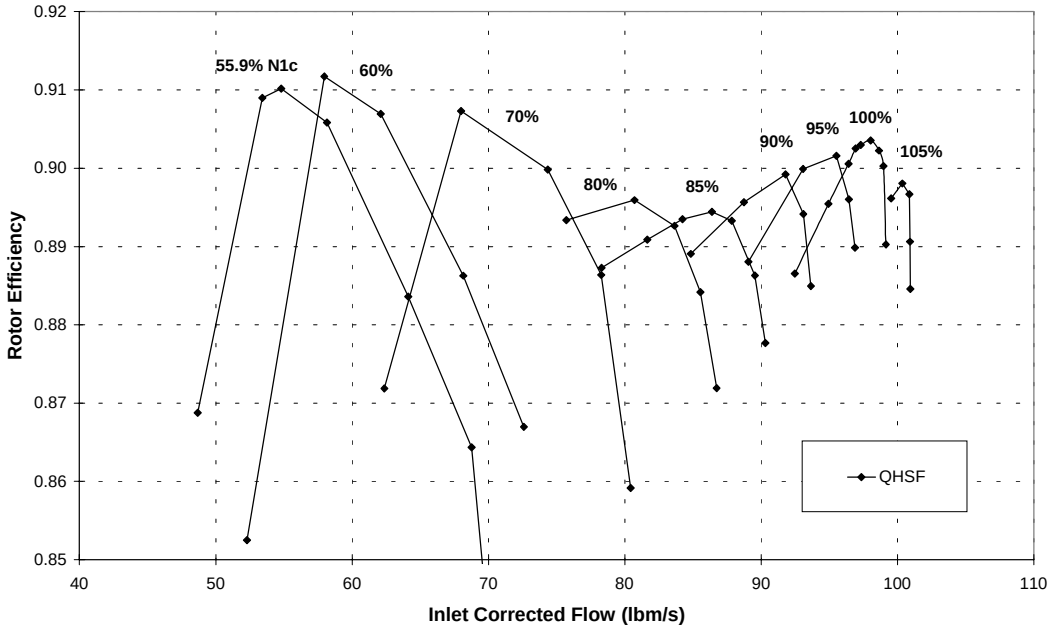

Figure 3-21. QHSF Predicted Map (Corrected Flow Versus Efficiency) Based on DAWES Analyses for the Rotor.

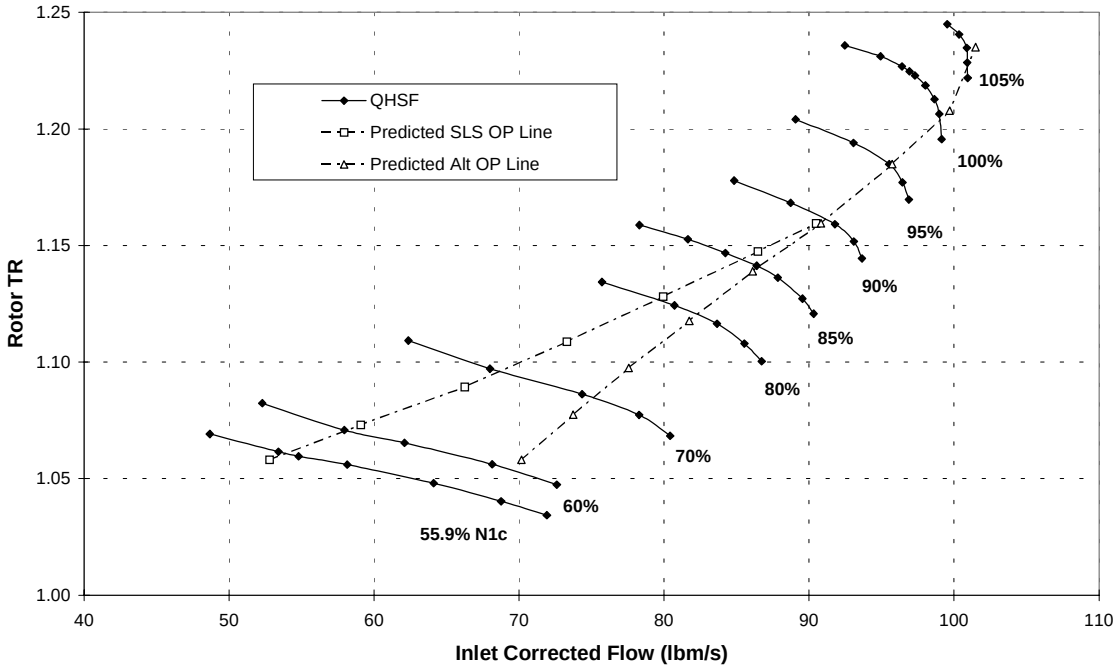

Figure 3-22. QHSF Predicted Map (Corrected Flow Versus Temperature) Based on DAWES Analyses With Predicted Operating Lines.

3.6 Stator Geometry

The analytical tools used in the stator design were the AXCAPS streamline curvature code and the DAWES 3-D viscous CFD code. AXCAPS does a 2-D streamline solution, calculating velocity triangles based on user-specified blade row performance profiles and also generates airfoil section coordinates for use in mechanical and CFD analysis. These airfoil sections are generated according to user specifications of chord, leading and trailing edge angles (or incidence and deviation), mean camber line angles, stacking, and thickness. AXCAPS was used mainly as a geometry generator since the extreme vane stacking was felt to make some of the 2-D calculations questionable.

The rotor exit velocity triangles that set the stator inlet velocity triangles were taken from the rotor DAWES solution at the design point. Some profile smoothing and adjustment was needed near the endwalls since AXCAPS does not impose a no-slip condition at the flowpath and airfoil. The flow used in the stator design AXCAPS cases was the flow predicted by the rotor DAWES model. The stator performance calculations used during the stator design were also done with DAWES. A DAWES model of the baseline stator produced good agreement with measured stator data.

The DAWES calculation grid used for this stator was as similar as possible to the grid used in the baseline stator DAWES model, with 41 nodes pitchwise, 71 nodes spanwise, and 121 nodes streamwise. The model was run through enough time steps to reach acceptable convergence. For the design point runs in the latter part of the design process, the model exit static pressure was adjusted so that the flow predicted by DAWES in the stator model matched the flow predicted by DAWES in the rotor model (and used in AXCAPS) to within 0.5 percent.

The final vane geometry was determined by the composite vane thickness. The vane leading and trailing edge, stagger, and camber angles are shown in Figure 3-23. The stator solidity, which is the same as the baseline stator, is shown in Figure 3-24. The vane maximum thickness to chord ratio, where the maximum thickness is defined as the tangential thickness, is shown in Figure 3-25.

The increase in thickness around 90 percent span is needed to maintain a desired normal thickness with an increasing vane lean angle. The waviness in the thickness distribution is not completely understood but is necessary to meet the required normal thickness profile. It is partially due to the fact that the vane lean angle at the maximum thickness location and at the trailing edge is slightly wavy. The maximum thickness is located at 60 percent of the mean camber line length as in the baseline vane. Mechanical, aerodynamic, and producibility considerations set this location. Figure 3-26 shows the chordwise distribution of mean camber line angle in dimensional form.

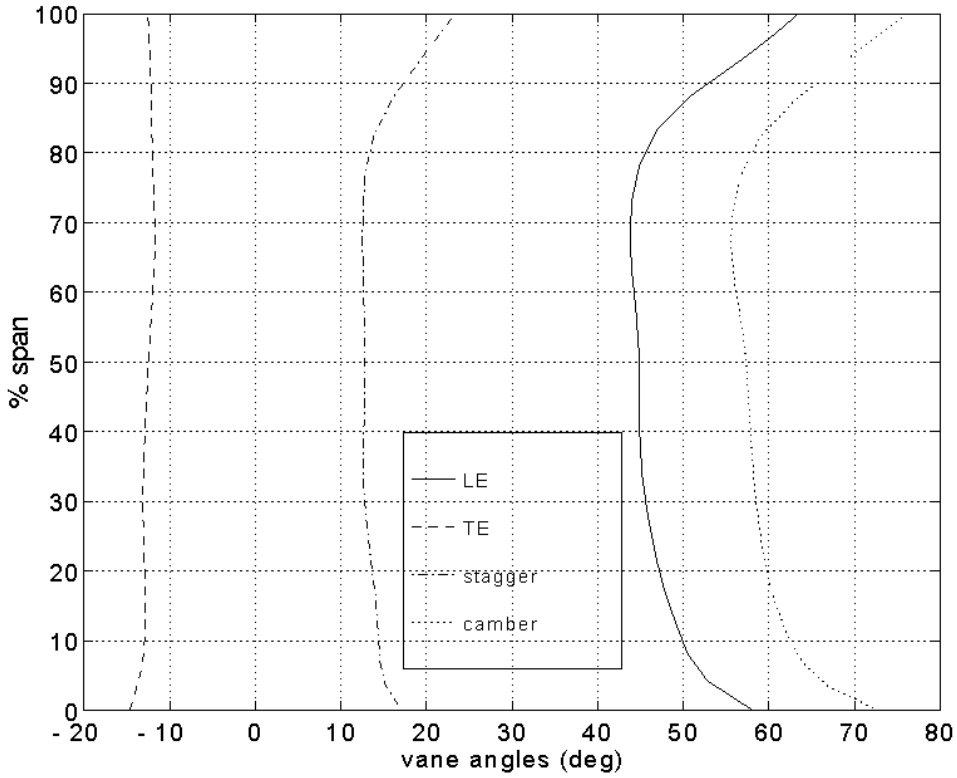

Figure 3-23. QHSF Vane Angles Show the Final Design.

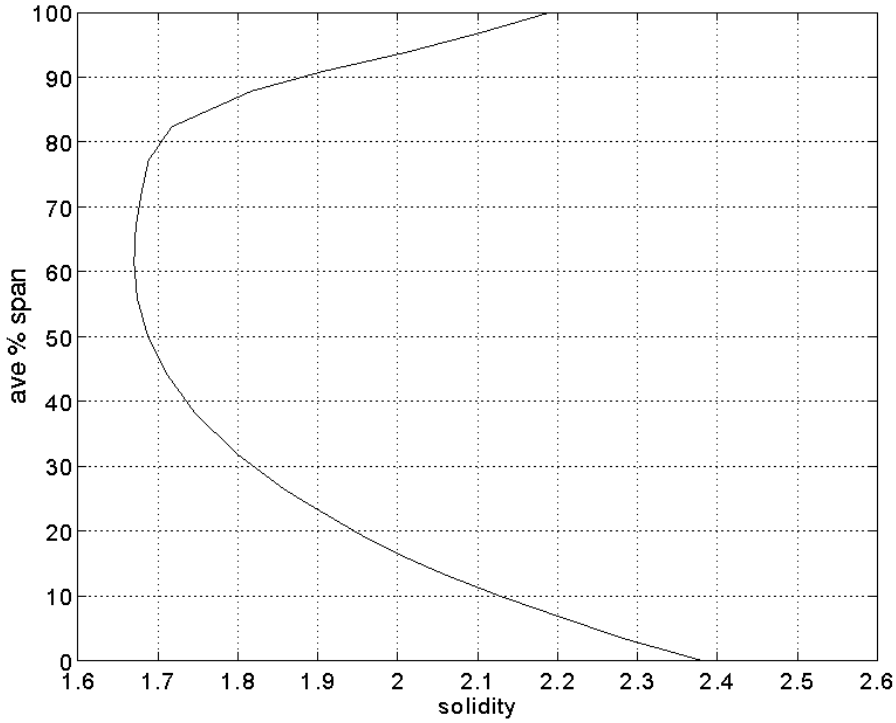

Figure 3-24. QHSF Stator Solidity for the Final Design.

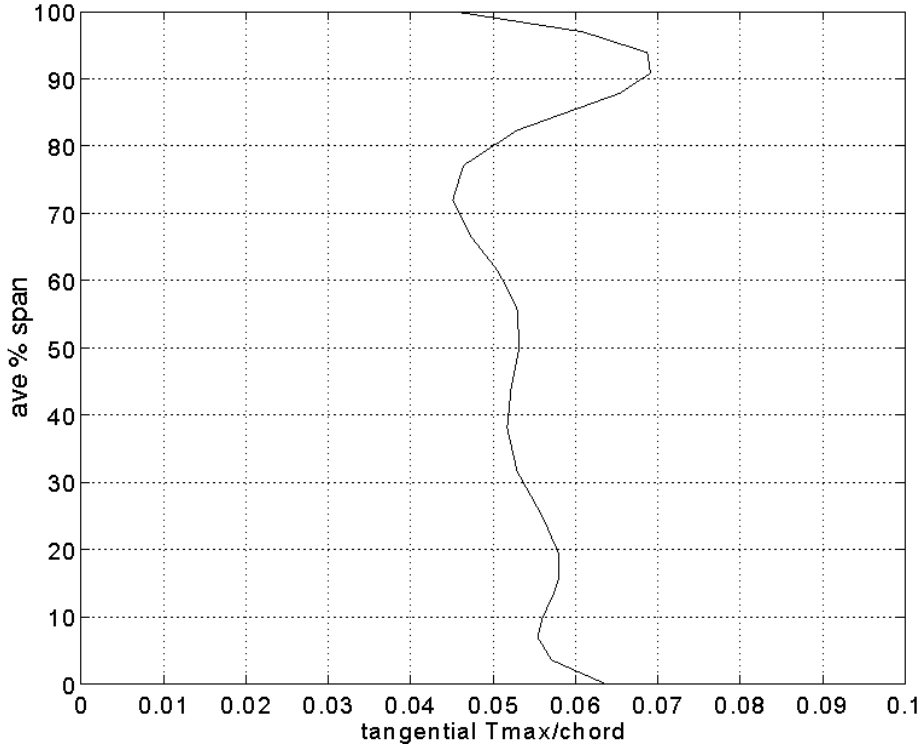

Figure 3-25. QHSF Stator Maximum Thickness Distribution for the Final Design.

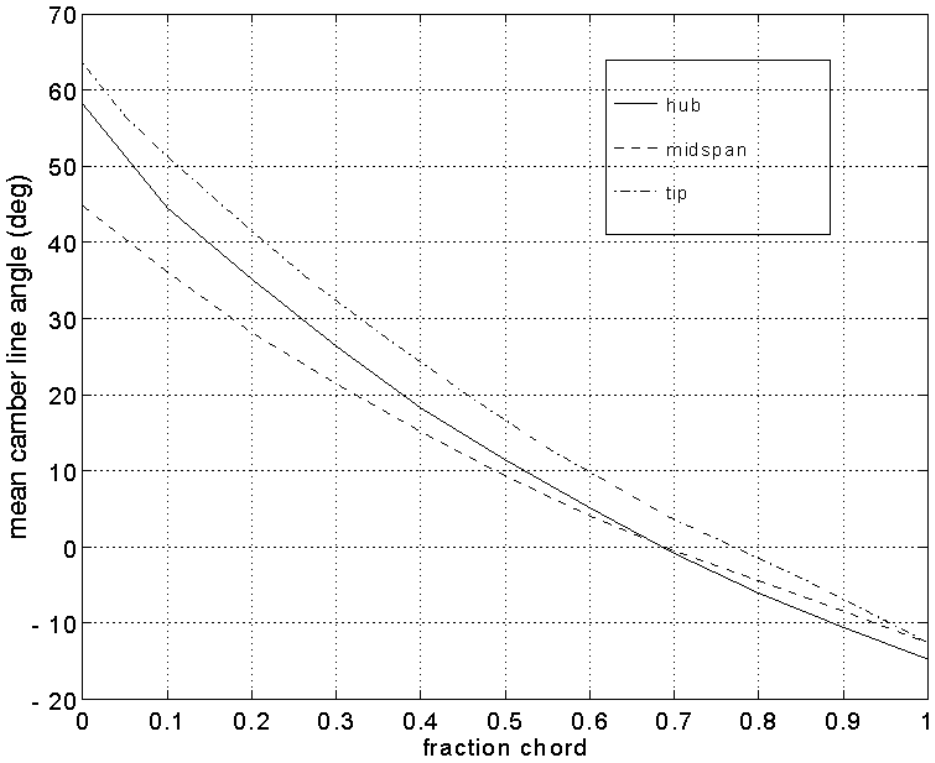

Figure 3-26. QHSF Stator Mean Camber Line Angles for the Final Design.

This graph shows how the vane camber is distributed from the leading edge (0) to the trailing edge (1). At the leading and trailing edge, these are the hub, mid-span, and tip angles from Figure 3-26. This figure provides a better idea of the actual curvature of different areas of the vane.

3.7 Stator Mechanical

The stator vanes for the QHSF were fabricated from composite materials using an Engines & Systems proprietary process. The composite construction allows the vanes to be made in any arbitrary 3-D shape. Figure 3-27 shows a schematic diagram of the vane construction.

Satisfying the empirical flutter criteria for vanes was a challenge for the aerodynamic and acoustic design. From an aerodynamic/acoustics perspective, a high degree of tangential bow is desirable. However, the addition of bow causes a significant change in the mode shape of the fundamental vibration mode. With small amounts of bow, this mode is predominantly a flexure mode, while a larger degree of bow changes it into a torsion mode. The problem arises because the flutter criteria based on reduced frequency, fc/V, is dependent on mode shape, with the torsion mode being much more difficult to satisfy. The recommended minimum for the empirical flutter parameter is 0.3 for the bending mode and 1.0 for torsion mode. Fundamental mode flutter parameters were found to be at least 25 percent lower than recommended value.

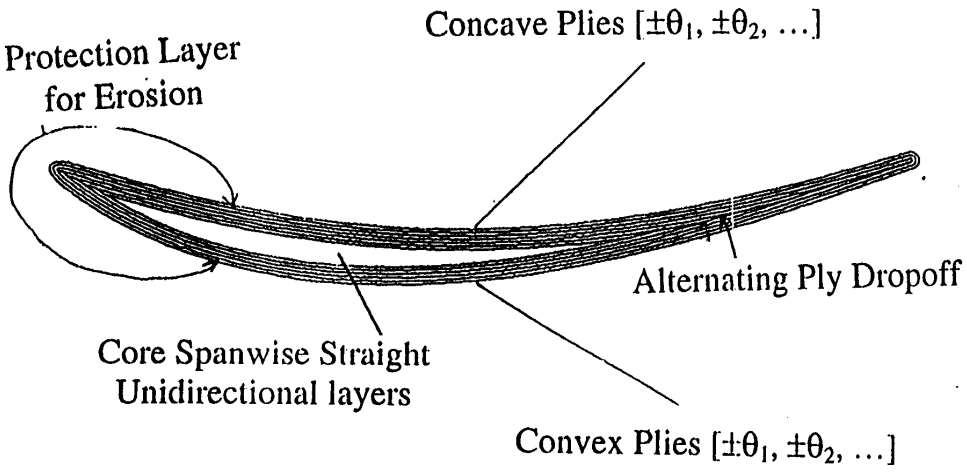

Figure 3-27. Fabrication Description of the QHSF Stator Vane.

A number of approaches were investigated to increase the frequency of the bowed stator vane, such as thickness increase, airfoil chord change, and attachment boundary condition modification. Vane hub and shroud attachment modifications were selected analytically that will increase flutter margin to baseline levels if vane flutter is seen in the Engines & Systems rig. The modification is to provide two retention bands instead of a conventional one-band retention scheme as used in the previous designs. This approach was found to consistently increase the flutter parameter by about 10 to 13 percent. This approach helps keep stator weight under control and provides new knowledge about the limits of vane flutter parameter while leaving a way out if flutter actually occurs. Figure 3-28 shows the two concepts for stator retention.

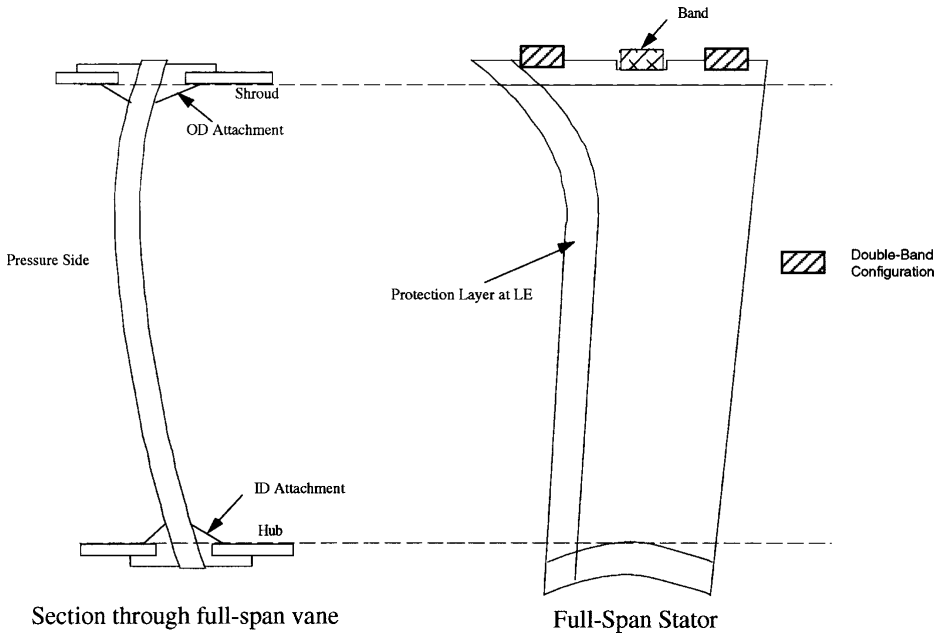

Figure 3-28. Retention Concepts for the QHSF Stator Vanes.

The static and vibration analysis results for the final QHSF stator design are presented for both the one and two band cases. Table 3-3 shows the frequency predictions for the two retention schemes. The mode shapes for first five modes are presented in Figure 3-29 for the one-band attachment. The mode shapes for the two-band approach are similar. In both the cases, the first mode is a torsion mode with frequency for the two-band concept about 14 percent higher than the one-band.

Table 3-3. Effect of Retention Scheme on Modal Frequencies.

Mode	Frequency, Hz		
	One-Band Scheme	Two-Band Scheme	% Change in Frequency
1	505.52	579.66	14.67
2	764.19	740.23	-3.14
3	861.4	867.59	0.72
4	997.33	1086.7	8.96
5	1296.1	1381.7	6.60

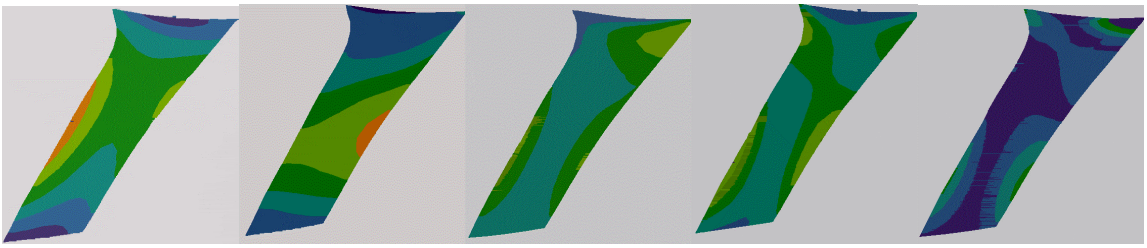

Figure 3-29. Vibratory Mode Shapes for the QHSF Stator Vane.

3.8 Stator Aerodynamics

After the final vane geometry was reached, the design point loss estimated by DAWES was applied to the AXCAPS model along with the design point rotor pressure ratio and temperature ratio profiles and flow predicted by DAWES. This evaluation was done to calculate performance information like stator D-factor that isn't easily extracted from DAWES results. Stator loss and D-factor profiles are shown in Figures 3-30 and 3-31.

The bump in D-factor around 25 percent span is caused by the flow splitter downstream of the vane trailing edge in AXCAPS. This causes streamtube area to increase as the flow moves radially inward and outward to get around the splitter, resulting in a local region of low stator exit velocity. This causes a local increase in D-factor. This may be exaggerated relative to real life but is probably present to some extent. The splitter wasn't modeled in DAWES because of

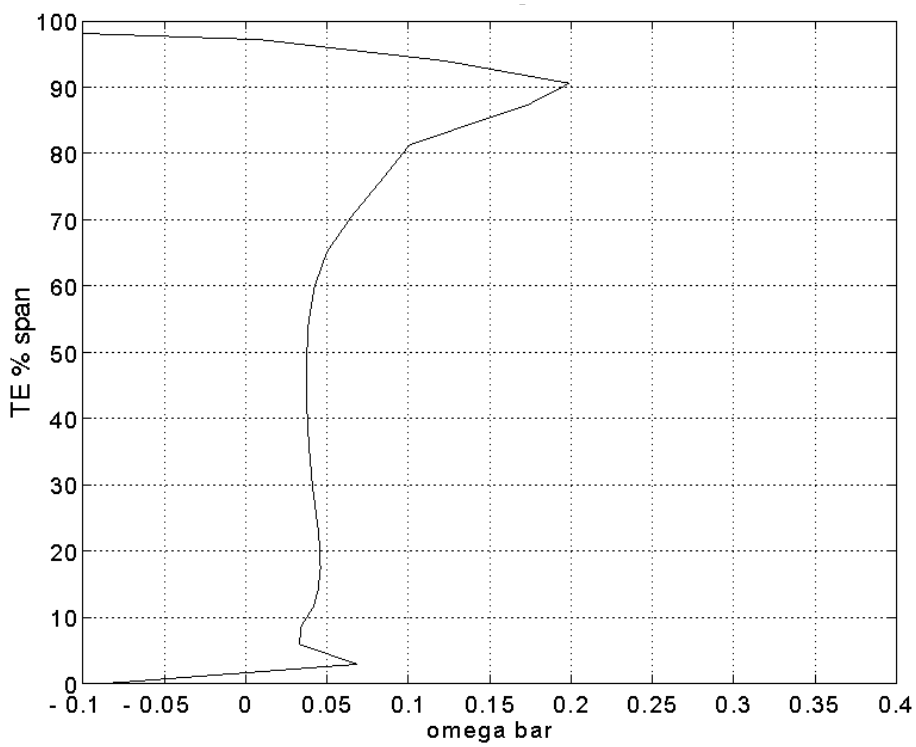

Figure 3-30. QHSF Stator Design Point Loss for the Final Configuration.

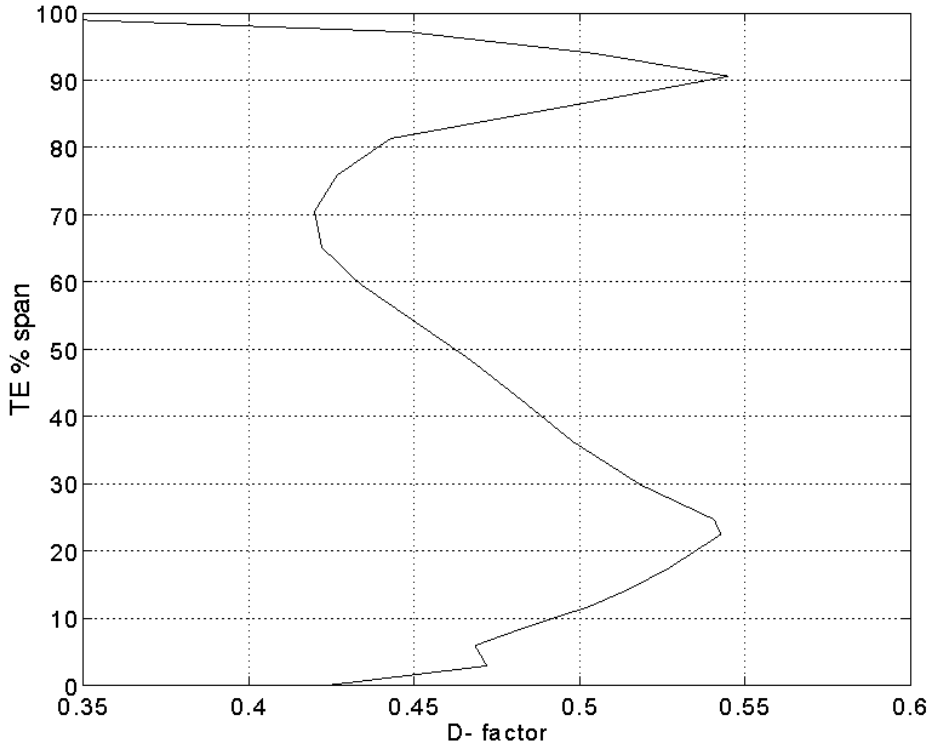

Figure 3-31. QHSF Stator Design Point D-Factor for the Final Configuration.

schedule constraints. The D-factor peak at 90 percent span is caused by the bump in the loss profile from DAWES. Since this loss bump is due to radial migration of lossy corner flow, the D-factor peak doesn't really indicate locally high stator loading. These D-factors, including the bumps, are in an acceptable range.

Figure 3-32 shows the leading and trailing edge Mach number profiles from AXCAPS. These profiles are slightly different than the actual DAWES profiles, particularly at the exit where DAWES doesn't include the effect of the splitter. These Mach number values are within previous Engines & Systems experience at the stator hub leading edge and at the core inlet region of the stator exit.

Figure 3-33 shows the efficiency at the stator trailing edge. This profile combines the DAWES predictions of rotor performance and stator loss and reflects the performance of the stage as a whole.

The stator performance at several off-design conditions was evaluated using DAWES. The points analyzed were on the sea level operating line at 55.9, 70, and 80 percent fan corrected design speed and on the altitude operating line at 90, 100, and 105 percent speed. The 55.9 percent speed point is a representative approach point where most of the acoustic V072 analysis has been done. The 100 percent speed operating line point is slightly lower on the speed line than the design point so a separate run was done here. The stator inlet conditions for the stator DAWES model came from rotor exit velocity triangles predicted by the rotor DAWES model at these points. Figures 3-34 and 3-35 show stator loss and leading edge Mach number profiles at these off-design conditions. The loss bump increases between 100 and 105 percent speed and affects more of the span.

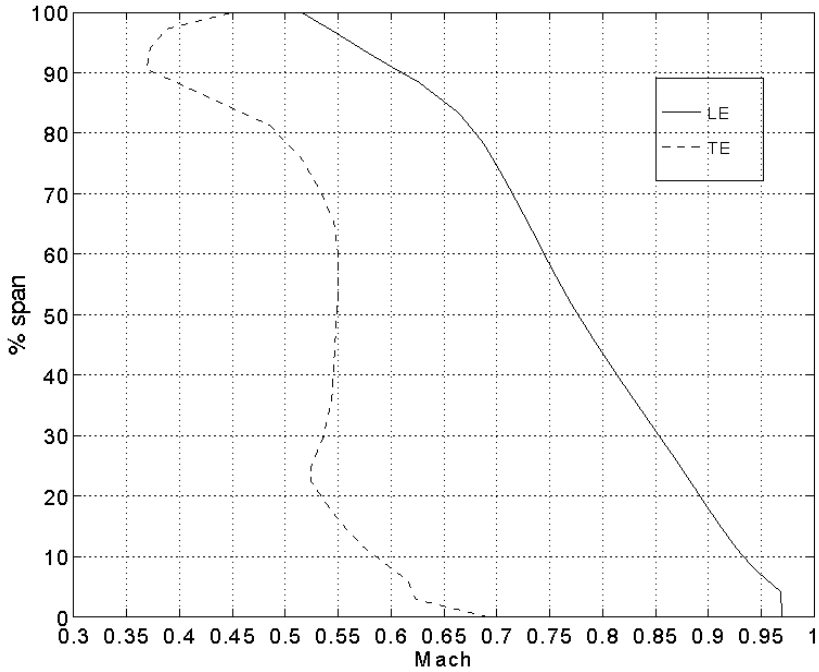

Figure 3-32. QHSF Stator Design Point Leading and Trailing Edge Mach Number Profile.

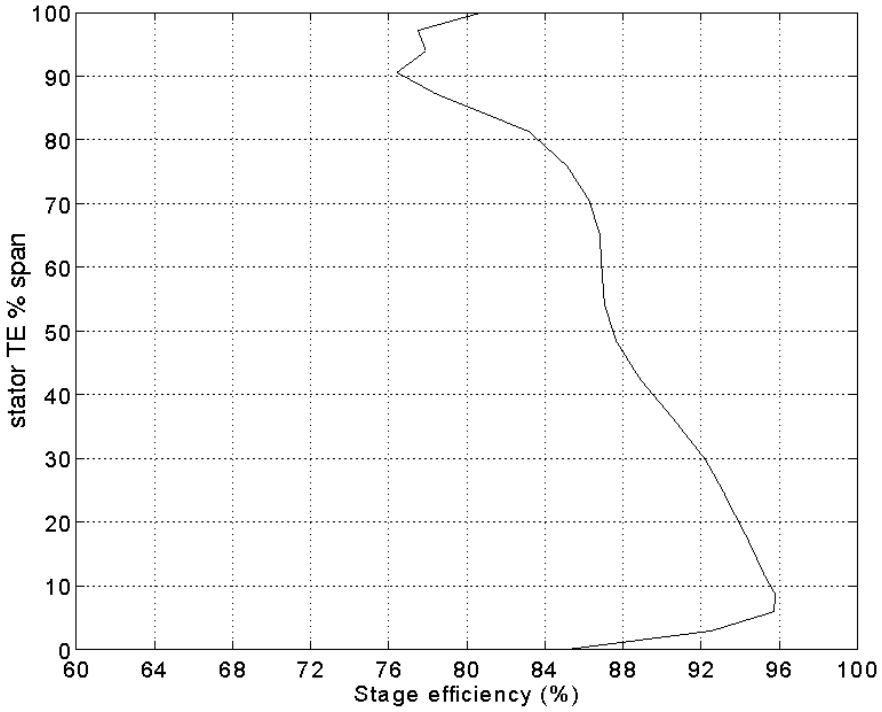

Figure 3-33. QHSF Stage Design Point Efficiency for the Final Design.

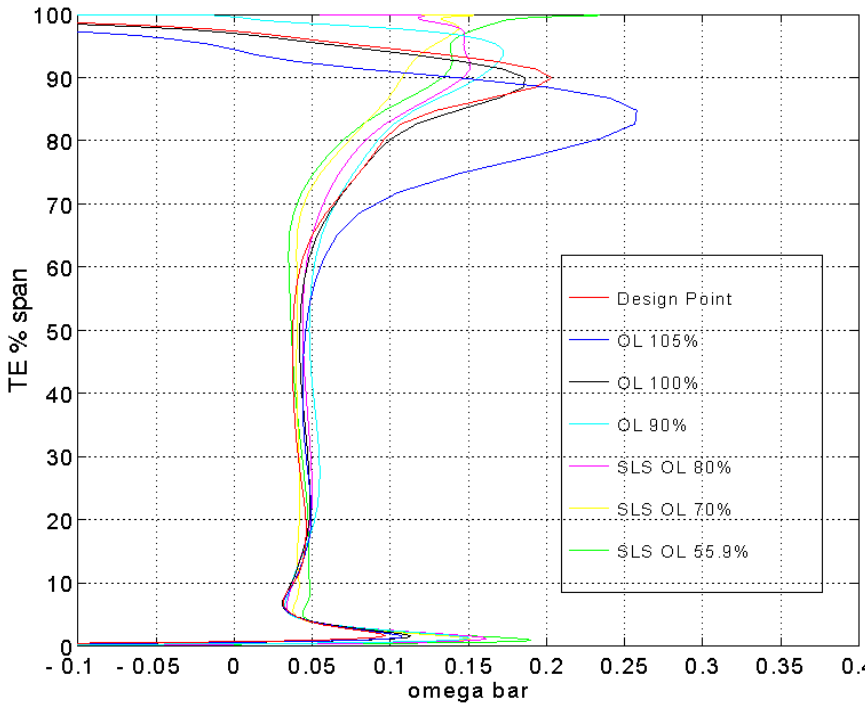

Figure 3-34. The QHSF Off-Design Stator Loss Is Well Behaved at Part Speed Conditions.

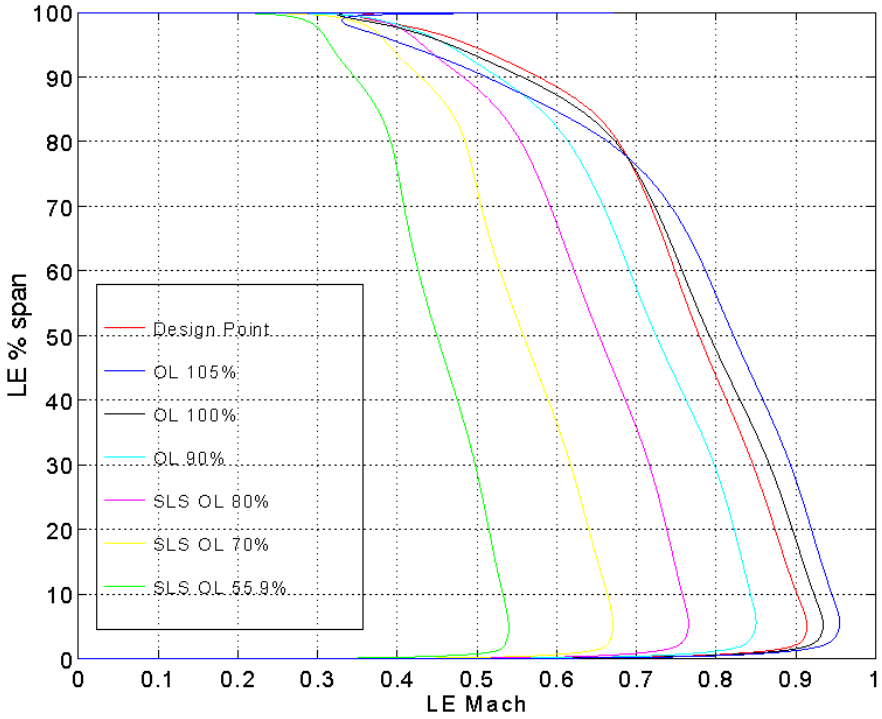

Figure 3-35. The QHSF Stator Leading Edge-Mach Numbers Remain Subsonic, Even at 105% Speed.

4. ADAPTIVE GRID AND FAN STAGE CFD MODELING

4.1 Introduction

The QHSF program included a Computational Fluid Dynamics (CFD) analysis activity. This modeling activity was in addition to the CFD analysis work performed as an integral part of the QHSF aerodynamic design process. It focused on specific analyses intended to provide an understanding of the flow physics impacting acoustic phenomena, and to extend the CFD analysis capability to include a fan stage, in addition to isolated rotor and stator blade rows.

Three CFD analysis tools were employed during the studies. The first program, DAWES (ref. 4), was the principal 3-D viscous design tool for the QHSF. The second program, RAMPANT (ref. 5), introduced the capability of adaptive unstructured meshing, in order to highly refine the computational mesh in the region of acoustically relevant flow structures. The third CFD tool, NASA's Adamczyk Average-Passage program (ref. 6 and 7), offered the capability of analyzing not only a single blade row, as DAWES could, but also provided the ability to analyze the full fan stage, in a steady-flow approximation, including blade-row interaction effects.

The primary emphasis during the CFD studies was on the prediction of rotor shock position. Accurate prediction of the shock location enabled prediction of the existence of Multiple Pure Tone (MPT) noise, a significant acoustic phenomenon in high-speed fans. Shock position was examined with the DAWES, RAMPANT, and Average-Passage programs. The DAWES predictions for the baseline and QHSF fan rotors were studied in detail to understand the flow physics related to the MPT noise. In addition, the special features of the RAMPANT and Average-Passage programs were employed to determine if the original DAWES analyses had been adequate for the task of shock location prediction. Stage analyses were performed with the Average-Passage program, for both the baseline and QHSF stages, to study the effect of blade-row interaction on rotor shock position.

The DAWES program was also used to study the behavior of the rotor wake/stator leading edge interaction for both the baseline and QHSF fans. This interaction of the rotor wakes with the downstream stationary blade row has the potential to generate substantial noise.

4.2 DAWES Predictions of Flow Physics as Related to Acoustics Issues

4.2.1 Overview

The DAWES program is capable of analyzing isolated blade rows in steady flow, in the relative frame of reference. It employs a finite-volume time-marching solver for the 3-D thin-layer Navier-Stokes equations. DAWES flow simulations for the baseline fan rotor and the final design of the QHSF rotor were examined in detail, in order to better understand the relationship between the flow characteristics and the associated acoustic behavior of the components. The studies focused on two acoustic phenomena related to fans: Multiple Pure Tone (MPT) noise and rotor wake/stator interaction.

4.2.2 Rotor Shock Position

To more fully understand the impact on MPT noise of the acoustic tailoring used in the QHSF rotor design, a comparison of shock structure for the baseline fan and the QHSF rotors was performed using CFD analyses. For purposes of comparison of the two rotors, operating points on the 70, 85, and 100 percent speed lines were studied. For the baseline fan, these points covered the range from near MPT onset (70 percent), to near maximum MPT noise (85 percent), to MPT cutoff, where the shock was contained within the rotor passage (100 percent).

A comparison of the baseline and QHSF fan rotor shock structures at 85 percent speed illustrates the difference in the two rotors. At 90 percent span, a strong shock is present on the suction surface of the baseline rotor blade (Figure 4-1A). This shock extends across the adjacent passage, approximately 10 percent axial chord upstream of the leading edge of the rotor. This type of shock structure corresponds to the conditions that can generate MPT noise, and indeed, at 86.5 percent speed, the acoustic test data from the baseline fan rotor indicated that MPT noise was near a maximum. At 70 percent span, shown in Figure 4-1B, the supersonic region extends far enough outward from the suction surface that a shock is present approximately 20 percent axial chord upstream of the leading edge of the adjacent blade. The meridional plot, depicted in Figure 4-1C, shows evidence of a shock along the entire span on the suction surface of the blade. In the mid-span region, the gradient is not as strong and the upstream influence of the shock is not significant. However, near the rotor blade tip, the shock becomes much more crisp on the suction surface, as well as becomes sharply defined immediately upstream of the leading edge, showing evidence of extending over several passages (indicated by the multiple sets of closed contours upstream of the initial shock).

In contrast, when the QHSF rotor is analyzed at 85 percent speed, no evidence of a shock is present at 90 percent span (Figure 4-2A), although the flow does decelerate to subsonic conditions immediately inside the covered passage. The flow then accelerates near the trailing edge on the suction surface, and decelerates back to near-sonic conditions at the trailing edge. At 80 percent span, an inlet shock structure is displayed, extending from the suction surface of the blade, across the passage, approximately 10 percent of axial chord upstream of the adjacent blade (Figure 4-2B). Moving further inboard to 70 percent span, as shown in Figure 4-2C, the inlet shock is stronger and extends across multiple passages, upstream of the rotor blade row. The meridional view, presented in Figure 4-2D, shows that the strongest shock on the suction surface is concentrated at approximately 60 percent span, where the blade has a lesser amount of leading edge sweep. In addition, the portion of the shock structure that extends upstream has its strongest influence in the region from approximately 60 to 80 percent span, inboard of the maximum sweep angle of the rotor leading edge. In the outermost span region, the shock structure is not present, with only a weak pressure wave extending upstream through the inlet. In contrast, the baseline fan (Figure 4-1) shows a well-defined shock structure at 90 percent span. However, at 70 percent span, the baseline rotor shock has somewhat less strength than the QHSF rotor shock.

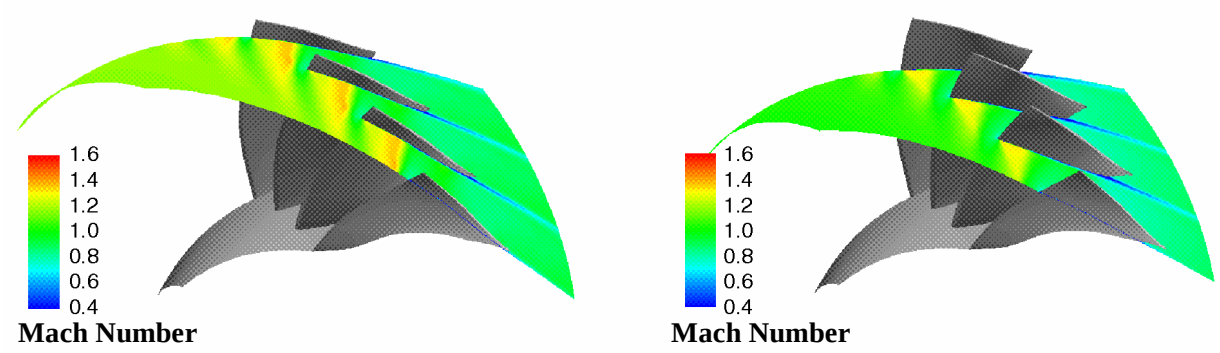

A. 90 Percent Span

B. 70 Percent Span

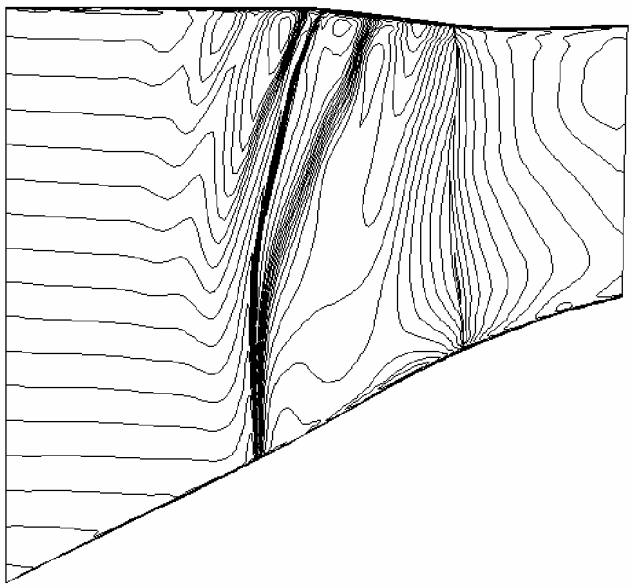

G7728-028A

C. 1.5 Percent Pitch From Suction Surface

Figure 4-1. A Strong Inlet Shock Structure Is Evident for the Baseline Fan Rotor at 85% Speed (Contours of Relative Mach Number).

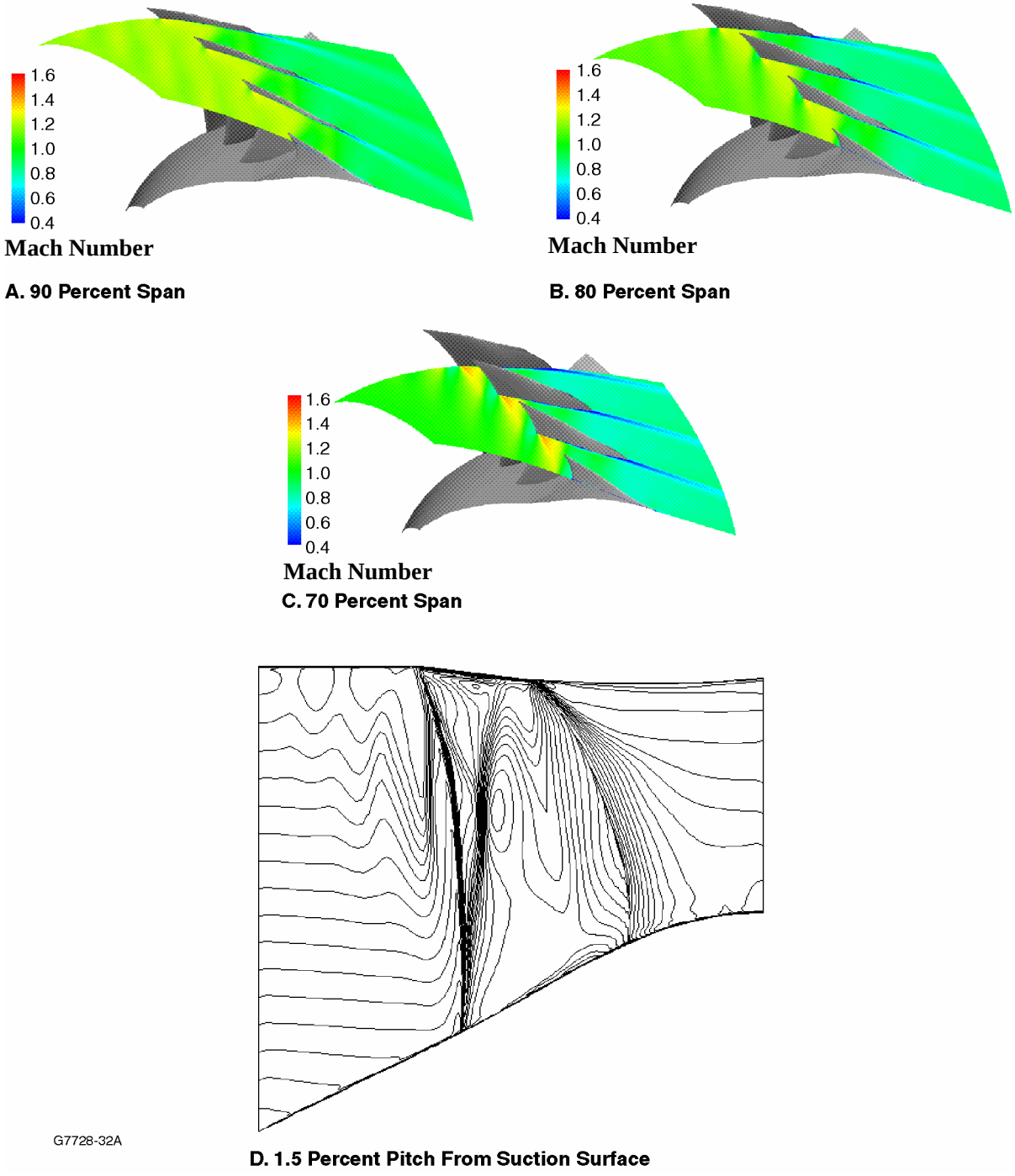

Figure 4-2. The Shock Structure for the QHSF Rotor at 85% Speed Is Much Weaker Near the Blade Tip, Compared to the Baseline Fan Rotor (Contours of Relative Mach Number).

4.2.3 Rotor Wake/Stator Leading Edge Interaction

In addition to the rotor inlet shock, which can produce MPT noise, another significant source of noise in fans results from the interaction between the rotor wake and the stator leading edge. If the trace speed of the rotor wake across the stator leading edge is supersonic, then noise will be present. To ensure that the trace speed is minimized, the wake should intersect the stator leading edge as closely as possible to orthogonal.

To graphically represent this, DAWES analyses for both the baseline fan and the QHSF were used to obtain contour plots of the rotor wake on a surface formed by tangentially sweeping the stator leading edge curve. By superimposing the stator leading edge curve on the rotor wake plot, the intersection of the rotor wake centerline and the stator leading edge could be displayed. The analyses were performed near approach speed, which is the operating condition at which rotor wake/stator interaction noise is most likely to dominate.

As may be seen in Figure 4-3, the rotor wakes for the baseline and QHSF fans at the stator leading edge surfaces are similar in shape, with both wakes becoming increasingly swept tangentially as radius increases. The baseline fan stator vanes are essentially radial in orientation. In contrast, the QHSF vanes have been designed with lean in the opposite direction to the rotor wake curvature, and with increasing lean near the shroud. This results in an almost orthogonal intersection between the wake and the vanes in the outer-span region, which would serve to substantially reduce the wake trace speed, and thus the rotor wake/stator interaction noise.

4.2.4 Summary

The studies of flow physics using the DAWES program showed that the use of a CFD tool is feasible for predicting flow behavior that impacts noise generation. The DAWES program was able to predict inlet shock location, and relate that location to the presence or absence of MPT noise, which permitted the use of shock location as a quality characteristic during the QHSF rotor Design of Experiments. In addition, the DAWES predictions of rotor wake shape at the stator leading edge allowed the design of a stator that would minimize the noise associated with rotor wake/stator interaction.

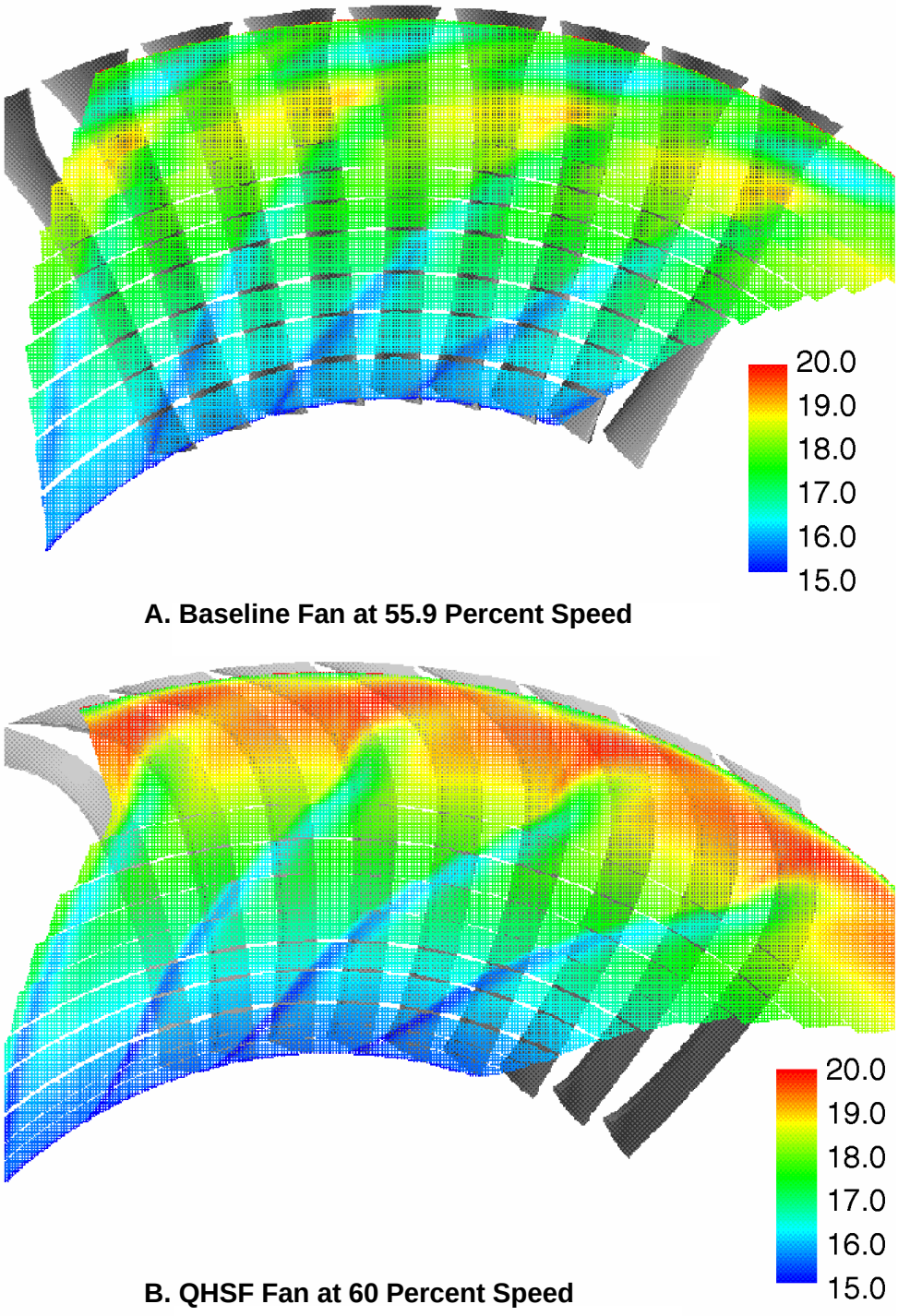

Figure 4-3. Contours of Relative Total Pressure (PSI) Depict the Rotor Wake at the Stator Leading Edge.

4.3 RAMPANT Analyses

Techniques to improve the prediction of rotor shock strength and position were the focus of the RAMPANT studies. The RAMPANT flow analysis program offers an adaptive mesh feature not found in the DAWES program. This capability allows the mesh to be refined in regions specified by the user, such as the zone around the rotor shock. By adapting the mesh in this manner, the analysis can then resolve the flow structures more precisely.

The RAMPANT program was applied to analyze the baseline fan rotor at the operating line point on the 81.1 percent speed line, which was within the MPT noise generation range. Comparison of the RAMPANT results, with and without the adaptive mesh, allowed a determination of the impact of selective mesh refinement on the prediction of shock position.

In order to assess the effect of grid adaptation, it was decided to initiate the RAMPANT analysis using a structured skewed-H DAWES-type grid. By starting the solution using a typical DAWES grid, the effect of grid adaptation in the vicinity of the rotor shock would represent a better comparison with "design-tool-quality" results.

A converged RAMPANT solution was first achieved. The adaptation capability was then applied to examine the effect on the rotor shock of increasing the grid resolution in the region near the shock. To accomplish this, two adaptations were performed based on static pressure gradient.

Examination of the rotor inlet shock behavior for the RAMPANT solution before and after grid adaptation (Figure 4-4) revealed that the inlet shock structure at 90 percent span had become more sharply defined with adaptation, but had not shifted position noticeably. At a location approximately 1.5 percent pitch from the suction surface, the appearance of the shock also remained virtually unchanged with adaptation. Thus, in this case, adaptation on static pressure gradient had no effect in shifting the shock position, because the initial grid appeared to offer sufficient resolution of the computational domain. However, adaptive meshing could have a significant benefit if the initial grid was sparse.

4.4 Adamczyk Average-Passage Analyses

4.4.1 Overview

The DAWES and RAMPANT programs provided predictions of fan rotor flow behavior for an isolated rotor blade row. In contrast, the Adamczyk Average-Passage program, SSTAGE, developed by NASA Glenn, offered the ability to obtain a steady-flow approximation of fan rotor-stator interaction via the average-passage model. By using this CFD tool to analyze both the isolated rotor and the stage, it was possible to determine the influence, if any, of the stator on the rotor inlet shock position.

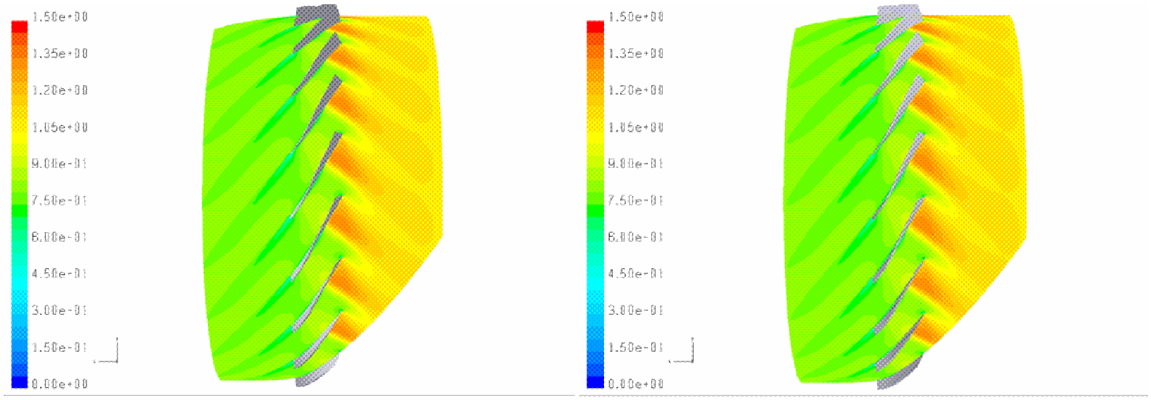

A. RAMPANT Mach Contours at 90 Percent Span

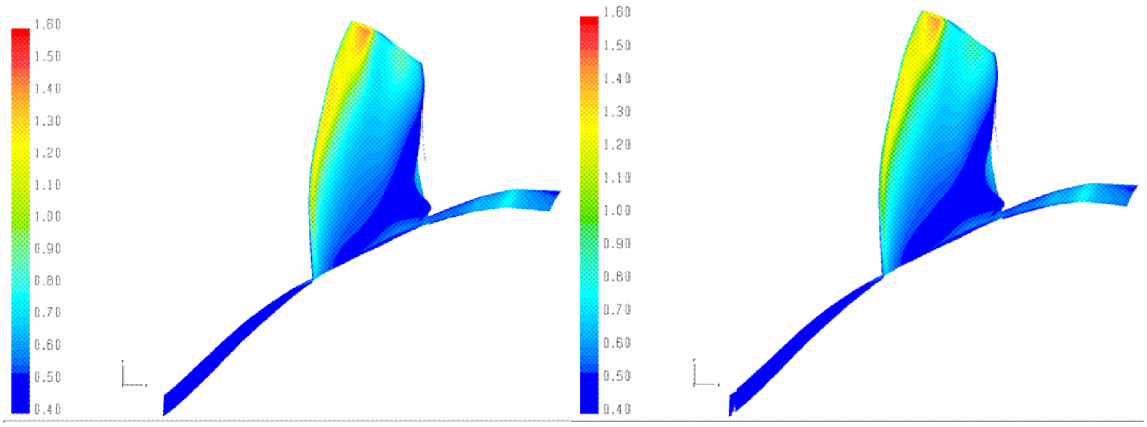

G7728-51B

B. RAMPANT Mach Contours at 1.5 Percent Pitch from Suction Surface

Figure 4-4. Comparison of Contours of Relative Mach Number for the Baseline Fan Rotor, Before and After Grid Adaptation on Static Pressure Gradient.

First, the isolated rotors of both the baseline and QHSF fans were analyzed on selected speed lines, using the Average-Passage program. Then, full fan stage analyses were performed, for both fans. Results of the rotor-only and stage solutions were then compared in order to identify any effects associated with rotor-stator interaction.

4.4.2 Rotor-Stator Interaction Studies

Shock shape was compared for the two rotors at 100 percent speed, using both the rotor-only and stage analyses of the Average-Passage program. As presented in Figure 4-5, for the baseline fan rotor, the general behavior of the shocks appears similar for the two analyses. However, some differences do exist. The passage shock at 90 percent span in the rotor-only solution appears oblique, with a acceleration downstream of the sonic region. This acceleration region is not evident in the stage solution. The passage shock is predicted to sit much further back in the rotor passage, when the stage analysis is performed. At 70 percent span, the stage solution shows a higher acceleration region near the suction surface trailing edge. In the meridional view, the stage prediction shows two shocks on the suction surface in the outer half of the span. The rotor-only solution shows only the forward shock. The common branch of the shock near the rotor tip is compressed closer to the shroud in the stage prediction.

The QHSF results at 100 percent speed are summarized in Figure 4-6. As with the baseline fan, the general behavior of the shocks is similar for the rotor-only and stage solutions. However, the rotor-only bow shock at 90 percent span has a slightly larger region of lower-speed flow than does the stage solution. At 70 percent span, the rotor-only prediction has a larger sonic region downstream of the oblique shock, upstream of the acceleration, and a slightly higher Mach number exists on the suction surface in the acceleration region. In the meridional view, the split shock has a stronger downstream branch in the outer span region for the stage analysis. The rotor-only solution has a stronger upstream branch in the outer span region.

When making comparisons between the rotor-only and stage analyses, it should be emphasized that the operating points analyzed in the two types of solutions were not located precisely at the same point on the speed line. Therefore, some differences seen between the two types of analyses may be attributed to shifted position on the speed line, rather than blade-row interaction effects.

4.4.3 Summary

The Adamczyk Average-Passage program, SSTAGE, was utilized to predict flow behavior for both the baseline and QHSF fan rotors, using both the rotor-only and stage analysis models. In general, shock behavior and shape were similar for the rotor-only and stage analyses. However, details of the shock structure were somewhat different. For the baseline fan rotor, the predicted rotor shock standoff distance was similar at part-speed, for the rotor-only and stage analyses; however, the passage shock location at 100 percent speed differed considerably.

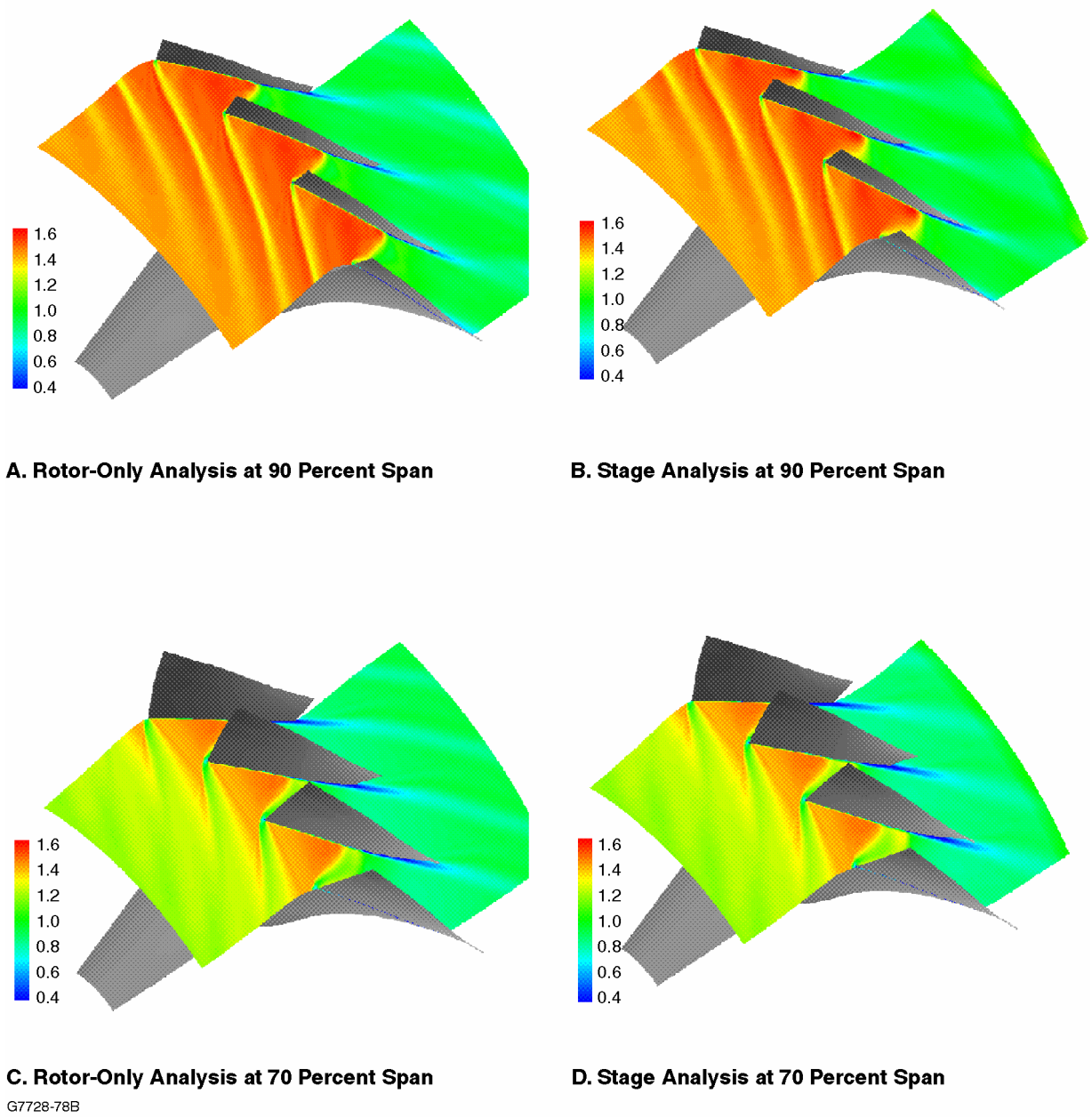

Figure 4-5. Comparison of Relative Mach Number Contours from Average-Passage Analyses for the Baseline Fan Rotor at 100% Speed, Using the Rotor-Only and Stage Models.

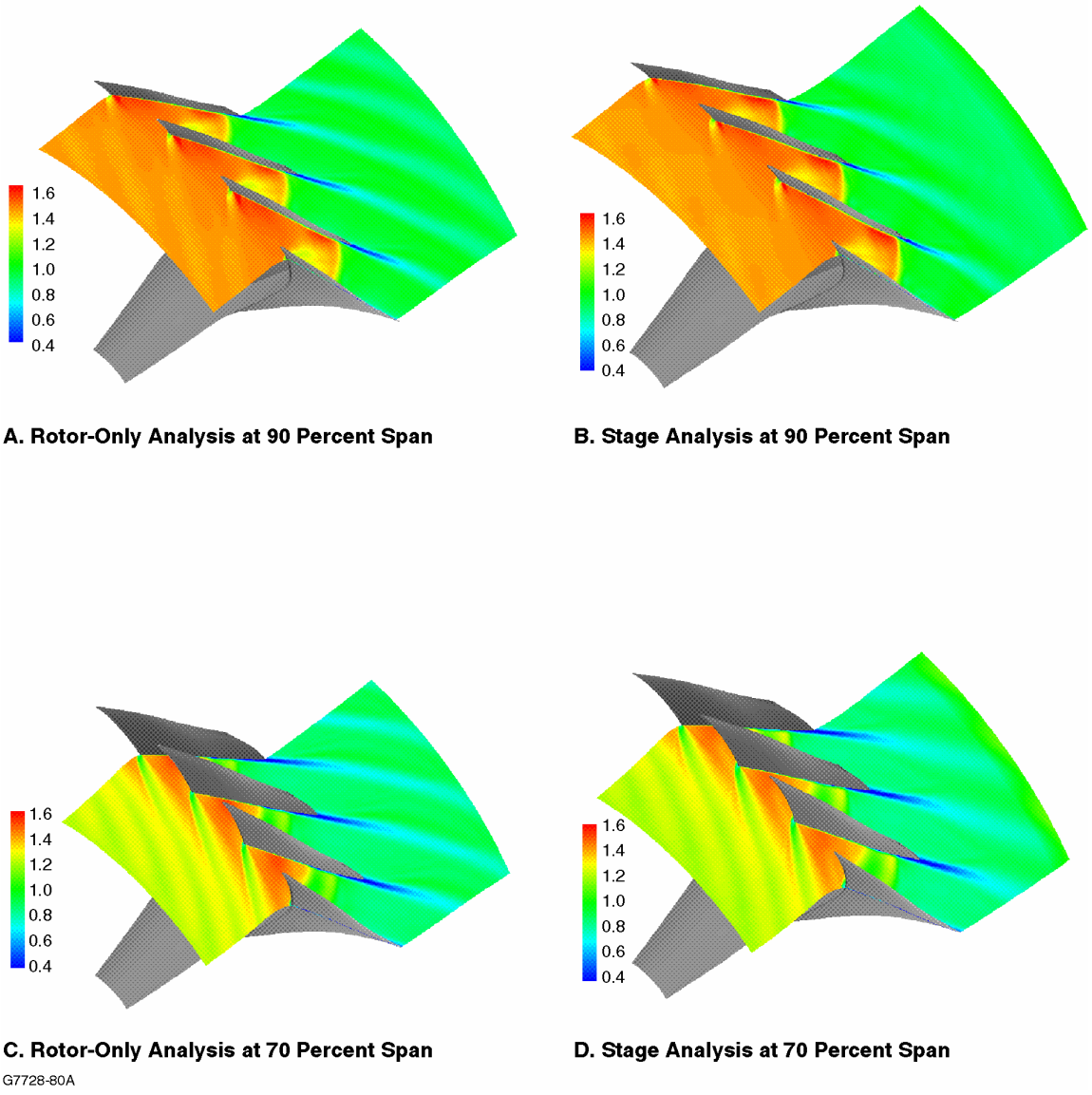

Figure 4-6. Comparison of Relative Mach Number Contours from Average-Passage Analyses for the QHSF Rotor at 100% Speed, Using the Rotor-Only and Stage Models.

4.5 Conclusions

The CFD predictions of flow physics related to acoustic issues performed in the CFD Modeling Subtask of the Quiet High-Speed Fan Program have shown that the use of such tools is feasible for predicting flow behavior that impacts noise generation. As a result of the insight into acoustic phenomena provided by CFD analyses during the design process, it is possible to tailor the fan geometry to reduce the influence of the principal noise generation sources.

Engines & Systems' principal CFD design tool, the DAWES program, was able to predict inlet shock location, and relate that location to the presence or absence of MPT noise, which permitted the use of shock location as a quality characteristic during the QHSF rotor DOE studies. In addition, the DAWES predictions of rotor wake shape at the stator leading edge allowed the design of a stator that would minimize the noise associated with rotor wake/stator interaction.

For the RAMPANT study, the use of grid adaption for shock position refinement did not appear to impact the solution substantially. However, the initial grid apparently provided adequate resolution of shock position. With a coarser initial grid, the adaption capability should prove beneficial.

The Adamczyk Average-Passage program, SSTAGE, was utilized to predict flow behavior, using both the rotor-only and stage analysis models. Comparisons were performed between the Average-Passage rotor-only results and the stage results. In general, the shock behavior and shape were similar for the two analyses, although details were somewhat different. At part-speed, the predicted rotor shock stand-off distance was similar, but the passage shock location at 100 percent speed differed considerably.

5. ACOUSTIC ANALYSIS

5.1 Multiple Pure Tone (MPT) Evaluation

5.1.1 Baseline Fan

The geometry and operating conditions of the baseline fan are such that the dominant shock structure consists of a normal shock emanating from the suction side of the rotor (passage shock). At all conditions except 100 percent corrected fan speed, the presence of a propagating passage shock (not contained within the blade passage) precludes the need for a bow shock at the blade leading edge since the flow is subsonic at this location (Figure 5-1). The literature discusses the effects of blade geometry and stagger angle variation on the strength and position of a bow shock (ref. 8 through 19). Evidently these studies were conducted on rotors that operated closer to choke where the passage shock was swallowed. It is assumed that the geometric variations classically assumed to be responsible for MPT noise generation due to their effect on bow shocks, in a similar way cause variations in the strength and propagation direction of the expelled (propagating) passage shocks.

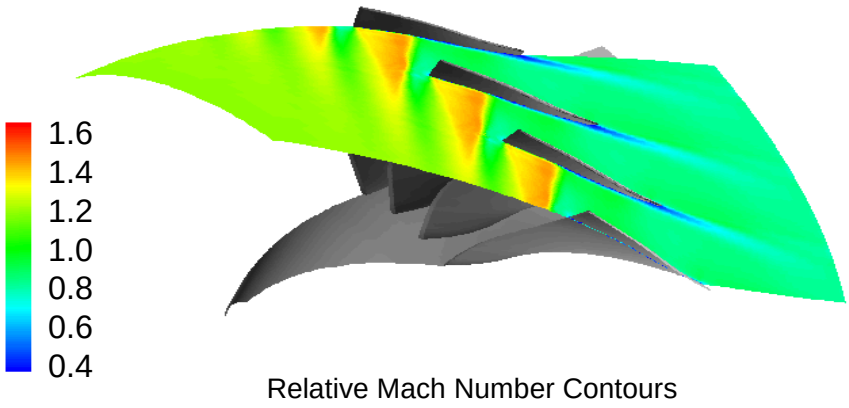

Figure 5-1. Sample CFD Calculation of the Shock Position Using the DAWES Code.

Using the DAWES program, the location of the passage shock relative to the leading edge of the following blade was predicted at a number of fan speeds. Figure 5-2 shows the linear relationship between shock location and wheel speed.

A correlation has been developed between the predicted rotor passage shock position relative to the leading edge of the downstream blade and the measured buzzsaw noise in the 500 Hz, 1 kHz, and 2 kHz octave bands which contain harmonics of shaft speed below the blade passage frequency (BPF). To capture noise level differences due to buzzsaw cut-on, inlet sound pressures (measured from 10 to 90 degrees from the inlet engine centerline) were summed over the three octave bands and normalized by the level at 75.3 percent corrected fan speed (the speed

above which MPT noise was cut-on). Initially, only the 2 kHz octave band was chosen to compare buzzsaw noise levels at different fan speeds, but further analysis showed that substantial acoustic energy existed at frequencies below 1 kHz (4/rev) at the higher speeds. Consequently, three octave bands were used to accurately reflect MPT noise levels.

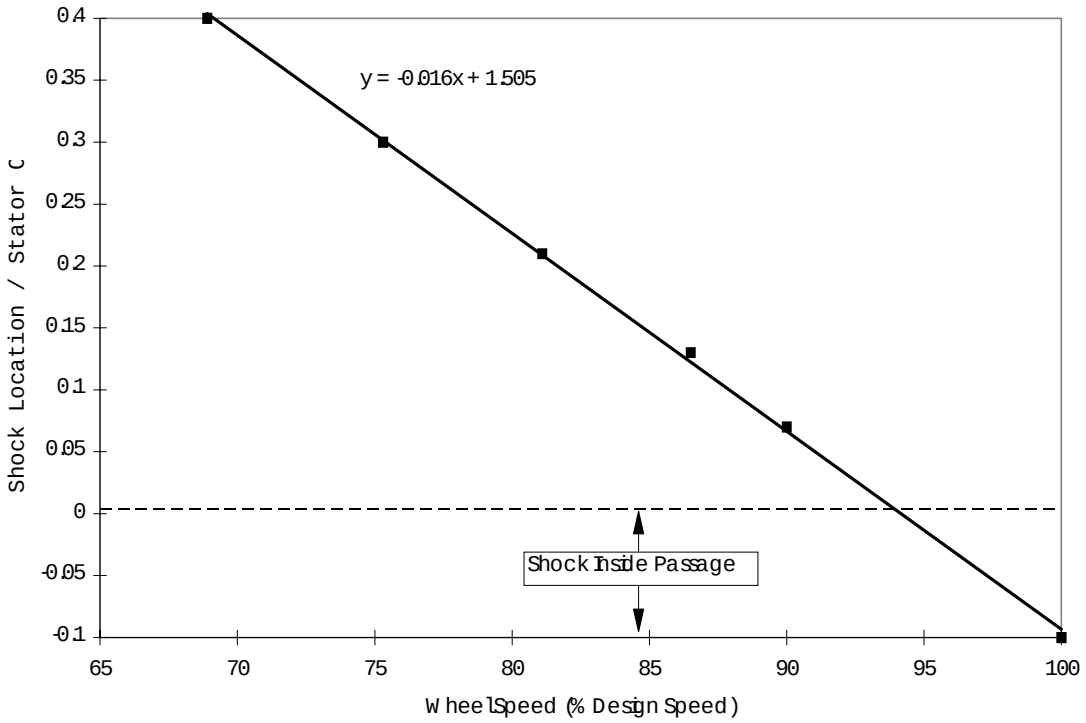

Figure 5-2. Variation of Inlet Shock Position With Wheel Speed, as Predicted by the DAWES Program, Indicates a Linear Relation.

Figure 5-3 shows the inlet-radiated noise versus passage shock position normalized by the rotor chord. As fan speed increases, the passage shock strength increases (Figure 5-4) as it moves closer to the leading edge of the following blade, and buzzsaw noise levels increase. Between 75.3 and 86.5 percent, speed the variation of measured sound pressure level is nearly linear with shock location following the equation:

$$SPL = -45.6(x) + 13.0$$

where SPL is the increase in level after MPT noise is cut-on, and x is the shock location divided by the rotor chord. From 86.5 to 90.0 percent speed, however, the correlation deviates from a linear behavior, showing little increase in noise level with increasing rotor speed and decreasing shock stand-off distance.

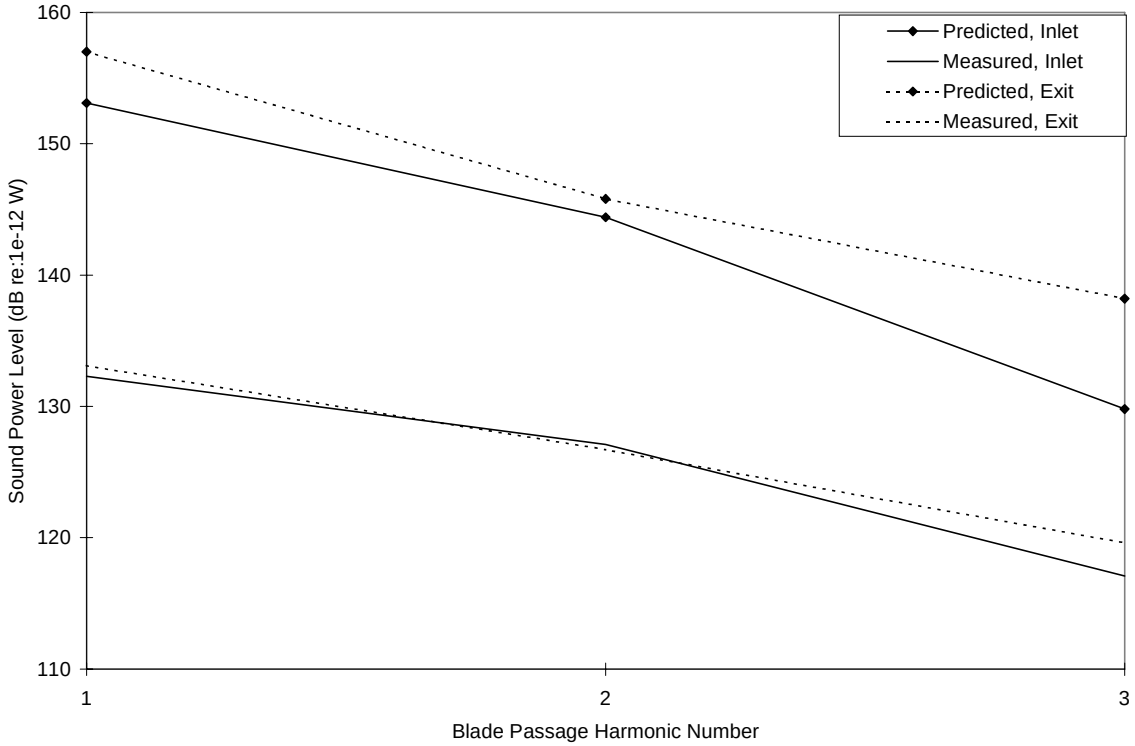

Figure 5-3. Correlation Between Passage Shock Position and Buzzsaw Noise for the Baseline Engine.

At 90 percent speed, the shock location is very near the leading edge of the downstream blade. It may be with asymmetric blade shapes and stagger angles, the leading edge of the following blade interferes with the propagation of the passage shock to the far field. From Figure 5-2, it can be inferred that near 95 percent speed, the passage shock is completely swallowed and buzzsaw noise is cut off. This is confirmed because in cruise (near 100 percent corrected fan speed), the baseline engine generates no buzzsaw noise.

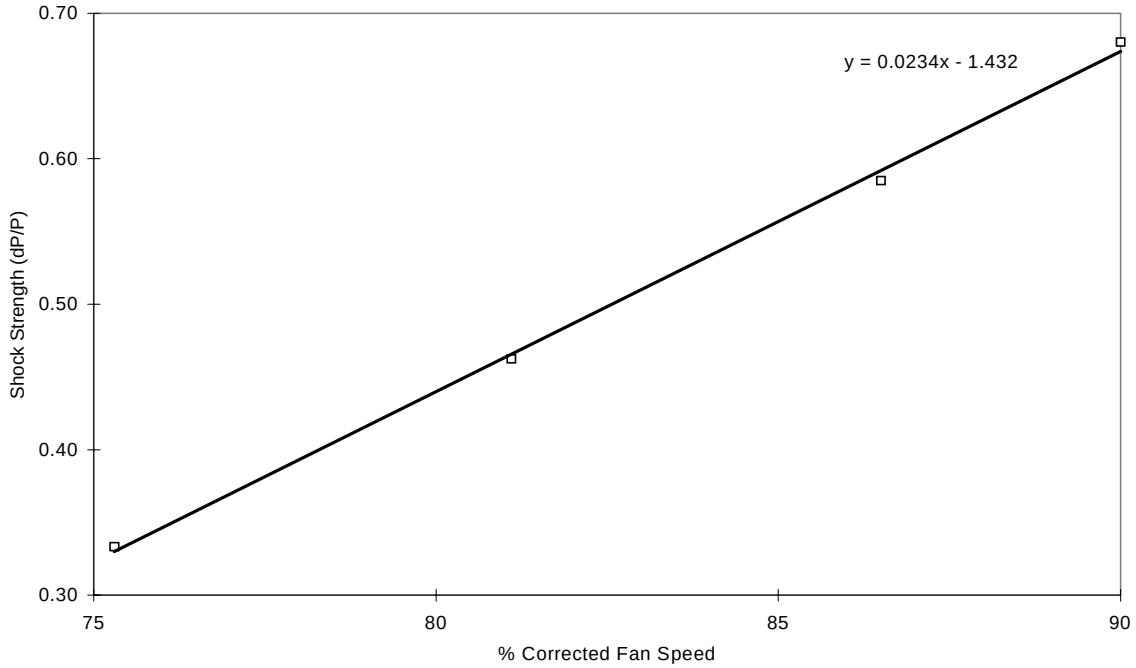

Figure 5-4. Predicted Strengths of Expelled Passage Shocks at the Rotor Corrected Speeds for Which Buzzsaw Noise Was Measured in the Baseline Fan.

5.1.2 Quiet High-Speed Fan

CFD analysis of the QHSF rotor was performed to evaluate the buzzsaw noise characteristics of the fan. As shown in the Mach contours of Figure 5-5, the spanwise distribution of effective sweep causes the passage shock location to vary with span at 100 percent speed. A strong shock is swallowed at 90 percent span, while a weaker shock is expelled at 70 percent span. As fan speed is reduced to near takeoff conditions (85 percent corrected speed), the strong tip shock dissipates leaving only a weak shock at 70 percent span (Figure 5-6).

Examination of the shock position at two radial locations along the rotor reveals that at 100 percent speed and 90 percent span, the QHSF passage shock is severely swallowed (Figure 5-7). The streamwise shock position at 90 percent span is not recorded for speeds below design because the computed pressure gradient at that location does not suggest the presence of a shock, but merely a gradual pressure rise (Figure 5-6). At 70 percent span, the QHSF passage shock is expelled, but the strength of this shock is much less than that of the baseline at 75 percent speed where buzzsaw noise is nearly cutoff (Figure 5-8). The shock at 90 percent span is relatively strong, but its position near the streamwise center of the rotor passage suggests buzzsaw noise cutoff.

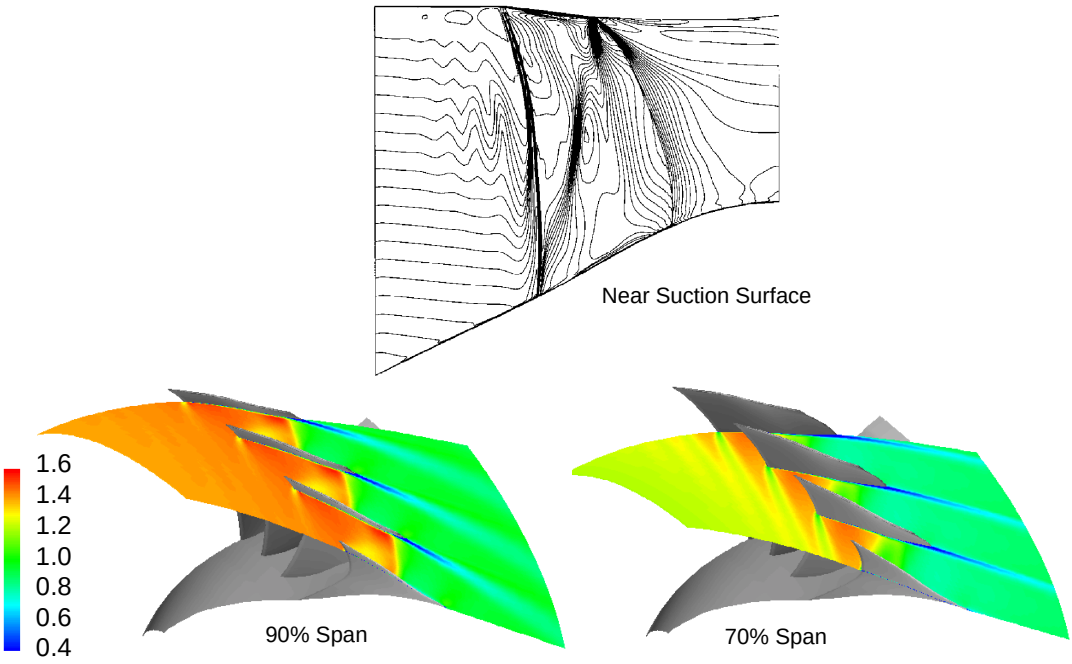

Figure 5-5. Mach Number Contours for the QHSF at 100% Speed Show the Shock Is Well Swallowed Near the Tip.

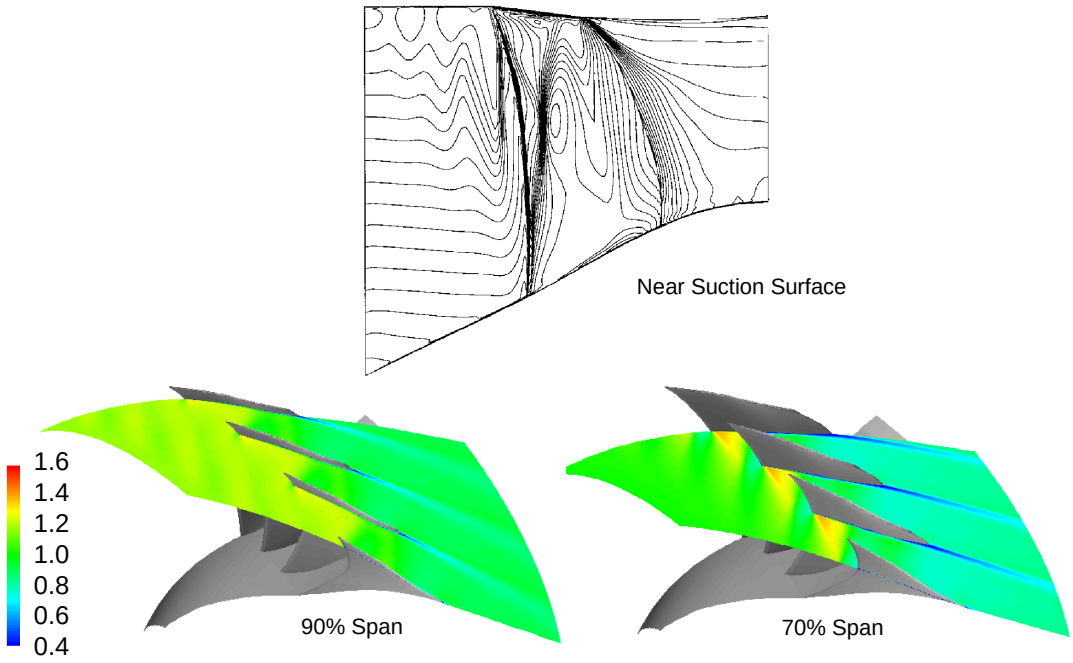

Figure 5-6. Mach Number Contours for QHSF At 85% Speed Show Reduced Shock Strength at the Takeoff Condition.

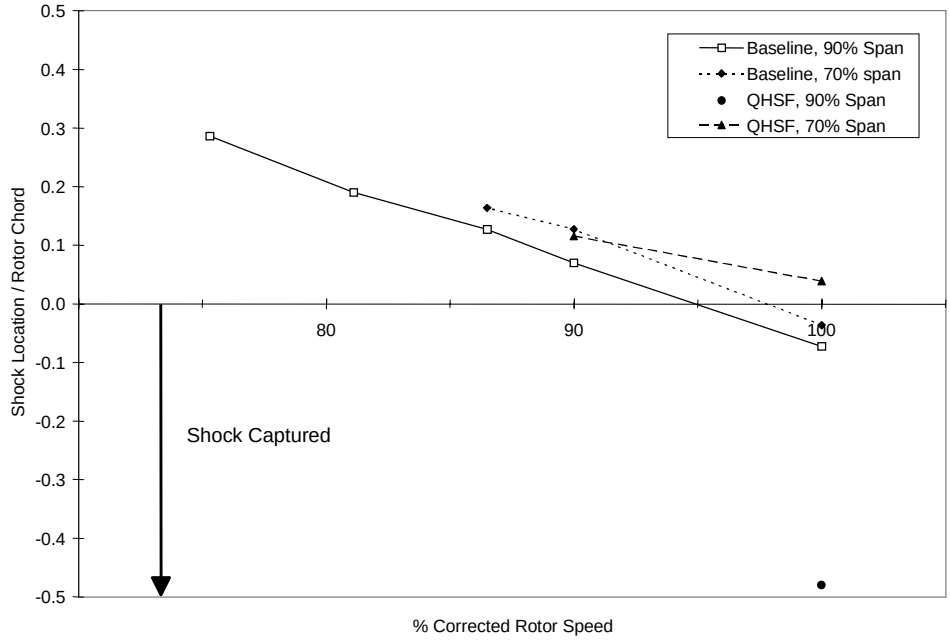

Figure 5-7. Comparison of Shock Locations for Baseline Fan and QHSF Show 90% and 70% Span Shock Locations.

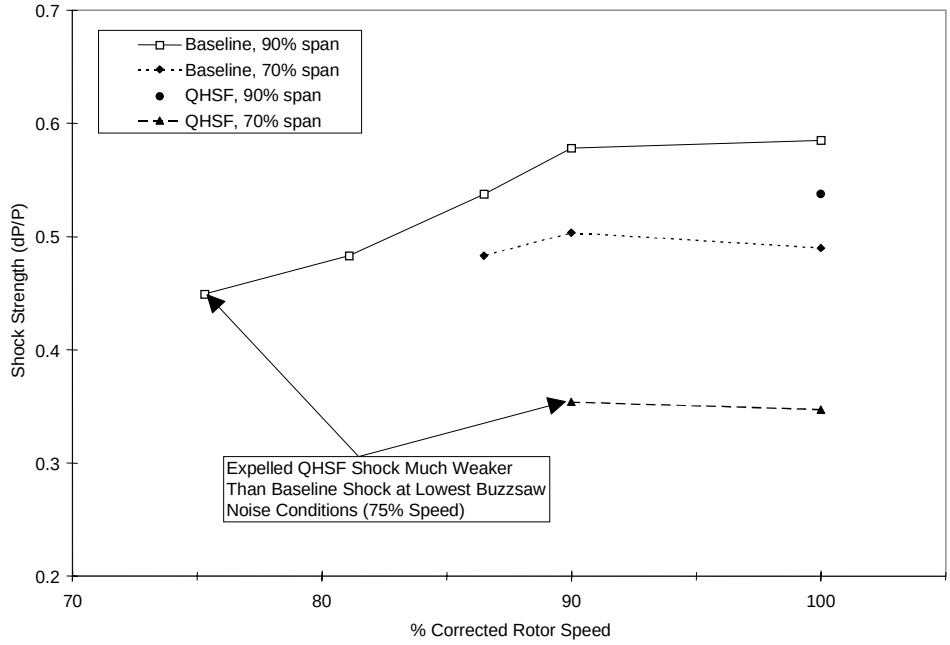

Figure 5-8. Comparison of Shock Strengths for Baseline Fan and QHSF (Strengths Extracted from Pressure Distribution Along 50% Pitch Streamline) Show Weaker QHSF Shocks.

5.2 Rotor/Stator Interaction Noise – V072

5.2.1 Baseline

To visualize the kinematics of wake propagation, wake traces were extracted from both DAWES and V072. A low total pressure was taken to be the indicator of wake position in the DAWES results, with data extracted at discrete radial locations along the stator leading edge. The wake trace calculations were also extracted from the V072 calculations. As shown in Figure 5-9, V072 predicts wake kinematics quite well as compared with the CFD calculations.

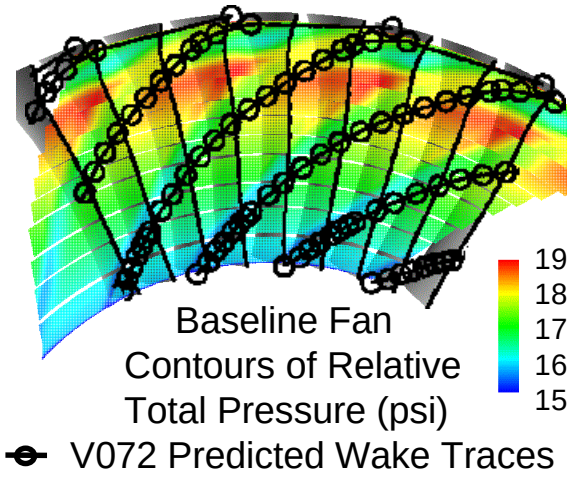

Figure 5-9. Wake Traces Predicted With DAWES and V072 Show Good Agreement for the Baseline Fan.

5.2.2 Quiet High Speed Fan

The relative benefit of stator lean was assessed through preliminary stator studies involving 15- to 30-degree leans with and without 30 degrees of sweep using the V072 code. As shown in Figure 5-10, leaning the stator in the rotor rotation direction and/or sweeping it axially produces benefits in fan inlet noise. Fan exit noise is higher for all cases. However, case pre-2 has nearly the same stator as the baseline fan showing that noise differences are due to the difference between the baseline and QHSF rotors. It was later determined that the part speed losses for the baseline rotor were unrealistically low, making the baseline computed noise levels lower than they really are.

In Figure 5-11, noise differences from an unleaned, unswept case are shown for stators with straight lean and no sweep. The benefit of leaning the stator with the direction of rotation is considerable, up to 22 dB. The penalty for leaning the stator against the direction of rotation is not as large. Note also that -30 degrees of lean is clearly better than -15 degrees.

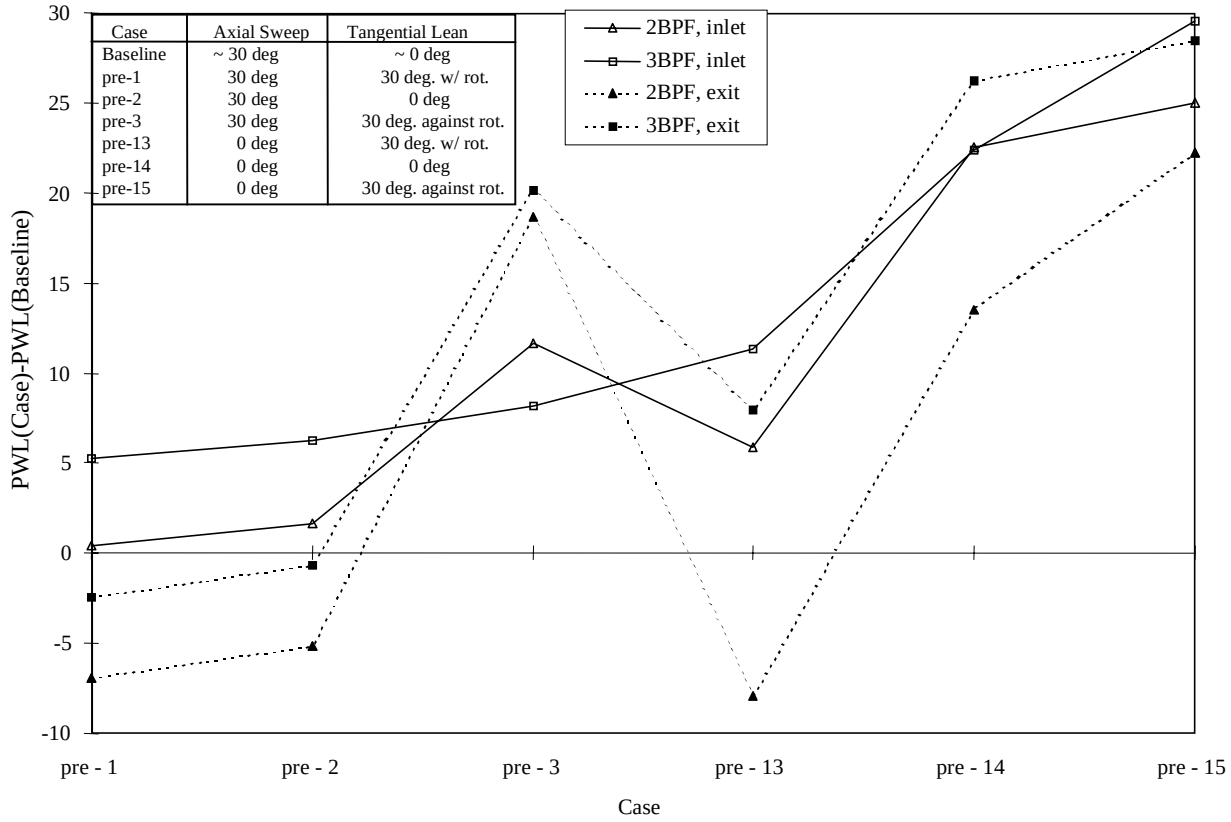

Figure 5-10. V072 Results for Stators With 30-Degree Sweep and/or Lean Show Effect of Stator Design.

Figure 5-12 shows the effect of similar leans on a stator swept aft 30 degrees. Note that the benefit of leaning the stator with the direction of rotation is rather small, 2 to 5 dB. However, the penalty for leaning the stator against the direction of rotation is much larger, up to 24 dB. Thus, at a high value of stator sweep, the benefits of a lean with rotation are much smaller than when no sweep is present. Since the 15-degree lean with rotation provided basically the same acoustic advantage as the 30-degree lean, both with 30 degrees of sweep, variations of the former were pursued in the stator DOE to determine if further noise reductions were possible.

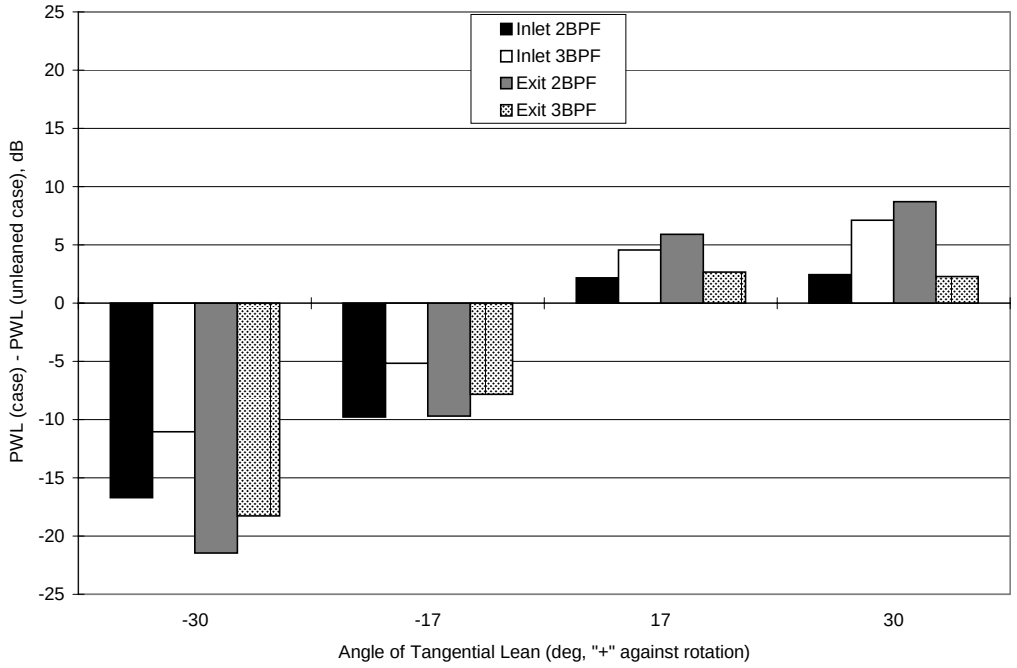

Figure 5-11. The Effect Of Stator Tangential Lean for Unswept Stators Is Clearly Shown.

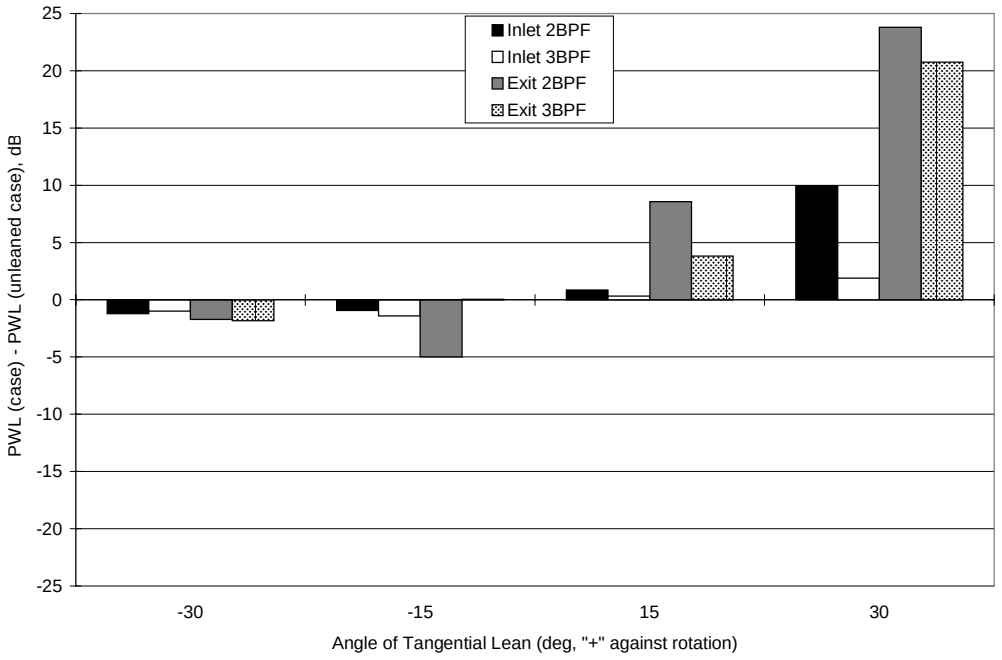

Figure 5-12. The Effect of Stator Tangential Lean for 30-Degree Swept Stator as Predicted With V072.

Correlation of the rotor loss model with the DAWES solution for the final configuration of the QHSF was completed. An accurate assessment of interaction noise was made using V072 (aerodynamic data for the baseline fan used as input to V072). Results of the interaction noise predictions on Approach (55.9 percent corrected speed) for the QHSF are shown in Figure 5-13 as differences from the baseline fan predictions. The final QHSF stage is predicted to be 3 to 5 dB quieter in all but the forward propagating 3*BPF harmonic. Recall that the 1*BPF tone is cut off at this speed. Although the predicted wake velocity deficit is greater for the quiet fan, the wake width is also greater and may at least partially offset the effect of the increased deficit. Reduced interaction noise is likely due to increased phase variation across the stator leading edge as shown in the wake traces of Figure 5-13. The pressure contours were extracted from a DAWES solution and reveal that the 2-D analysis of V072 may predict greater wake leans than exist in a 3-D flow. However, variation between the V072 and DAWES predictions appears to be the same for both the baseline fan and the QHSF.

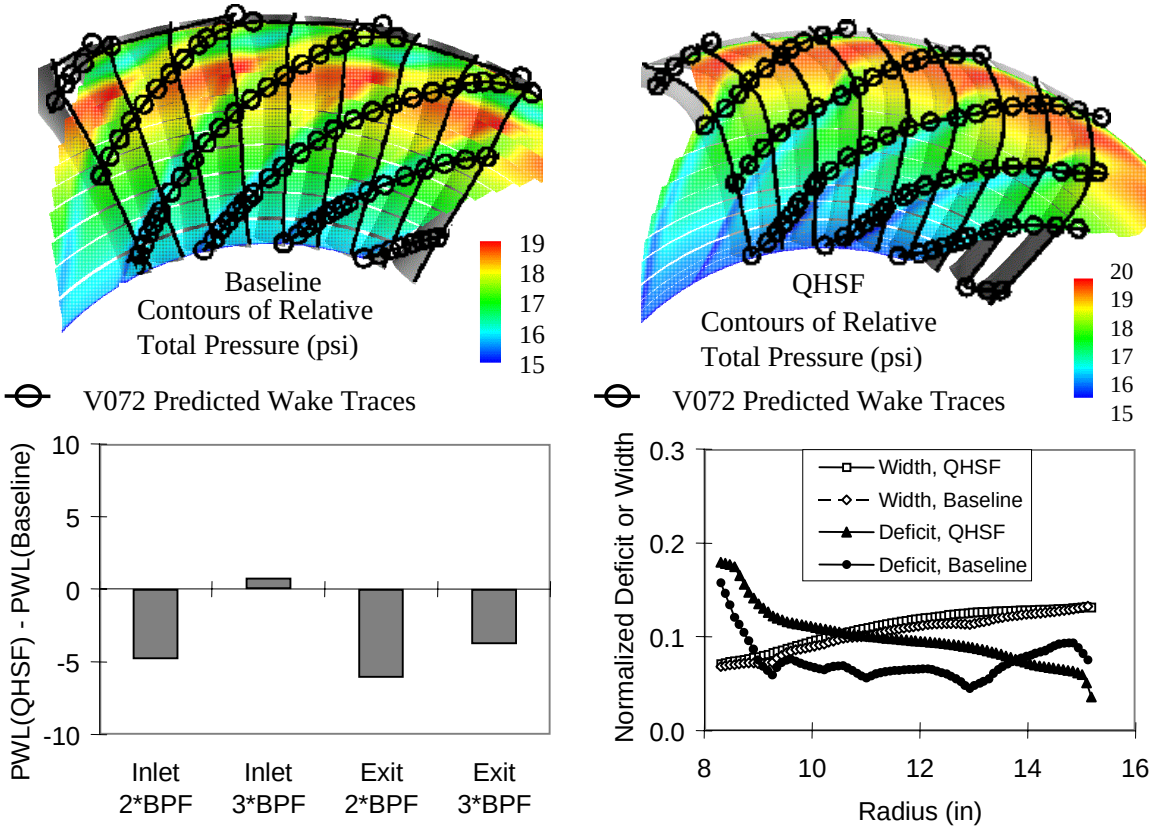

Figure 5-13. V072 Predictions for Final QHSF Rotor and Stator at 55.9% Speed.

In an attempt to understand the V072 predictions made for the baseline fan and the final configuration of the QHSF, the rotor losses for each were examined. Rotor loss is used to predict rotor wake width and velocity deficit in V072. The losses for both fans were derived from DAWES results at part speed, however, some extrapolation was necessary to obtain an estimate of the losses at the approach corrected speed of 55.9 percent. Figure 5-14 shows the

rotor loss coefficients used to make the V072 noise predictions. It is apparent that the losses for the baseline fan are much lower than the QHSF.

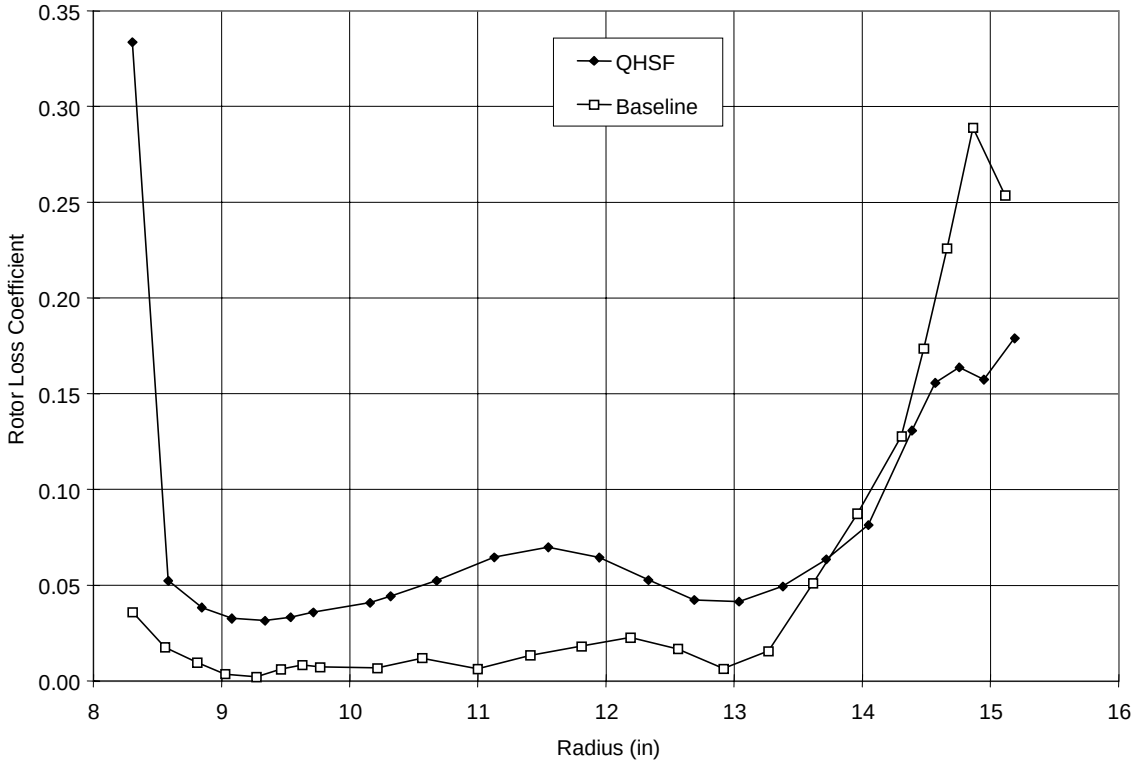

Figure 5-14. Predicted Rotor Loss Coefficients Used In V072 Noise Predictions.

At higher speeds, the losses for the two fans are comparable and indicate that the differences seen at 55.9% speed are not correct, with those of the baseline being too low. Comparisons of the average calculated loss coefficient, at three engine speeds, show consistent results between the QHSF and baseline as follows:

Percent Fan Speed	Baseline fan	QHSF
100	0.0950	0.1003
85	0.0814	0.0800
70	0.0662	0.0655

An adjustment to the loss model could be made so as to provide a more realistic loss coefficient for the baseline fan. This would give a better estimate of the flow-field downstream of the rotor and, consequently, of the interaction noise of the baseline fan.

5.3 Far-field Radiation – Eversman code

5.3.1 Inlet Radiation

Figure 5-15 shows the results of Eversman farfield predictions using each of five meshes for the baseline fan at 55.9 percent speed. Table 5-1 provides a description of each mesh. Note that the medium, large, and huge meshes produce nearly the same solution. Even the small mesh solution is close over most of the domain, suggesting that the criterion of five elements per wavelength could be relaxed a little. (Note: the tiny mesh prediction is the solid line with the highest SPL at 70 degrees).

Table 5-1. Parameters Associated With the Grid Size Criterion.

55.9% Speed 2BPF
ETAR=31.55
VMIN=0.37

MESH	N_R	N_{le}
tiny	18	2.3
small	22	2.8
medium	32	4.0
large	42	5.3
huge	64	8.0

Since it appeared that the huge mesh provided adequate resolution for reduced frequencies up to nearly 50, it was used to generate farfield predictions for the inlet noise of the baseline fan. Figures 5-16 through 5-19 provide a comparison of the noise predictions for the 2BPF frequency at three speed points, 55.9, 68.9, and 75.3 percent, and the 3BPF frequency at 55.9 percent speed. For the 2BPF harmonic, the m=-8 mode is cut-on at all speeds. For the 3BPF frequency at 55.9 percent speed, the m=14 and the m=-38 modes are cut-on. The V072 program provided the reduced frequencies and complex modal amplitudes used in the radiation code. (For the V072 predictions, stator leading edge radii were used since that provided a better match to the data; also WKEFAC and VELFAC were set to 1 and loaded rotor wake profiles were used).

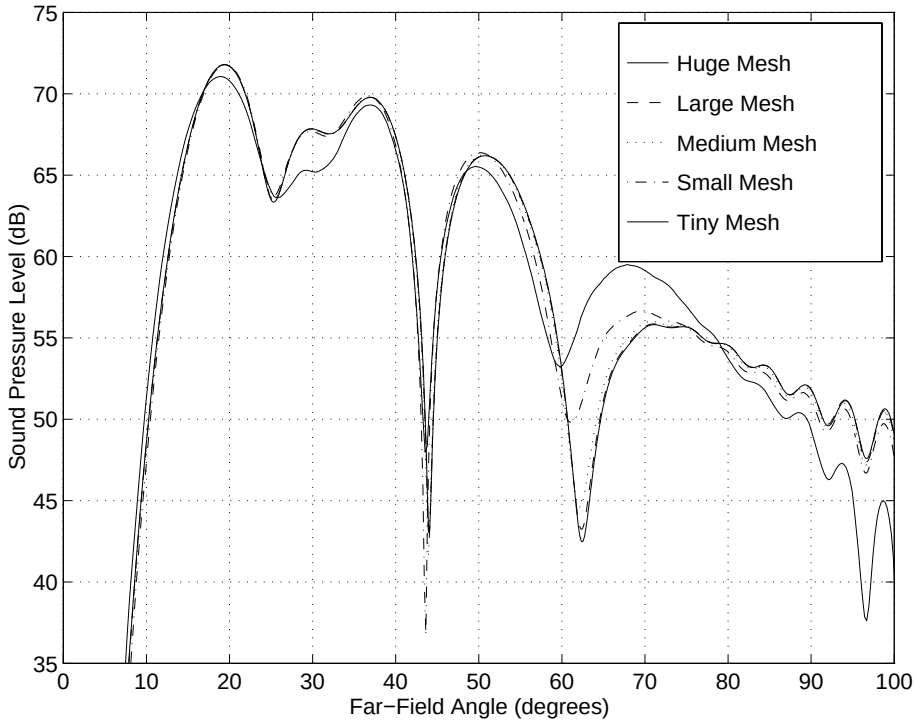

Figure 5-15. Farfield Noise Predictions With the Eversman Code for the Baseline Fan, 2*BPF, 55.9% Speed Showing Sensitivity to Mesh Density.

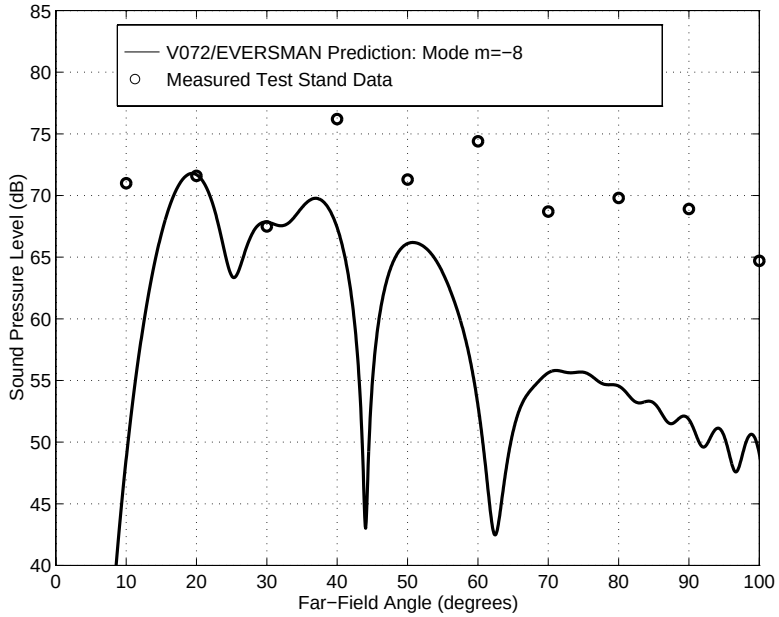

Figure 5-16. Comparison of Measured and Predicted Farfield SPL for the Baseline Fan, 55.9% Speed, 2*BPF.

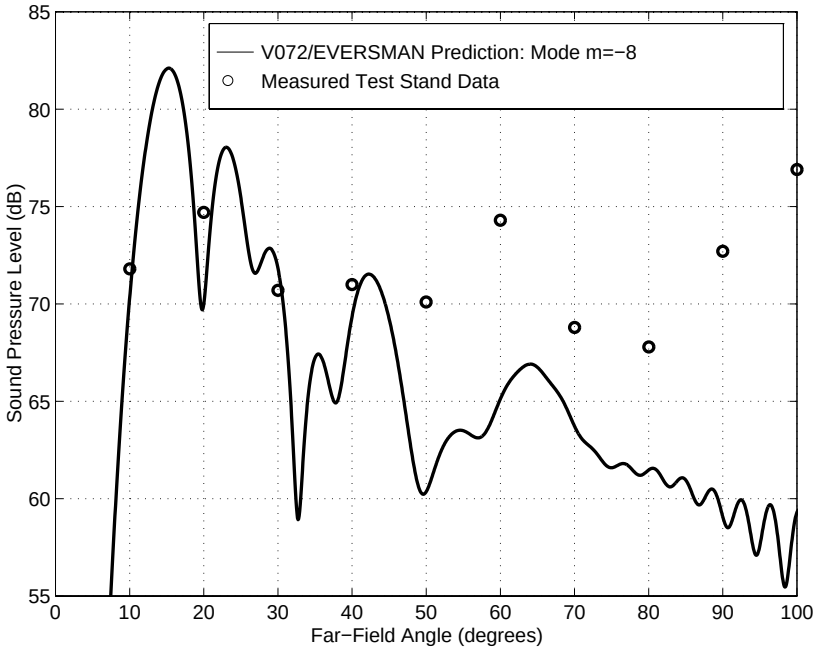

Figure 5-17. Comparison of Measured and Predicted Farfield SPL for the Baseline Fan, 68.9% Speed, 2*BPF.

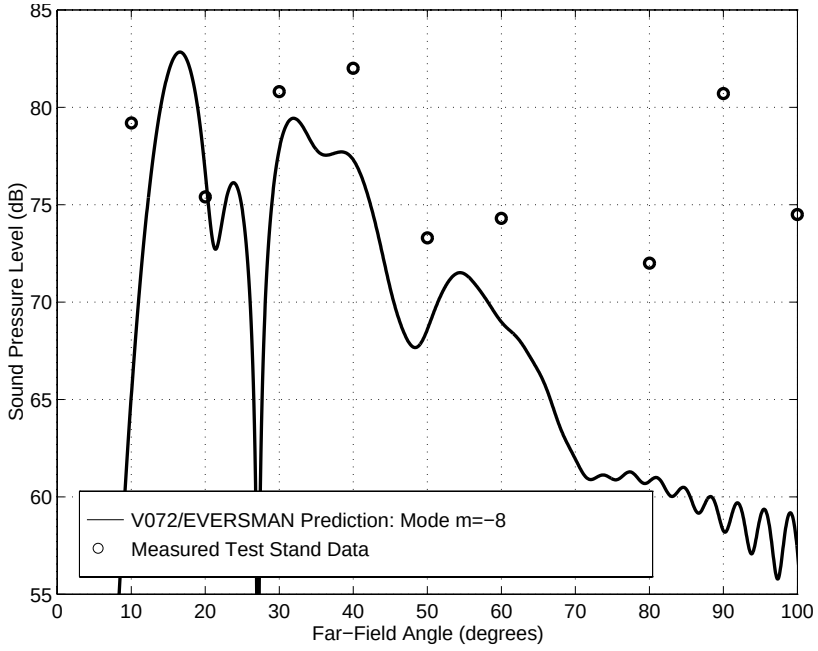

Figure 5-18. Comparison of Measured and Predicted Farfield SPL for the Baseline Fan, 75.3% Speed, 2*BPF.

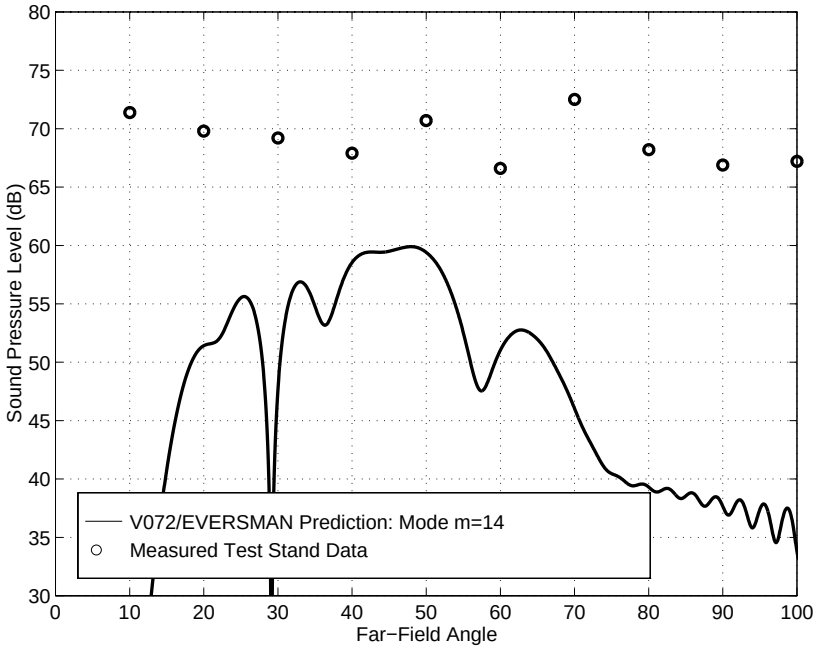

Figure 5-19. Comparison of Measured and Predicted Farfield SPL for the Baseline Fan, 55.9% Speed, 3*BPF.

The reduced frequencies and inlet Mach numbers used in the Eversman predictions are given in Table 5-2. Note that the unmodified Eversman code, with a maximum of 5,000 elements and 21,000 nodes, is expected to provide good results for reduced frequencies up to 35 (ref. 10, P. 99). The high-reduced frequencies considered here necessitate modification of the code to accept larger mesh sizes.

Table 5-2. Reduced Frequencies and Mach Numbers Used in the Eversman Predictions.

Prediction	ETAR	VMIN
55.9% Speed 2BPF	31.549	0.370
68.9% Speed 2BPF	38.414	0.455
75.3% Speed 2BPF	41.918	0.481
55.9% Speed 3BPF	47.324	0.370

At 55.9 percent speed, the farfield sound pressure levels are under-predicted, particularly at the higher angles. Notice that the 3BPF prediction is worse than the 2BPF prediction. This difference is due to the fact that V072 predicted duct power levels at 3*BPF much lower than those at 2*BPF in contrast to the small measured differences between farfield harmonic levels. The directivity lobe structure is difficult to compare since the measured data is so sparse, most of the predicted lobes vary significantly over 10 degrees. A more refined estimate of the modal amplitudes would probably be necessary to produce a more accurate prediction (i.e., in V072, a more accurate wake input or an improved stator response that accounts for such things like stator camber).

5.3.2 Aft Radiation

Figures 5-20 and 5-21 show the finite-element and wave envelope regions of the aft radiation mesh, respectfully, generated for the baseline fan. Because the engine cowlings were removed during the static engine noise measurements, the "nacelle" is represented as a thin sheet of metal to correspond to test conditions. Due to the length of the bypass duct (and subsequent number of elements needed to model it), only a portion of it is modeled. Because the modal amplitude input boundary is not the same as that used for the inlet predictions (namely the stator leading-edge hub axial location), the phase is not preserved and so any phase cancellation or reinforcement between the inlet and aft radiation is not taken into account.

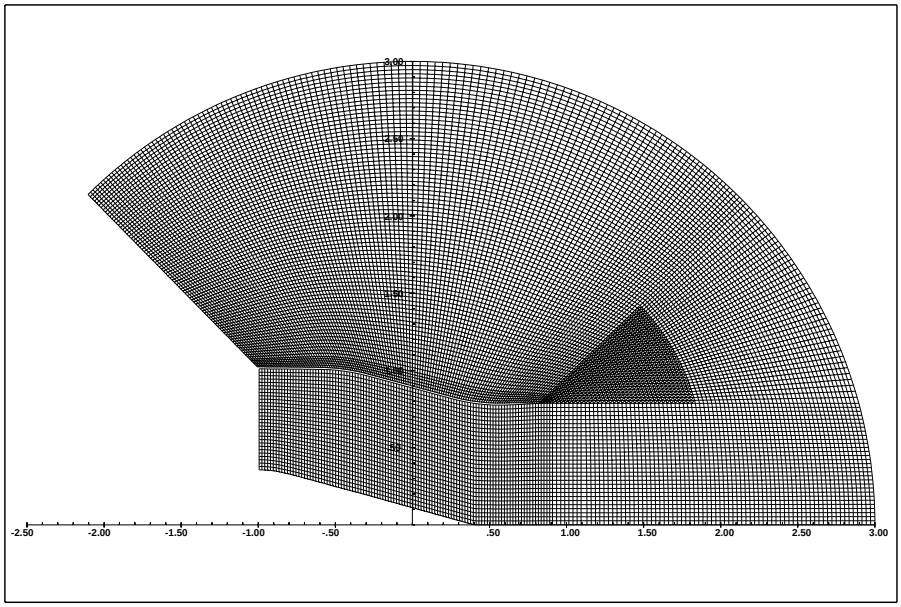

Figure 5-20. Finite-Element Region of Aft Mesh for the Baseline Fan.

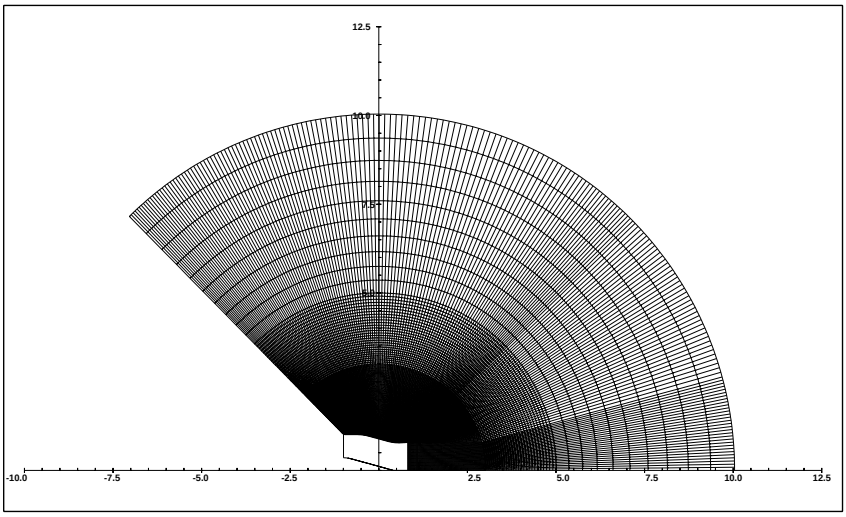

Figure 5-21. Wave Envelope Region of the Aft Mesh for the Baseline Fan.

Also, the radiation of the sound past the splitter plate and into the bypass is not taken into account, and the change in duct geometry is considerable. The modification of the structure of the noise as it propagates aft from the stator past the splitter and into the bypass duct is an important concern. Regardless, the V072 aft-propagating modal amplitudes at the stator leading edge were used for the bypass duct as a first approximation.

There are other simplifications that are introduced: the engine contains a lobed mixer nozzle that is not modeled, and its associated core flow cannot be modeled with the aft radiation code. Comparison of the measured and predicted farfield noise for the 2*BPF frequency at 55.9 percent speed is shown in Figure 5-22 along with the inlet noise levels. In view of the additional simplifications that were introduced, the aft prediction is surprisingly good, certainly as good as the inlet prediction. The predicted absolute levels are of the same order of magnitude as the measured data. However, the prediction misses the measured peak lobe (at around 130 degrees) in the aft direction by about 20 degrees. Also, the inlet and aft results still show a significant under prediction of the data in the range of 60 to 90 degrees.

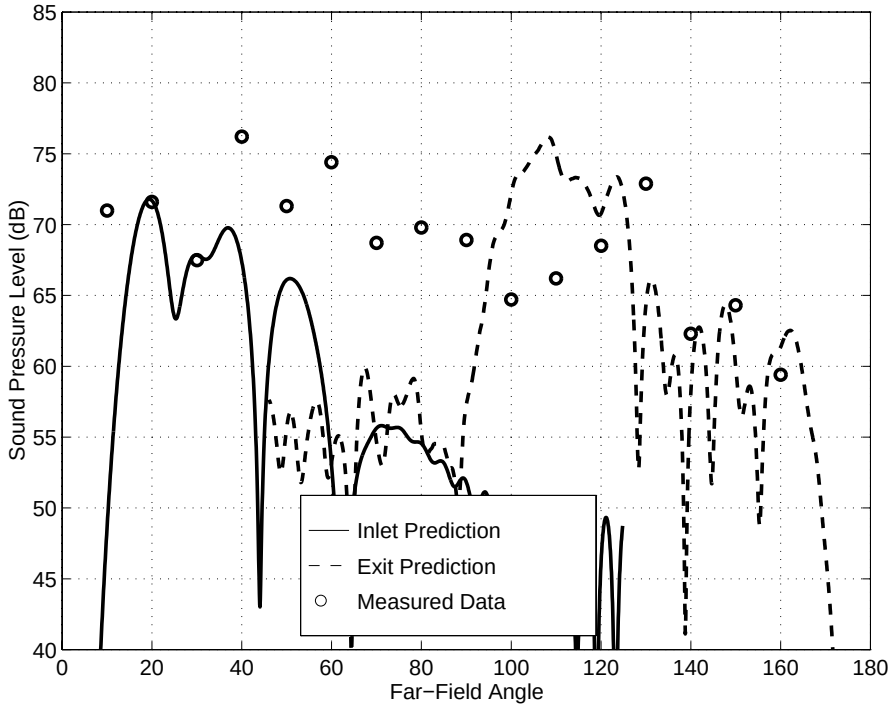

Figure 5-22. Inlet/Aft Prediction for the 55.9% Speed, 2BPF (Phase Not Preserved) for the Baseline Fan.

5.4 Fly-Over Noise Predictions

Static-to-flight predictions were made using measured baseline engine static noise data and the Honeywell General Aviation Synthesis Program (GASP). The measured data were separated into jet noise (JET) and tonal (TNB) and broadband (TBB) turbo-machinery noise. To simulate

the effect on buzzsaw noise of the QHSF, all tones except the rotor/stator interaction tones were manually extracted from the turbomachinery narrow-band noise data. The three engine noise components were used as input to GASP along with a semi-empirical airframe noise prediction (AFM). Engine configurations (number and location on the aircraft) and flight profiles, for both business and regional aircraft, were modeled in Full Power Takeoff, Cutback Takeoff, Sideline, and Approach conditions.

Tables 5-3 and 5-4 and Figures 5-23 and 5-24 show the results of the static-to-flight predictions. The first column in Table 5-3 is an average of the measured noise levels of business jets (two engines mounted on the fuselage) with 1992 technology (ref. 20). The next column shows the same aircraft with the current baseline engine. For Sideline, Takeoff, and Cutback conditions, the buzzsaw noise has been eliminated for the QHSF predictions shown in column three. As a limiting value, the final column of Table 5-3 shows the estimated fly-over noise levels if no tones were present (total made up of jet, turbomachinery broadband, and airframe noise). Similar predictions were made for a regional jet having four wing-mounted engines (Table 5-4 and Figure 5-24).

Table 5-3. Static-to-Flight Predictions for Business Aircraft.

Flight Condition		1992 AST Baseline	Baseline Engine	QHSF	No Tones
Sideline	Jet	87	79	79	79
	Fan	78	80	78	76
	Total	89	84	84	82
Takeoff	Jet	*	77	77	77
	Fan	*	77	75	73
	Total	*	82	81	80
Cutback	Jet	79	71	71	71
	Fan	70	73	73	68
	Total	81	78	78	76
Approach	Jet	81	71	71	71
	Fan	86	84	84	83
	Total	92	90	89	89

Table 5-4. Static-to-Flight Predictions for Regional Aircraft.

Flight Condition		Baseline Engine	QHSF	No Tones
Sideline	Jet	82	82	82
	Fan	84	82	80
	Total	88	87	86
Takeoff	Jet	80	80	80
	Fan	81	79	77
	Total	86	85	84
Cutback	Jet	76	76	76
	Fan	80	80	75
	Total	85	85	82
Approach	Jet	74	74	74
	Fan	89	89	88
	Total	94	94	93

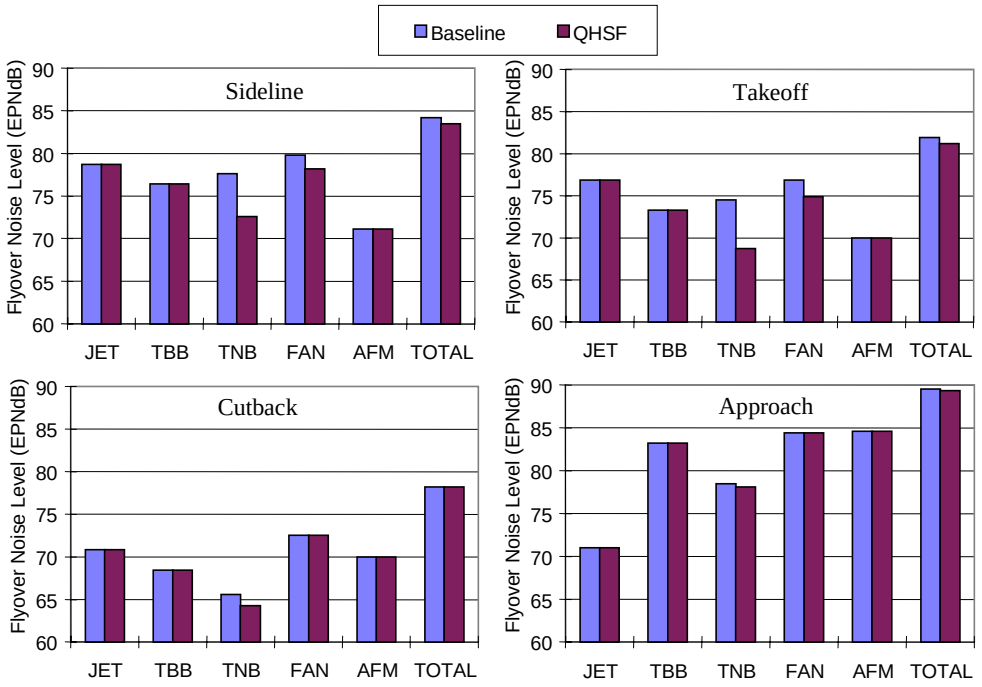

Figure 5-23. Static-to-Flight Predictions for Business Aircraft.

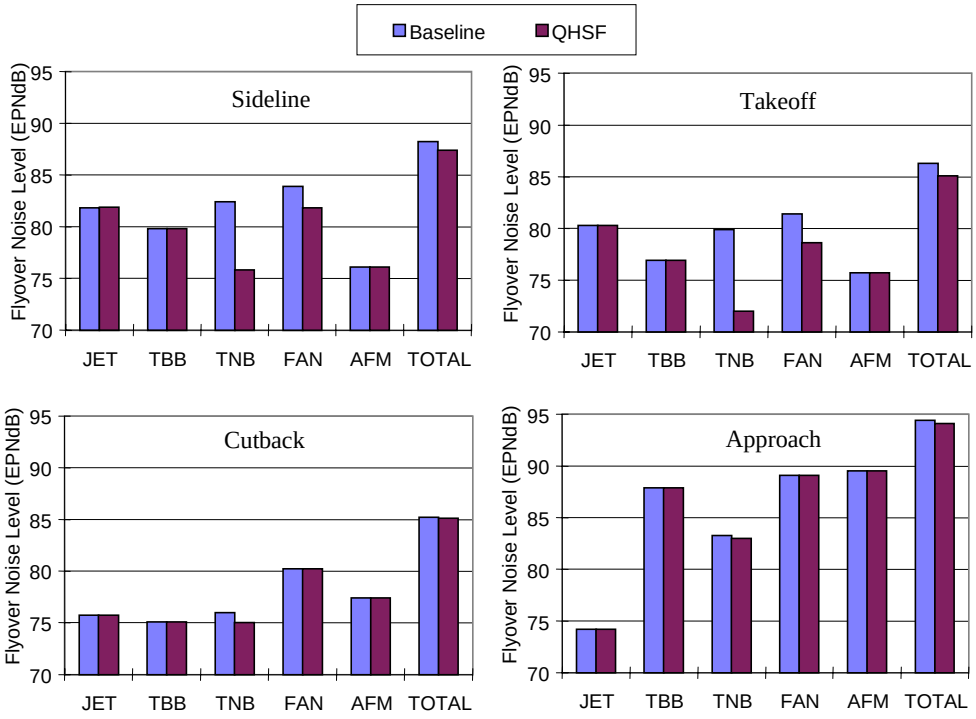

Figure 5-24. Static-to-Flight Predictions for Regional Aircraft.

For Takeoff and Sideline, conditions at which the baseline buzzsaw noise is pronounced, the QHSF will provide a 2 EPNdB reduction in fan noise. Once the MPT noise is eliminated, overall aircraft noise levels are controlled by jet noise for these conditions. Therefore, predicted aircraft noise levels dropped by only 1 EPNdB. At Cutback fan speed, the baseline engine does not generate significant buzzsaw noise so no engine or aircraft noise reductions are expected for the QHSF at this engine setting. Elimination of both buzzsaw and interaction tones from the fan noise signature gives a 4 EPNdB reduction in fan noise and a 2 EPNdB reduction in aircraft fly-over noise.

A study was performed to investigate the predicted effect of reductions in fan broadband noise on aircraft fly-over noise levels. Broadband noise of the QHSF may be lower than that of the baseline fan due to the large geometric differences between the two, like the lean of the stators.

Fly-over noise predictions were made for the business and regional aircraft for Approach, Full-Power Takeoff, Cutback Takeoff, and SideLine. Within the GASP static-to-flight noise prediction procedure, the baseline fan tonal levels were first reduced as described above. Broadband fan noise levels were then manually in 1 dB increments. Figure 5-25 shows the reduction in overall fan noise levels (tonal and broadband) along with the reduction in overall aircraft noise levels (fan, jet, and airframe) from the baseline fan.

It was seen that 3 dB of broadband fan noise reduction provided 1.5 to 2 EPNdB of overall fan fly-over noise reduction for all but the Cutback Takeoff condition. The relationship appeared to

be approximately 0.5 EPNdB fly-over fan noise reduction per 1 dB of broadband noise reduction. At Cutback, the fan tonal noise dominated overall fan noise levels, preventing larger reductions.

Total aircraft fly-over noise levels were predicted to drop by about 1 EPNdB due to buzzsaw noise reduction at the Sideline and Full-Power Takeoff conditions. Broadband noise reduction did not have a pronounced effect. Airframe and jet noise were comparable or higher than fan noise, thereby limiting the possible aircraft noise reduction due to a quieter fan. Aircraft noise levels for the Approach condition were reduced by as much as 1 EPNdB with lower fan noise due mainly to the reduced broadband noise (fan broadband noise dominated tone noise on Approach). Airframe noise was the largest contributor to overall Approach levels. Fan broadband levels at Cutback were lower than fan tonal, jet, and airframe noise so no aircraft noise reduction was realized with broadband level reduction.

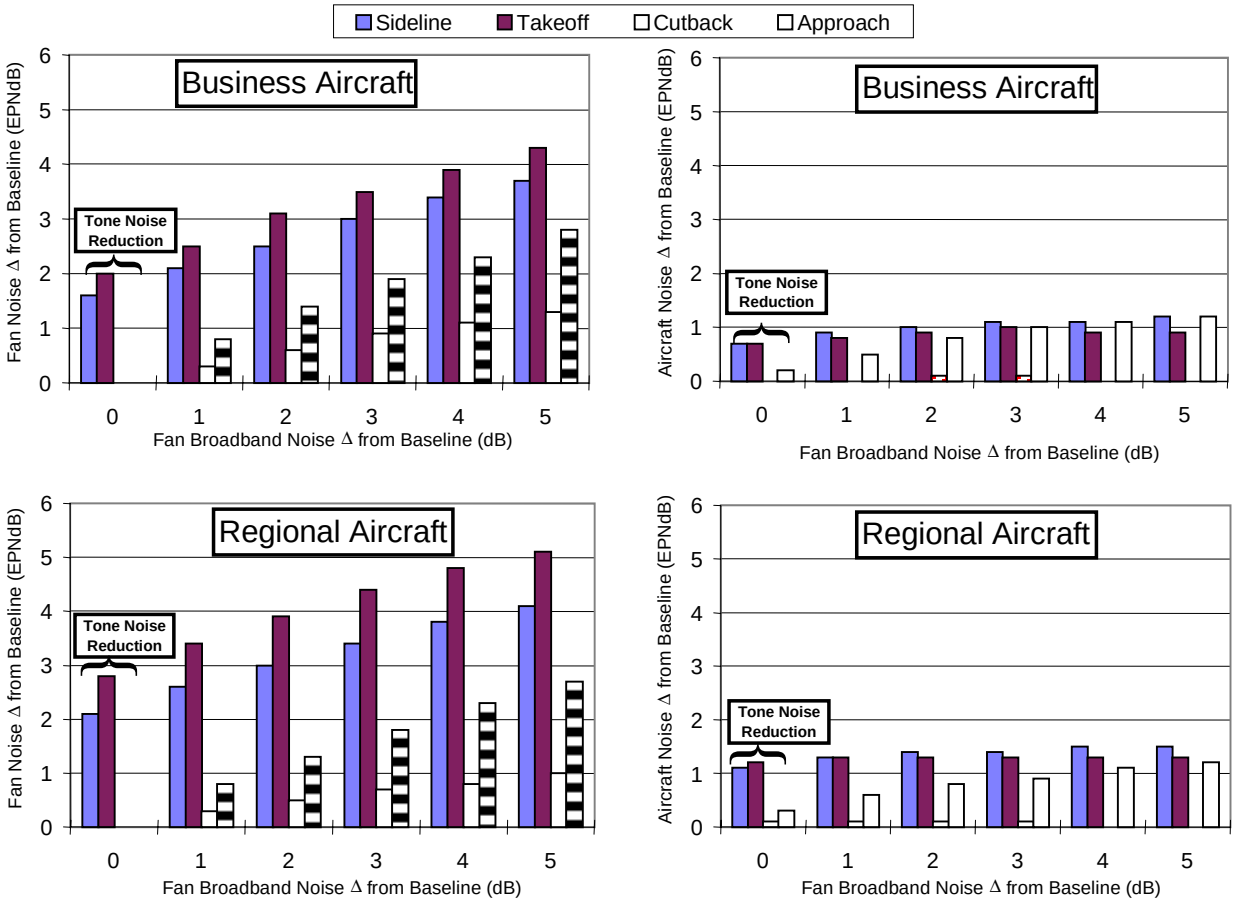

(a) fan noise (b) total noise

Figure 5-25. Predicted Flyover Noise Levels with Fan Tonal and Broadband Noise Reductions.

6. AEROELASTIC ANALYSIS

6.1 TURBO-AE

6.1.1 Baseline Fan Evaluations

The TURBO-AE code has been installed and compiled on the Engines & Systems workstation network. The baseline-fan test case F2 (Figure 6-1) was chosen for the initial TURBO-AE analyses. A CFD grid coarser than the grid used in the DAWES code (Figure 6-2) reduced computational time. Many operational script and code changes were suggested by Engines & Systems and incorporated by the NASA code developers. All TURBO-AE analyses were completed with inviscid calculations as computational problems within the viscous routine. These are being addressed at Mississippi State University.

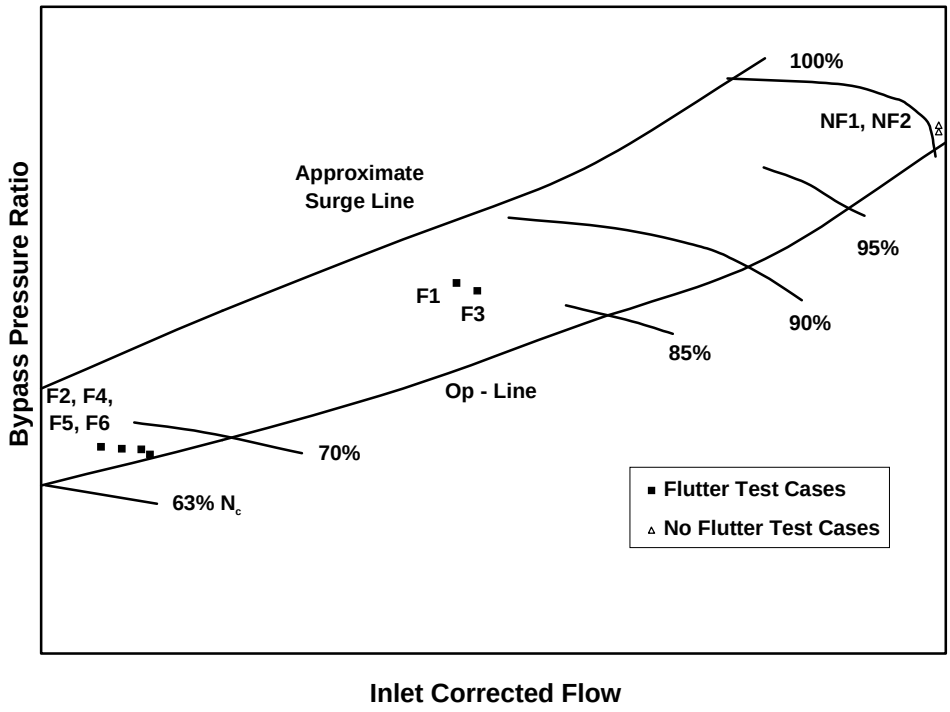

Figure 6-1. Fan Blisk Measured Flutter Data Test Cases Were Used for the TURBO-AE Evaluation.

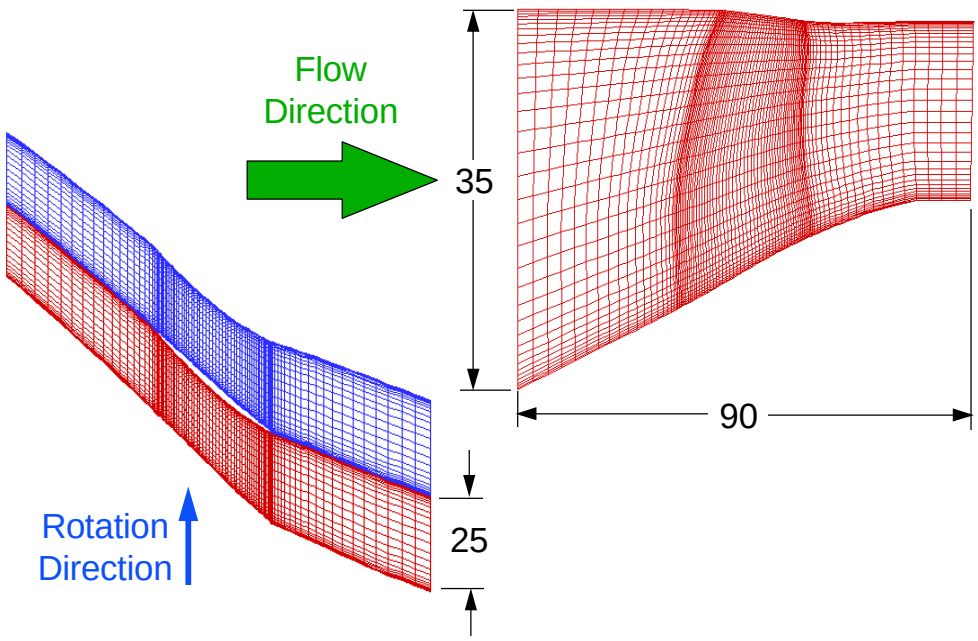

Figure 6-2. The TURBO-AE Computational Grid for Fan Blisk Case F2 Shows the Coarse Structure for Computational Efficiency.

Steady-state comparisons with the DAWES code showed excellent correlation at both mid and 95 percent span as shown in Figures 6-3 and 6-4. Discussions with Engines & Systems CFD specialists indicated that this agreement is well within the acceptable range, especially when noting that the TURBO-AE grid was coarser than the one used in DAWES and that the viscous routines are inactive in the TURBO-AE analyses.

Several unsteady analyses were completed to develop an understanding of the code behavior with varying vibration amplitude, Inter Blade Phase Angle (IBPA), and number of iterations per vibrational cycle. Results from this effort are shown in Table 6-1 for IBPAs of zero and 180 degrees. In the first three rows of Table 6-1, the number of iterations per cycle was fixed at 400, IBPA was set to zero, and the vibration amplitude was varied from 0.003 to 0.300 inches at the blade tip. For the 0.003 and 0.030 cases the code showed linear behavior in the work per cycle computation as indicated by the work/(amplitude)^2 computation which was in the 220 range. The 0.300 case had execution errors that were not unexpected due to the large vibration amplitude.

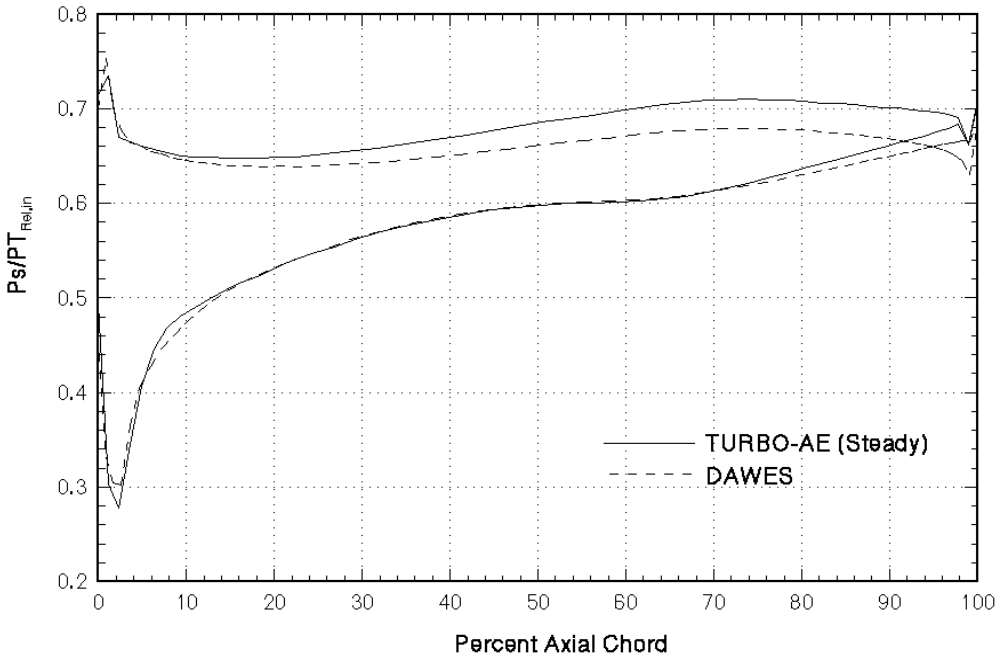

Figure 6-3. TURBO-AE Case F2 Steady Pressure Loading Shows Good Comparison With DAWES at Mid-Span.

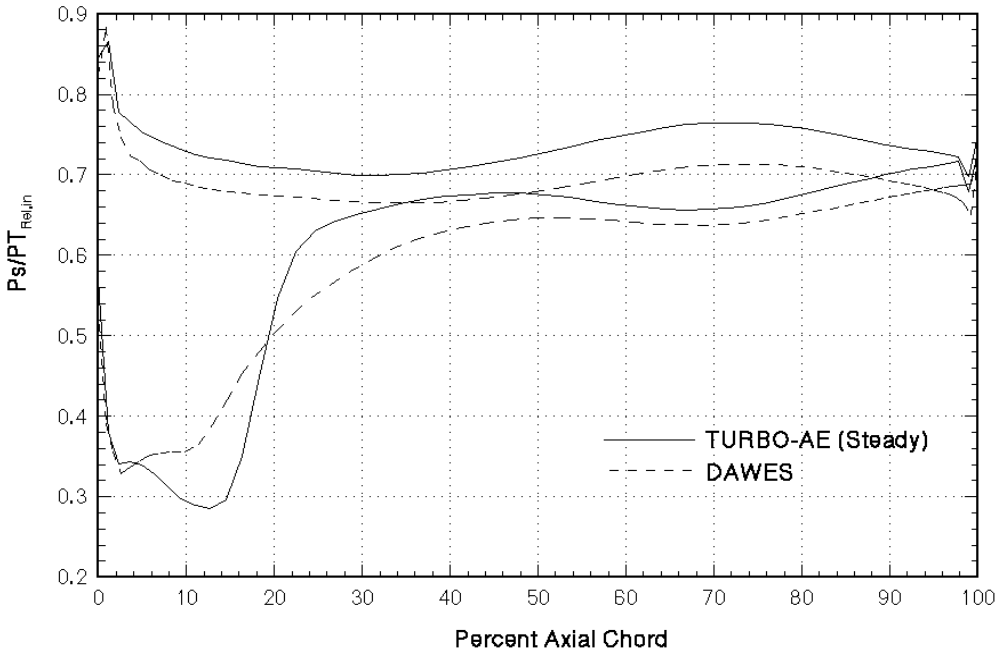

Figure 6-4. TURBO-AE Case F2 Steady Pressure Loading Shows Good Comparison With DAWES at 95% Span.

The next three rows in Table 6-1 were for IBPA equal to 180 degrees and again showed linear results for the 0.003 and 0.030 vibration amplitudes. Again, as with the 0 degree case, the 0.300-inch vibration amplitude analyses produced execution errors.

Additional analyses were completed to determine the sensitivity of the unsteady solution to variations in the number of iterations per cycle. The last six rows of Table 6-1 provide results from these analyses for 200, 400, and 800 iterations per cycle. As expected, the 200 iter/cycle runs had execution errors as the time step was too large for code convergence. The 800 iter/cycle cases provided some concern for IBPA equal to zero degrees as the work per cycle dropped substantially from the 400 iter/cycle value. This reduction was not present in the 180 degree IBPA analyses. Several discussions with NASA researchers were held to analyze this issue and the common conclusion was that the problem will likely disappear when the non-reflecting boundary condition version of the code becomes available.

Table 6-1. TURBO-AE Unsteady Results for Case F2.

		Work / Cycle		Work/(Amplitude^2)	
IBPA	**Amplitude**	**Passage 1**	**Passage 2**	**Passage 1**	**Passage 2**
0	0.003	0.0019	-	210.7	-
0	0.030	0.2108	-	234.2	-
0	0.300	*	-	*	-
180	0.003	0.0208	0.0211	2307.8	2345.3
180	0.030	2.0607	2.0625	2289.7	2291.7
180	0.300	*	*	*	*

* Amplitude too large for code convergence.

		Work / Cycle		Work/(Amplitude^2)	
IBPA	**Iterations/ Period**	**Passage 1**	**Passage 2**	**Passage 1**	**Passage 2**
0	200	**	**	**	**
0	400	0.2108	-	234.2	-
0	800	0.1237	-	137.4	-
180	200	**	**	**	**
180	400	2.0607	2.0625	2289.7	2291.7
180	800	2.3734	2.3707	2637.1	2634.1

** Execution error after fourth vibration cycle.

6.1.2 QHSF Evaluations

The QHSF evaluations with the TURBO-AE code were only partially completed during the program due to problems with the TURBO-AE software. Beginning with the steady (no blade vibration) flow solution, significant difficulty was encountered getting TURBO-AE to converge to a solution. Acceptable convergence was finally obtained when using a stretched grid in both the upstream and downstream directions. Results from this effort are summarized in Table 6-2 for the Design Point and F3 operating conditions. The mass flow matched reasonably well but the pressure ratio predictions were higher than the DAWES steady 3-D CFD code. These differences are probably caused by the TURBO-AE operating in an inviscid mode.

Pressure loadings for the F3 operating condition are shown in Figure 6-5 and Figure 6-6 for the 50 and 95 percent spans, respectively. The 50 percent span results match well with the DAWES predictions, while the shock location is shifted forward for the 95 percent span condition. Possible explanations for these loading discrepancies include tip clearance (zero with TURBO-AE), mass flow differences (DAWES higher), and viscous effects (TURBO-AE inviscid).

Table 6-2. QHSF TURBO-AE Steady Flow Solutions.

QHSF Steady Aerodynamic Analysis		
	DAWES	**TURBO-AE Inviscid**
Design point		
Total Pressure Ratio	1.851	2.194
Corrected flow (lbm/s)	188.37	187.74
Run Time (hrs)*	56	57
F3		
Total Pressure Ratio	1.626	1.734
Corrected flow (lbm/s)	159.28	166.66
Run Time (hrs)*	85	61

* DAWES grid finer than TURBO-AE

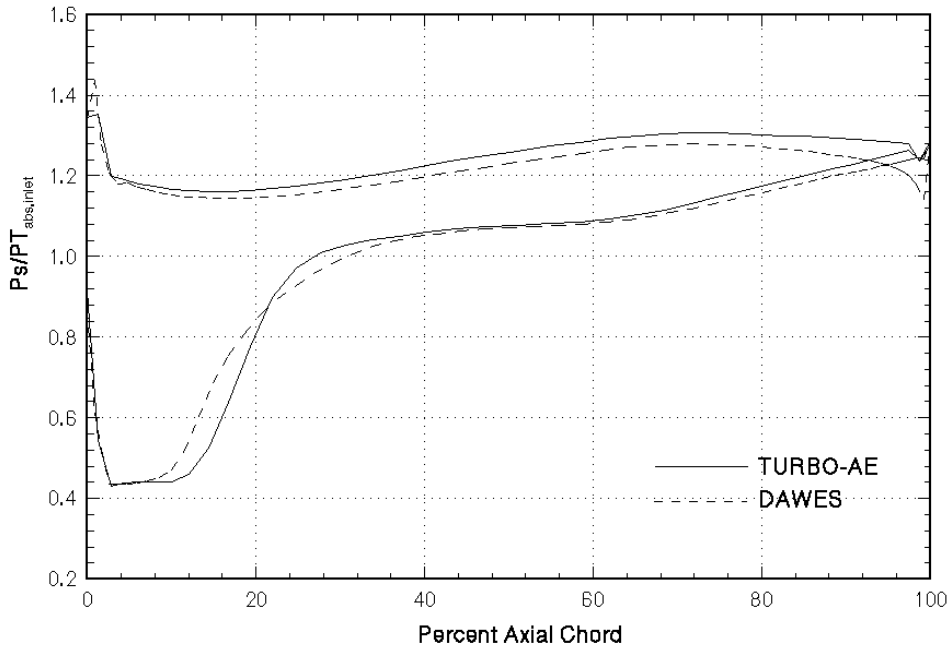

Figure 6-5. TURBO-AE OPTM3 Case F3 Pressure Loading At Mid-Span Shows Good Agreement With DAWES Results.

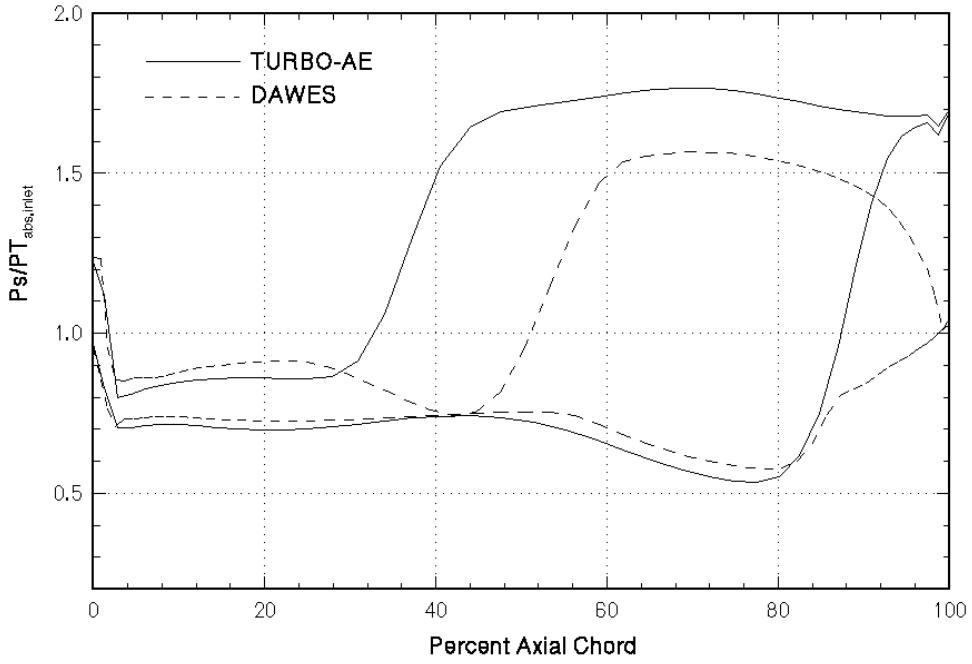

Figure 6-6. TURBO-AE QHSF Case F3 Design-Point Pressure Loading at 95%Span Shows Some Differences from the DAWES Results.

TURBO-AE unsteady evaluations for the QHSF were attempted for the design point and F3 conditions with IBPA = 0, 180, and 32.7 degrees. None of these runs were successfully completed at the time the QHSF aeroelasticity activity was completed.

6.2 FREPS

At the suggestion of Dennis Huff at NASA Glenn, a LINFLO preprocessor is being developed which will bypass the SFLOW code that is having difficulties performing the transonic flow analyses required for high speed fan rotors. The suggested approach is to use the pressure field computed from any steady state solver in conjunction with the potential flow assumptions to compute the corresponding potential function and velocity field. This approach maintains the same amount of loading generated by the flow field on the rotor blades and satisfies the potential flow conditions. Several steps have been completed to evaluate this concept using the available steady-state solvers at Engines & Systems (mainly the 3-D DENTON code). This procedure has tremendous potential for the engine manufacturers as the existing, calibrated, steady design codes can be used rather than adding an additional flow solver (SFLOW) to the design toolbox.

To begin this evaluation, 3-D DENTON solutions were obtained for the Quiet High-Speed Fan (QHSF) at design and off design conditions. These solutions were used to develop and test the different modules of the LINFLO preprocessor. Appropriate subroutines have been developed and integrated as part of the AEROUT package, which is used by Engines & Systems to post-process DENTON flow solutions. These subroutines strip 2-D sections from the supplied 3-D solution and convert all the computed data into a frame of reference relative to the solved blade. Another subroutine was created to compute the grid metric coefficients based on the finite difference approach. The grid shape, aerodynamic data, and metric coefficients were then fed into the main flow solver to compute the proper potential function distribution.

As a first try, a simple procedure to compute an irrotational velocity field based on the supplied pressure field was tested. In this process, the total pressure is computed from the inlet conditions and assumed to be fixed everywhere. A local Mach number is then calculated from the energy equation that in turn produces a static temperature distribution based on the inlet total temperature. Combining the local Mach number and static temperature produces a local total velocity that is kept fixed for the subsequent analyses. Next, local velocity components are estimated by marching from the specified inlet section, applying the irrotationality constraint to get the y-velocity component, and computing the x-velocity from the fixed total value. That approach when tested was found to be highly dependent on the grid topology and produced an oscillatory velocity field in case of coarse grids. Since the unsteady LINFLO is sensitive to the velocity gradient and requires a smooth velocity field, the above procedure was aborted.

The FREPS steady-flow solver SFLOW is unable to converge when using the transonic flow cases prevalent in Engines & Systems fan rotors. In order to resolve this issue, an effort was conducted to bypass the SFLOW solver and use steady-flow solutions from the Engines & Systems 3-D Euler code DENTON.

A flow chart of this process is shown in Figure 6-7 in which the DENTON steady flow solution is post-processed by the existing AEROUT code to provide a result file for the FREPS preprocessor. At the end of the QHSF aeroelasticity activity, Engines & Systems had nearly completed this effort and was working on the third step (solve continuity equation for potential flow). Once this and the final step are finished, the bypassing of the SFLOW solver will be complete.

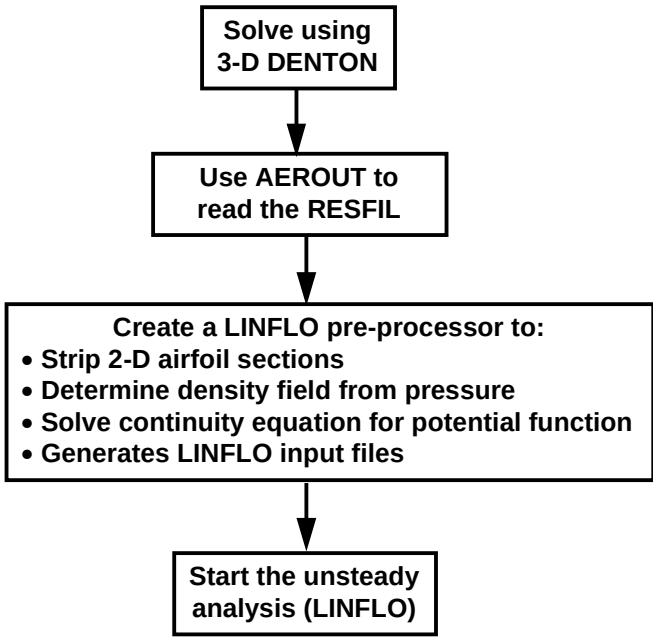

Figure 6-7. FREPS/DENTON Interface Development Flowchart Outlines Process to Bypass the SFLOW Solver in FREPS.

6.3 UNSFLO

A forward-swept QHSF fan blade design optimized for the greatest flutter margin by Engines & Systems empirical flutter criteria was chosen for the initial application of UNSFLO. A systematic flutter analysis procedure starting from the hot-bank file and ANSYS hot-structural model has been developed. The procedure includes hot-to-onpoint conversions of structural and aerodynamic input files and onpoint steady inviscid, steady viscous and unsteady viscous, analyses using UNSFLO. The procedure has been successfully applied at the 100 percent speed operating point and the design has been found to be flutter-free at this condition. Currently, efforts are continuing to streamline the procedure at off-design conditions and to reduce the user interaction time in flutter analysis.

The results produced by UNSFLO for a QHSF rotor design were analyzed and compared to empirical correlations. It was found that the correlations with blade frequency and twist/flex ratio were counter-intuitive. To resolve this issue, an effort was initiated to compare the UNSFLO results for a flat plate cascade with classical analytical results. A thin NACA airfoil was generated as a test case. It was found that Mach numbers from steady inviscid UNSFLO results compared poorly with analytical results. Efforts to isolate the problem did not succeed. Steady viscous UNSFLO results compared well with results generated by a DAWES analysis that served as a benchmark for the steady analysis. The comparison of unsteady analysis results has not been completed at the present time. It is clear from this effort that Engines & Systems requires much more work to fully understand the UNSFLO computer code.

7. FAN DESIGN AND FABRICATION

7.1 Rotor Blades

BNB Manufacturing fabricated the rotor blades for both the baseline fan and QHSF. A photograph of the QHSF rotor blade is shown in Figure 7-1.

Figure 7-1. Photograph of the QHSF Rotor Blade.

Acoustic ring signature data were taken for all blades to ensure that the actual blade vibration modes were consistent with the results predicted by ANSYS during the design. The results in Table 7-1 show excellent consistency in the blade set and good agreement with prediction of the frequencies of the first five blade vibratory modes.

Acoustic holography data was also taken on one blade to verify the calculated mode shapes. Figure 7-2 shows the measured results and comparison with the predictions. Note that the calculated results are presented in a slightly different aspect angle than the photographed results, creating the appearance of a different blade chord distribution.

Table 7-1. Acoustic Ring Results for the QHSF Fan Blades.

	Mode				
Blade	1	2	3	4	5
1	170	503	910	1115	1575
2	175	517	920	1135	1575
3	180	522	930	1135	1560
4	180	522	932	1140	1575
5	177	520	930	1140	1575
6	177	520	927	1135	1570
7	180	515	930	1125	1560
8	175	515	920	1135	1575
9	177	517	922	1135	1570
10	182	527	940	1140	1555
11	175	517	925	1140	1575
12	182	525	940	1145	1580
13	180	520	932	1135	1565
14	177	520	930	1140	1575
15	175	515	925	1140	1595
16	182	525	930	1140	1560
17	175	515	917	1135	1580
18	180	522	935	1140	1555
19	177	517	922	1130	1565
20	177	520	925	1135	1575
21	177	520	930	1140	1580
22	180	522	927	1135	1560
23	177	520	925	1135	1565
24	170	515	917	1145	1590
25	182	525	940	1150	1585
avg	178	519	927	1137	1572
pred	172	520	879	1136	1521
stdev	3.25	4.76	7.28	6.62	10.19
high	182	527	940	1150	1595
low	170	503	910	1115	1555
range	12	24	30	35	40

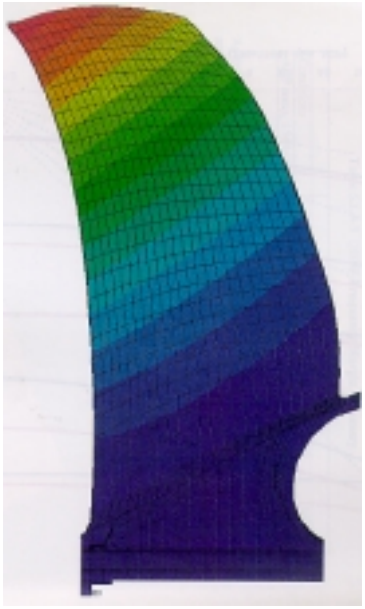

172 Hz - calculated

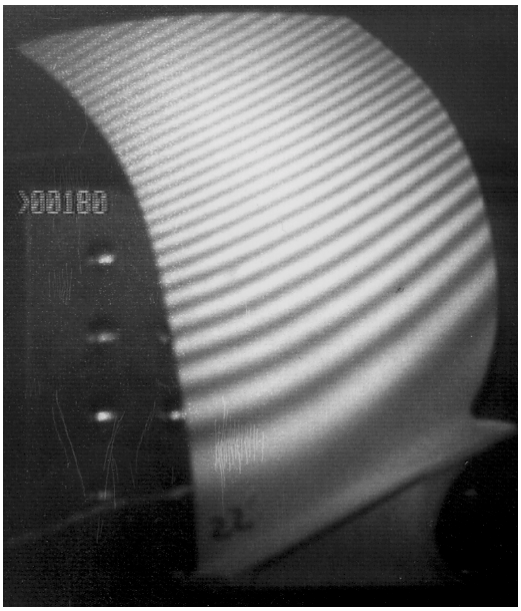

180 Hz - measured

(a) Mode 1

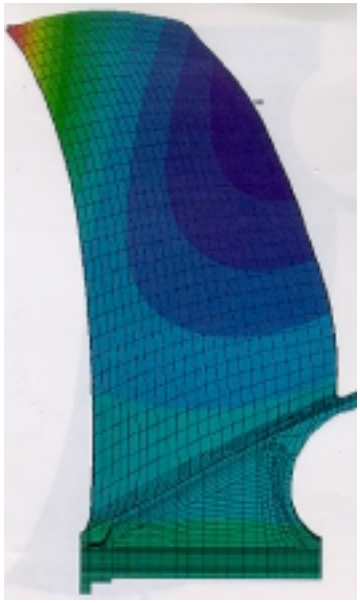

520 Hz - calculated

521 Hz - measured

(b) Mode 2

Figure 7-2. Acoustic Holography Results for the QHSF Fan Blade.

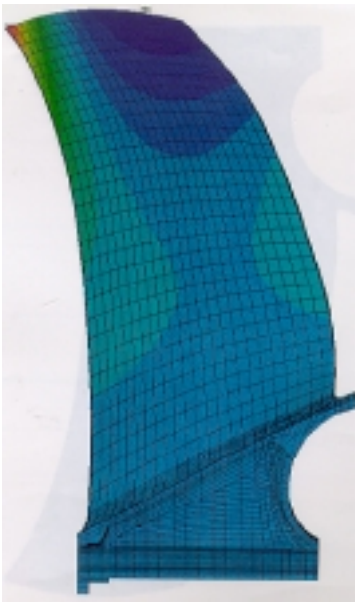

879 Hz - calculated

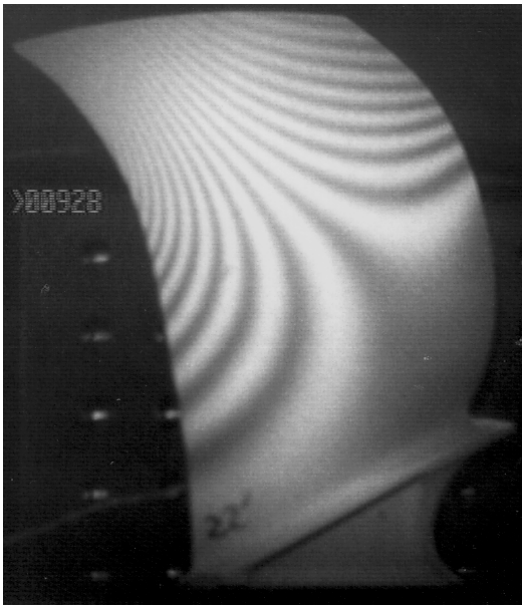

928 Hz - measured

(c) Mode 3

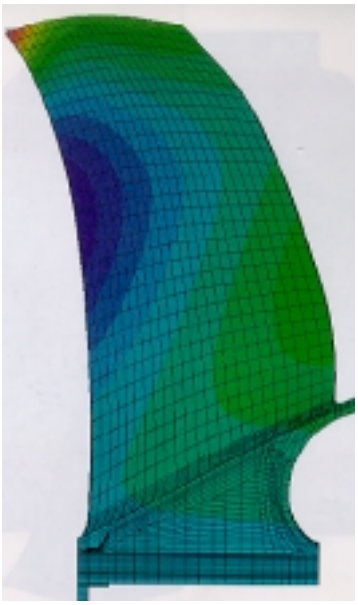

1136 Hz - calculated

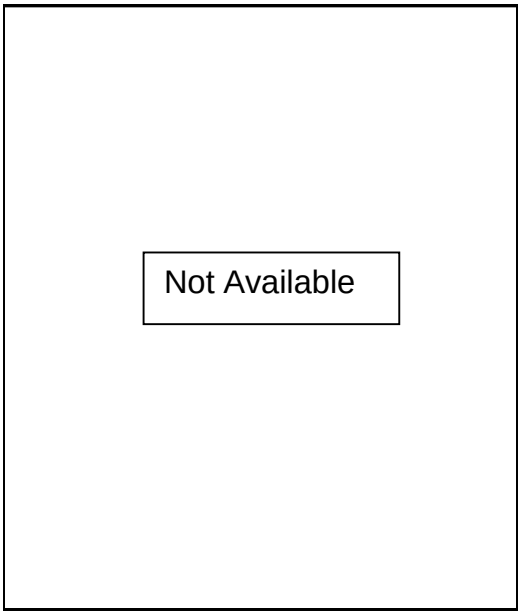

Mode 4

(d) Mode 4

Figure 7-2. Acoustic Holography Results for the QHSF Fan Blade (Cont).

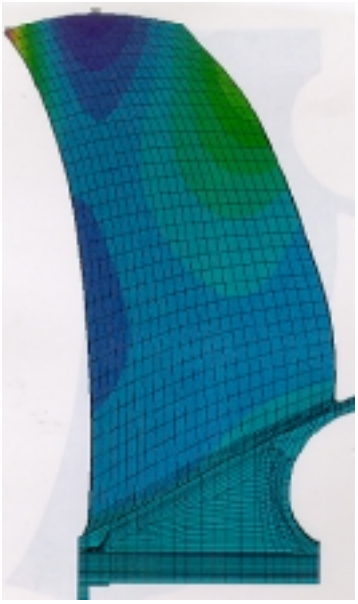

1521 Hz - calculated

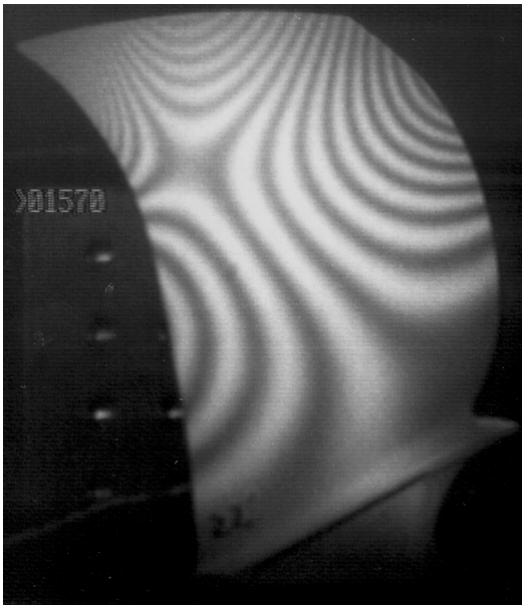

1570 Hz - measured

(e) Mode 5

Figure 7-2. Acoustic Holography Results for the QHSF Fan Blade (Cont).

7.2 Stator Vanes

Engines & Systems manufactured the composite stator vanes for both the baseline fan and QHSF. A photograph of the QHSF stator vane is shown in Figure 7-3.

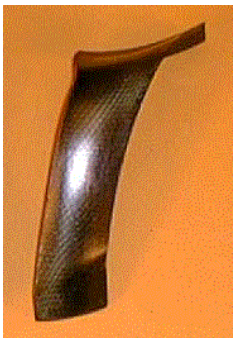

Figure 7-3. Photograph of the QHSF Stator Vane.

7.3 Disk

The disk was machined from a C-250 forging according to the design presented in Figure 3-14.

7.4 Front Frame

The front-frame electronic model was produced by Micro Craft. Figure 7-4 shows the final design.

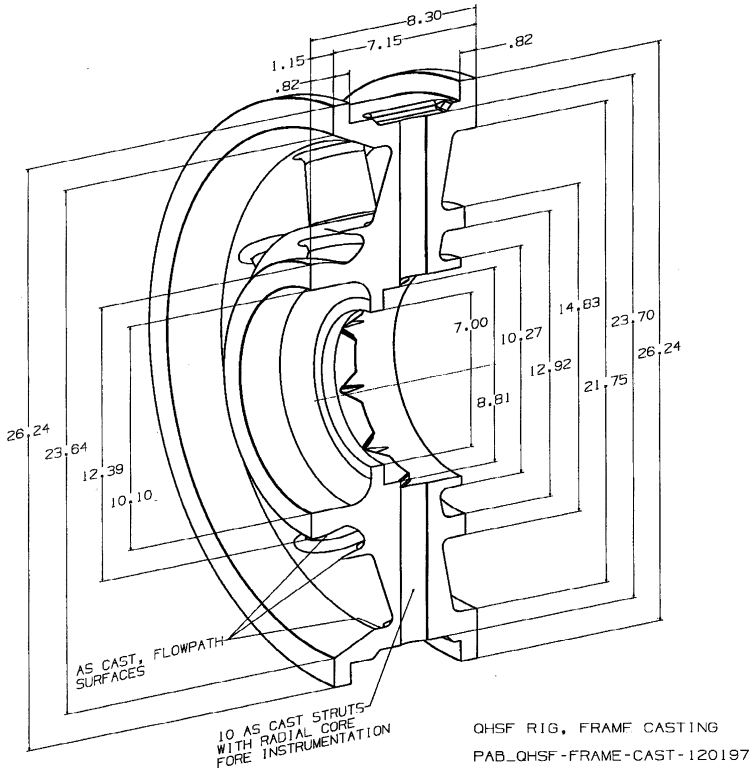

Figure 7-4. 22-inch Rig, QHSF Front-Frame Solid Model.

The initial casting of the front frame using the rapid prototyping process was unsuccessful. The outside flange was not filled properly due to some runners that solidified too early in the process. A second casting was completed, but had a relatively small shrinkage area in the inner rim (Figure 7-5) and various surface inclusions that required welding. It was decided to accept the second casting and omit the instrumentation passage in the strut nearest the shrinkage area. The nacelle structural analysis (see ref. 1) showed that stresses were very low in that area.

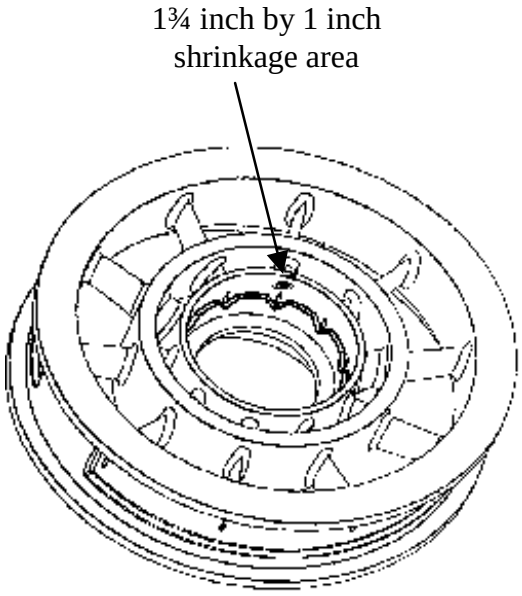

Figure 7-5. 22-inch Rig. QHSF Front-Frame Casting Showing Shrinkage Area.

8. NACELLE DESIGN AND FABRICATION

8.1 Nacelle Aerodynamic Design

The external flow path for the nacelle was defined based on the baseline aircraft geometry. Although the aircraft inlet is drooped and asymmetric to accommodate the accessory gearbox, the 3 o'clock (or 9 o'clock) aerodynamic contour will be used for the rig. Table 8-1 summarizes the inlet geometry in rig scale.

Table 8-1. Summary of Rig Inlet Geometry.

Throat Area, sq. in.	324.3
Highlight Area, sq. in.	415.9
Maximum flow, lb/sec	102.7
Maximum Throat Mach Number	0.72

The model nacelle must also deviate from the baseline nacelle design in two areas: (1) The nacelle maximum diameter in rig scale is too large to fit inside the support ring for the rotating boom microphone for making inlet and exhaust modal measurements. Figure 8-1 identifies the region of the outer skin that will be removed to fit the support ring; and (2) The scaled nacelle is too long for the UHB fan rig and must be shortened. Figure 8-2 shows the approximate position of the nacelle termination to avoid interference. It was determined that the minimum inside radius for the core flow is 5.125 inches.

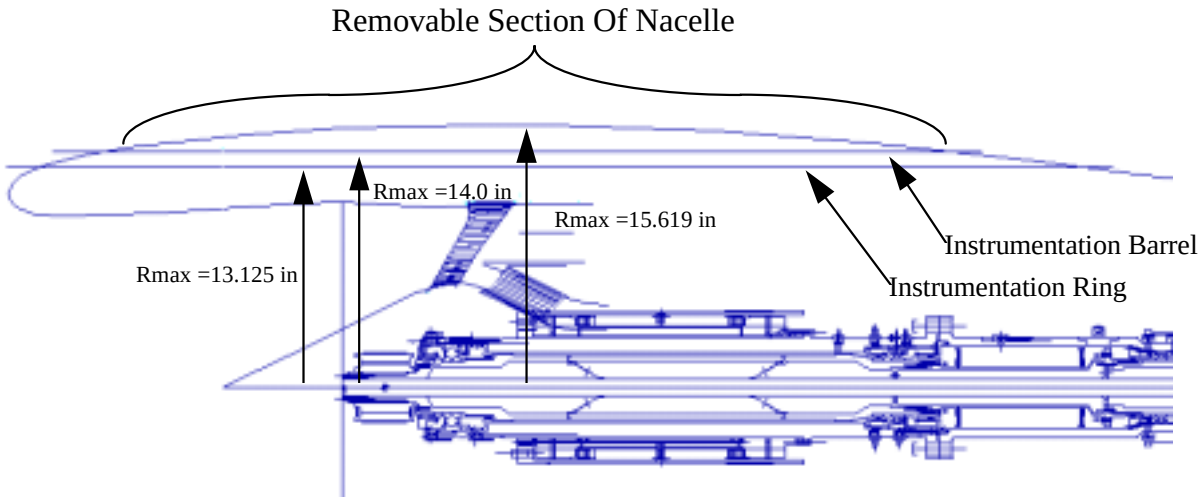

Figure 8-1. Nacelle Will Have Removable Section to Accommodate Rotating Microphone Boom for Modal Measurements.

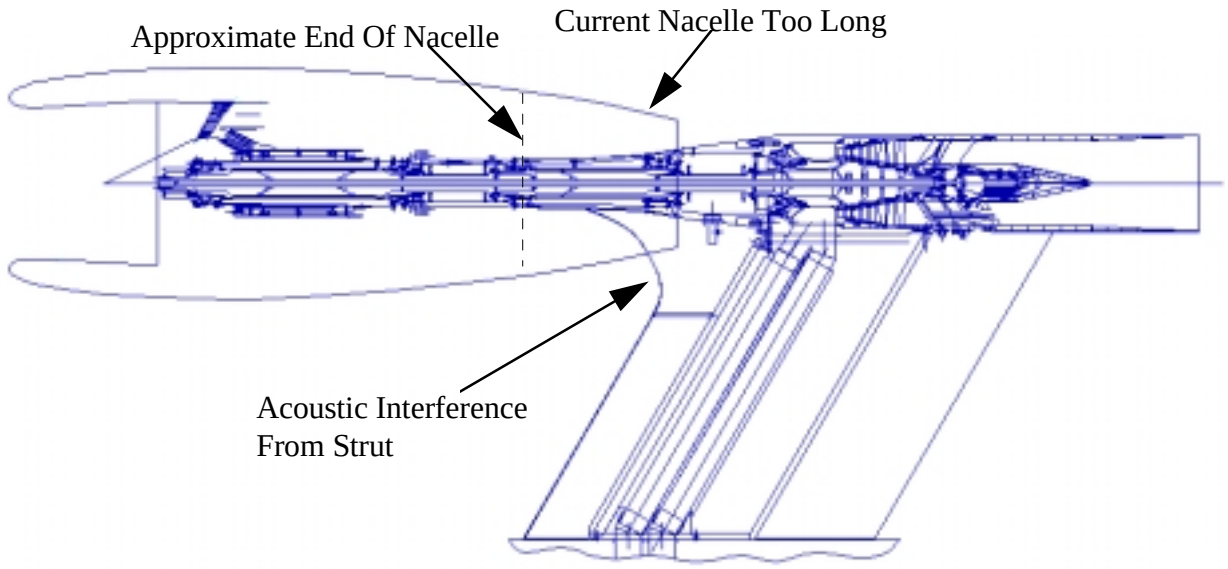

Figure 8-2. Scale Drawing of Baseline Nacelle on UHB Fan Rig Shows Need for Shortening the Nacelle and Redefining the Core Flowpath.

Final core, bypass, nozzle, and aft nacelle aerodynamic lines were defined to simulate the baseline engine flow path as closely as feasible. The final configuration contains a sliding core plug to vary the bypass ratio and a non-variable nozzle exit area. The nozzle-exit area was sized to provide a compromise flow rate through the nozzle at the 100, 85, 70, and 56 percent N1 conditions. With the constant-area exit nozzle, the nozzle flow rate should deviate less than 4 lb/sec from the optimal value at these four engine cycle conditions. The final nozzle area was undersized by three percent to allow for trimming during the wind tunnel test. Figure 8-3 contains Mach number contours in the finalized geometry at the N1 = 85 percent engine condition.

Figure 8-4 shows the calculated total rig corrected flow as a function of fan speed as compared to the corresponding scaled engine flow data. Table 8-2 provides a summary of the plug position, bypass ratio, and flow rates as computed.

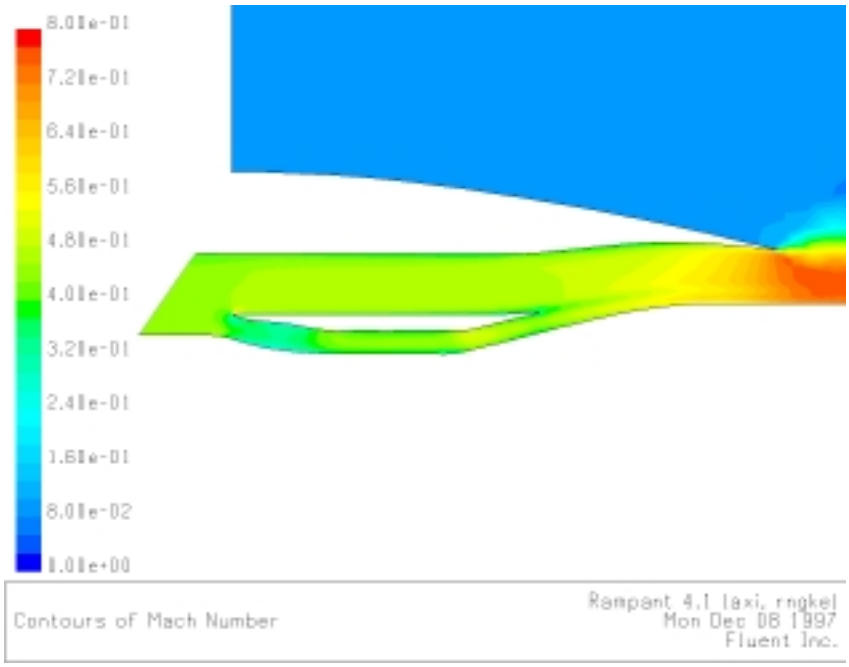

Figure 8-3. Mach-Number Contours of the Fan-Rig Exit-Flowfield at 85% Engine Speed.

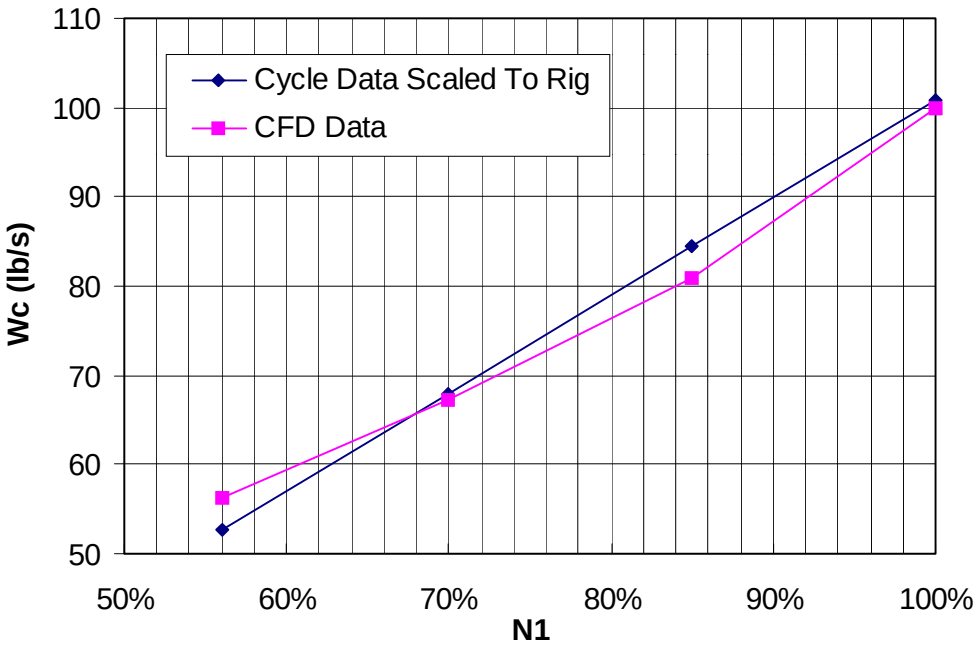

Figure 8-4. The Calculated Rig Total Flow Matches the Scaled Engine Data.

Table 8-2. Corrected Flow Value Comparison of CFD Results with Scaled Engine Cycle Data.

	Cycle Values	Rampant Analysis					
N1	Cycle Data Scaled To Rig	CFD Data	%diff	Wc byp (lb/s)	Wc core (lb/s)	BPR	Plug Position (in)*
100%	100.89	99.99	-0.90	78.89	20.91	3.77	2.72
85%	84.45	80.98	-4.10	65.96	15.03	4.39	3.63
70%	68.01	67.32	-1.01	56.93	10.39	5.48	4.63
56%	52.66	56.35	7.01	49.59	6.76	7.33	7.22

*Note: Zero position is when the plug is translated as far forward as possible, when the plug touches the opposing core shroud surface

8.2 Nacelle Structural Analysis

Micro Craft built a structural analysis model of the rig as shown in Figure 8-5. The model was run in ANSYS 5.3. The frame is constructed of solid bricks and the nacelle structure is constructed of shells. The vanes are modeled as simple beams. The structural loads for the model are summarized in Table 8-3. Modal analyses of the rig were also performed.

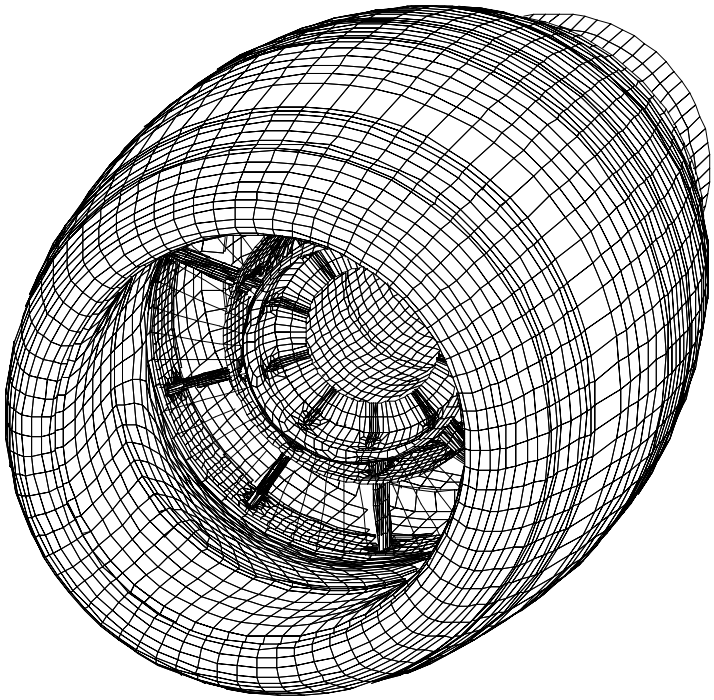

Figure 8-5. ANSYS Structural-Analysis Model of the Rig.

Table 8-3. Load Matrix Used for the Structural Analysis of the Rig.

Load Set	Model Configuration	Unit	Gravity	Gas Loads	Angle of Attack	Stall Pressures	Rub Force	Impact Force
Unit	Flt Nacelle	X						
	Bellmouth	X						
Normal	Flt Nacelle		X	X	X			
	Bellmouth		X	X				
Limit	Flt Nacelle		X	X	X	X	X	
	Bellmouth		X	X		X	X	
Ultimate	Flt Nacelle		X	X	X	X	X	X
	Bellmouth		X	X		X	X	X

The loads described in Table 8-3 are defined as follows:

- Unit Loads:
  - 1 lb./vane axial forward
  - 1 lb./vane tangential in direction of rotation – CCW FLA
  - 1 lb./vane radial outboard
  - Applied at each stator vane at 8.60 radius (52 locations total)
- Gravity Loads:
  - 1g acceleration upward
- Gas Loads:
  - 7.8 lb./vane axial forward
  - 29.2 lb./vane tangential in direction of rotation
  - Applied at each stator vane at 8.60 radius (52 locations total)
  - 16.1 lb./strut axial (forward) at middle of core strut (10 locations total)
  - 0.4 lb./strut axial (aft) at middle of bypass strut (10 locations total)
- Angle of Attack Loads:
  - The pressure loads on the outer nacelle are shown in Figure 8-6 for an angle-of-attack of 20 degrees. The pressure increase at the inner wall at station 170.0 represents the 1.839 pressure ratio increase at the rotor. Pressures on the strut, the outer wall of the splitter, and in the core duct were assumed to be 24.2 psi.

- Stall loads:
  - 31.5 psi stall pressure will be applied to the outer nacelle inner wall aft of the fan blades and forward of the stator vanes.
- Blade-out rub loads:
  - 350 lb. tangential (CCW FLA) & 2,200 lb. radially outboard
  - Applied at station 170, distributed along 180-degree sector centered at top dead center
- Blade-out impact loads:
  - 13,291 lb. radially outboard Applied at station 170, converted to a pressure and applied at 3 elements near bottom

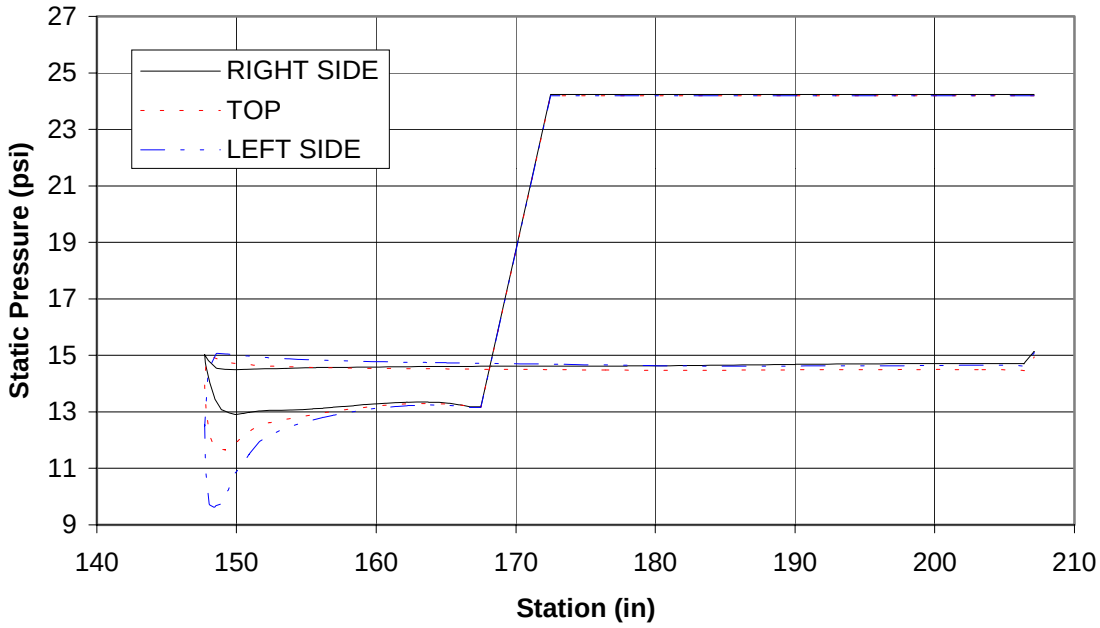

Figure 8-6. Aerodynamic Pressure Loads at Angle of Attack = 20 Degrees Used for the Structural Analysis of the Rig.

The following is a list of assumptions used in the Ultimate Load Case:

- The impact load/blade-out load used the entire blade including the dovetail. The dovetail would most probably remain inside the dovetail slot. Therefore, the mass of the fragment would be reduced, decreasing the normal force of the fragment.
- The normal force of the blade-out fragment is 40,398 pounds. For an impact load case, it is considered a conservative estimate to assume that the effective load experienced is twice the actual load (Reference Blodgett, O, "Design of Welded Structures"). This conservative load estimate (80,796 pounds) has been used in this analysis.

- The impact load/blade-out load was a static solution approximation. This analysis assumed that the blade, including the dovetail, is contained by the fan casing and that all of the load would be transmitted through to the fan frame. In reality, the fan casing would not contain the blade fragment. Therefore, the fan frame would take only a portion of the normal force of the blade fragment.

- All bolts at the fan casing to the fan-frame flange are assumed to remain in place, to fully transmit the blade-out load into the fan casing. In reality, some of these bolts would probably fail.

- The inlet guide vanes are modeled as rigid beams, completely fixed at the inner diameter and bolted at the outer diameter to the fan frame. This effectively restricts the deflection of the fan frame at the bolted joints. In reality, the vanes will pull out at the inner diameter, and the vanes will not restrain the fan frame. This would decrease the stress at the bolted joint locations in the fan frame.

- The radial bolts located between the fan casing, rings, and panels are assumed to fail over 20 degrees, ±10 degrees, from the event. This would allow the bolted flanges of the fan frame to carry additional load.

Figures 8-7 to 8-11 show equivalent, radial, hoop, axial, and third principal stresses in the inner frame. The yield strength of the fan frame for designated and non-designated areas is 35 and 28 ksi, respectively. None of the stresses in the inner frame exceed the yield strength of the non-designated area. The analysis shows that the load in the fan frame has been dissipated from the two struts at bottom dead center through the rest of the fan fame.

Figure 8-12 is an ANSYS plot of the nodal forces at the constraints of the inner fan-frame flange. Figure 8-13 is a chart showing the radial, circumferential, and axial nodal forces at each of the constrained nodes. There are eight evenly spaced bolts in the inner fan-frame flange (the bolts used are 3/8 in diameter, Inconel 718, with a yield strength of 145 ksi). These bolts will take the axial load, while the radial load will be taken through the long piloted joint at the interface to the static balance at the fan-frame inner diameter. The circumferential loads will be taken by two alignment/shear pins, which are located at 112.5 and 247.5 degrees. Table 8-4 summarizes the forces at each bolt and alignment pin location. Bolt 1 is at top dead center. The nodal forces were summed from the bolt center to half way between the adjacent bolt center (both sides). Table 8-5 lists the bolt axial/tensile stress and factor of safety for each bolt in the Ultimate Load Case. Table 8-6 calculates the shear load taken by the alignment pins due to the circumferential rub and vane loads in the limit load operation. This table assumes that the alignment pins will take the entire circumferential shear load. The alignment pins also take the circumferential load in the Ultimate Load Case. There are two different assumptions of how the pins can be loaded. The first assumes that only the right pin (located at 112.5^{o}) takes the load on the right side (0-180 degrees), while the left pin (located at 247.5 degrees) takes the load on the left side (180-360 degrees). The second assumption sums the circumferential forces over the entire 360 degrees. Hence, the loads on the right and left-hand sides counteract one another. Table 8-7 shows the forces/factors of safety of the alignment pins for both assumptions (the first two rows are for the first assumption and the third row is for the second assumption).

All bolts have a factor of safety for axial loading in this conservative analysis. The piloted joint at the fan-frame inner-diameter/static-balance interface will take the shear loading in the radial direction. The circumferential shear load is within the limits of the alignment pins.

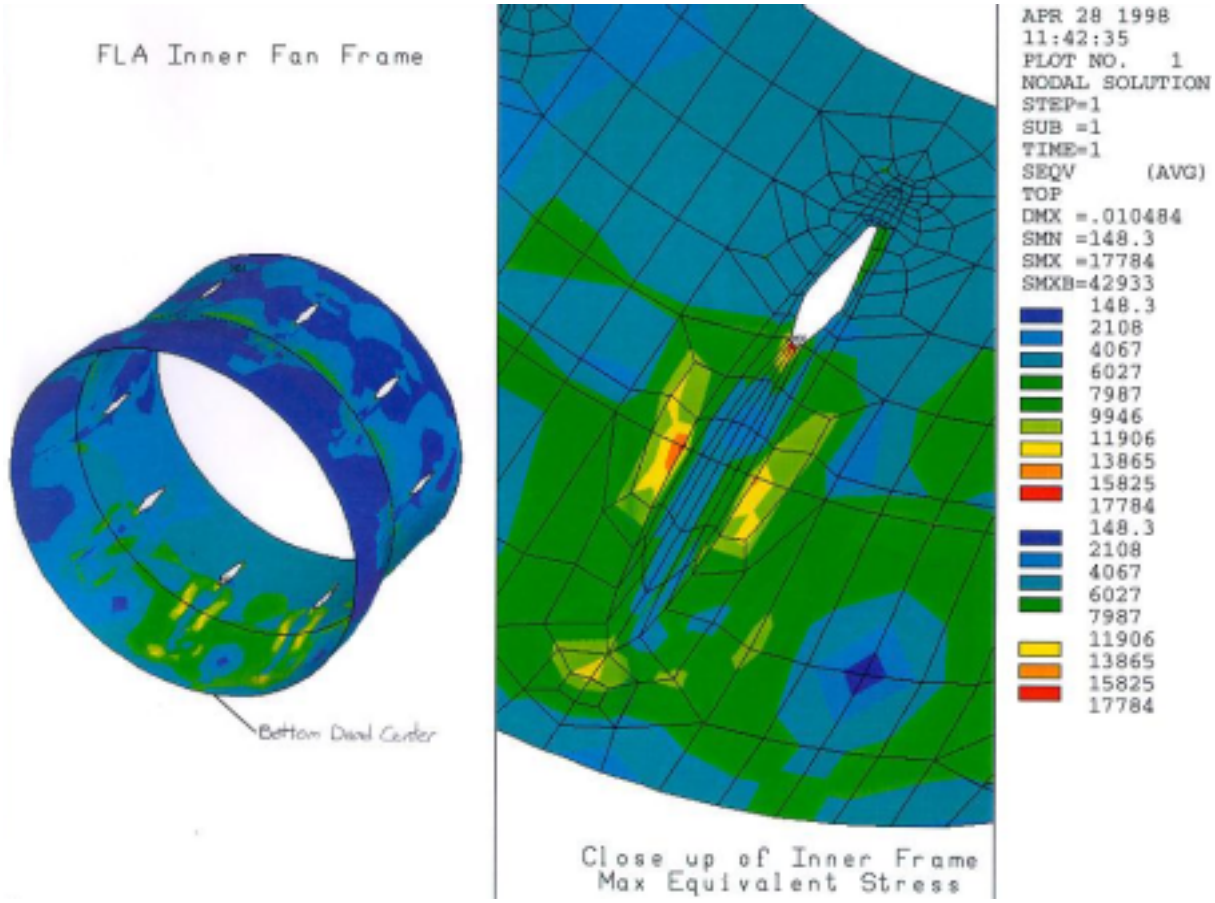

Figure 8-7. Equivalent Stress Distribution in the QHSF Front Frame and Case for the Ultimate Load Case.

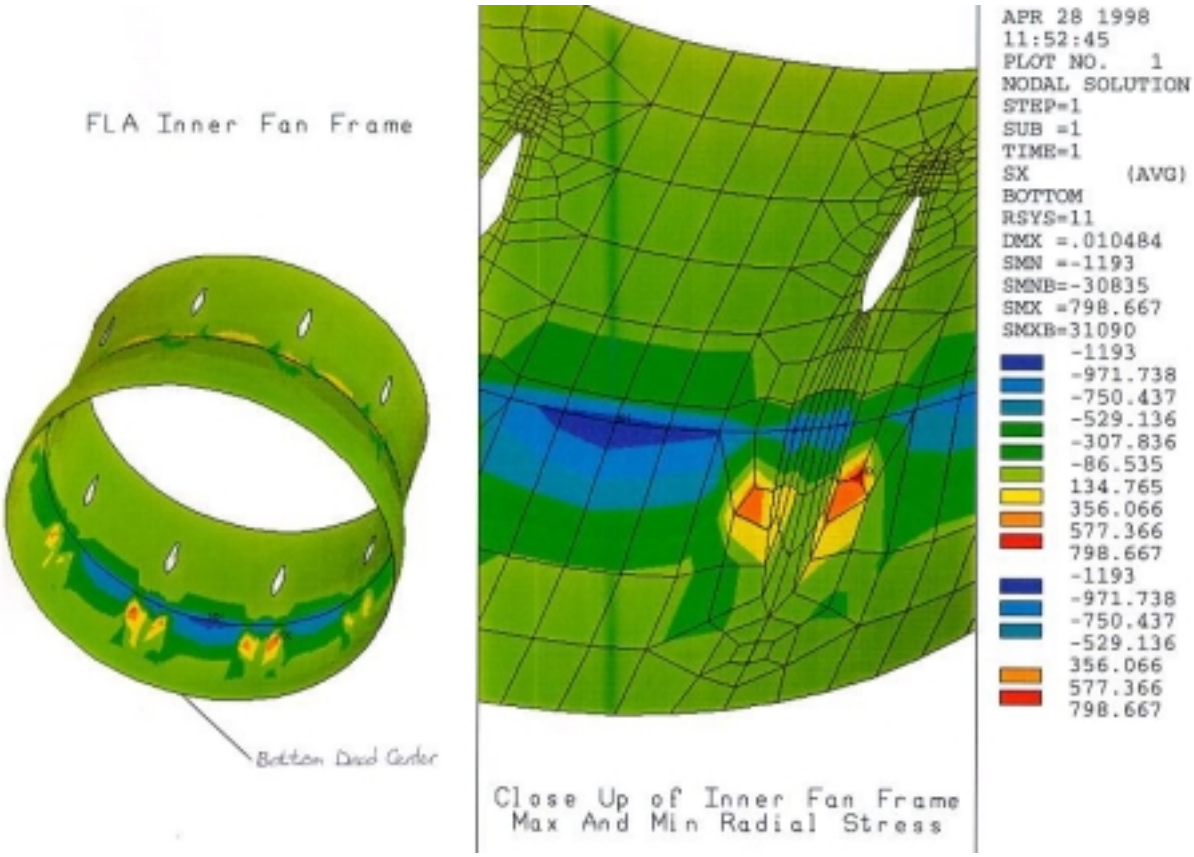

Figure 8-8. Radial Stress Distribution in the QHSF Front Frame and Case for the Ultimate Load Case.

Table 8-4. Inner Fan-Frame Flange Bolt and Alignment-Pin Forces.

Bolt And Pin Number	Bolt Hole Center Location (Degrees)	Lower Range For Location (Degrees)	Upper Range For Location (Degrees)	Axial Summation of Tensile Forces (lbf)
Bolt 1	0	337.5	22.5	10,391
Bolt 2	45	22.5	67.5	10,202
Bolt 3	90	67.5	112.5	7,282
Bolt 4	135	112.5	157.5	5,939
Bolt 5	180	157.5	202.5	4,294
Bolt 6	225	202.5	247.5	5,927
Bolt 7	270	247.5	292.5	8,123
Bolt 8	315	292.5	337.5	9,288

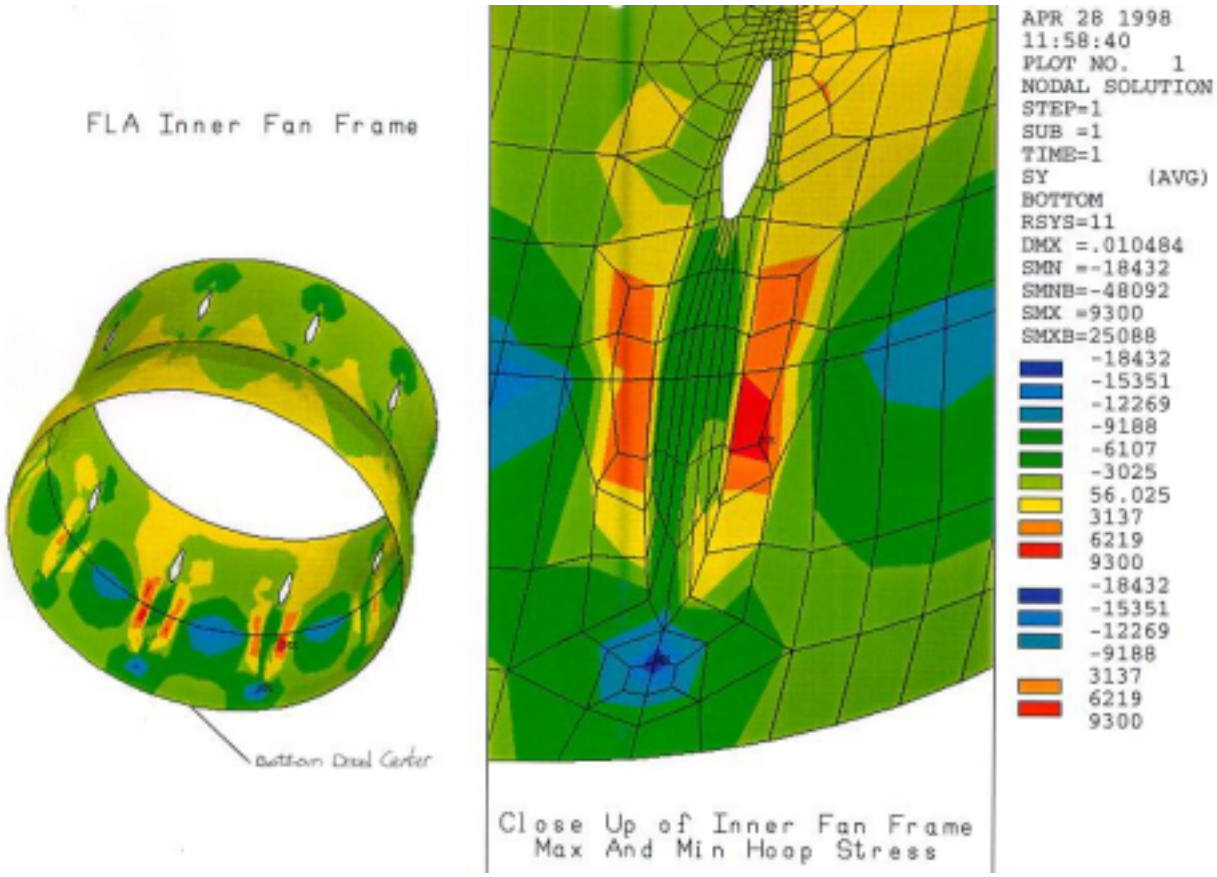

Figure 8-9. Hoop-Stress Distribution in the QHSF Front Frame and Case for the Ultimate Load Case.

Table 8-5. Inner Fan-Frame Flange Bolt Axial/Tensile Stresses and Factors of Safety.

Bolt And Number	Bolt Diameter (in)	Bolt TSA Area (in2)	Bolt Yield Strength for Inco 718 (psi)	Bolt Axial or Tensile Force (lbf)	Bolt Axial or Tensile Stress (psi)	Bolt Factor Of Safety
Bolt 1	0.375	0.0878	145,000	10,391	118,351	1.2251713
Bolt 2	0.375	0.0878	145,000	10,202	116,190	1.2479537
Bolt 3	0.375	0.0878	145,000	7,282	82,941	1.7482354
Bolt 4	0.375	0.0878	145,000	5,939	67,646	2.1434969
Bolt 5	0.375	0.0878	145,000	4,294	48,909	2.9646759
Bolt 6	0.375	0.0878	145,000	5,927	67,500	2.1481445
Bolt 7	0.375	0.0878	145,000	8,123	92,515	1.567307
Bolt 8	0.375	0.0878	145,000	9,288	105,791	1.3706225

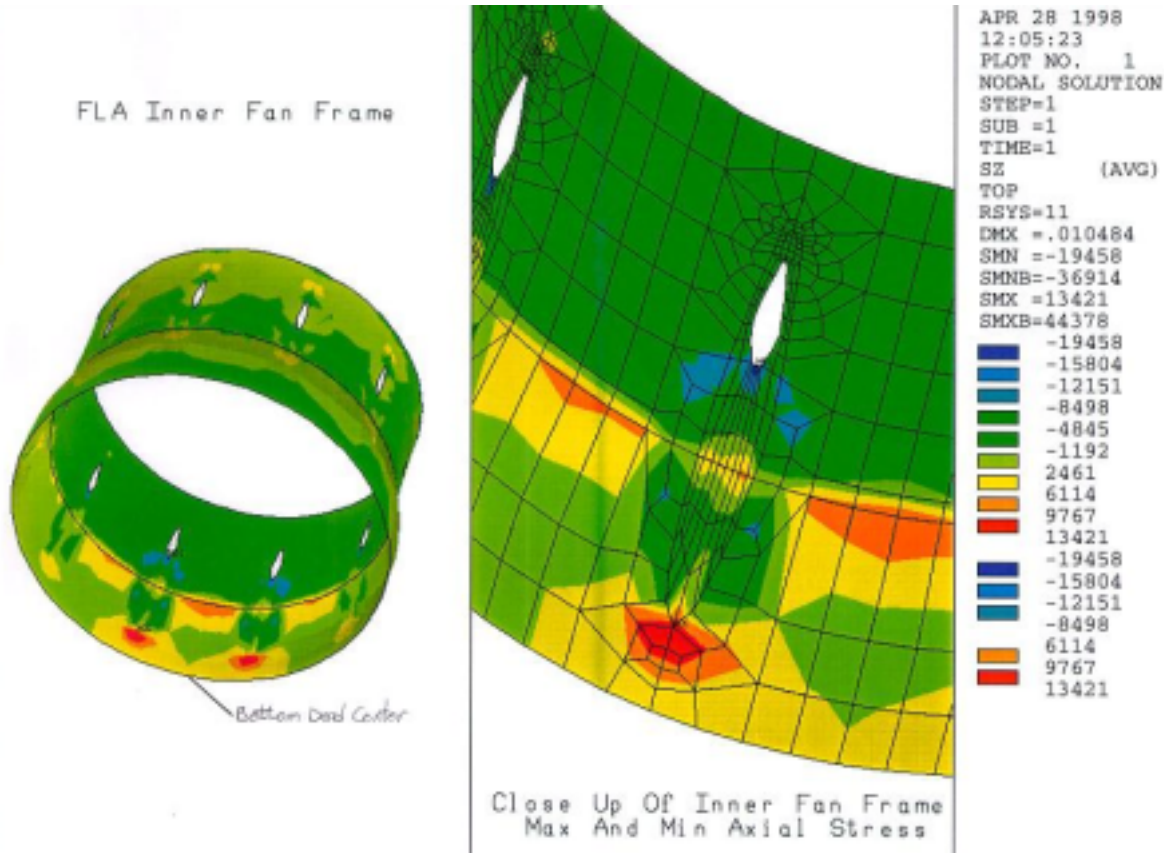

Figure 8-10. Axial Stress Distribution in the QHSF Front Frame and Case for the Ultimate Load Case.

Table 8-6. Circumferential Shear Load Due To Vane and Rub Loads.

Item	Value	Units
Vane Data		
Vane No. Radius of Load Load/Vane (Circum.)	52 8.46 29.2	 in lbf
Rub Load Data		
Circum. Load Radius of Load	700 12	lbf in
Alignment Pin Data		
Number of Pins Radial Location Pin Diameter Unbrako Double Shear Strength	2 3.5 3/8 33150	 in in lbs
Summation of Torque (700*12.0) + (29.2*52*8.46) = (2*3.5)*F		
Shear Force Taken By Each Pin Factor Of Safety	3,035 10.92	lbf

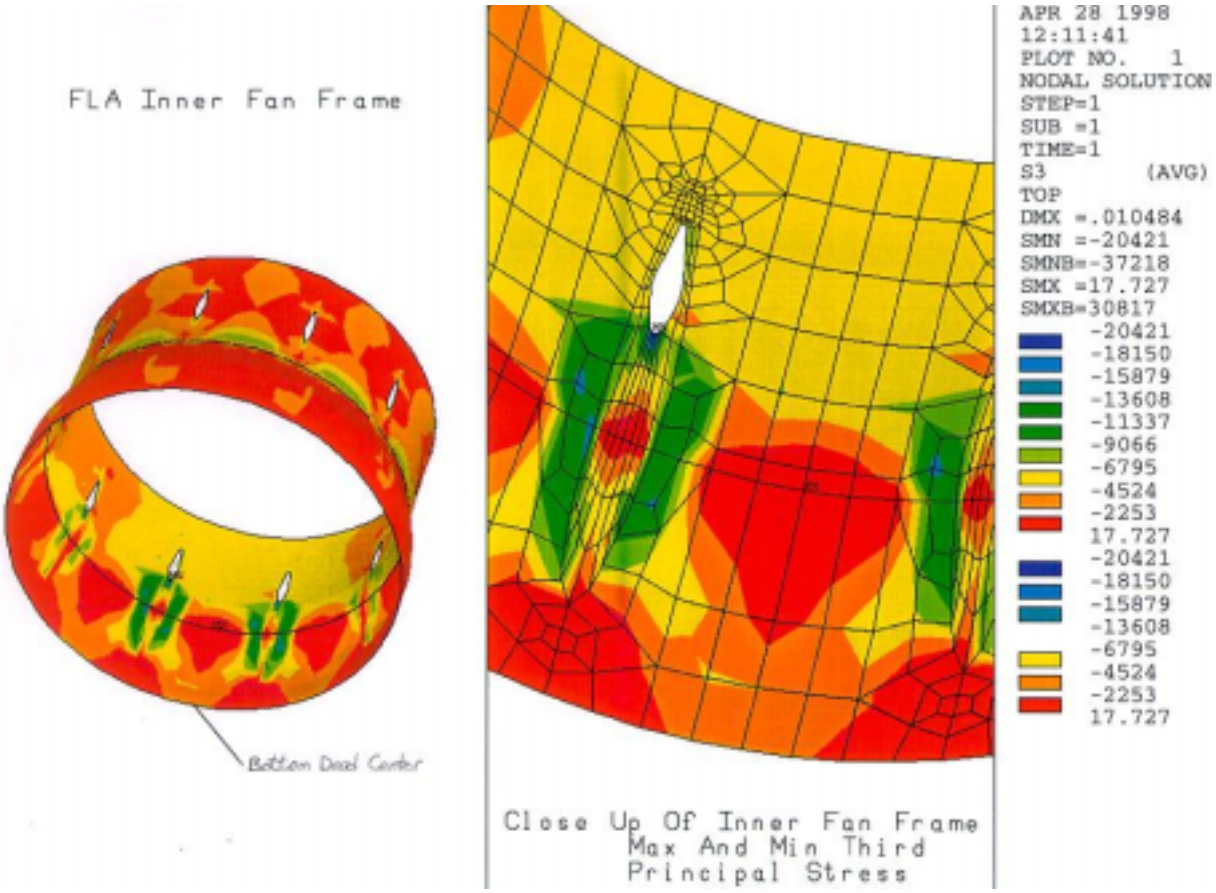

Figure 8-11. Third Principal Stress Distribution in the QHSF Front Frame and Case for the Ultimate Load Case.

Table 8-7. Forces/Factor of Safety for Alignment Pins in the Ultimate Load Case.

Circum. Forces	Load (lbf)	Shear Strength (lbf)	Safety
Right Side 0-180^{o}	-18051.7	33150	1.8
Left Side 180-360^{o}	19242.1	33150	1.7
Full Flange 0-360^{o}	1190.4	33150	55.7

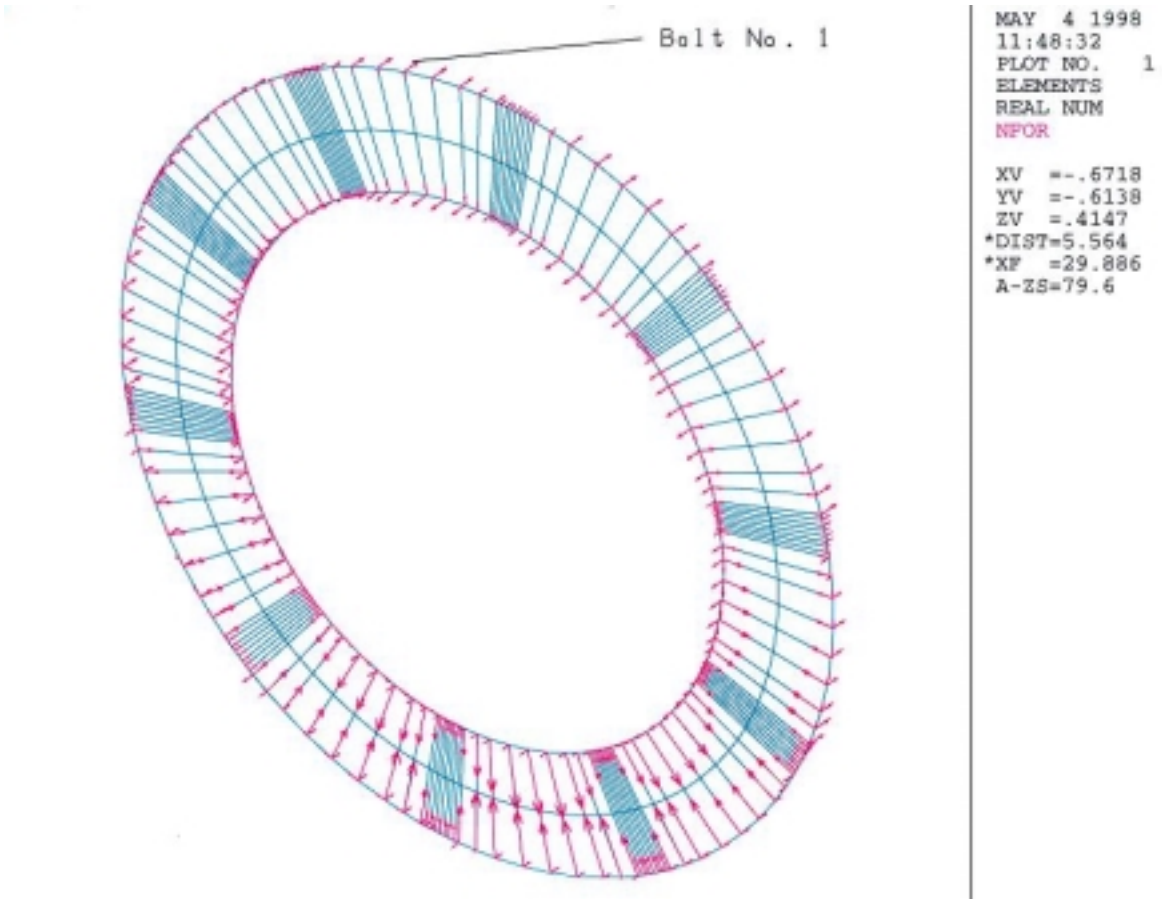

Figure 8-12. ANSYS Plot of the Nodal Forces at the Constraints of the Inner Fan-Frame Flange.

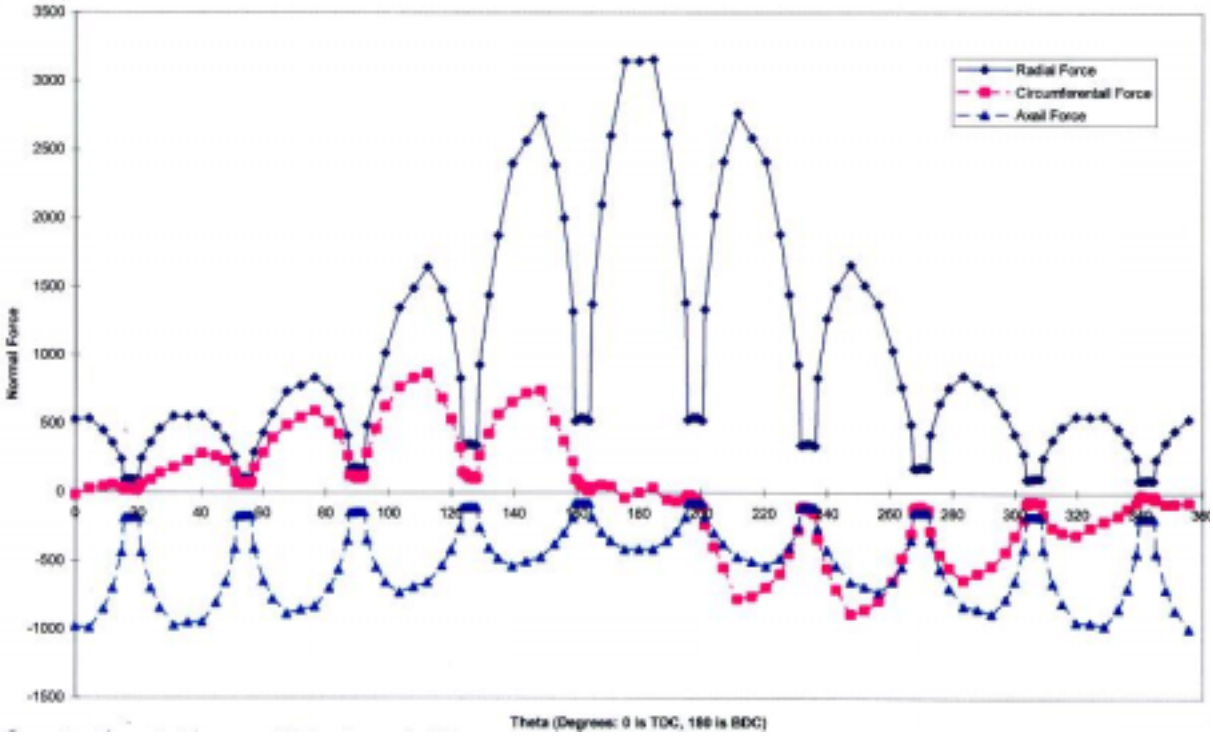

Figure 8-13. Comparison of the Radial, Circumferential, and Axial Nodal Forces at Each of the Constrained Nodes.

8.3 Rotor Assembly Analysis

8.3.1 Description and Materials

Based on the rotor blade and disk design, a rotor assembly model was developed by Micro Craft. Key features of the assembly are the spinner, torque sleeve, rotating seal, and rotational speed pick-up teeth. The blade and rotor mass properties for the rig dynamic analysis are summarized in Table 8-8. A diagram of the rotor assembly is presented in Figure 8-14.

Table 8-8. Blade and Rotor Mass Properties for the Rig Dynamic Analysis.

Blade Mass Properties

	Weight, lb	Mass, lb-sec^2/in	Rcg, in	Zcg, in
Complete Blade	0.8311	0.0022	5.9969	0.1705
Airfoil only	0.4631	0.0012	7.4466	0.0706
Airfoil + attachment above dovetail min-neck	0.7482	0.0019	6.2898	0.1963

Rotor Mass Properties

	Weight, lb	Mass, lb-sec^2/in	Id, lb-in-sec^2	Ip, lb-in-s^2	Zcg, in
Blades (22)	18.2849	0.0474	1.0017	1.9340	0.1705
Disk	16.2922	0.0422	0.2156	0.3709	0.0003
Complete Rotor	34.5772	0.0896	1.2180	2.3049	0.0903

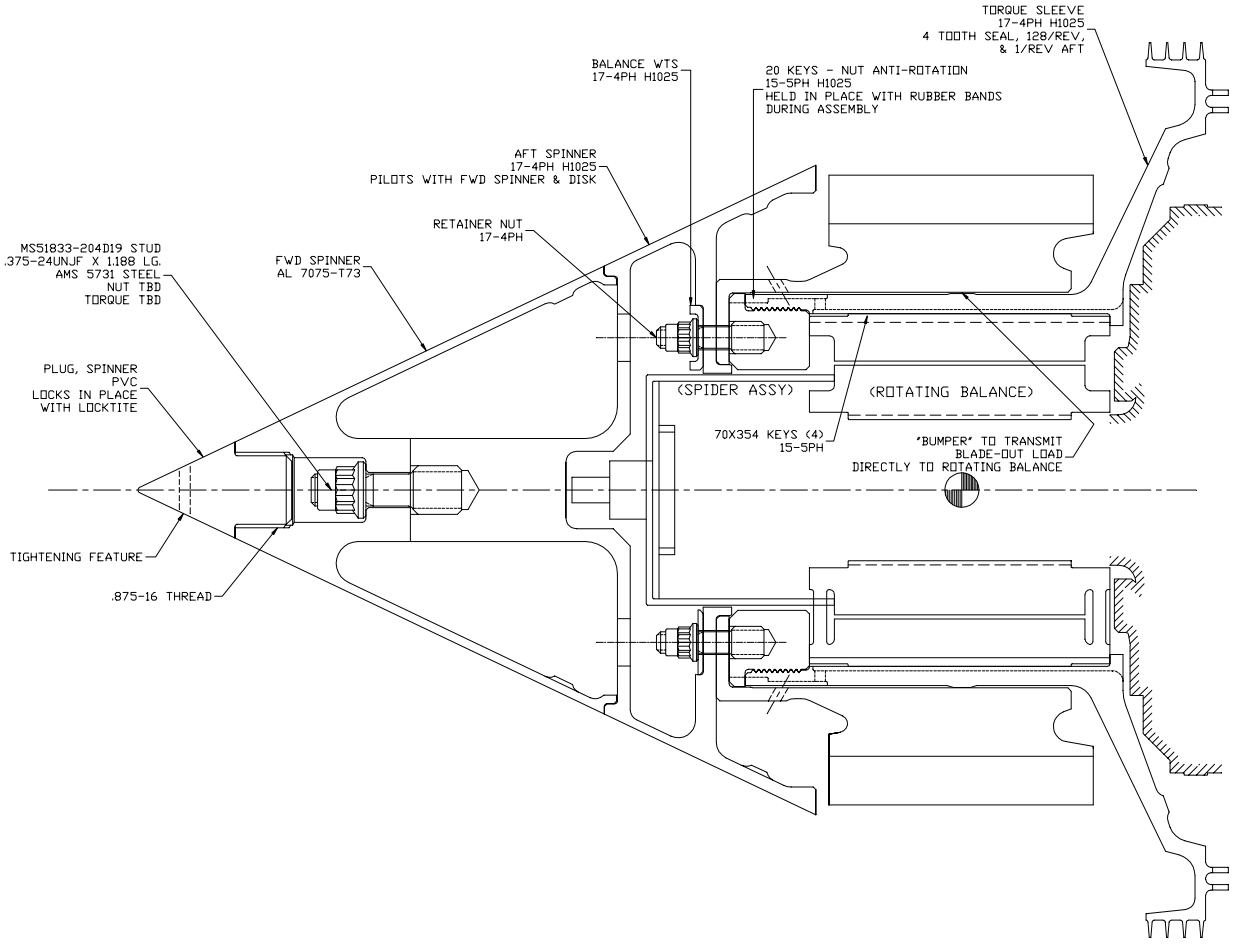

Figure 8-14. The QHSF Final Rotating Assembly Design Features a One-Piece Torque Sleeve and Rotating Seal with a Retaining Nut To Hold the Disk.

Parameter values for the analysis of the rotating-assembly are presented in Table 8-9.

Table 8-9. Material and Design Parameters for Analysis of the 22-inch QHSF Rig Rotating Group.

Specification	Material	H.T.	p lb/in^3	Ftu lb/in^2	Fty lb/in^2	Fsu lb/in^2	Where Used:
AMS 5643	17-4PH	H1025	0.283	155,000	145,000	95,000	Rotor Structure
AMS 5659	15-5PH	H1025	0.283	155,000	145,000	97,000	Shear Keys
QQ-A-367	Al 7075	T73	0.101	61,000	52,000	-	Spinner
-	PVC	-	0.048	-	5,500	-	Spinner Plug
AMS 6322	4140 Steel	-	0.283	160,000	142,000	96,000	Studs
SPS Steel	Steel	HRC 60	-	-	-	150,000	Dowel Pins

DESIGN PARAMETERS

Number of blades	22
Inlet tip diameter (QHSF Rig)	22.000 inches
Rotor speed (mechanical design point)	15,444 rpm 100% physical speed at 65F
Corrected tip speed (mech. design point)	1,474 ft/sec
Forward cavity pressure	25.5 psi (1.78 PR)
Forward cavity temperature	93.1F
Aft cavity pressure	14.3 psi
Aft cavity temperature	194.0F
Estimated	
Blade mass (total for 22)	0.043556 lb.-sec^2/in
Blade radius, center of gravity	7.35 in

Condition	Speed, N		w	Tip speed	AF Load	Torque
	%	RPM	rad/s	ft/s	lb	in-lb
Mechanical design point*	100%	15,444	1,617.3	1,482	1,870	15,180
Maximum test speed	110%	16,988	1,779.0	*1,631*	2,430	19,164
Maximum operating speed	121%	18,687	1,956.9	*1,794*	*2,900*	24,912

* 100% physical speed at 65°F scaled to rig

8.3.2 Bolted Joint and Key Analysis

The main rotor joint, shown in Figure 8-15, consists of the retainer nut, which is threaded into the torque sleeve with a 4.25-16 thread. The retainer nut is held in place with twenty anti-rotation keys. The nut has twelve 0.250-28 studs which provide axial retention for the fan disk. Torque is transmitted to the disk using four SPS Unbrako 0.3125-inch diameter dowel pins. The four keys that transmit torque from the rotating balance to the torque sleeve are also examined. The following assumptions were made in performing the analysis:

- In the main rotor joint, dowel pins take all shear loads and studs take all tension loads.

- The disk will be located on the balance retainer nut using a temporary pilot joint during assembly. The disk will be bolted to the retainer nut using the twelve 0.25-28 studs. Then the four dowel pins will be line-drilled through the disk and nut. The assembly will then be separated and the pilot will be machined off of the retainer nut.

- Radial shear load in the pins is 1,955 pounds at 121 percent speed (from finite-element analysis).

- The rotor acts as a beam fixed at one end and simply supported on the other to calculate moment loading on studs.

- The aft spinner material was steel to provide a more favorable joint stiffness ratio. (The flange should be approximately twice as stiff as the bolt.)

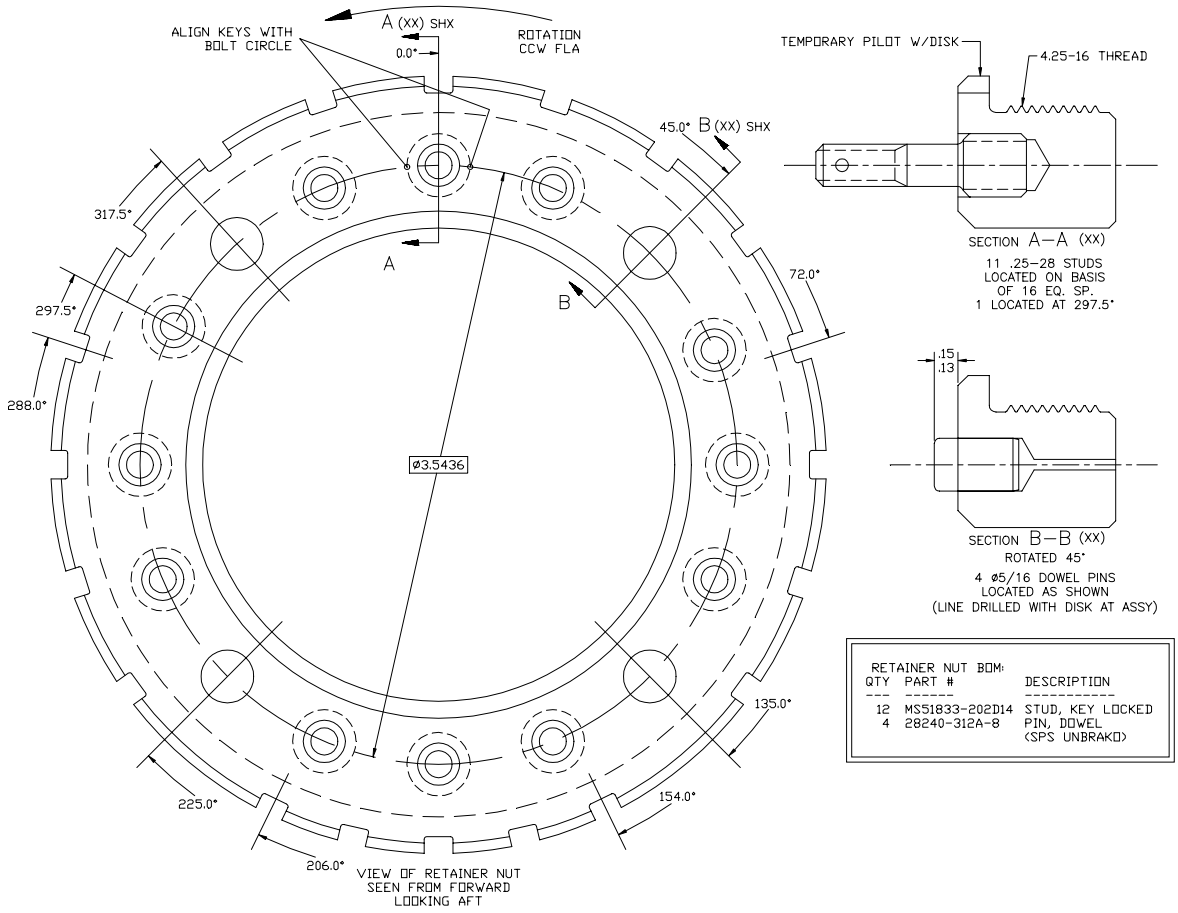

Figure 8-15. Rotor Bolt Circle in Retaining Nut Showing Bolt and Key Locations.

A summary of the results is presented in Table 8-10. Capacities are based on tensile strength or shear strength multiplied by the component area.

Table 8-10. Results of the Bolted Joint and Key Analysis.

Tension Component	Capacity Ftu * A, lb	Load @ 121%N, lb	Safety Factor,	Blade-out Load lb	Safety Factor
0.250-28 stud (12)	4,107	971	4.2	2,341	1.8
4.250-16 thread (1)	> 57,324	2,900	> 19.8	< 6,994	> 8.2

Shear Component	Capacity Fsu * A, lb	Load @ 121%N, lb	Safety Factor	Blade-out Load, lb	Safety Factor
0.3125 Pin (4)	11,505	3,423	3.4	5,333	2.2
2.4 x 1.75 Key (4)	407,400	6,166	66.1	-	-
0.10 x 0.17 Key (20)	1,649	460*	3.6	-	-

*Based on deceleration load: 1,705 ft-lb.

Joint Axial Flexibility Ratio (K_{STUD}/K_{FLANGE}) = 0.58

8.3.3 Rotor Assembly Finite-Element Analysis

A 2-D axially symmetric model was used to determine stresses and deflections in the torque sleeve, retainer nut, and spinner and to ascertain forces in the bolted joint and pilots. The model was run with three loading conditions: Assembly Loads only, Design Point (100 percent speed), and maximum operating speed (121 percent speed).

Micro Craft created the model geometry in AutoCad LT for Windows, then converted the geometry to a “prt” file in Unigraphics. This file was then imported into Patran, where the original mesh was generated. The mesh from Patran was then converted to an ANSYS input file and run in ANSYS Version 5.3. A summary of the results of the stress analysis is provided in Table 8-11.

The following points should be noted about the maximum effective stress:

- Stresses in the spinner plug do not include torque stress on the threads (elements were coupled to the forward spinner).
- The maximum stress location in forward spinner is under bolt head at a spot where the spinner is coupled to a bolt element. The maximum stress away from the couple occurs at the bottom of the counter-bore and is 20 ksi for case 3 (121 percent speed).
- Stresses in disk are approximate due to estimated blade loads and are listed here for information and comparison with disk analysis (see Section 3.4).
- Stresses in retainer nut do not include torque stress on the threads. See the bolted joint analysis (Section 8.3.2) for these stresses.
- Maximum stress in the torque sleeve occurs at the aft side of the rotating seal in the fillets between the 1/rev sensor and the 128/rev sensor. However, the fatigue life should be in the 104 Order of Magnitude according to MIL-HDBK-5.

Table 8-11. Maximum Effective Stress in Rotor Components.

Real No.	Description	Case 1 Assy, ksi	Case 2 Des Pt, ksi	Case 3 Max Sp, ksi	Ftu, ksi	Location
1	Spinner Plug	0.0	0.2	0.2	5.5	Aft Thread
2	Forward Spinner	33.6	32.1	32.3	61.0	Under bolt head
3	Aft Spinner	43.4	42.3	42.7	155.0	Case 1&2: bolt head; 3: aft end
4	Disk	20.2	124.3	181.5	-	Information Only. Case 1 Flange ID; 2&3 near aft bore
5	Retainer Nut	17.7	17.3	22.1	155.0	Case 1&2 under bolt; 3 flange ID
6	Torque Sleeve	6.7	48.3	72.8	155.0	Case 1 aft thread; 2&3 fillet @ 128/rev

The loads at various contact planes are presented in Table 8-12 for the locations shown in Figure 8-16. The following points should be noted about the contact plane loads:

- Contact in all of the pilots is increasing as the speed increases.
- Contact elements (Real Number 43) were intentionally omitted from the model.

- Contact does not occur at Real Number 46 in normal operation. The pad with a clearance of 0.005 inch is there to transmit unbalance load from blade loss directly to the rotating balance.

- Real Number 49 represents bolt preload for the 12 studs.

- Real Number 50 represents bolt preload for 0.375-28 forward spinner bolt.

Table 8-12. Load in Contact Elements, Pounds.

Real No.	Description		Assy	Des Pt	Max Sp
41	Aft Spinner - Forward Spinner (at pilot)	Axial	-16	-38	-63
42	Aft Spinner - Forward Spinner Pilot	Radial	-772	-1,041	-1,266
44	Disk - Shear Pin (Ret Nut)	Radial	-1,617	-1,774	-1,955
45	Aft Spinner - Disk Pilot	Radial	-5,325	-7,164	-8,164
46	Torque Sleeve - Disk	Radial	0	0	0
47	Retainer Nut - Disk	Axial	-35,568	-32,487	-31,981
48	Disk - Aft Spinner	Axial	-35,568	-33,422	-32,916
49	Aft Spinner - Nut	Axial	-35,568	-34,357	-33,851
50	Forward Spinner - Nut	Axial	-7,541	-7,190	-7,194
51	Aft Spinner - Forward Spinner (at bolt)	Axial	-7,524	-7,152	-7,130
52	Bolt, Forward Spinner - Forward Spinner	Radial	-122	-200	-182
	Total Load, All Contact Elements		-129,621	-124,825	-124,702

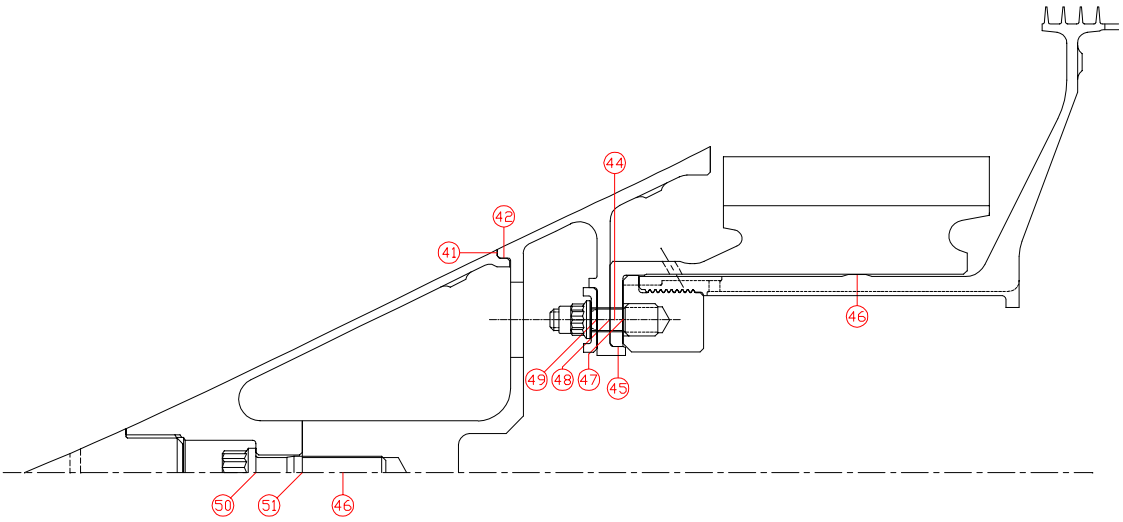

Figure 8-16. Contact-Element Locations.

Figures 8-17 through 8-26 show the results of the finite-element analysis. It can be seen from the pictures that all of the relevant deflections and stresses are within desired limits as summarized in Table 8-11.

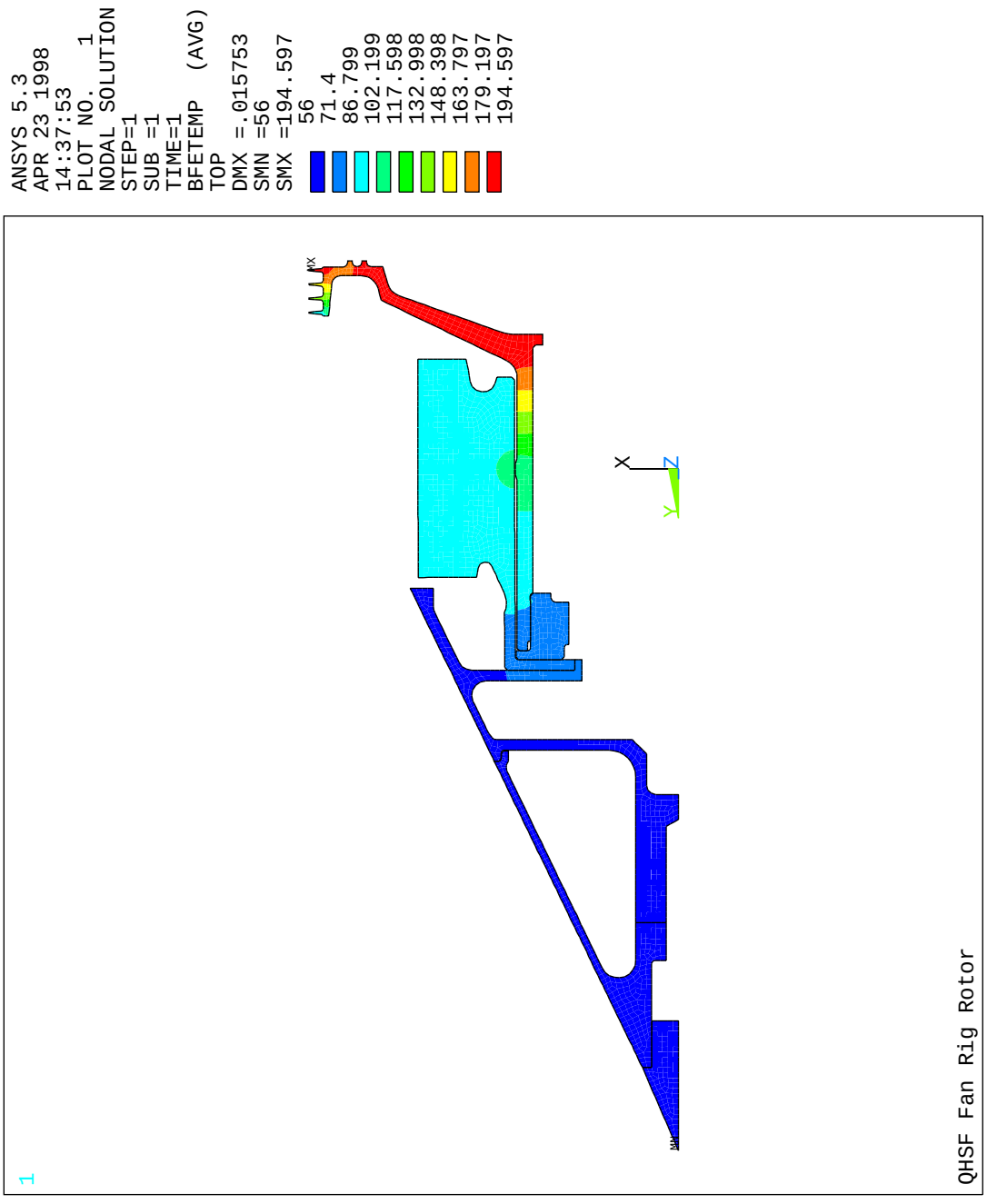

Figure 8-17. Temperature Profile.

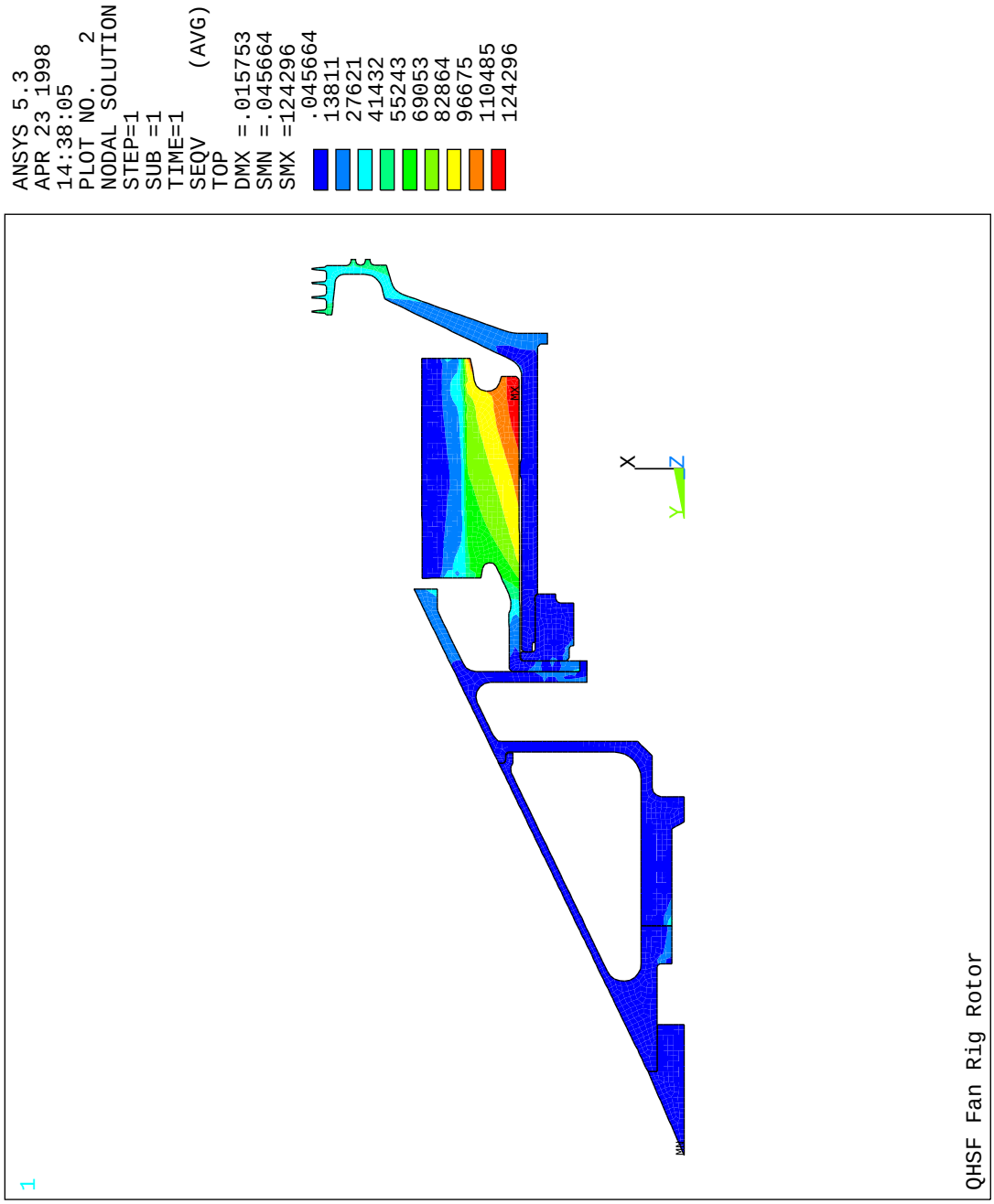

Figure 8-18. Rotor Equivalent Stresses.

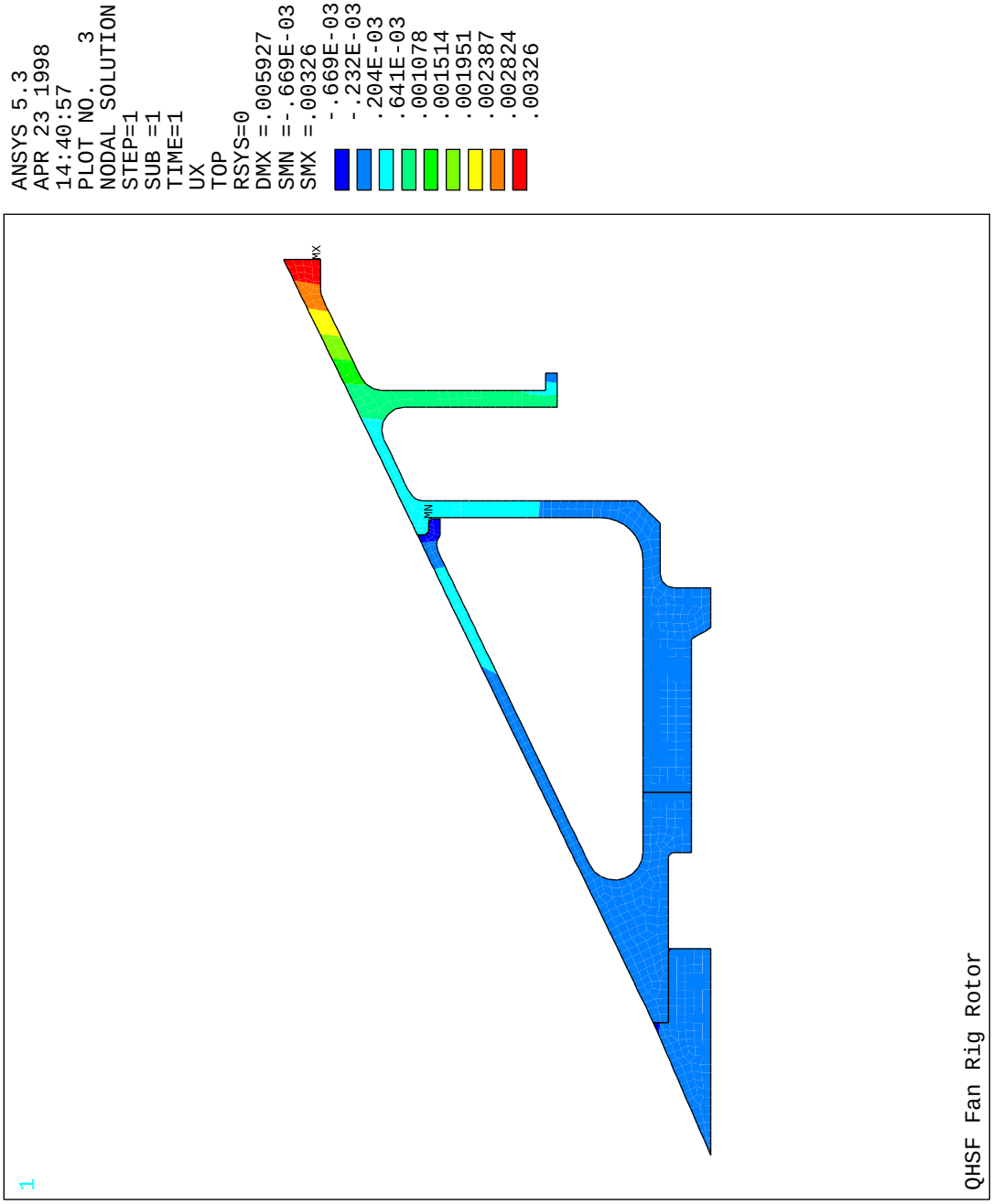

Figure 8-19. Spinner Radial Deflection.

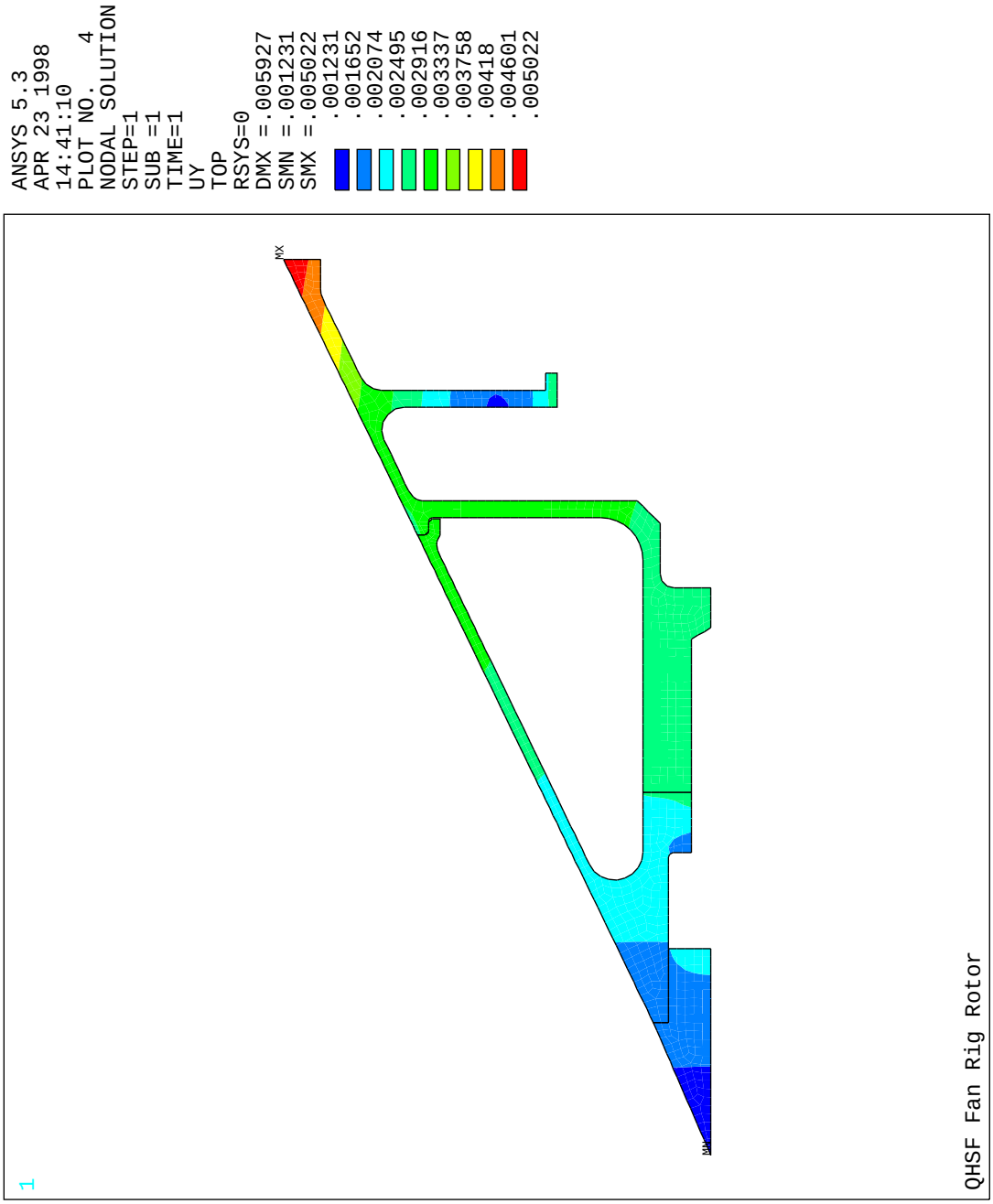

Figure 8-20. Spinner Axial Deflection.

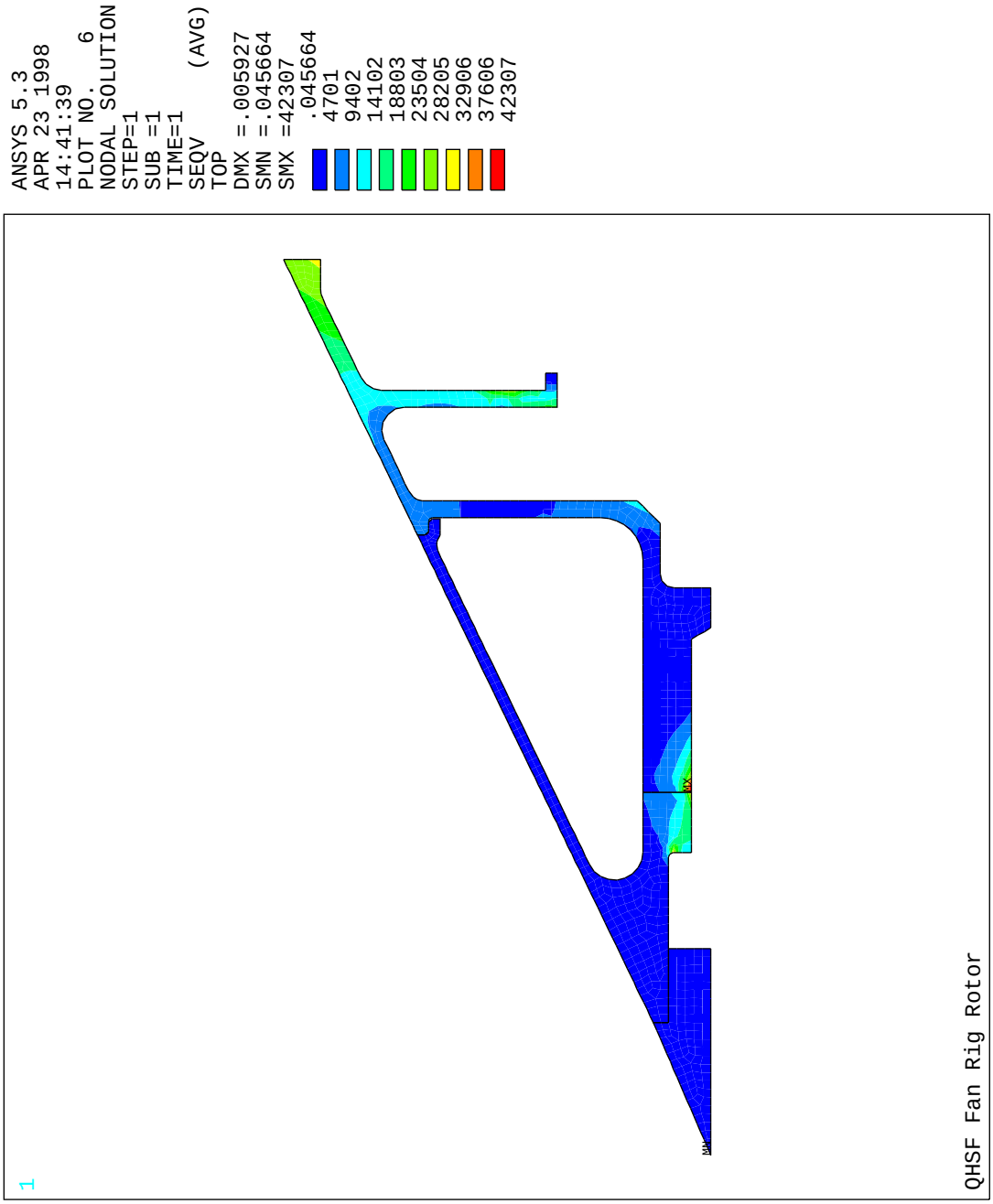

Figure 8-21. Spinner Equivalent Stress.

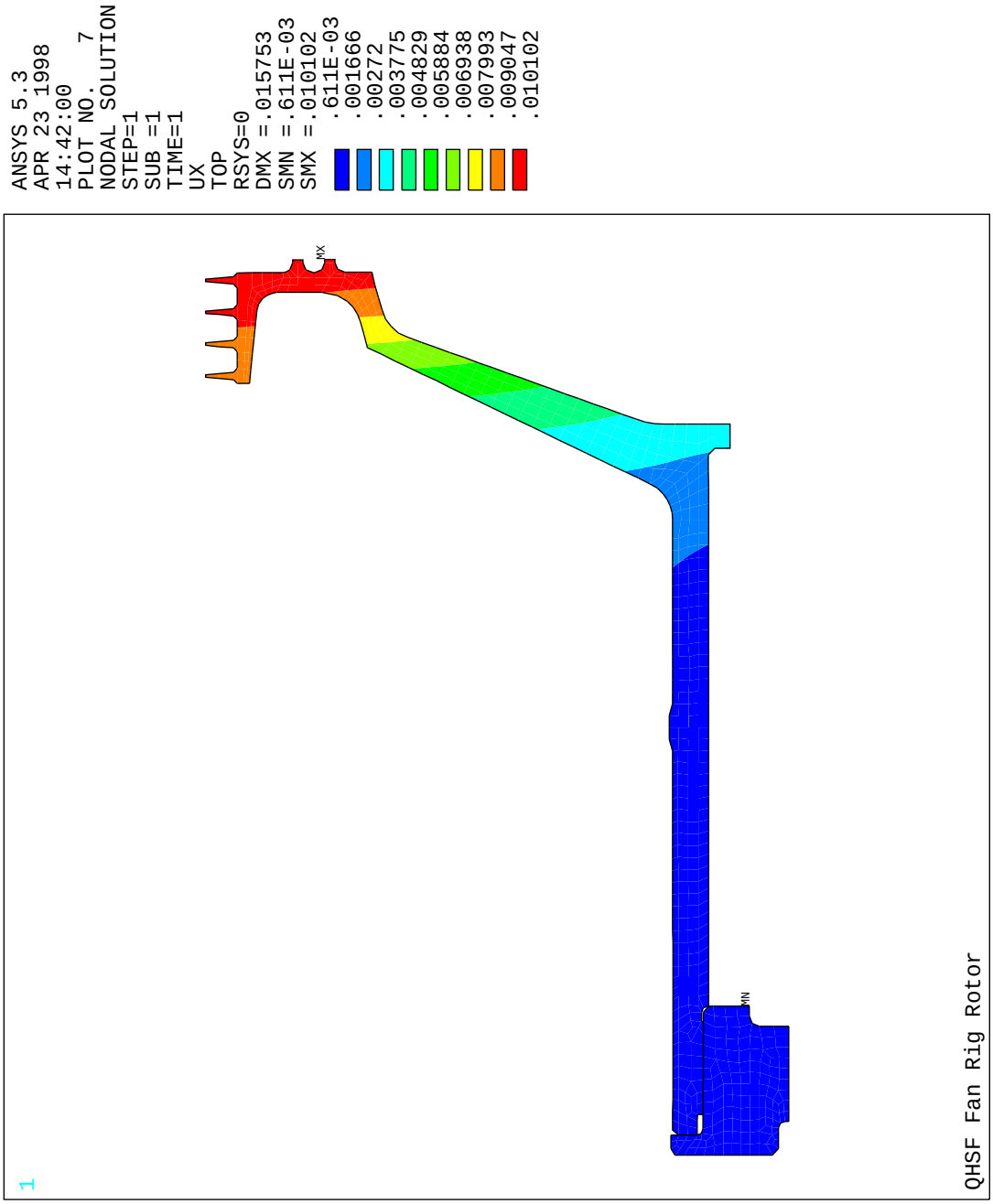

Figure 8-22. Torque Sleeve and Retainer Nut Radial Deflection.

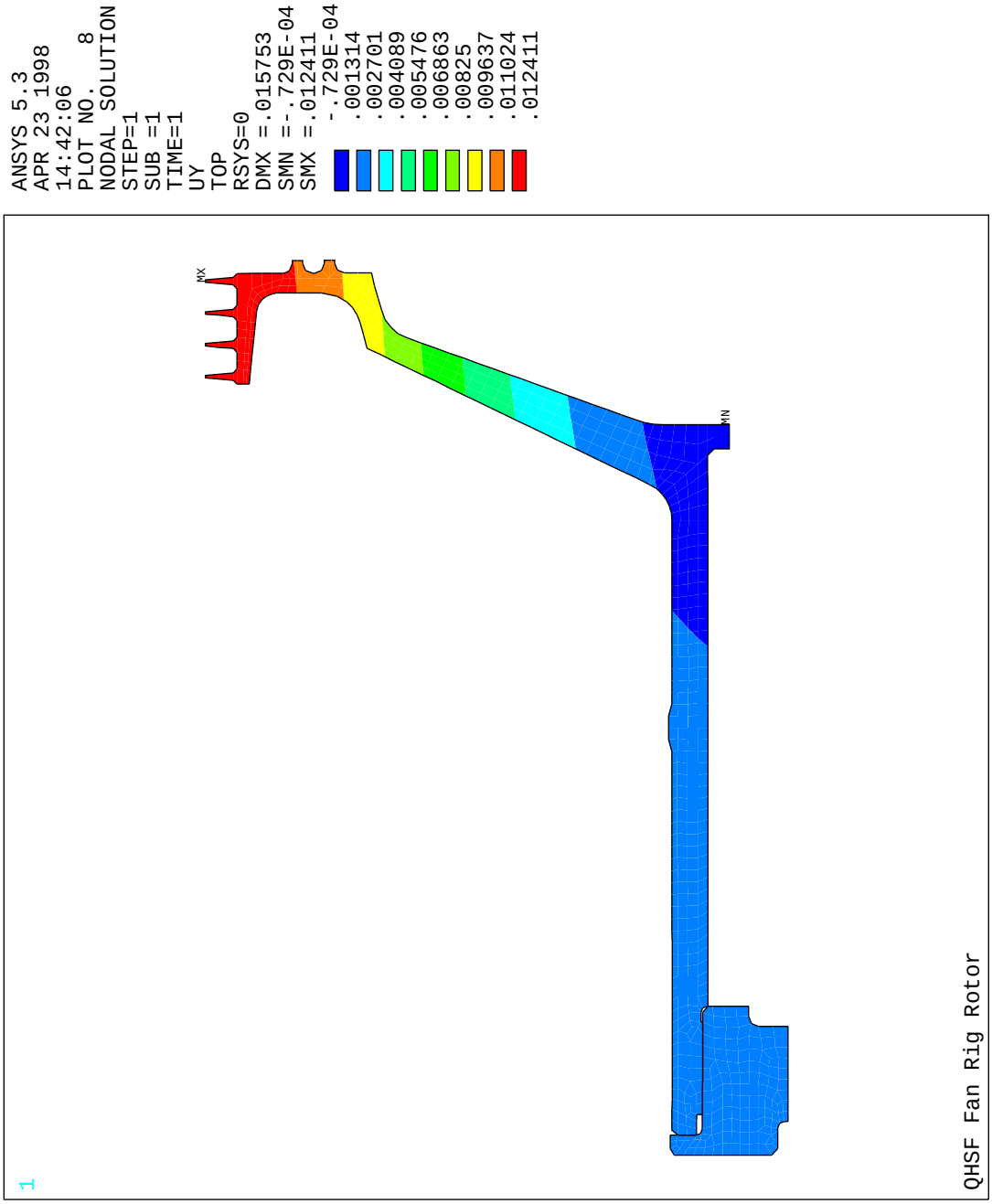

Figure 8-23. Torque Sleeve and Retainer Nut Axial Deflection.

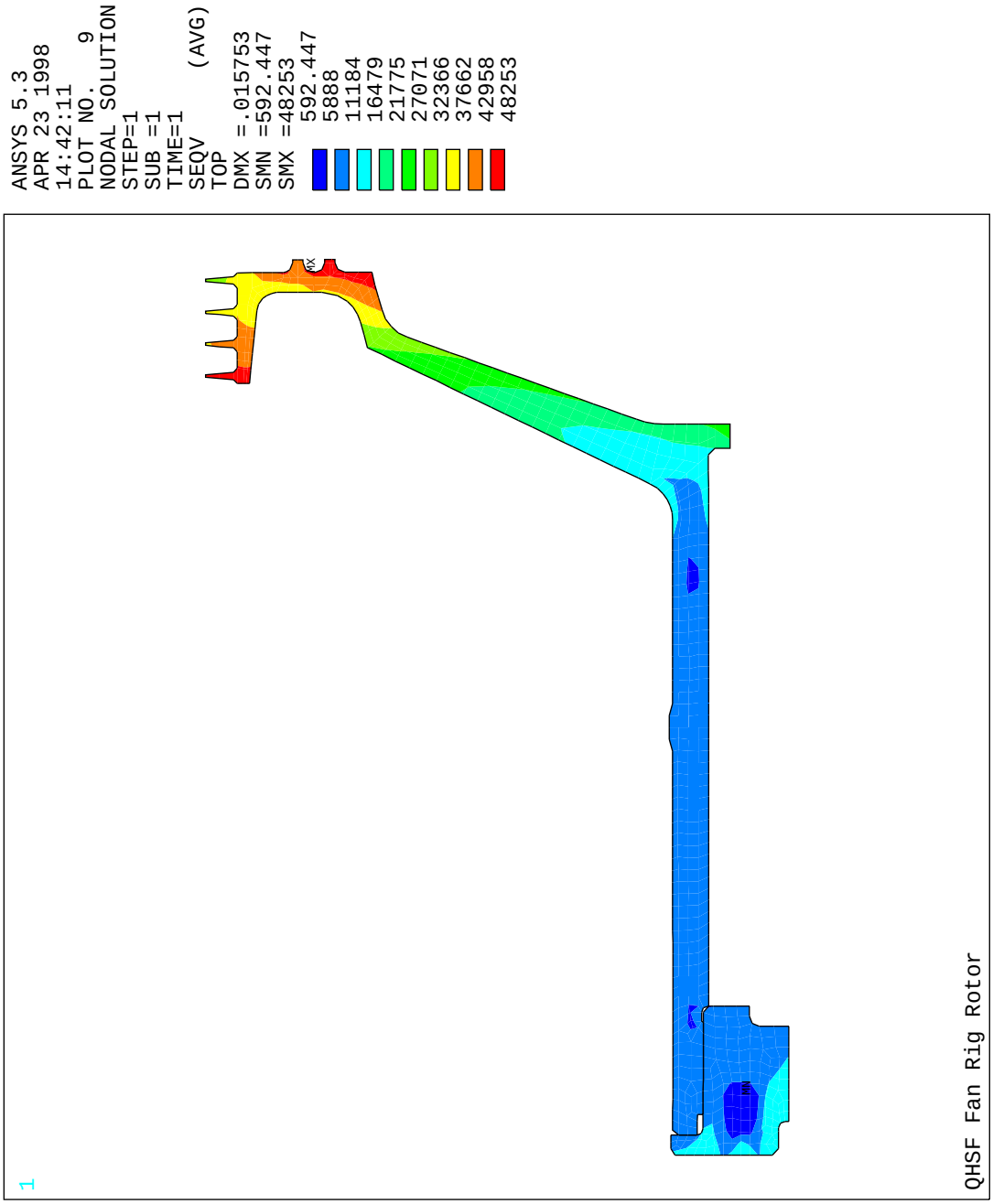

Figure 8-24. Torque Sleeve and Retainer Nut Equivalent Stress.

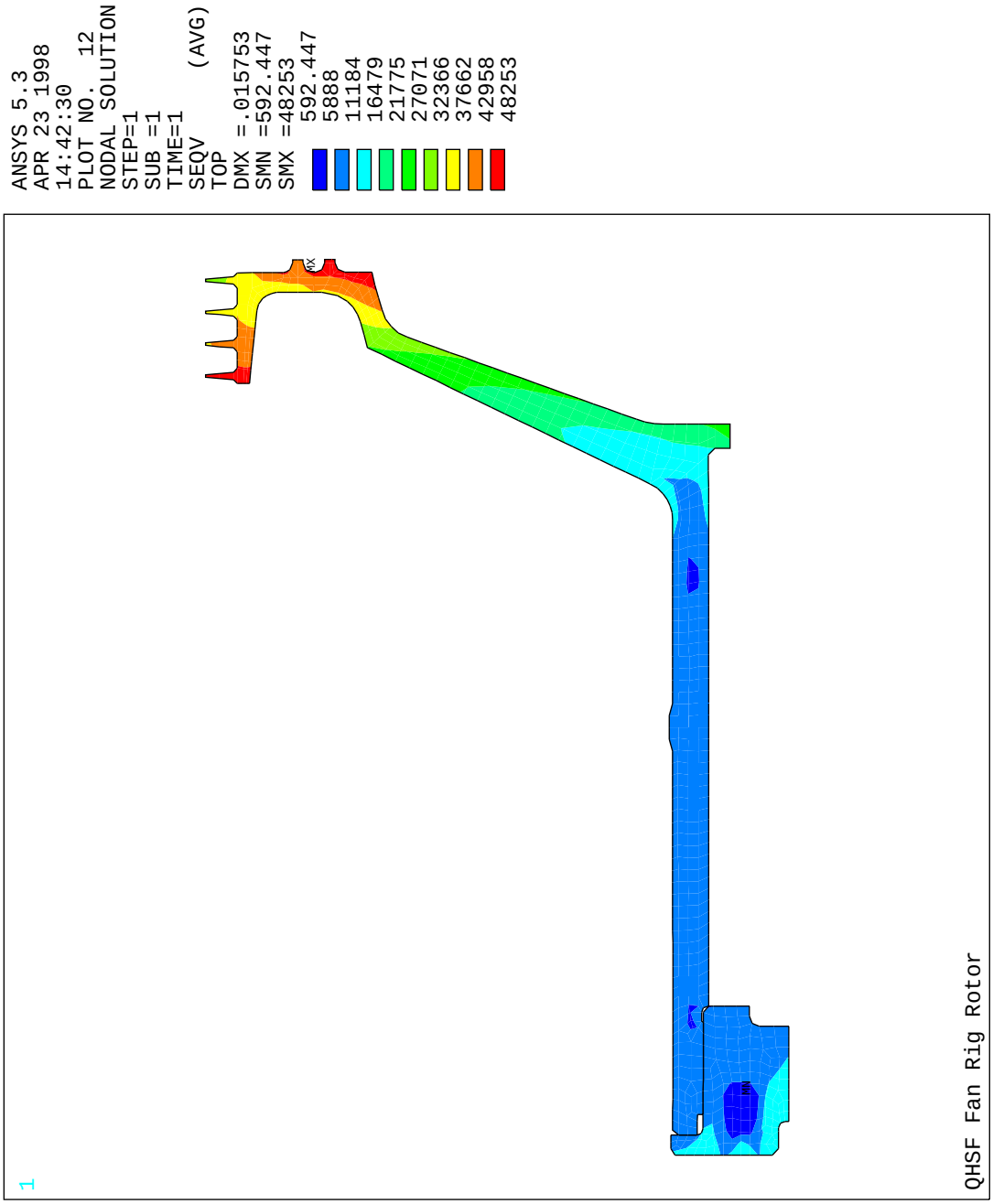

Figure 8-25. Torque Sleeve and Retainer Nut Hoop Stress.

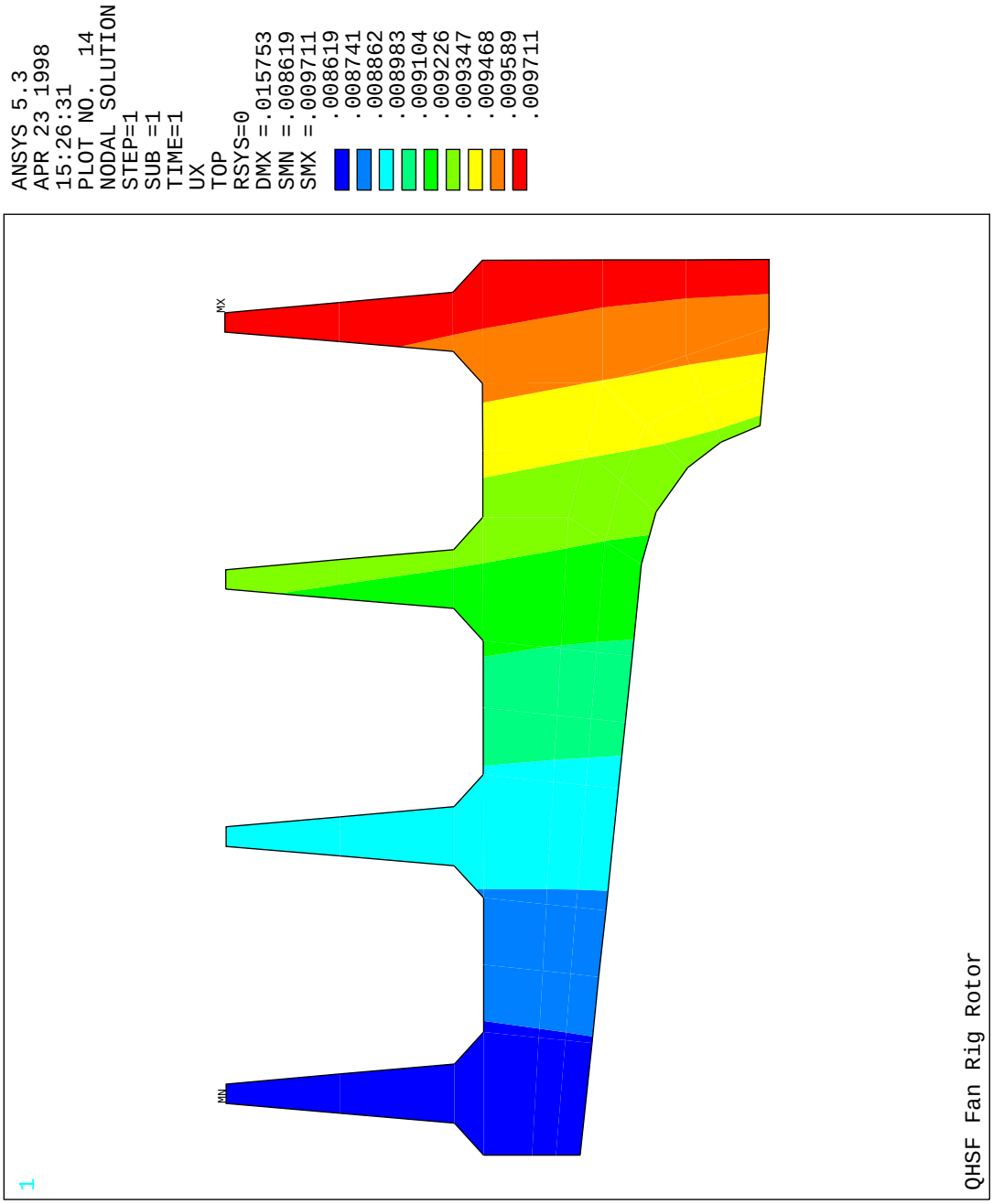

Figure 8-26. Rotating Seal Radial Deflection.

8.4 Instrumentation

The instrumentation list for the QHSF 22-inch wind-tunnel rig is presented in Table 8-13. A general description of each item follows the table. The Instrumentation Master Number List is provided in Appendix I.

Table 8-13. Instrumentation List for the 22-inch, Quiet High-Speed Fan Wind-Tunnel Rig.

Number	Measurement	Instrumentation	Description	Responsibility
1	Inlet Pressure	Wall Static Pressures	10 locations	AE
2		Inlet Boundary Layer Rakes	5 rakes/ 10 immersions	AE
3		Wind Tunnel	Total Pressure	NASA
4	Inlet Temperature	Wind Tunnel	Total Temperature	NASA
5	Vane exit pressure	Strut leading edge probes	10 immersions/ 5 struts	AE
6		Wall static pressure	Pressure taps on inner and outer wall	AE
7	Vane exit temperature	Strut leading edge probes	10 immersions/ 5 struts	AE
8	Rotor Exit Velocities	Rotor Exit Survey - LDV	1 Window	NASA/AE
9	Total Mass Flow	Bellmouth in place	Throat static pressures	NASA
10		Flight inlet in place	Static pressure taps downstream of inlet	AE
11	Core Mass Flow	Strut leading edge probes & wall statics		AE
12		Wall static pressure	Pressure taps on inner and outer wall	AE
13	Rotor Shock Positions	Outer casing static pressure	10-15 surface Kulites	AE
14		Interblade shock position - LDV	1 Window	NASA/AE
15		Pressure Sensitive Paint	blade surface shock position	NASA
16	RPM	Speed sensor	monopole / counter	NASA
17	Noise	Far field microphones	Traversing / fixed microphones	NASA
18		Mode measurement system	Rotating microphone rig	NASA
19	Vibration	Accelerometers	Fan Frame TDC, axial & 90 degrees	AE
20	Fan Tip Clearance	Capacitance probe	CAP PROBES	NASA
21	FAN Tip Displacement	Optical Probe - Light Probe	NASA system	NASA
22	Rotor blade strain	Strain gauges	Critical modes/ 15 gages	AE
23	Static Pressures in core	Wall static taps	10 locations on shroud	AE
24	Pressure/ Area Measurements	Wall static taps	20 locations on shroud	AE

1. Static pressure measurements for boundary layer probes. Ten wall static-pressure taps shall be installed equally spaced ½ way between each boundary layer rake at station 155.090 in part number MCP-0004003. These pressures will be used with the boundary layer rakes to measure inlet velocity profiles and mass flow. Figure 8-27 shows the locations and master numbers of the static-pressure ports.

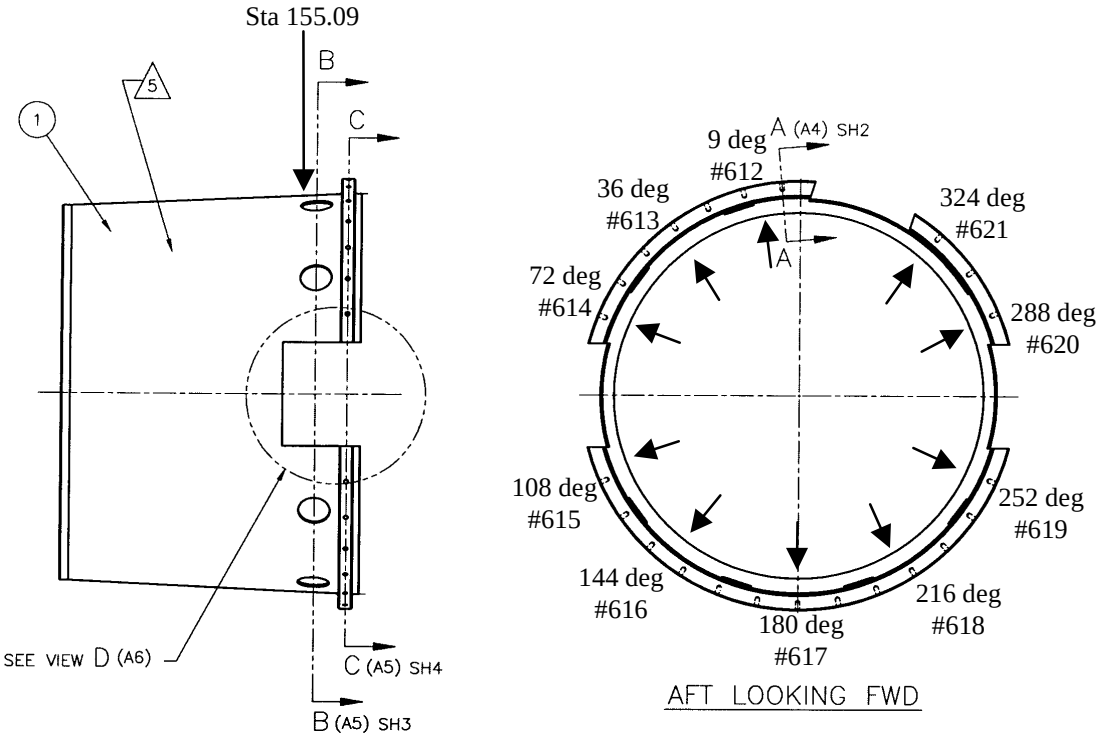

Figure 8-27. Ten Static Pressure Ports Will Be Used to Determine the Average Static Pressure for the Boundary Layer Rakes.

2. Inlet Boundary Layer Rakes. The immersions for the boundary-layer rakes were directly scaled from the baseline-engine-flight-test nacelle. Five rakes with ten total pressure probes on each rake shall be equally spaced in the circumferential direction and installed with the probe tip at station 155.090 as shown in Figure 8-28. The ten probes on each rake shall be positioned at radial immersions of 0.482, 0.517, 0.571, 0.679, 0.822, 0.965, 1.109, 1.252, 1.395, and 1.539 inches from the wall. Figure 8-28 shows a diagram of the boundary layer rake configurations.

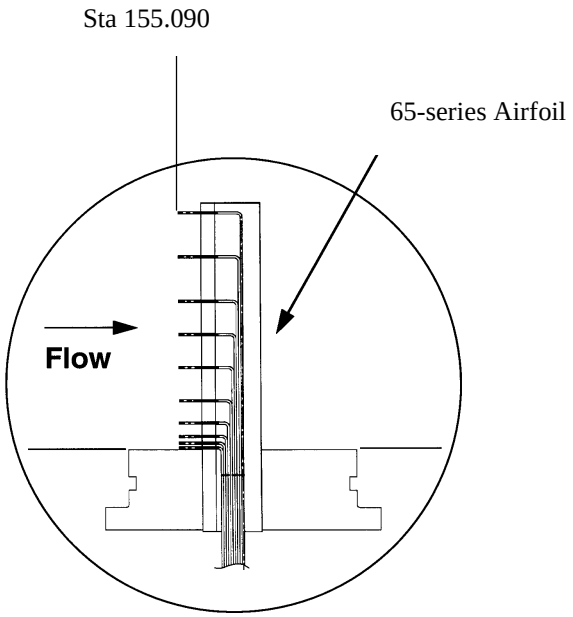

Figure 8-28. Boundary Layer Rakes for the 22-inch QHSF Rig.

3. Wind Tunnel Total Pressure. The standard tunnel interface will be used to obtain the total pressure at the wind tunnel test section inlet (STA 2.2 at the ceiling).

4. Wind Tunnel Total Temperature. The standard tunnel interface will be used to obtain the total temperature at the wind tunnel test section inlet (STA 2.2 at the ceiling).

5. Vane exit pressure - strut leading edge probes. Fifty Kiel combo (pressure and temperature) probes will be mounted 10 each on five front frame struts. Six probes will be spaced at 8.3, 25, 41.7, 58.3, 75 and 91.7 percent of the bypass radial dimension, and 4 probes will be spaced at 12.5, 37.5, 62.5, and 87.5 percent of the core radial dimension as shown in Figure 8-29.

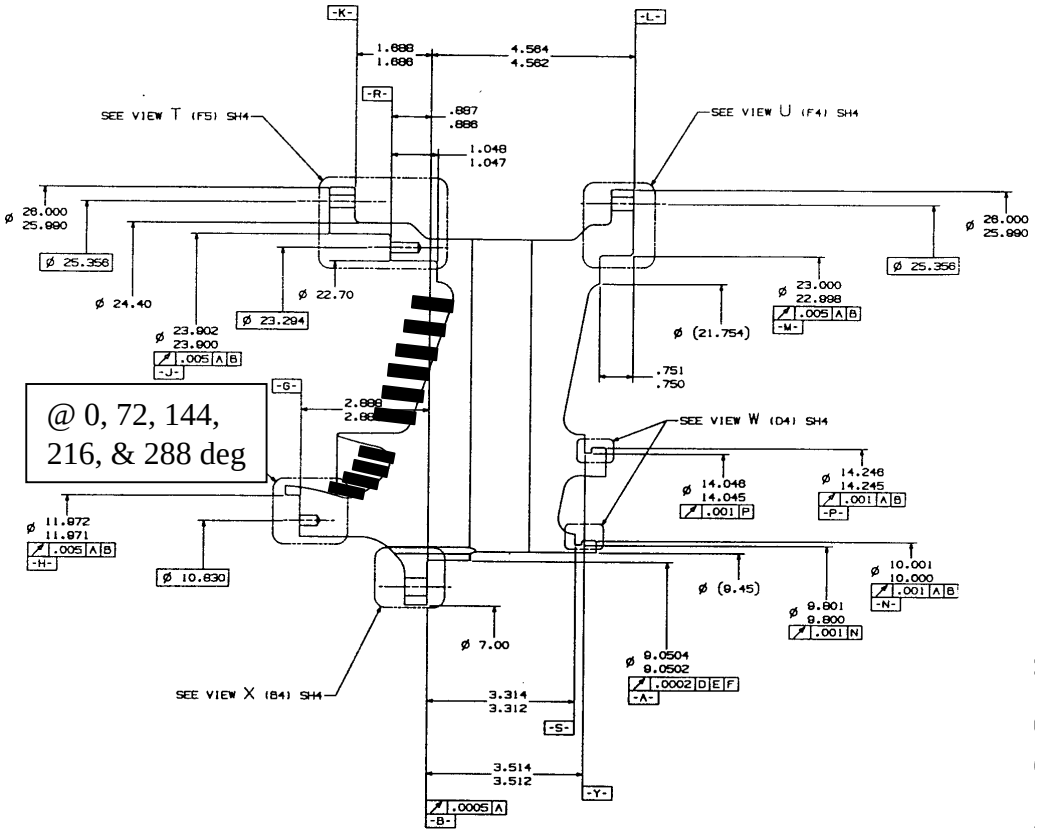

Figure 8-29. Description of Strut Leading Edge Probes on QHSF 22-inch Fan Rig.

6. Vane exit-pressure – wall static pressure. Twenty static-pressure taps are installed in the most forward portion of the front frame to measure the inner and outer wall static pressure for both the core and bypass. Each tap will be midway between two struts. Therefore, there will be 5 taps equally distributed circumferentially on each of the 4 walls. The axial and radial coordinates for the taps (referenced from datum G on Part MCP-0004042) are (axial, radial): (3.542, 10.877), (1.932, 7.533), (1.771, 7.125), and (0.805, 5.985). The wall static-pressure holes are described in Figure 8-30.

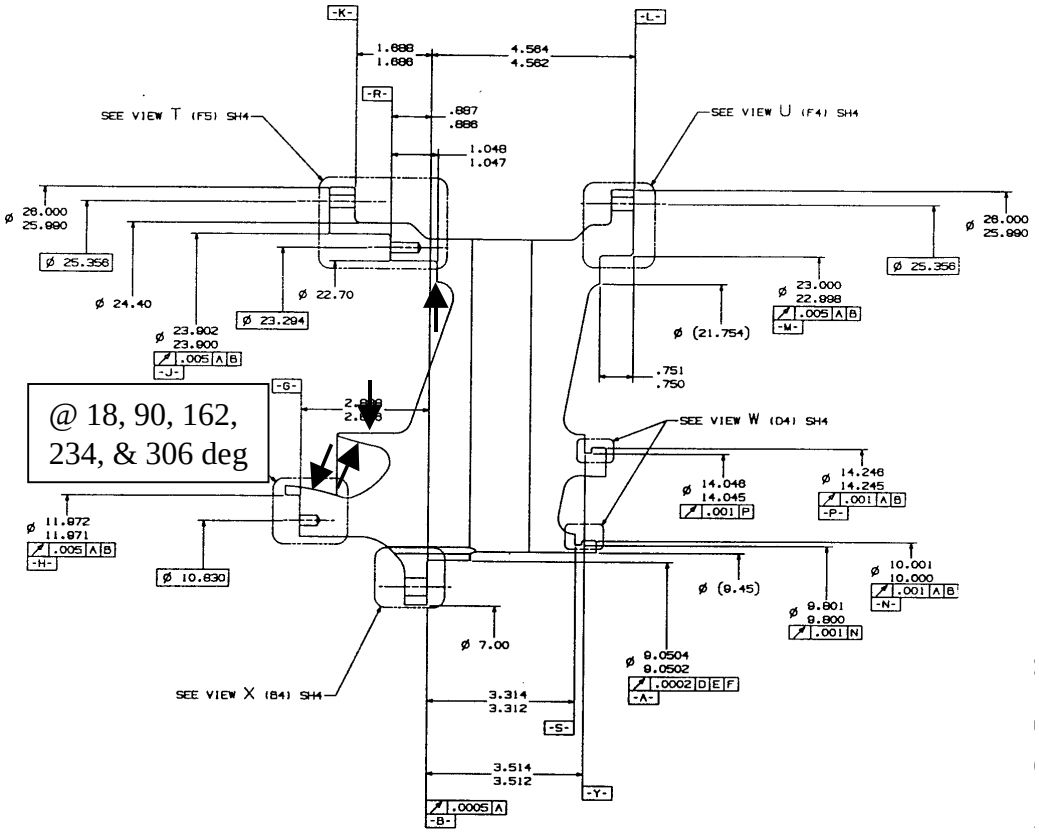

Figure 8-30. Description of Wall Static Pressure Holes on QHSF 22-inch Fan Rig Frame.

7. Vane exit temperature - strut leading edge probes. Fixed Kiel combo probes (see Number 5) will be used for temperature measurement.

8. Rotor exit velocity survey - Laser Doppler Velocimetry (LDV). NASA will add an LDV window to the rig, shown schematically in Figure 8-31. It is desirable to measure both the flow-field in the inter-blade passages and downstream of the rotor. NASA will fabricate the windows and perform all LDV data gathering and analysis.

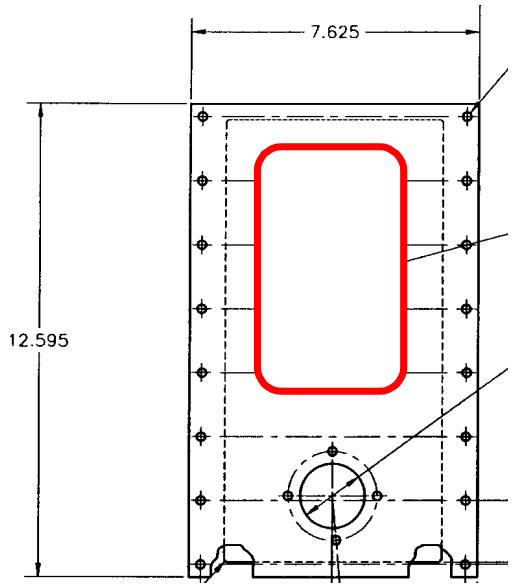

Figure 8-31. QHSF 22-inch Rig Instrumentation Plug (MCP-0004007) Showing Conceptual Location of LDV Window.

9. Total mass flow – bellmouth. Existing static-pressure taps in the bellmouth will be connected to the NASA instrumentation to measure mass flow.

10. Total mass flow - flight inlet. The inlet static-pressure taps (see Number 1) will be used to estimate total mass flow with the flight inlet in place. Bellmouth mass-flow calculations (see Number 9) will be correlated with the inlet static-pressure readings.

11 and 12. Core mass flow. The Kiel combo probes from the vane exit pressure (see Number 5) and the wall static pressures in the front frame (see Number 6) will be used to calculate core mass flow.

13. Rotor-shock-position dynamic pressures. Dynamic-pressure sensors will be mounted flush on the fan-rotor outer flow in an instrumentation plug (MCP-0004007) as shown in Figure 8-32. Fifteen absolute sensors will be mounted flush on the fan-rotor outer-flow path at the following coordinates (referenced from datum A circumferentially and datum B axially):

QHSF Fan Case Plug		Baseline Fan Case Plug	
Axial	**Circumf.**	**Axial**	**Circumf.**
0.306	7.245	2.236	7.245
0.690	6.770	2.620	6.770
1.073	6.295	3.003	6.295
1.456	5.820	3.386	5.820
1.839	5.345	3.769	5.345
2.222	4.870	4.152	4.870
2.605	4.395	4.535	4.395
2.988	3.920	4.918	3.920
3.371	3.445	5.301	3.445
3.754	2.970	5.684	2.970
4.137	2.495	6.067	2.495
4.520	2.020	6.450	2.020
4.903	1.545	6.833	1.545
5.286	1.070	7.216	1.070
5.669	0.595	7.599	0.595

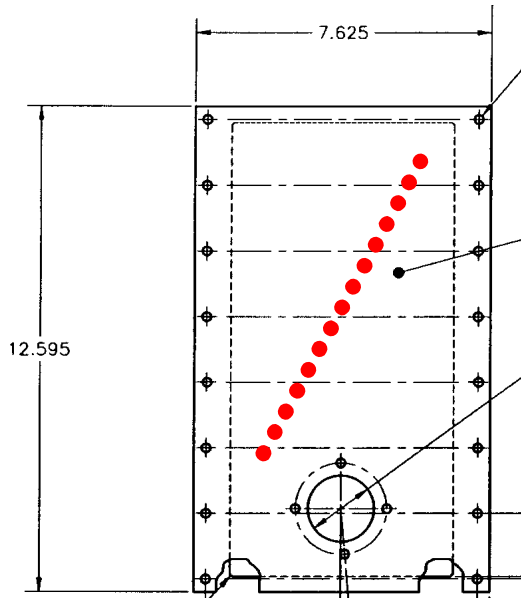

Figure 8-32. QHSF 22-inch Rig Instrumentation Plug (MCP-0004007) Showing Approximate Locations of Dynamic-Pressure Transducers.

14. Rotor-shock position – LDV. The LDV window from Number 8 will extend forward or a second window will be fabricated to allow measurements in front of the rotor to evaluate shocks radiating toward the inlet.

15. Pressure-sensitive paint. Pressure-sensitive paint will be applied to the fan-rotor blades to show the shock position in the blade passage as a function of radius and verify the tip shock location.

16. RPM. The standard-drive rig-speed sensor will be used. In addition, a tooth has been added to the torque sleeve to determine actual disk rpm as shown in Figure 8-33.

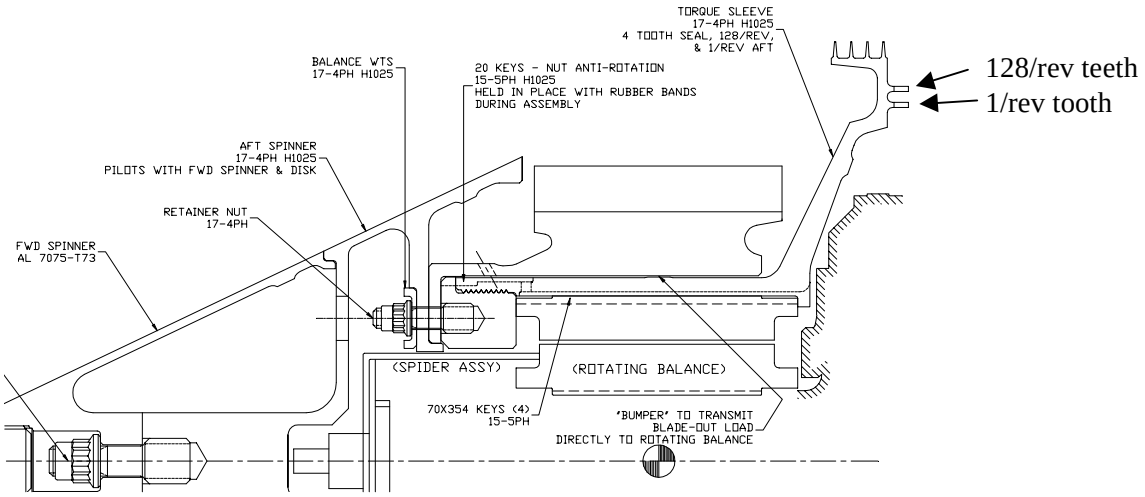

Figure 8-33. The Torque Sleeve in the Rotating Assembly Has a 1/rev Tooth for rpm Measurement and 128/rev Teeth for Synchronizing the Rotating Rake (See Number 18).

17. Noise - far field. The standard traversing and fixed microphones will be used for far-field noise.

18. Noise - mode measurements. The outer nacelle is removable to accommodate the NASA Glenn rotating-microphone rig.

19. Vibration. In addition to the standard rig-health monitoring, three accelerometers will be added to the fan front frame to measure horizontal, vertical, and axial vibrations as shown in Figure 8-34.

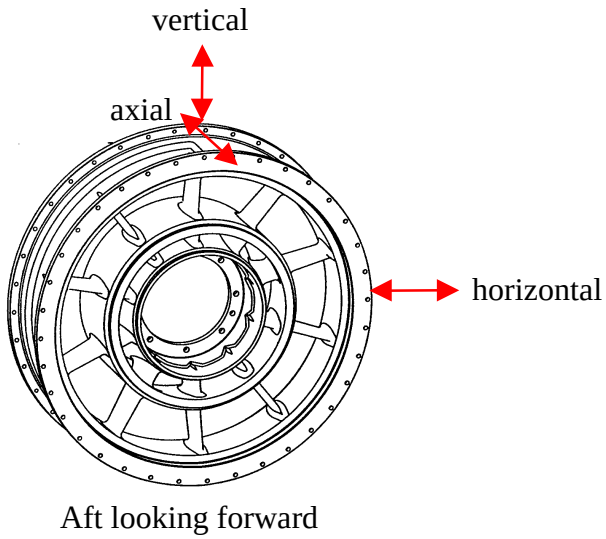

Figure 8-34. Accelerometer Locations on the QHSF 22-inch Rig Front Frame.

20. Fan-tip clearance. NASA will install tip-clearance instrumentation in an instrumentation plug (MCP-0004007).

21. Fan tip displacement. NASA will install tip displacement instrumentation in an instrumentation plug (MCP-0004007).

22. Rotor blade strain. Five rotor blades will be instrumented with three strain gauges each. There will be five different positions with a double redundancy as shown in Figure 8-35.

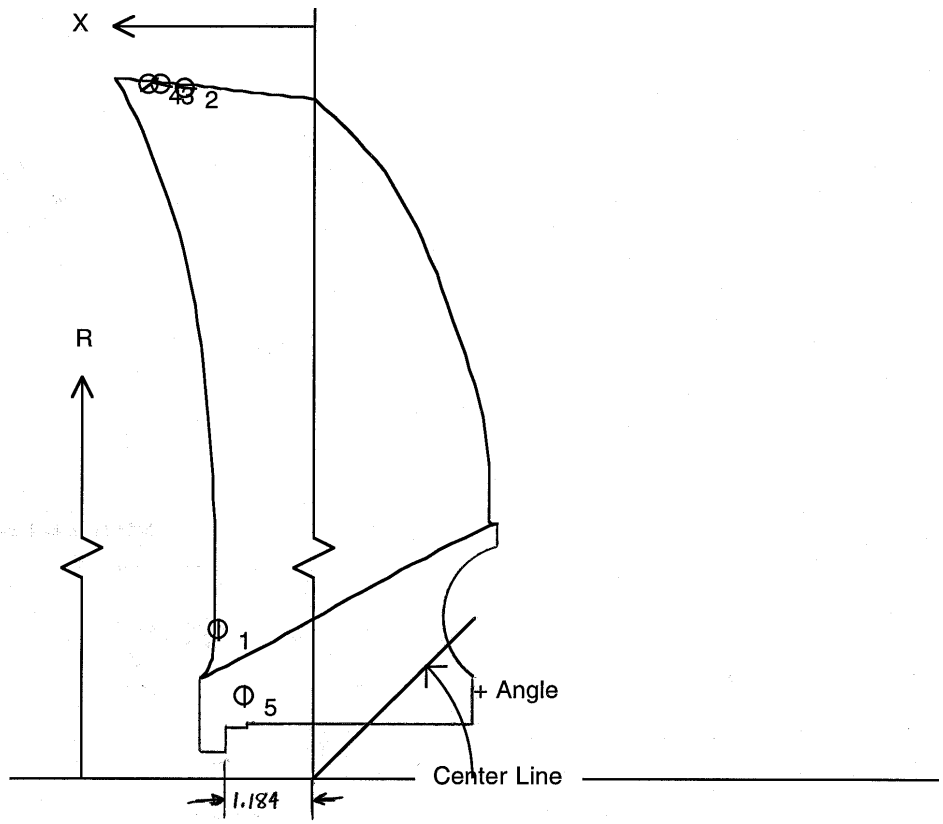

Loc #	Blade Side	Gauge Center (in) X	Gauge Center (in) R	Angle (deg) *	Direction Points (in) X	Direction Points (in) R	Actual Location (in) X	Actual Location (in) R
1	Pressure	1.112	4.362	90.0	1.112	4.462	1.112	4.262
2	Suction	1.523	10.829	-7.0	1.424	10.817	1.623	10.842
3	Suction	1.805	10.870	-11.0	1.706	10.851	1.903	10.889
4	Suction	1.955	10.870	34.0	1.872	10.926	2.038	10.814
5	Pressure	0.810	3.549	90.0	0.810	3.649	0.810	3.449

* Angle is provided for reference only. Direction points should be used to locate gauge.

Figure 8-35. Strain Gage Locations on 22-inch QHSF Rotor Blades.

23. Static pressures in core flow. Ten static-pressure taps will be spaced in the outer wall opposite the core plug to determine location and magnitude of peak Mach number on the plug at the axial locations (from datum A of MCP-0004044) of 1.618, 2.758, 3.898, 5.038, 6.178, 7.318, 8.458, 9.598, 10.738 and 11.878 inches, as shown in Figure 8-36.

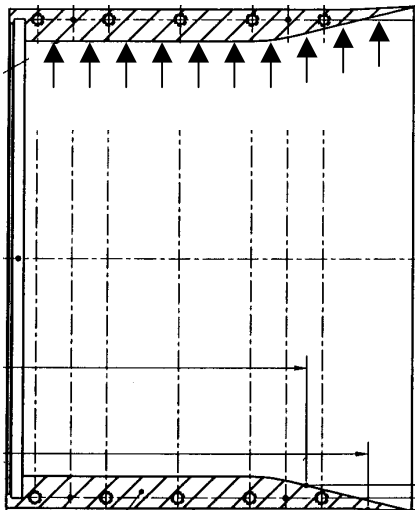

Figure 8-36. Static-Pressure-Measurement Locations in the Core Flow Nozzle.

24. Balance-pressure-area measurements. Static-pressure measurements will be taken in four locations to determine thrust correction in part MCP-0004034 as shown in Figure 8-37.

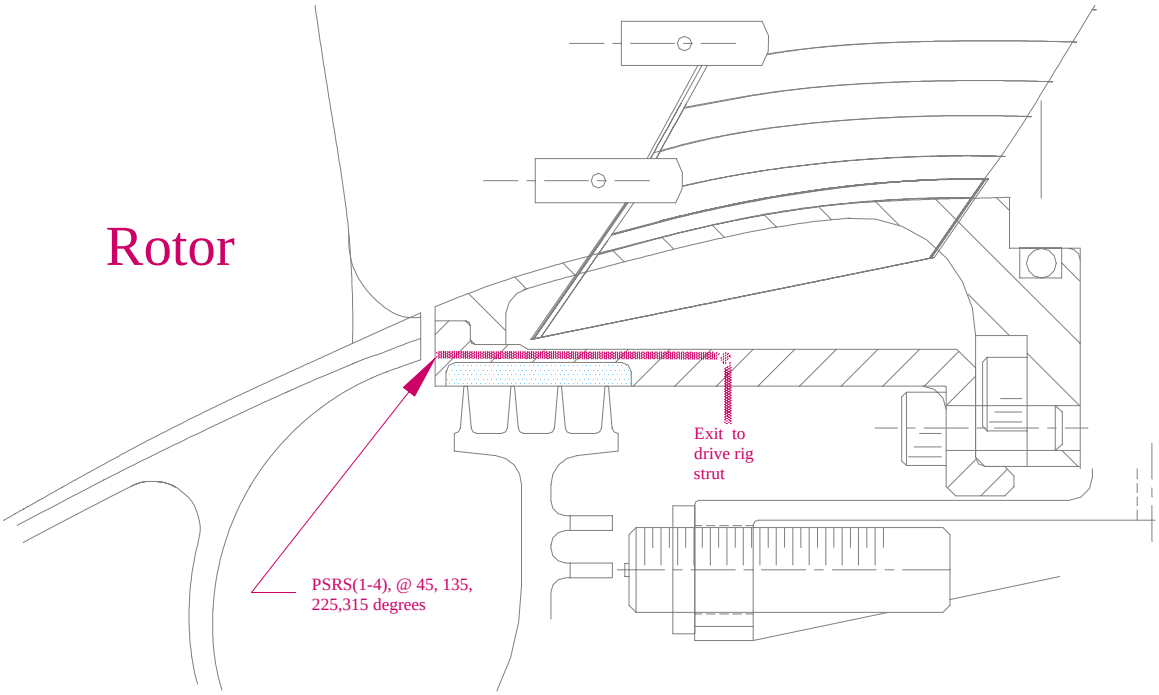

Figure 8-37. Balance-Pressure-Area Measurements for the Thrust-Correction Calculation.

8.5 Assembly Procedure for Quiet High-Speed Fan (QHSF) Rig

8.5.1 Notes for Assembly

1. The nozzle, skin panels, and selected flow-path pieces are made from fiberglass reinforced plastic. These parts should be treated as fragile objects and should not be dropped or over-torqued.

2. All part numbers and drawing numbers mentioned are abbreviated. For example, part "MCP-0004052" will appear as "4052" in the text.

8.5.2 Overall Procedure

1. Aft-seal assembly and the aft half of the inner core (4048) is mounted on the drive rig semi-permanently. The sliding-plug guides will also be pre-assembled on the aft half of the inner core (Figure 8-38).

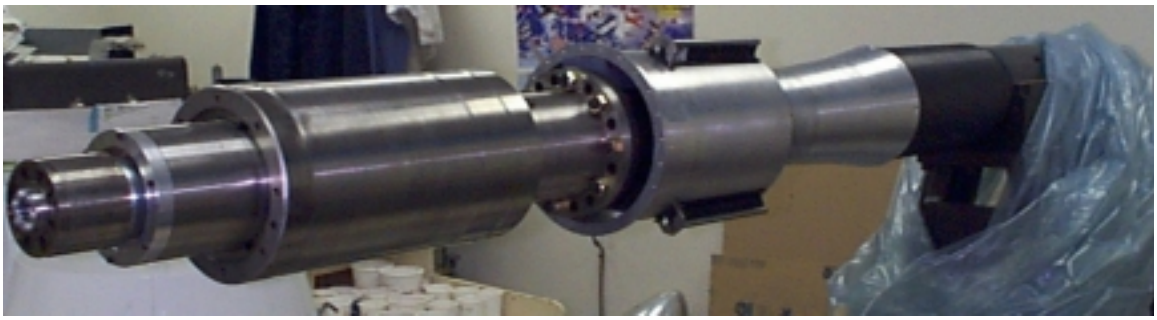

Figure 8-38. Fan-drive Rig Before Assembly.

2. Fan nozzle and fan-nozzle liner (4018 & 4019) will be pre-assembled before installation. Place nozzle assembly temporarily on the drive rig (Figure 8-39). Use padding to protect the flow-path surfaces from being scratched.

3. The aft duct and aft-duct liner (4016 & 4017) will also be pre-assembled before installation. Place aft-duct assembly temporarily on the drive rig (Figure 8-39). Use padding to protect the flow-path surfaces from being scratched.

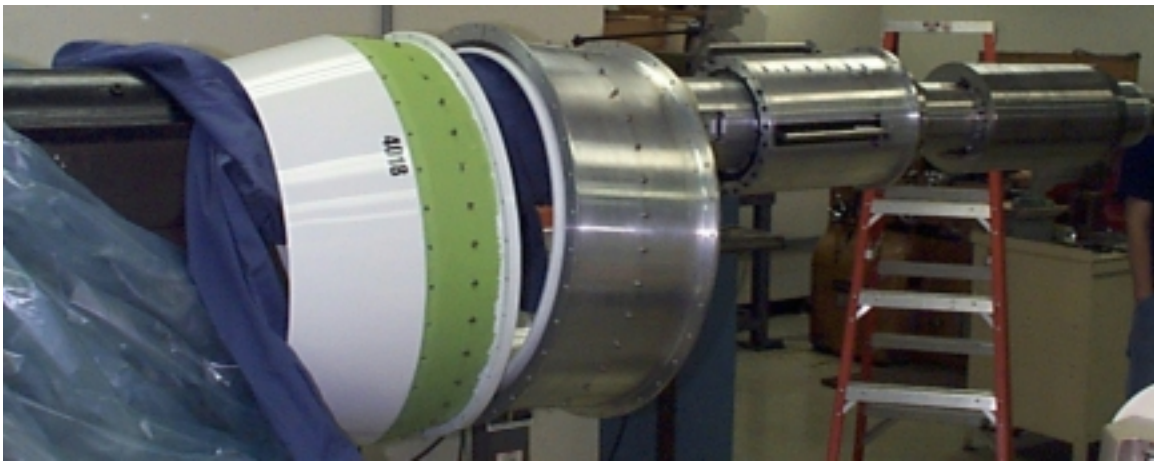

Figure 8-39. Placing Parts on Drive Rig for Later Assembly.

4. Mount fan frame (4042) on drive rig. Torque to 30 ± 5 ft-lbs (Figure 8-40).

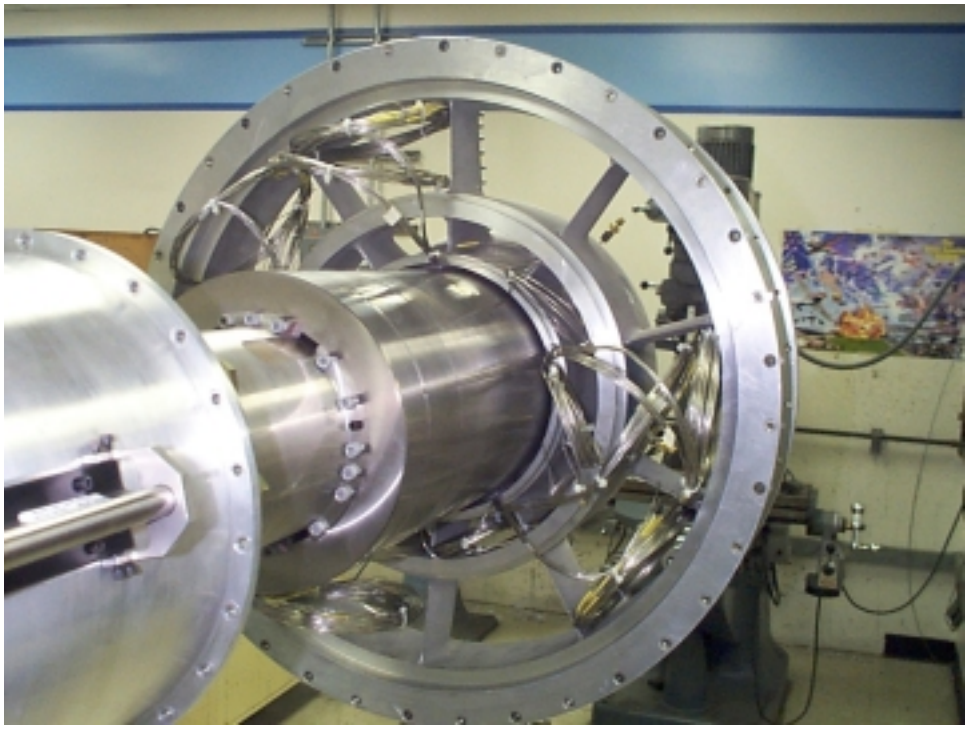

Figure 8-40. Mount Fan Frame.

5. Route fan-frame instrumentation leads through aft half of inner core (4048). Secure leads to drive rig with tape (Figure 8-41).

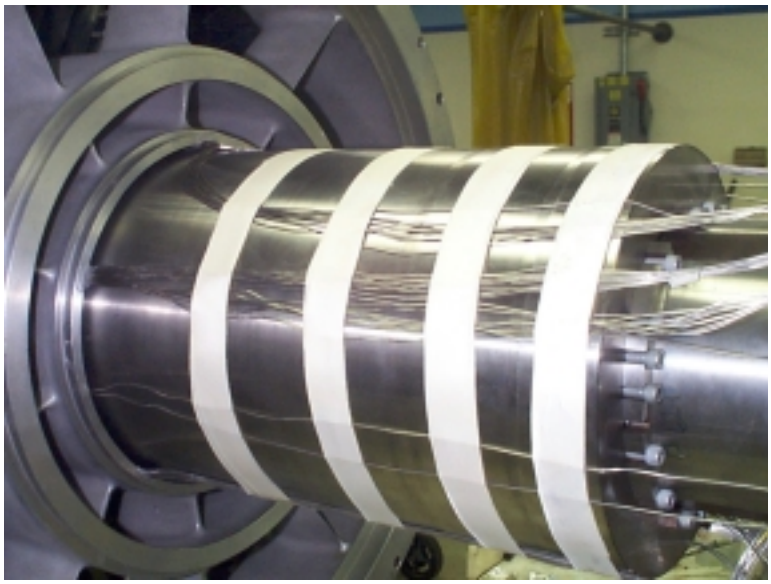

Figure 8-41. Instrumentation Leads Routed and Secured.

6. Install forward part of inner core (4048). Make sure alignment pins match fan-frame holes and attach to the aft section (Figure 8-42). The aft half will slide aft for better clearance.

7. Loosely attach the actuator to the aft of the inner core (4048). Position the actuator at top dead center (Figure 8-42).

Figure 8-42. Install Fan Frame, Inner Core, and Actuator.

8. Install right-forward (aft, looking forward) sliding plug (4055).

9. Install left-forward sliding plug (4056) (Figure 8-43).

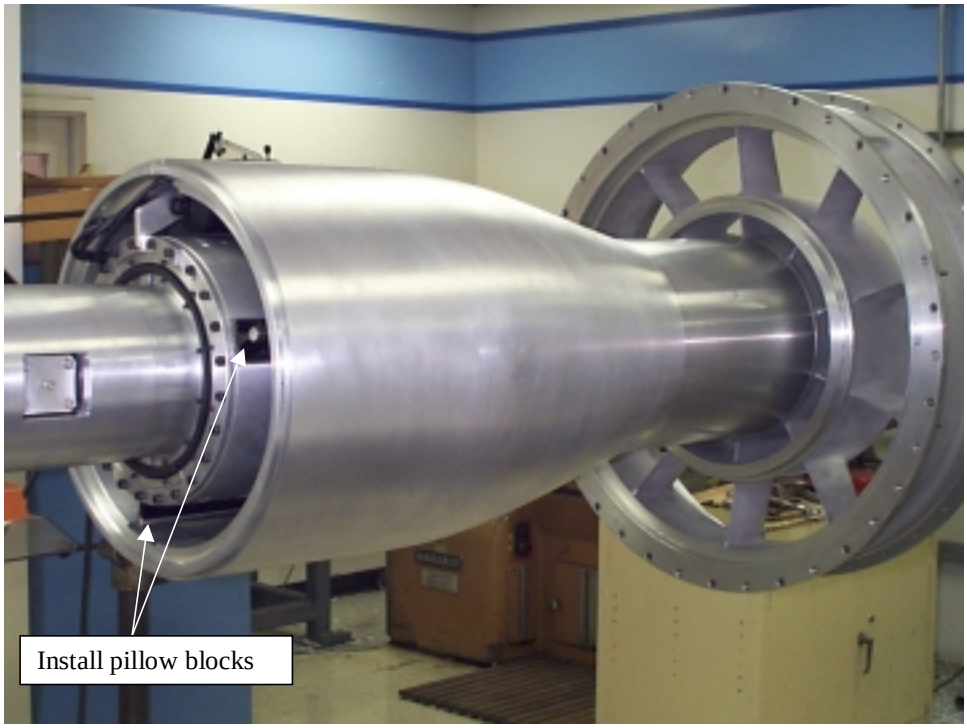

Figure 8-43. Install Halves of Sliding Plug.

10. Install/attach pillow blocks. Carefully slide pillow blocks onto the actuator guides so as not to dislodge the ball bearings (see Figure 8-43).

11. Tighten actuator bolts and route the actuator wire.

12. Install core nozzle (4044) halves attaching to fan frame. Nozzle halves are pinned for alignment. Core-nozzle instrumentation leads must be routed through fan frame and covered with epoxy.

13. Attach aft-duct liner and aft-duct (4016 &4017) assembly to fan frame (4042) along with support rings (4022) (Figure 8-44).

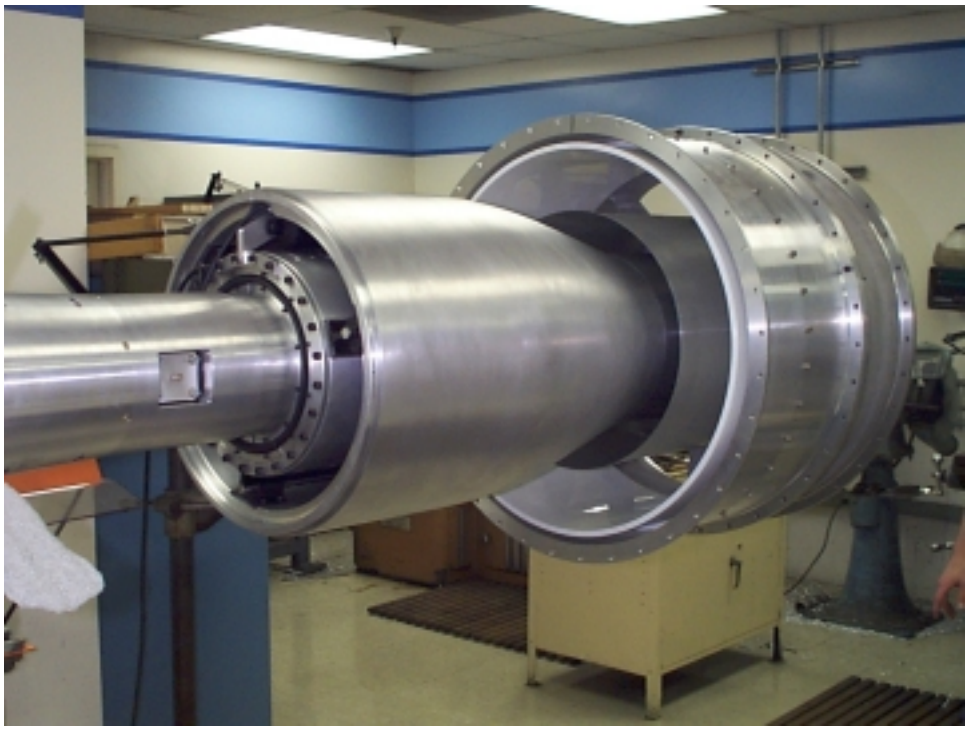

Figure 8-44. Install Core Nozzle and Aft-Duct Assembly.

14. Install halves of aft sliding plug (4057, 4058) (Figure 8-45).

Figure 8-45. Aft Sliding-Plug Halves Installed.

15. Attach fan nozzle and nozzle-liner (4018 & 4019) assembly to aft duct case along with support rings (4021). Make sure nozzle (4018) fits flush to aft duct case (4017) flange. Use ¼-28 1½-inch nuts and bolts. **Do not try to seat the part with bolt tension!** This action may crack the parts.

16. Attach fan-nozzle skin panels (4023) to fan nozzle and support rings (Figure 8-46). Torque to 15 in-lbs. Attach screws in the center of panels and work toward ends.

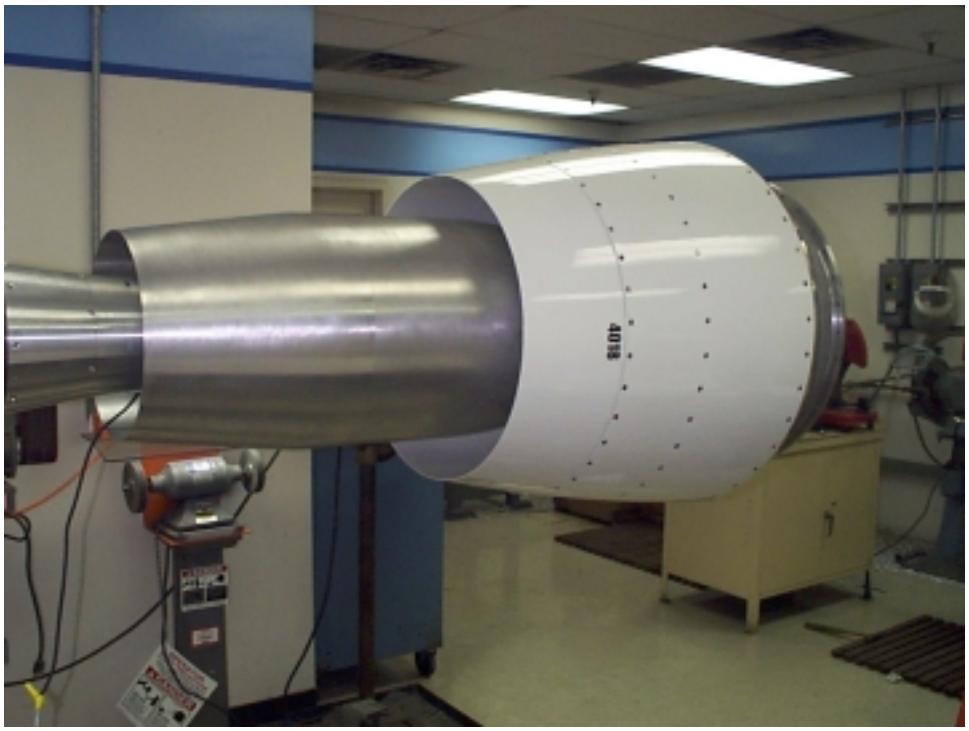

Figure 8-46. Nozzle Assembly and Nozzle Skins Installed.

17. Install selected stator-ring assembly and retention band (4068).

18. Install torque-sleeve stationary seal (4034) and connect instrumentation leads to connectors on the fan frame (Figure 8-47).

19. Install 1/rev bracket (4029).

20. Install 1/rev transducer and route wiring.

21. Attach fan case (4011) to the fan frame with fan-case support rings (4024).

Figure 8-47. Stator Assembly and Stationary Seal Installed.

8.5.3 Acoustic Configuration

22. Slide in selected abradeable ring.

23. Pre-assemble torque-sleeve key (4053), torque sleeve (4031), retaining nut (4032) (ref. Dwg. 4033), fan-rotor, fan blades, and aft spinner (4014). See drawing 4090 for torque values.

24. Install rotor assembly.

25. Attach forward spinner (4012).

26. Install inlet liner (4052).

27. Install cap plugs (4069) and plug-rake caps (4046).

29. Install inlet-duct case (4002) and support rings (4006) (Figure 8-48).

30. Attach mid skins (4015) and fan-case skins (4009).

31. Attach inlet lip (4054) to duct case (4002).

32. Attach inlet skins (4004).

Figure 8-48. Forward Ducting Installed.

8.5.4 Performance Configuration

22. Slide in selected abradeable ring.

23. Install fan case plugs (4007) matching abradeable.

24. Pre-assemble torque-sleeve key (4053), torque sleeve (4031), retaining nut (4032) (ref. Dwg. 4033), fan rotor, fan blades, and aft spinner (4014). See drawing 4090 for torque values.

25. Install rotor assembly.

26. Attach forward spinner (4012).

27. Install fan case liner (4003).

28. Install boundary-layer rakes (4008) or blank plugs (4008).

29. Install inlet-duct case (4002) and support rings (4006) (Figure 8-48).

30. Attach mid skins (4015) and fan case skins (4009).

31. Attach inlet lip (4054) to duct case (4002).

9. ENGINES & SYSTEMS RIG TEST

9.1 18-Inch Rig Hardware

Due to budget and schedule issues, it was decided to perform the performance evaluation of the QHSF in the Engines & Systems 18-inch fan rig in Phoenix, AZ. The fan rig is a 0.578 scale version of the engine and a 0.807 scale of the NASA Glenn UHB rig. A schematic of the rig is shown in Figure 9-1. Airflow enters the rig through a calibrated ASME bellmouth and is dumped into a settling tank. Inside the tank is a series of flow straighteners that remove any tangential component of the flow. Aft of the flow straighteners is inlet pressure and temperature instrumentation. The flow then passes through a second bellmouth and into the fan test section.

The fan test section simulates the fan rotor, fan core and bypass stators, front-frame struts, and transition ducts of the engine. The fan speed and throttle position are controlled by varying power setting of the drive turbine and adjusting the core and by-pass discharge valves. Figure 9-2 shows a cross-section diagram of the rig showing the QHSF configuration.

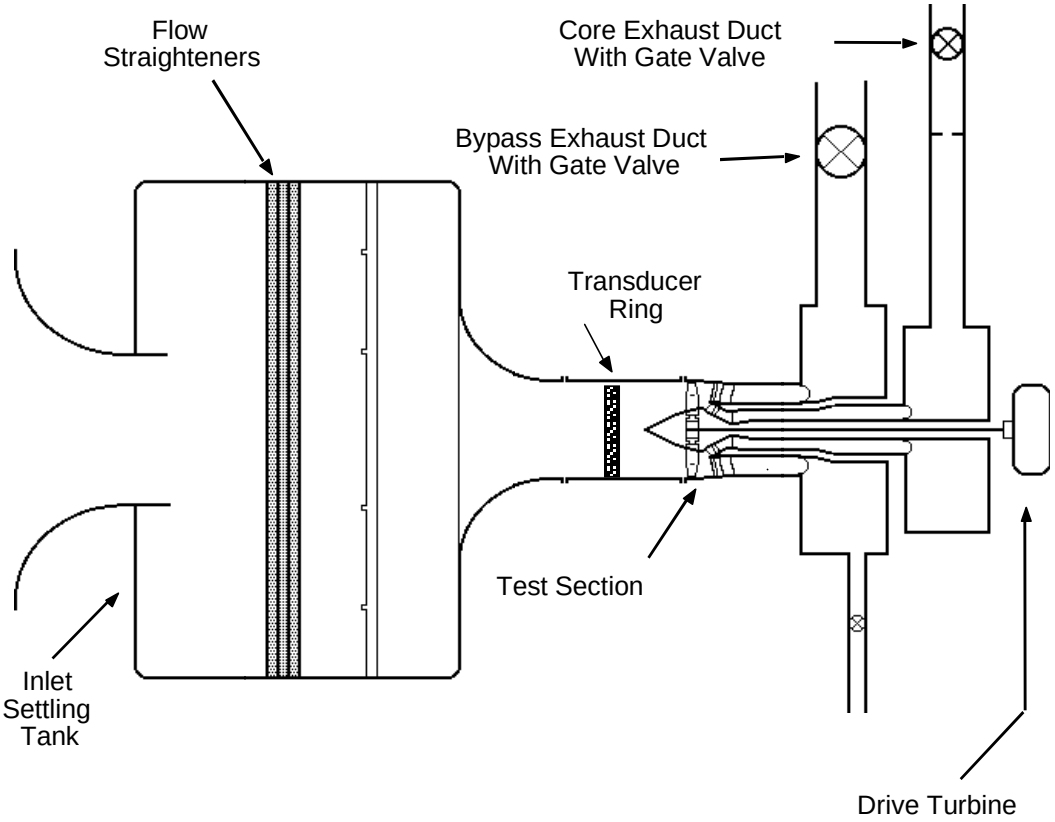

Figure 9-1. Schematic Diagram of the Engines & Systems 18-Inch Fan Rig.

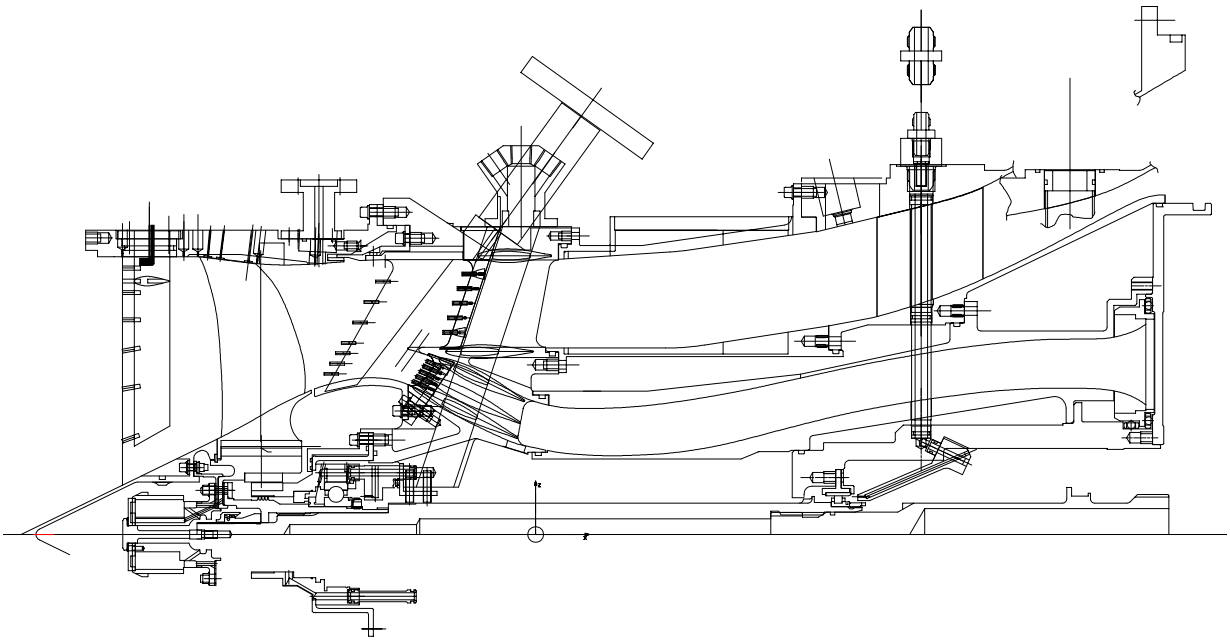

Figure 9-2. Cross-Section Diagram of the QHSF Test Section in the Engines & Systems 18-Inch Fan Rig.

BNB Manufacturing fabricated the 18-inch QHSF rotor blades for the rig. Acoustic ring signature data was taken for all blades to ensure that the actual blade vibration modes were consistent with the results predicted by ANSYS during the design. The results in Table 9-1 show excellent consistency in the blade set and good agreement with prediction of the frequencies of the first five blade vibratory modes.

Acoustic holography data was also taken on one blade to verify the calculated mode shapes. Figure 9-3 shows the measured results and comparison with the predictions. Note that the calculated results are presented in a slightly different aspect angle than the photographed results, creating the appearance of a different blade chord distribution.

Table 9-1. Acoustic Ring Results for the 18-Inch QHSF Fan Blades.

	Mode				
Blade	1	2	3	4	5
1	215	610	1120	1435	1830
2	225	610	1150	1435	1820
3	225	610	1125	1445	1850
4	220	605	1110	1425	1815
5	220	605	1100	1425	1790
6	220	600	1080	1420	1790
7	220	615	1100	1455	1820
8	225	635	1110	1485	1820
9	220	615	1110	1450	1805
10	225	630	1105	1475	1825
11	225	610	1120	1440	1820
12	220	615	1100	1450	1825
13	225	605	1100	1440	1810
14	220	605	1090	1445	1820
15	220	620	1100	1465	1815
16	220	600	1105	1445	1830
17	220	605	1095	1435	1820
18	220	600	1095	1440	1810
19	220	625	1110	1465	1835
20	220	600	1100	1430	1815
21	222	645	1098	1385	1840
22	219	611	1075	1335	1813
23	223	625	1082	1348	1810
24	225	638	1090	1363	1830
avg	221	614	1103	1431	1819
pred	213	644	1089	1408	1885
stdev	2.6	12.5	15.5	36.7	13.4
high	225	645	1150	1485	1850
low	215	600	1075	1335	1790
range	10	45	75	150	60

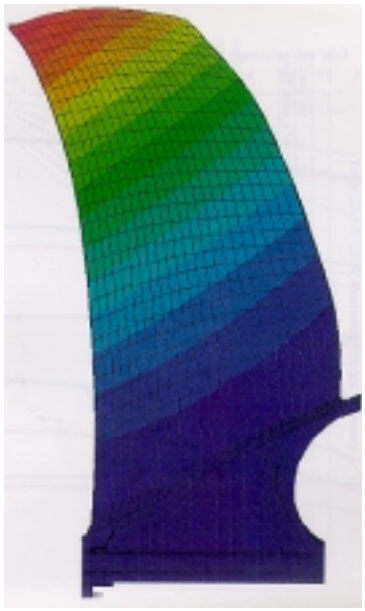

213 Hz - calculated

221 Hz - measured

(a) mode 1

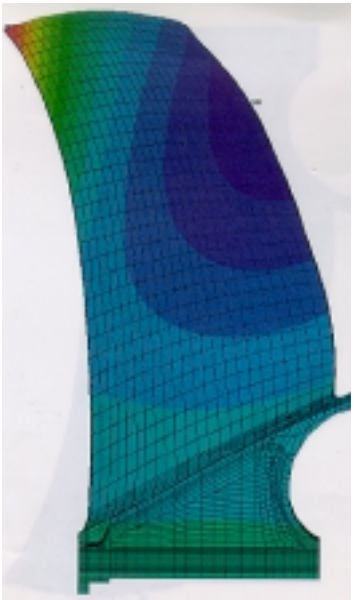

644 Hz - calculated

616 Hz - measured

(b) Mode 2

Figure 9-3. Acoustic Holography Results for the 18-Inch QHSF Fan Blade.

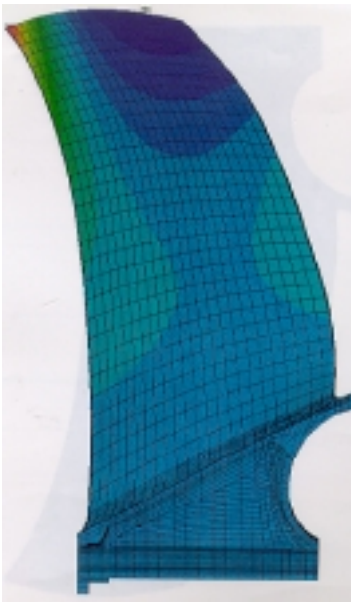

1089 Hz - calculated

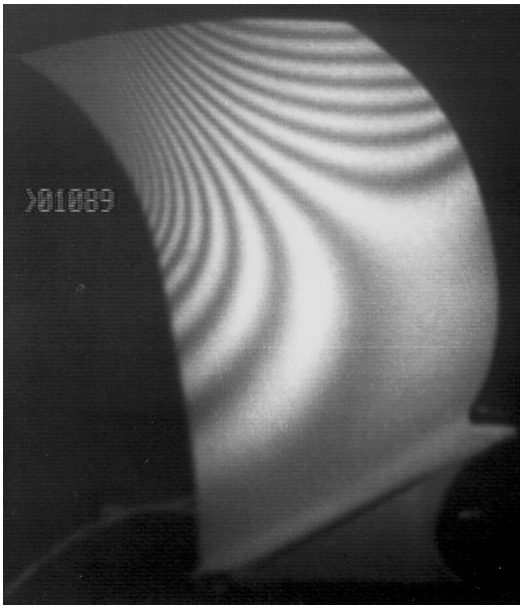

1089 Hz - measured

(a) mode 3

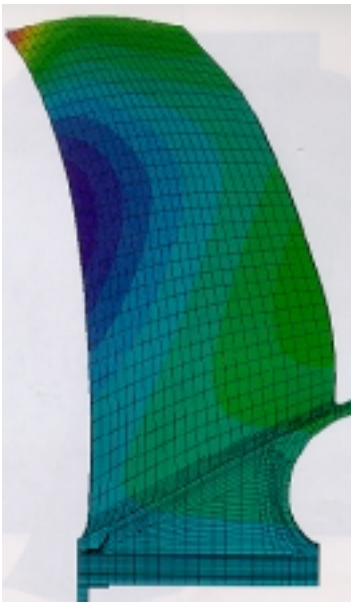

1408 Hz - calculated

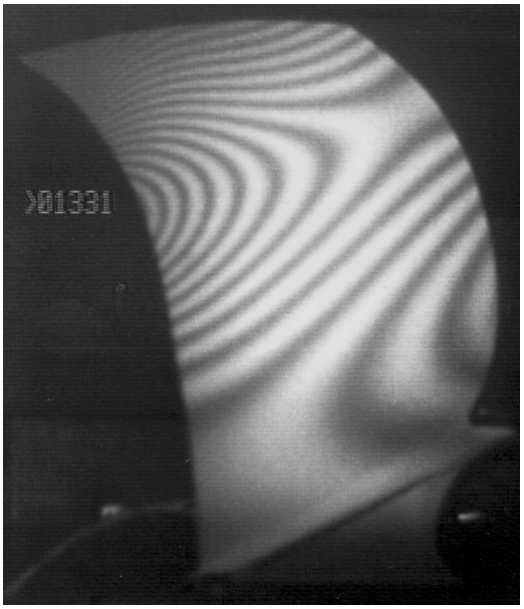

1331 Hz - measured

(b) Mode 4

Figure 9-3. Acoustic Holography Results for the 18-Inch QHSF Fan Blade (Cont).

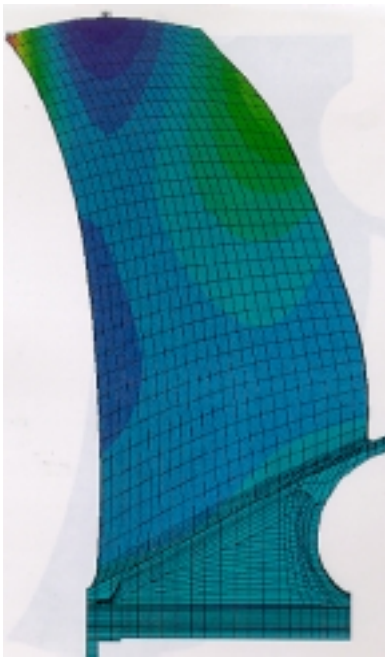

1885 Hz - calculated

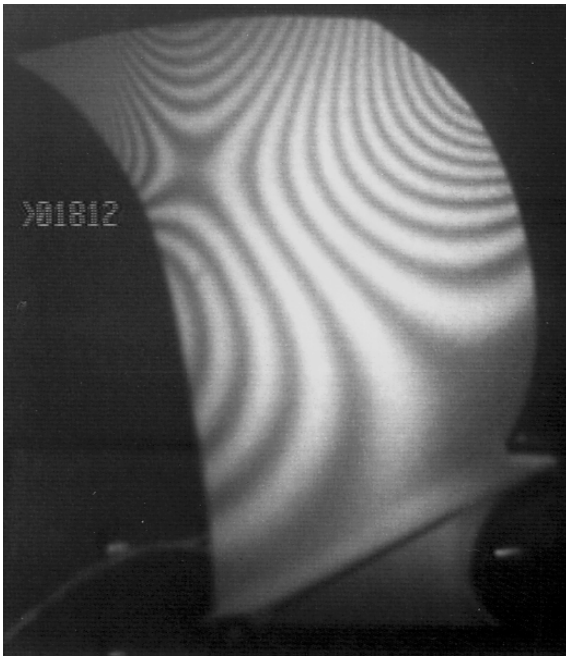

1812 Hz - measured

(b) Mode 5

Figure 9-3. Acoustic Holography Results for the 18-InchQHSF Fan Blade (Cont).

Engines & systems manufactured the composite stator vanes for the 18-inch QHSF, and new stator retaining rings were designed and fabricated. The existing fan disk, spinner, and front frame from the baseline fan rig were used. The existing fan case was modified to match the QHSF flowpath. Reuse of this hardware and existing instrumentation significantly reduced the cost to perform the performance testing.

9.2 Test Rig Operation

9.2.1 Purpose and Objectives

The objective of this test was to perform aerodynamic, mechanical, acoustic, and operability testing of the 18-inch QHSF. Results of this test will be used to support the planned 22-inch QHSF, as well as future Engines & systems fan design efforts.

Specific objectives are listed below:

- Ensure mechanical integrity of the fan rotor throughout the anticipated range of fan speeds
- Obtain early verification of fan performance
- Develop the fan performance map, including stall/stability line

- Define radial distributions of rotor and stator performance
- Define fan acoustic characteristics to support the forward swept design concept
- Determine performance and operability sensitivities to rotor tip clearance and to bypass ratio

9.2.2 Instrumentation

The following instrumentation was included in the 18-inch QHSF Rig measurements:

- Inlet Flow Measurement: A standard ASME bellmouth with eight static pressures
- Inlet Conditions: Temperature and pressure measurements aft of the flow straighteners in the inlet tank.
- Inlet Distortion: Ten rakes with six total pressure elements each forward of fan rotor
- Inlet Boundary Layer Rakes: Two rakes with five pressure elements to determine magnitude of inlet boundary layer.
- Vane Leading Edge Instrumentation: Four of the stator vanes had leading edge instrumentation consisting of seven total pressure and temperature elements each.
- Fan Core and Bypass Instrumentation: Four radial total pressures and temperatures at five circumferential locations in the core, and six radial total pressures and temperatures at five circumferential locations in bypass on the leading edge of core and bypass front frame struts.
- Bypass Duct Exit Performance: Four rakes with six radial total pressures and temperatures.
- Flow-path Static Pressure: Located at critical locations on hub and shroud, including core, bypass, and vane leading edge measurement planes.
- Exit Flow Measurements: A standard ASME sharp-edge orifice-plane downstream of the core discharge plenum measured core flow.
- Rotor Exit Radial Survey: Two survey locations, one for a self-null cobra probe and one for performance probe.
- Vane Exit XY Survey: One location for performance probe surveys at the vane exit.
- Dynamic Pressure Measurements (Operability): Two dynamic pressure transducers aft of the fan rotor.
- Inlet Thermocouple: Bare-bead thermocouple on the shroud forward of the fan rotor.

- Acoustic Instrumentation: 16 PCB piezoelectric transducers mounted flush on the fan screen rotator ring for inlet acoustic measurements and three Kulites in the bypass duct to measure aft radiated noise.

- Rotor Clearance: Four capacitance probes at rotor leading edge and four at trailing edge.

- Rig Speed and Shaft Excursion Measurements: A monopole transducer measuring splines located on the fan shaft and Bently probes to measure shaft excursions.

- Rotor Strain Gauges: Ten gauges mounted on critical stress areas of five rotor blades (two per blade), as described in Reference 3. A rotor-shaft mounted telemetry system was used to transmit signals from gauges to a high-speed magnetic tape recorder and real-time analyzer.

- Mechanical Integrity Instrumentation: Forward-bearing temperatures were monitored from the console. One thermocouple was mounted on the forward bearing race to monitor bearing temperature. Oil pressure, inlet oil temperature and scavenge oil temperature was monitored. The pressure difference across the carbon seal was monitored. Accelerometers mounted on the rig provide continuous vibration data.

9.3 Performance Test Results

9.3.1 Data Quality

Vane Leading Edge Instrumentation: The vane did not have an element beyond 81 percent span to include in the performance calculation. Additional vane leading edge elements would have better defined the total pressures and temperatures near the shroud. Therefore, the pressure and efficiency calculated from the vane leading edge instrumentation were higher than actual. Overall, the pressure and temperature vane leading edge data were either in close agreement or slightly lower than the rotor exit survey measurements. Because of the limited amount of rotor survey data, the rotor performance maps (Figures 9-4 through 9-15) were based on the vane LE data adjusted to the rotor survey results. The instrumented vanes were at circumferential positions of 48.5, 117.7, 228.5, and 332.3 relative to top dead center, aft looking forward.

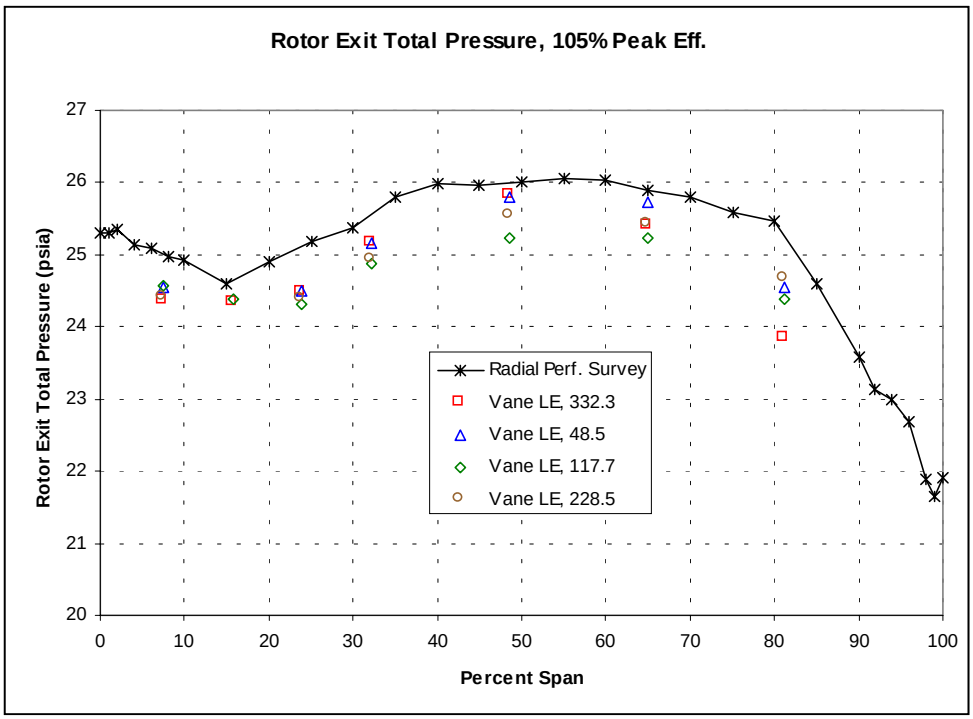

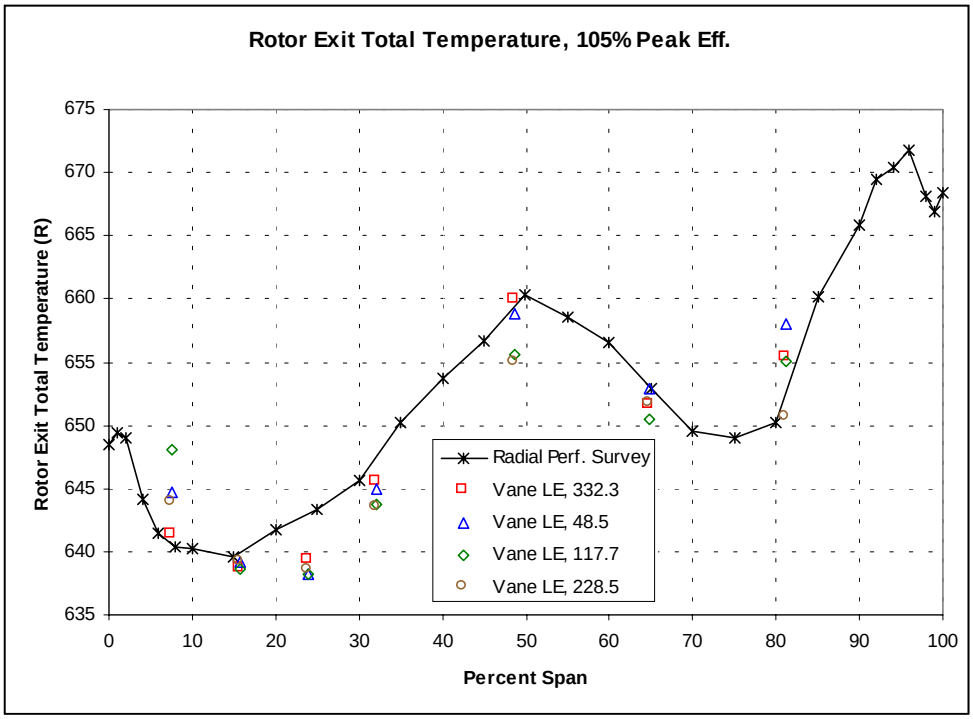

Figure 9-4. Rotor Exit Survey Data Compared to Vane LE Instrumentation at 105% N1c Near Peak Efficiency.

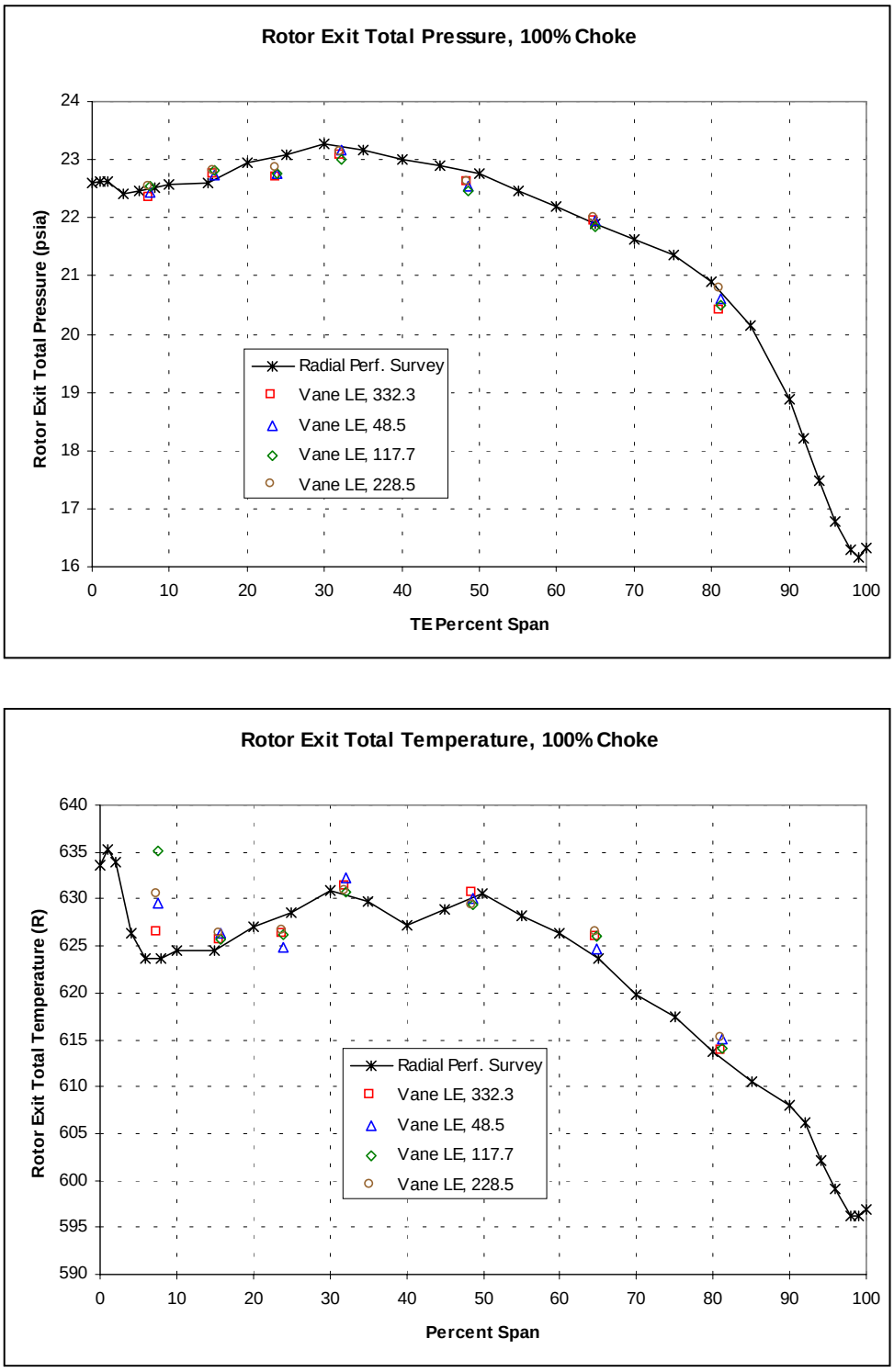

Figure 9-5. Rotor Exit Survey Data Compared to Vane LE Instrumentation at 100% N1c Choke.

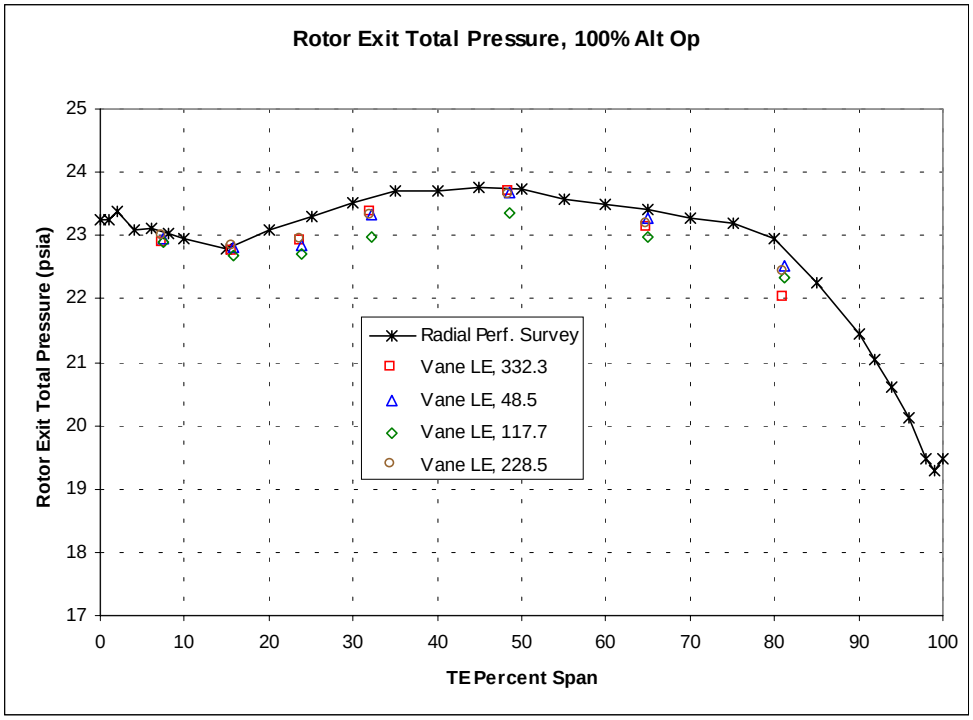

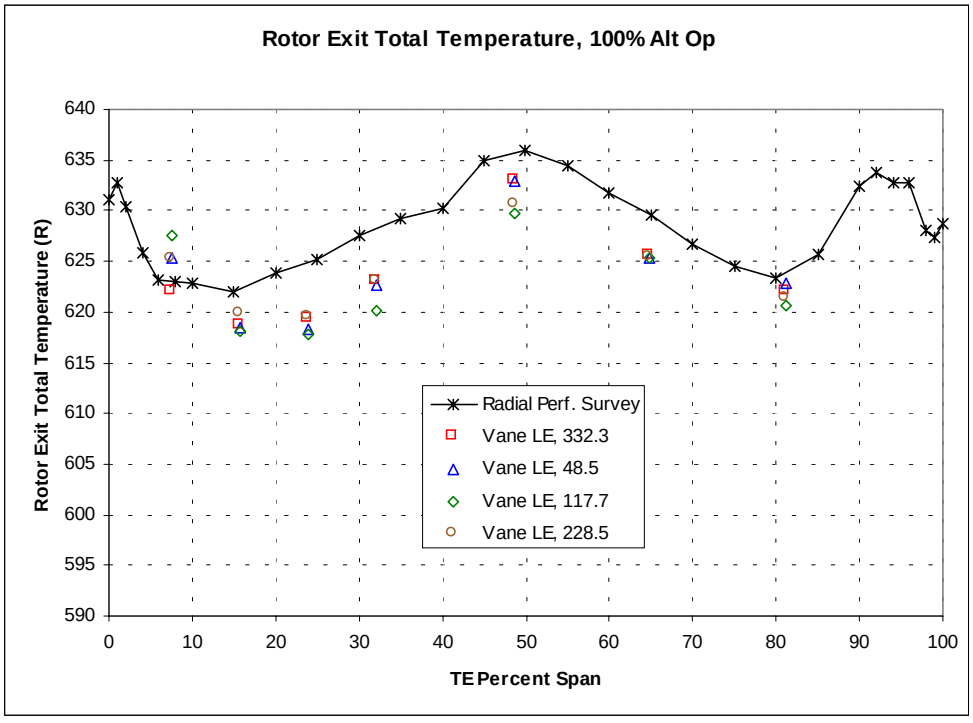

Figure 9-6. Rotor Exit Survey Data Compared to Vane LE Instrumentation at 100% N1c Near Altitude Operating Line.

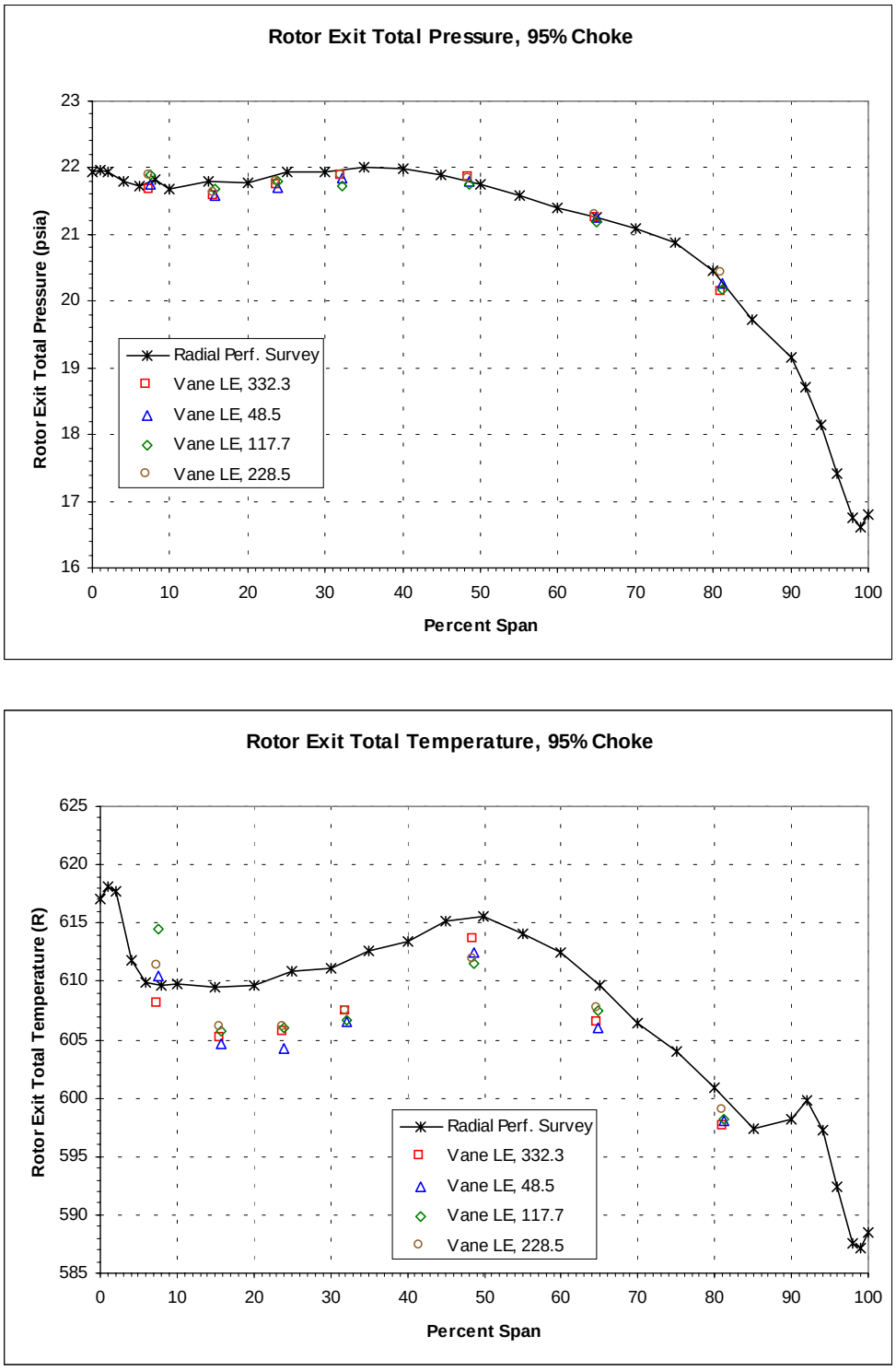

Figure 9-7. Rotor Exit Survey Data Compared to Vane LE Instrumentation at 95% N1c Choke.

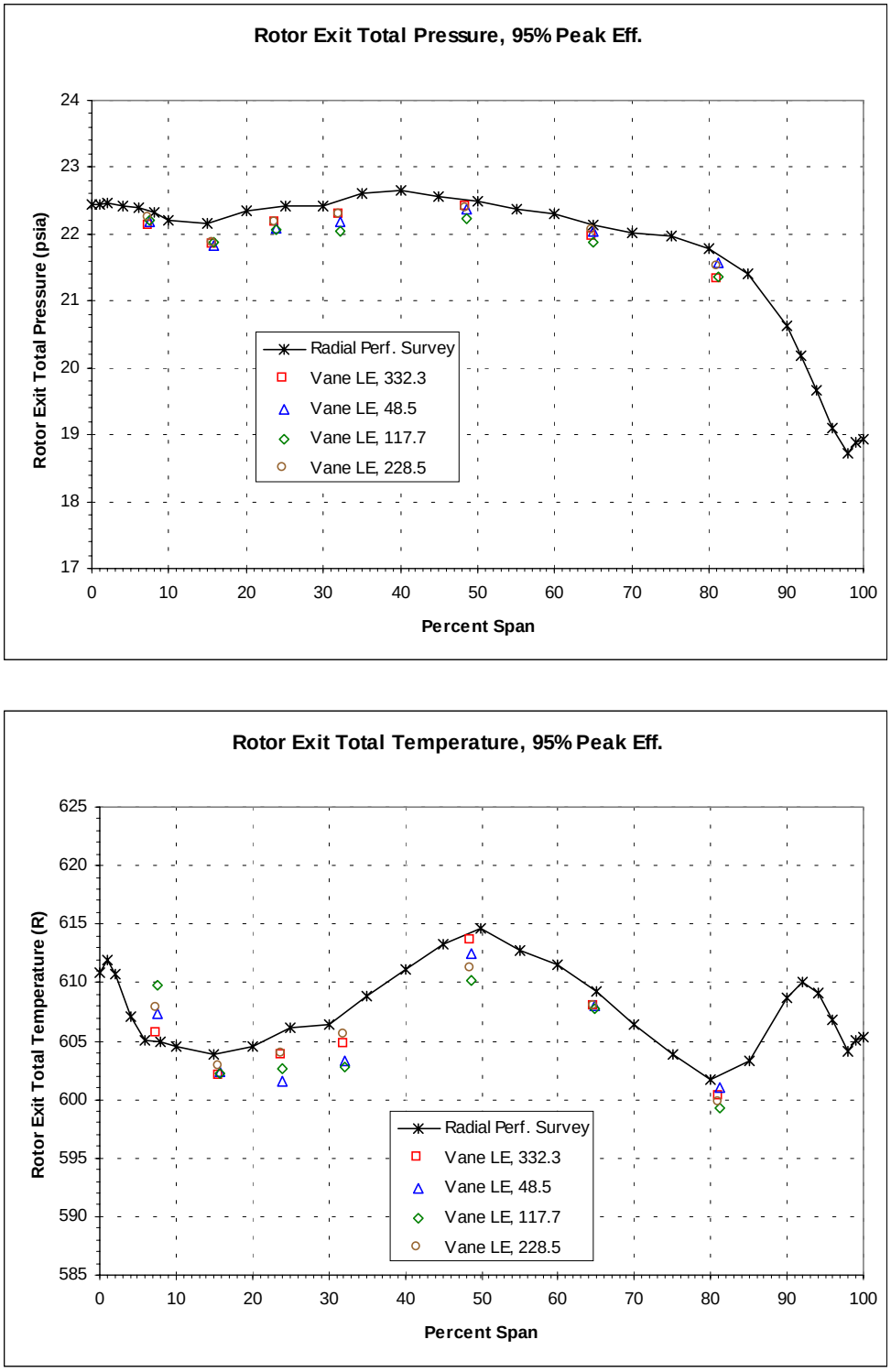

Figure 9-8. Rotor Exit Survey Data Compared to Vane LE Instrumentation at 95% N1c Near Peak Efficiency.

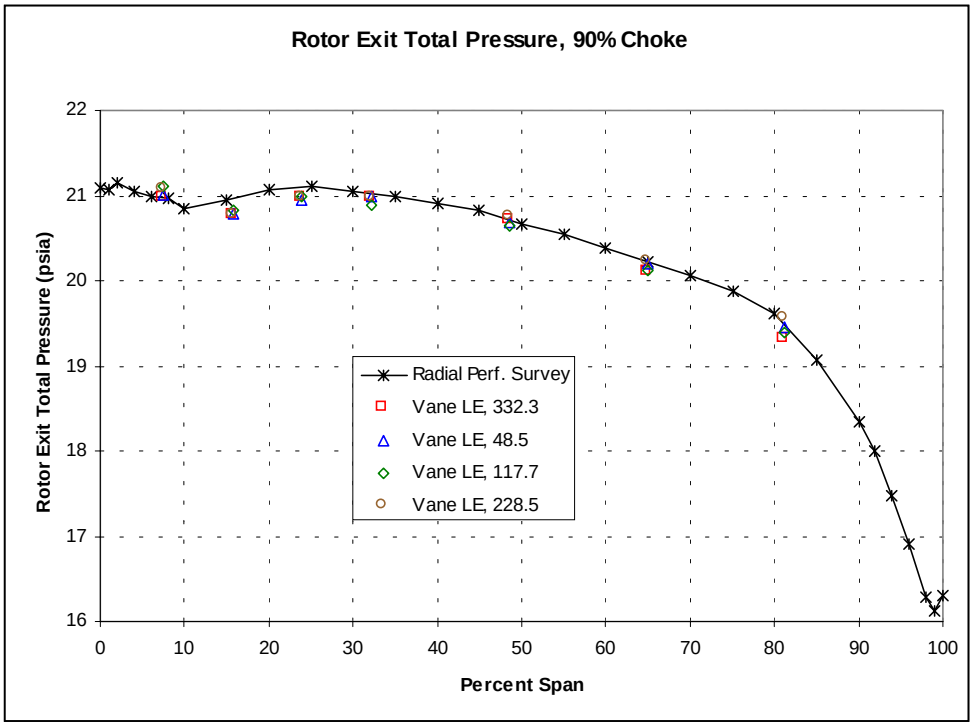

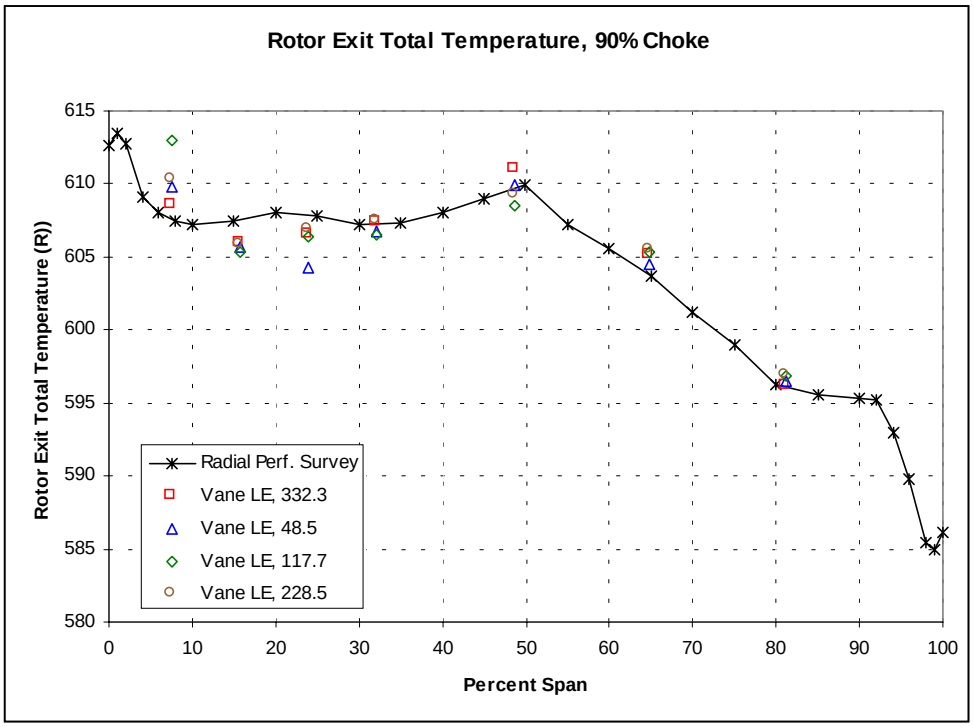

Figure 9-9. Rotor Exit Survey Data Compared to Vane LE Instrumentation at 90% N1c Choke.

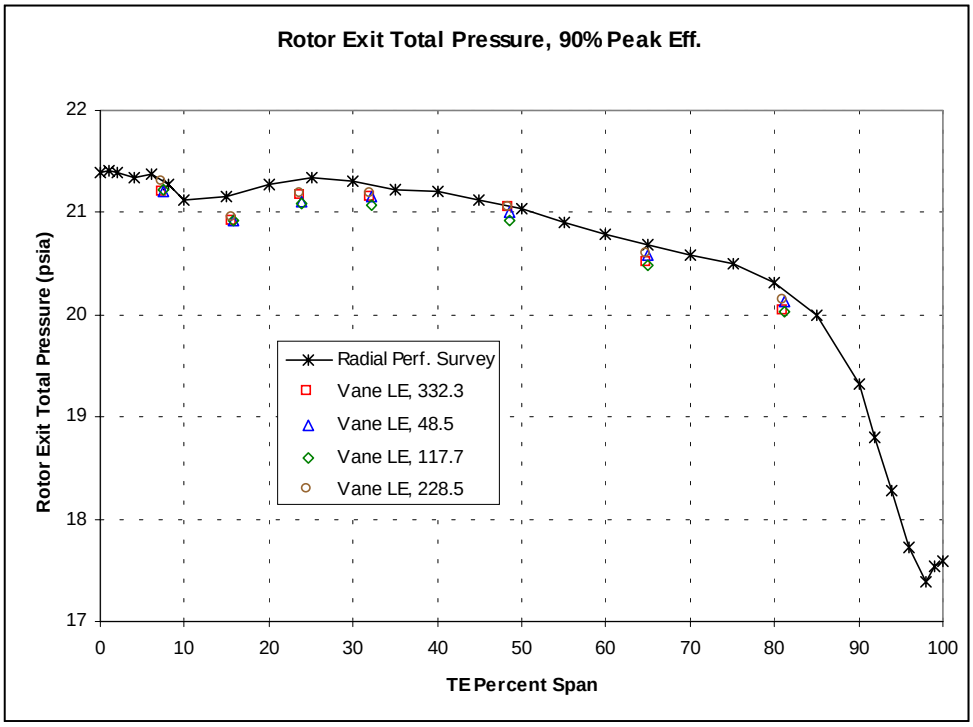

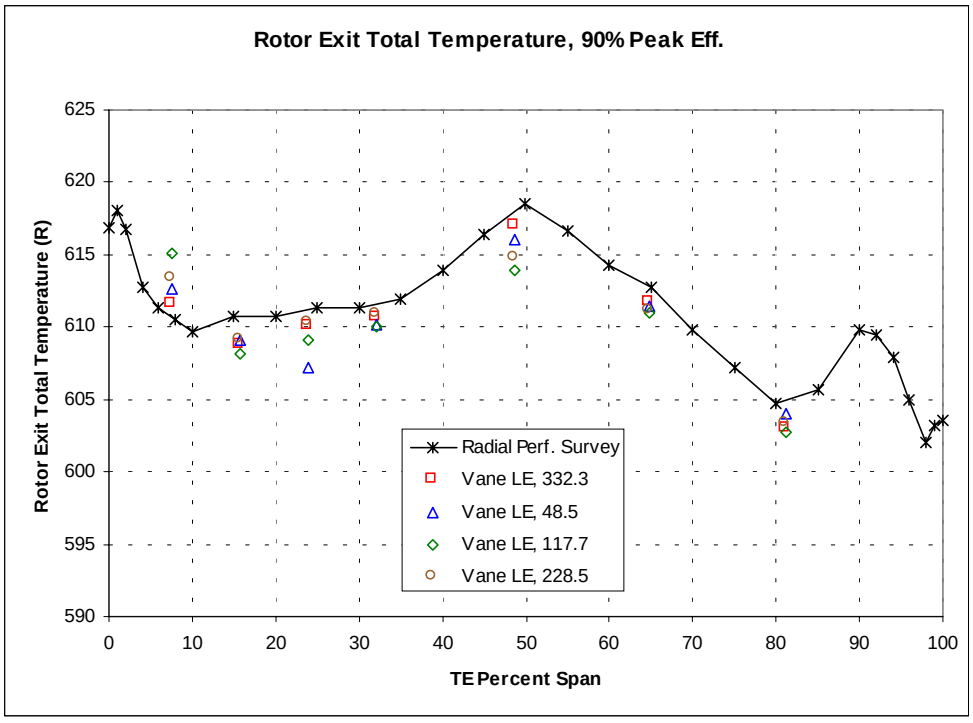

Figure 9-10. Rotor Exit Survey Data Compared to Vane LE Instrumentation at 90% N1c Near Peak Efficiency.

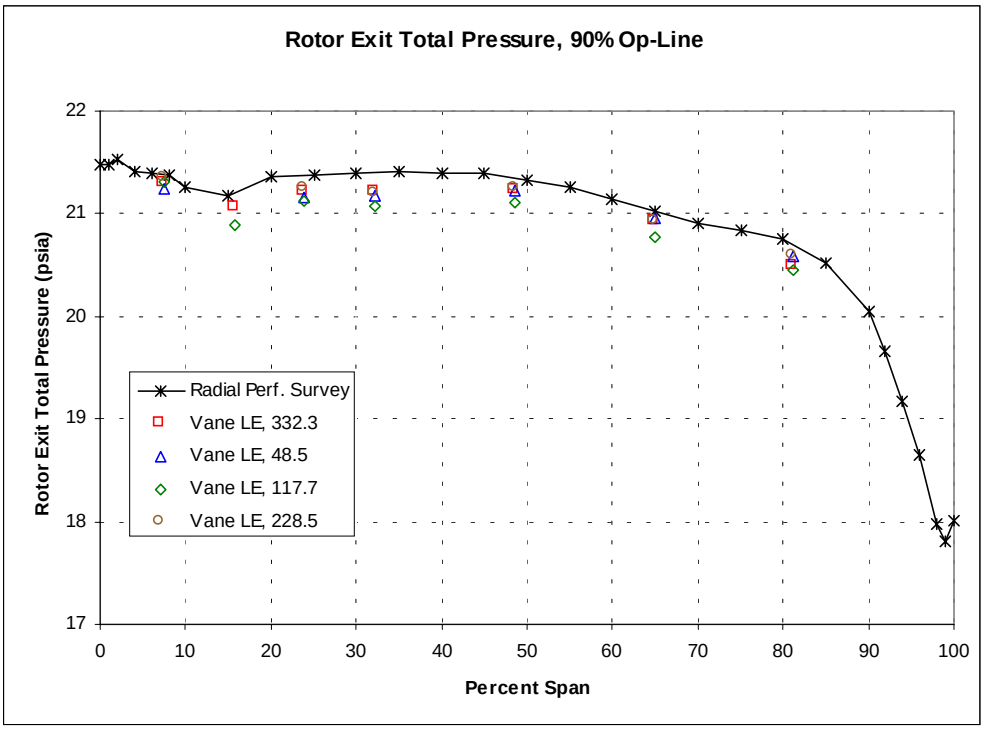

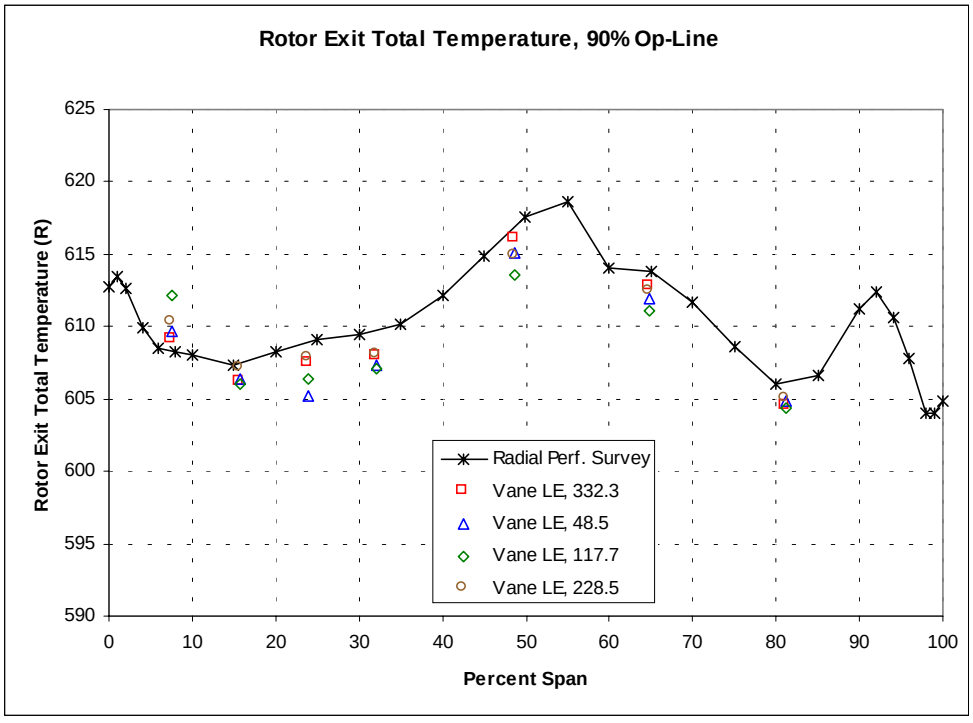

Figure 9-11. Rotor Exit Survey Data Compared to Vane LE Instrumentation at 90% N1c SLS Operating Line.

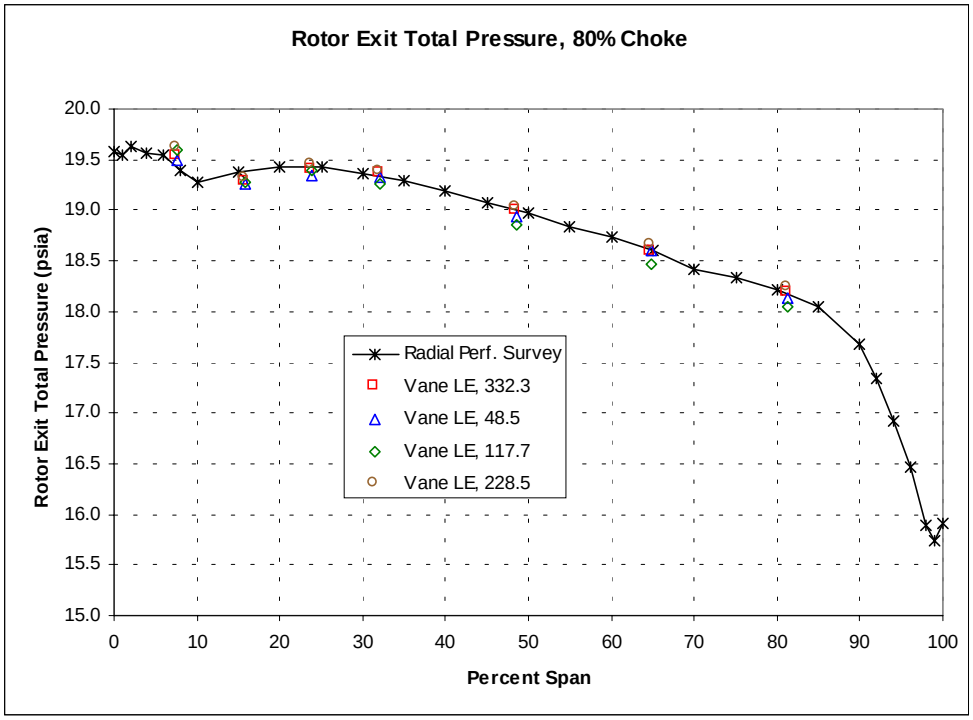

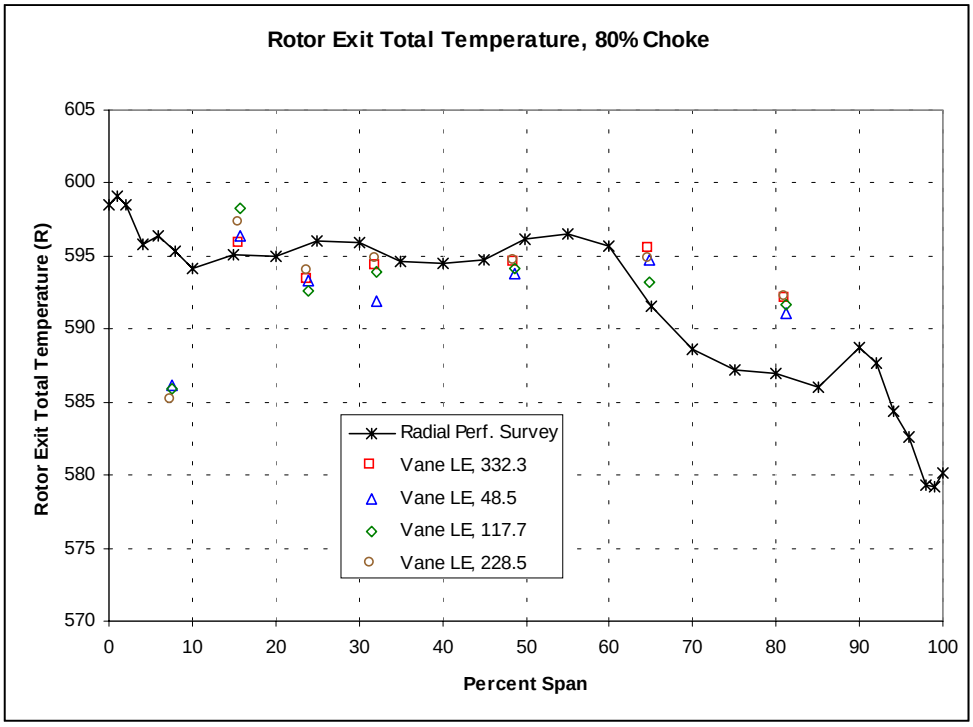

Figure 9-12. Rotor Exit Survey Data Compared to Vane LE Instrumentation at 80% N1c Choke.

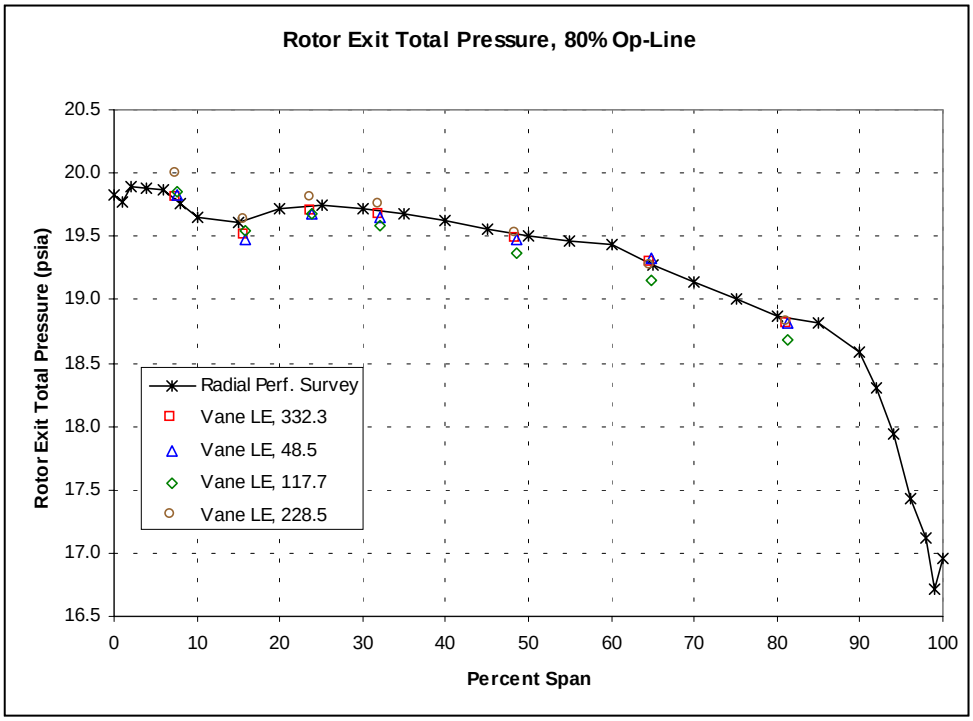

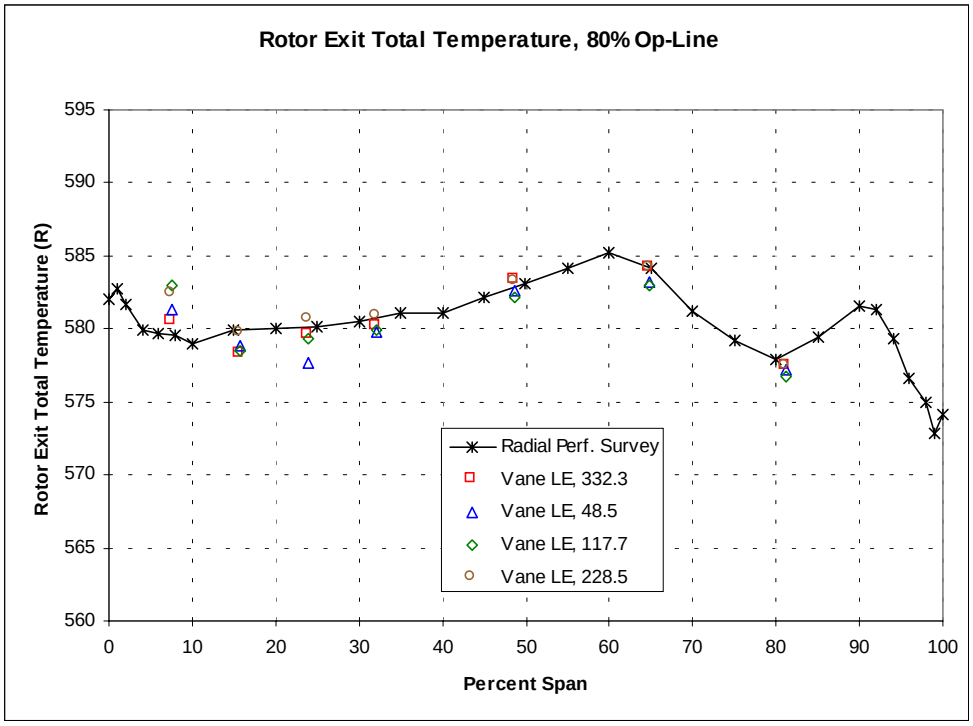

Figure 9-13. Rotor Exit Survey Data Compared to Vane LE Instrumentation at 80% N1c SLS Operating Line.

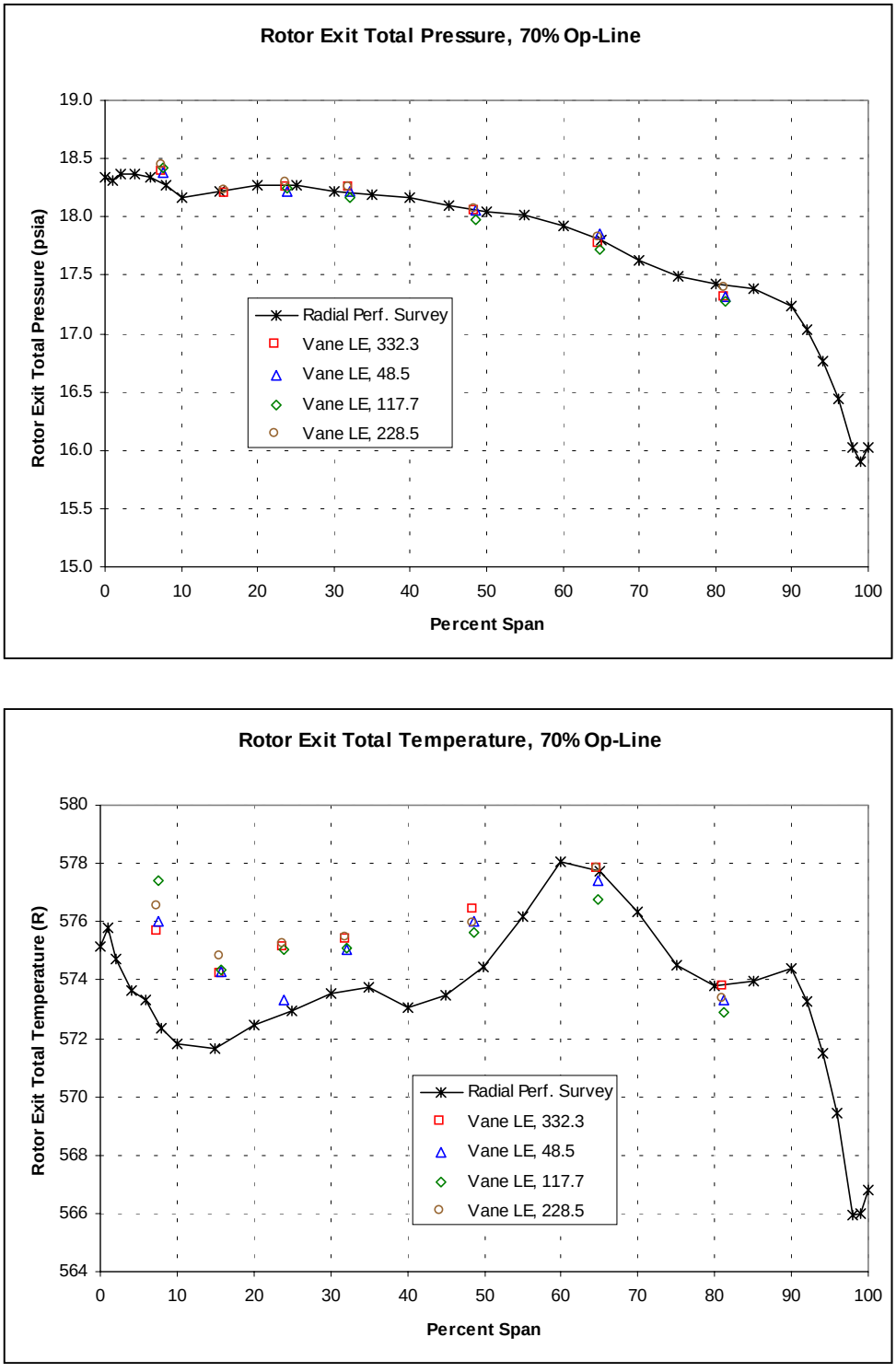

Figure 9-14. Rotor Exit Survey Data Compared to Vane LE Instrumentation at 70% N1c SLS Operating Line.

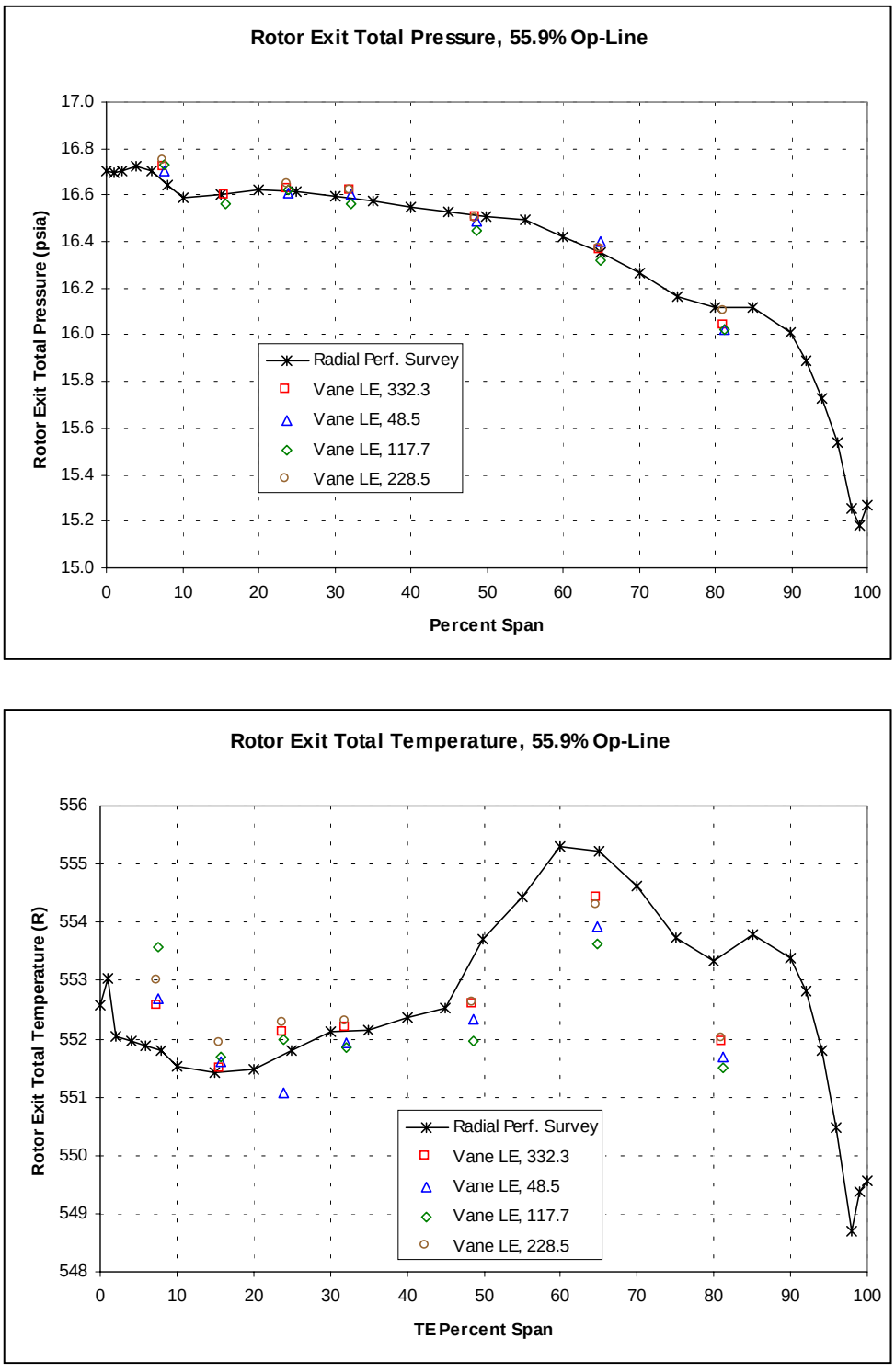

Figure 9-15. Rotor Exit Survey Data Compared to Vane LE Instrumentation at 55.9% N1c SLS Operating Line.

Core and Bypass Level 2 Rakes: Data compared very well in the bypass to the limited data obtained with the stator exit x-y survey. Stage maps were based on the Level 2 rake data.

Rotor Capacitance Probes: Capacitance probes agreed well with cold build clearance measurements. Of the three sets of four (LE, mid, and TE), and during the testing presented in this report: one was bad at the LE (9 o'clock FLA), one was bad at mid (BDC), and two were bad at the TE (TDC and 9 o'clock). An average of the working capacitance probes is presented in Figure 9-16.

Rotor Exit Traverse: The use of two probes; one cobra, and one performance worked well. The cobra probe was used to determine the exit air angle, to which the performance probe angle was adjusted prior to data being acquired. The lack of survey data at critical points caused some questions in the final maps generated.

Stator Exit X-Y Surveys: Of the run numbers that it worked, the data seemed to be consistent with the bypass Level 2 data. Contour plots showed the core region to be non-symmetric with respect to the vanes. While the rotor was being reworked for flutter testing, the stator exit probe traverse pattern was inspected and determined to deviate from intent near the hub. A Cobra probe was used for the design point exit air angle calculation, which seemed to provide reasonable results.

Torquemeter: Although the torquemeter was used throughout the test, the results implied a work scaler of 7 percent between torquemeter and Level 2 at design speed. The large difference was believed to be in the torque meter, either with the calibration or calculated tare loss, but nevertheless, was not incorporated in generating the final performance maps (Figure 9-17).

9.3.2 Post Test Inspection Verification

The cold build tip clearance on the rig was found to be nominal at the trailing edge and tight at the leading edge. Cap probe measurements during the initial run-up provided confirmation of these numbers. The fan case was subsequently re-shimmed aft by 0.20 inch to give adequate LE clearance to prevent high-speed rubs. As a result, the trailing edge operated with a larger than desired clearance through the remainder of the test. After the test, the pertinent hardware was examined in an effort to uncover the cause for the insufficient LE tip clearance.

Profile data was received from the vendor for each blade for the three sections defined on the drawing. This data showed that the hub and mid span section were predominantly within blueprint tolerances. The tip section however, had significant deviation from the blueprint, up to 0.024 inch toward the suction side on a mean line basis.

A study was performed to assess the effect of the deviation on steady-state blade deflection and running clearance. The nominal blade geometry was altered to reflect the measured section deviations and a static analysis run to the design speed (19,142 rpm) where the tip closure (deflection normal to the clearance gap) was calculated. This calculation takes both radial and axial deformation into account since there is a 7-degree tip slope.

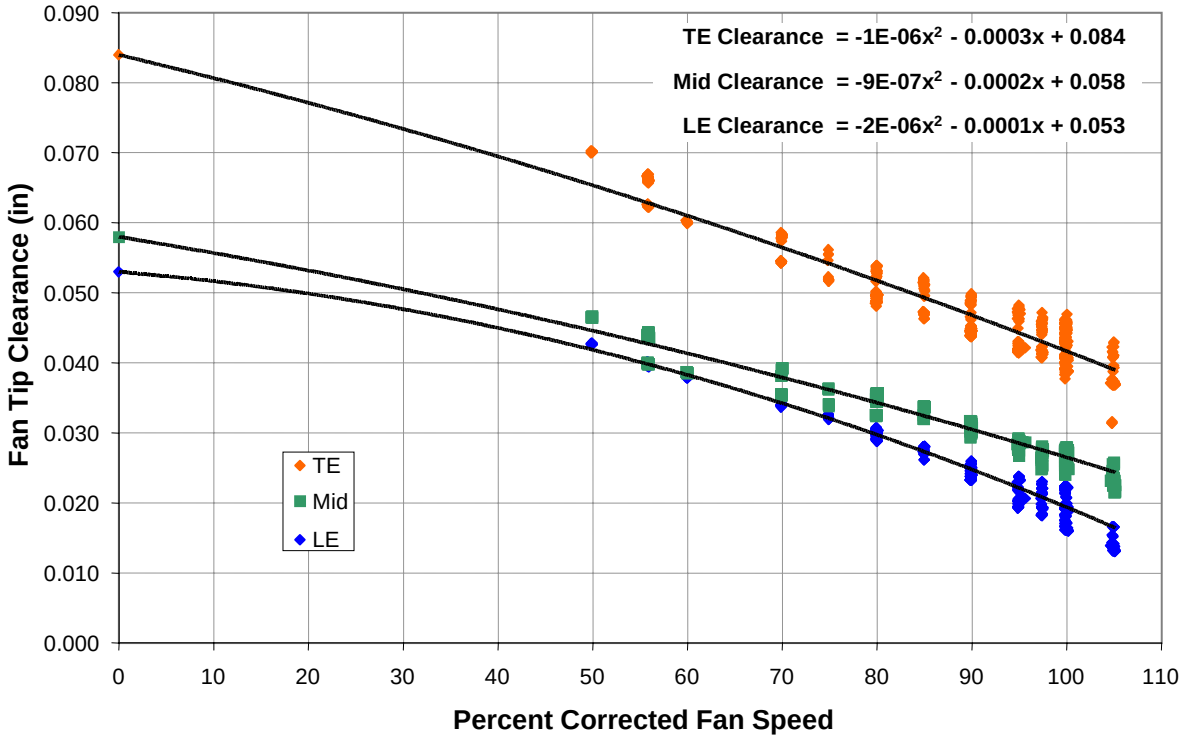

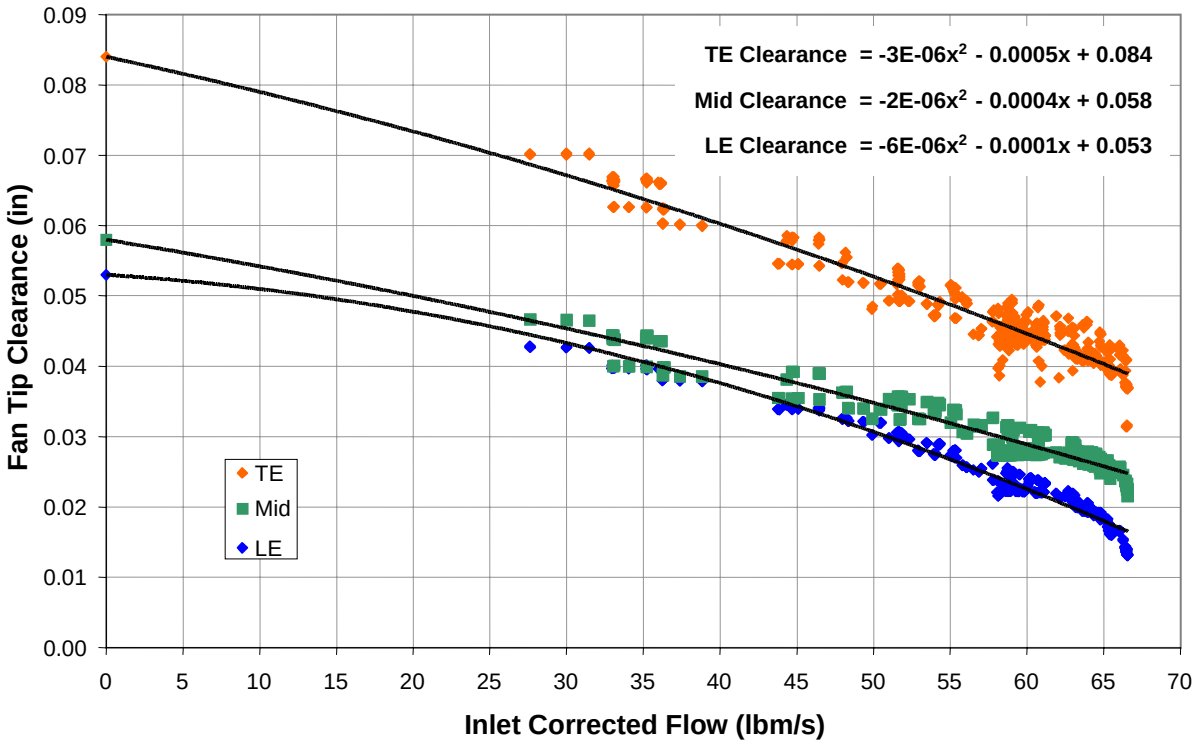

Figure 9-16. Fan Tip Clearance With Corrected Speed and Flow.

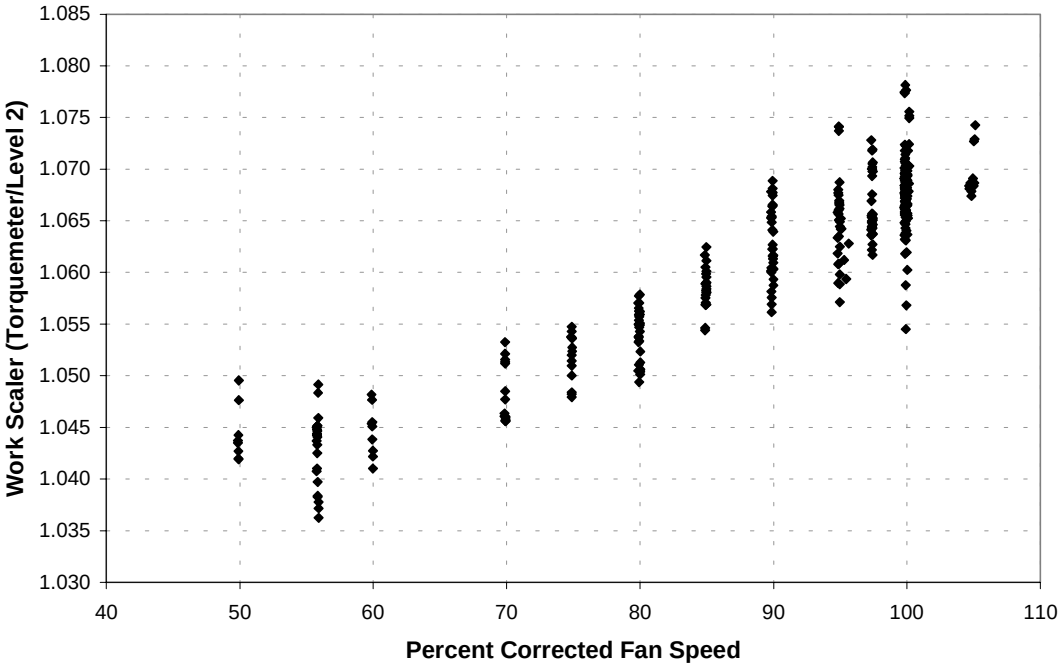

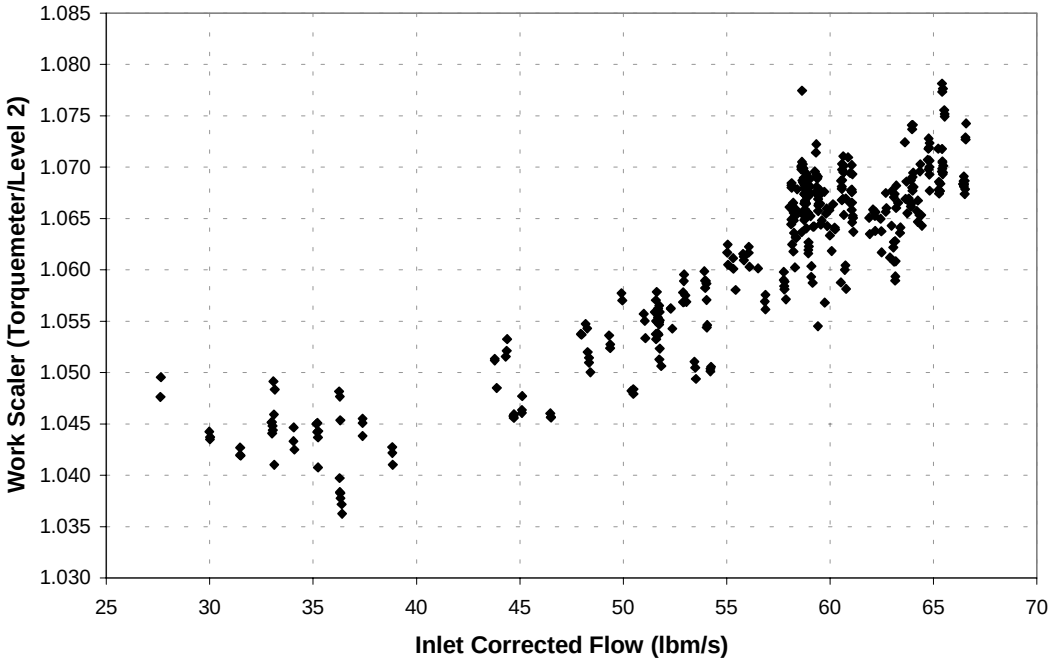

Figure 9-17. Work Scaler (Torquemeter/Level 2) With Corrected Speed and Flow.

With nominal dimensions, the leading edge closes approximately 0.075 in and the trailing edge approximately 0.045 in. An exaggerated, worst-case envelope of the deviations (0.050 inch suction-side shift above 60 percent span) resulted in a tip closure deflection of 0.076 and 0.049 inch on the LE and TE respectively. On the basis of these results, it appears the surface contour deviations play only a small role in the overall running tip clearance.

Tip contour, on the other hand, has a direct impact on tip clearance. Three blades were inserted in the broach block and tip profile measured. The results are shown in the following chart. Both blades are slightly shorter than nominal indicating a wider tip clearance, but the data doesn't explain the tight leading edge observed during the rig test. Figure 9-18 illustrates the inspection results. The fan case was found to be within blueprint tolerances as well.

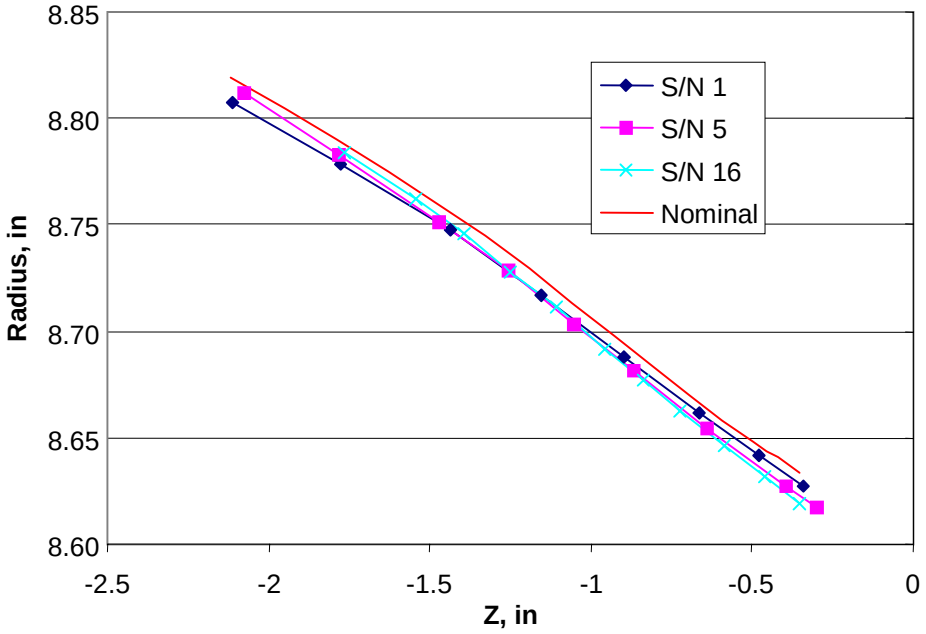

Figure 9-18. Results of Tip Contour Measurements of the 18-Inch QHSF Blades.

9.3.3 Stage Performance and Operability

Fan bypass and core stage performance maps were based entirely on Level 2 instrumentation, and are shown in Figures 9-19 through 9-24. The "final map" is a best-fit map through the measured data. The data were speed corrected and include the data with bypass ratios close to the desired levels. The stability line shown represents the onset of flutter, rotating stall, or surge. At 75 percent N1c, the stability line intersected the SLS operating line. Also shown in the figures is the desired surge line. Various tests were completed to expand the stability line toward the desired surge line by incorporating various amounts of leading edge tip clip (10 percent chord and 20 percent chord) as well as radial distortion screens. These hardware changes had minimal effect on moving the stability line.

The maps show bypass peak efficiency to be 0.865, at an inlet corrected flow of 65.0 lbm/sec (99.82 lbm/sec at 22 inch DIA), and a pressure ratio of 1.79. The corresponding efficiency and pressure ratio in the core is 0.880 and 1.76, respectively. At the design work level of 1.212 the inlet corrected flow was 64.72 lbm/sec (99.39 lbm/sec at 22 inch DIA), the bypass efficiency was 0.860 and the pressure ratio was 1.800. The corresponding efficiency in the core was 0.881 and the pressure ratio is 1.757. The tested baseline fan stage data showed bypass pressure ratio of 1.844 (+2.4 percent) with an efficiency of 0.889 (+0.9 point), while the core was 1.718 (-2.3 percent) with an efficiency of 0.918 (+2.9 point).

9.3.4 Rotor Performance

Rotor performance maps were based on both the rotor exit survey data and the vane leading edge data. Figures 9-25 through 9-27 show the rotor exit survey data compared against the DAWES predicted results.

It would appear that the measured efficiency of the rotor was approximately 1 point higher than predicted at the design point. However, of the two surveys taken at 100 percent N1c, the one closest to the design point was actually more than a point lower than the choked case. Also, the survey data did not agree with the vane leading edge data and the prediction. Figures 9-28 to 9-31 show the speed-corrected vane leading edge data. Although the vane leading edge data produced higher efficiency values, the speed lines are continuous and consistent with predictions. There was no indication that the efficiency decreased as the rotor was throttled from choke to the operating line.

Spanwise comparison plots were created for all the survey data to the closest analysis point from DAWES. Figures 9-32 through 9-43 show comparisons of pressure ratio, temperature ratio, efficiency, and exit absolute air angle for each of the pertinent points. The plots clearly show the low-pressure region near the tip, which may be attributed to the open clearances at the blade trailing edge. Although the compared profiles may not represent exactly the same point, it is evident that the tip region is different between the analysis and test. The work profile, above the choke operating point, has a low region between 70 and 85 percent span coupled with a large increase in work from 85 to 95 percent span not evident in the analyses. The low work region was not reflected in the pressure ratio profile, but instead manifested itself as a very efficient region. Because the work in the tip region increased as the rotor was back-pressured, the survey data would support rotor peak efficiency to be somewhere between choke and the operating line, below that of design intent.

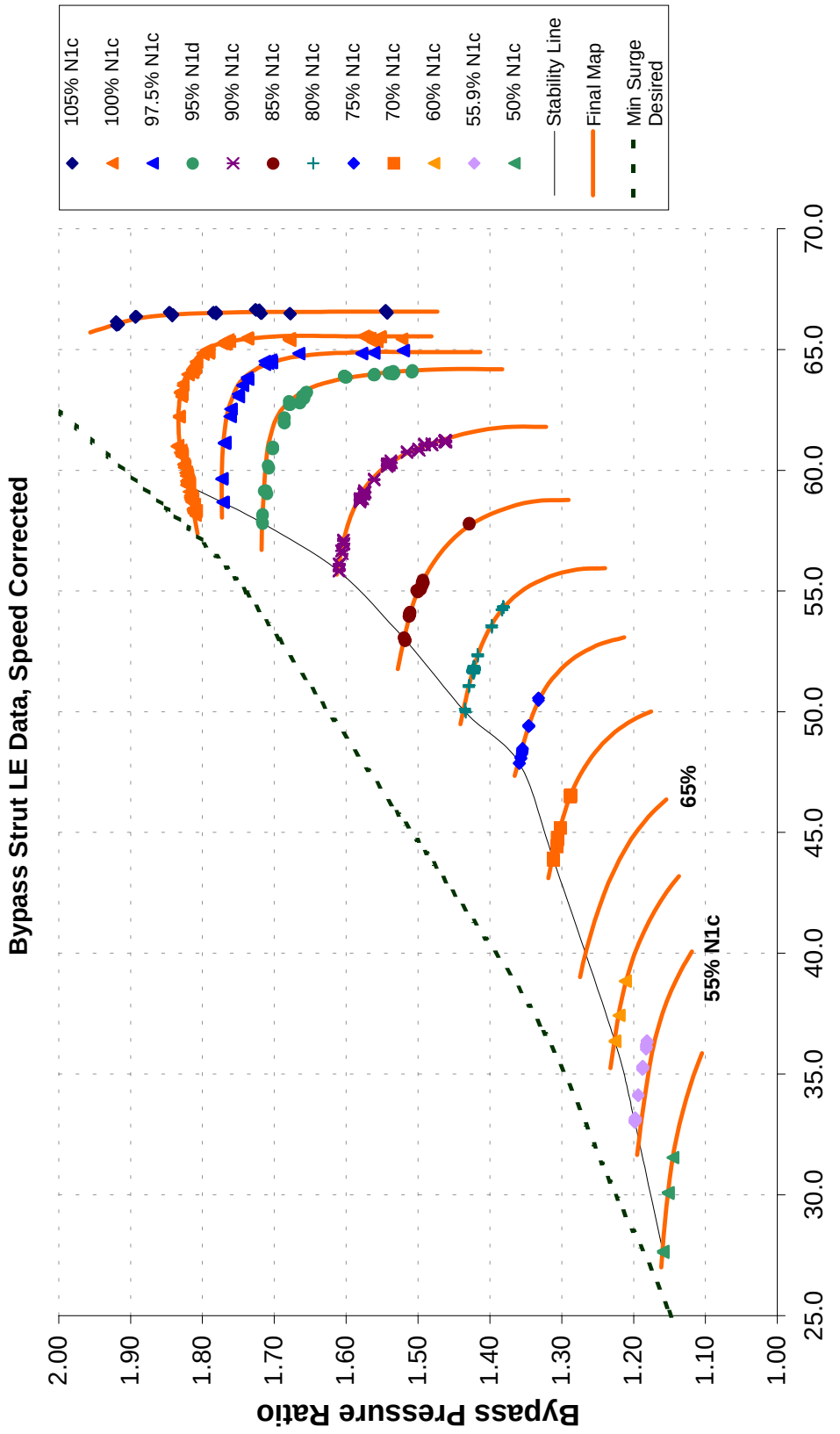

Figure 9-19. Bypass Performance Map (Wc Versus PR) Overlayed on Level 2 Data.

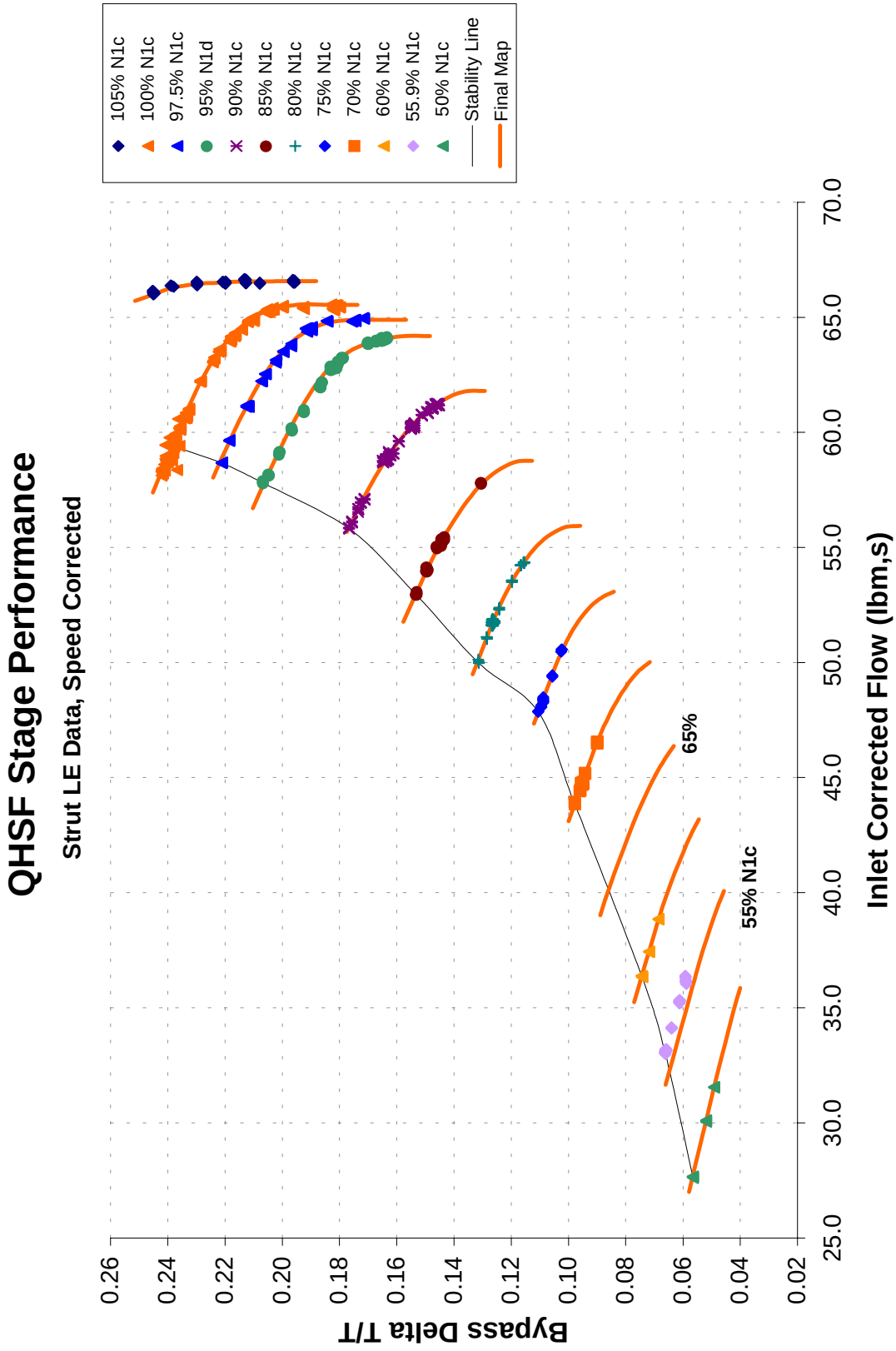

Figure 9-20. Bypass Performance Map (Wc Versus ΔT/T) Overlayed on Level 2 Data.

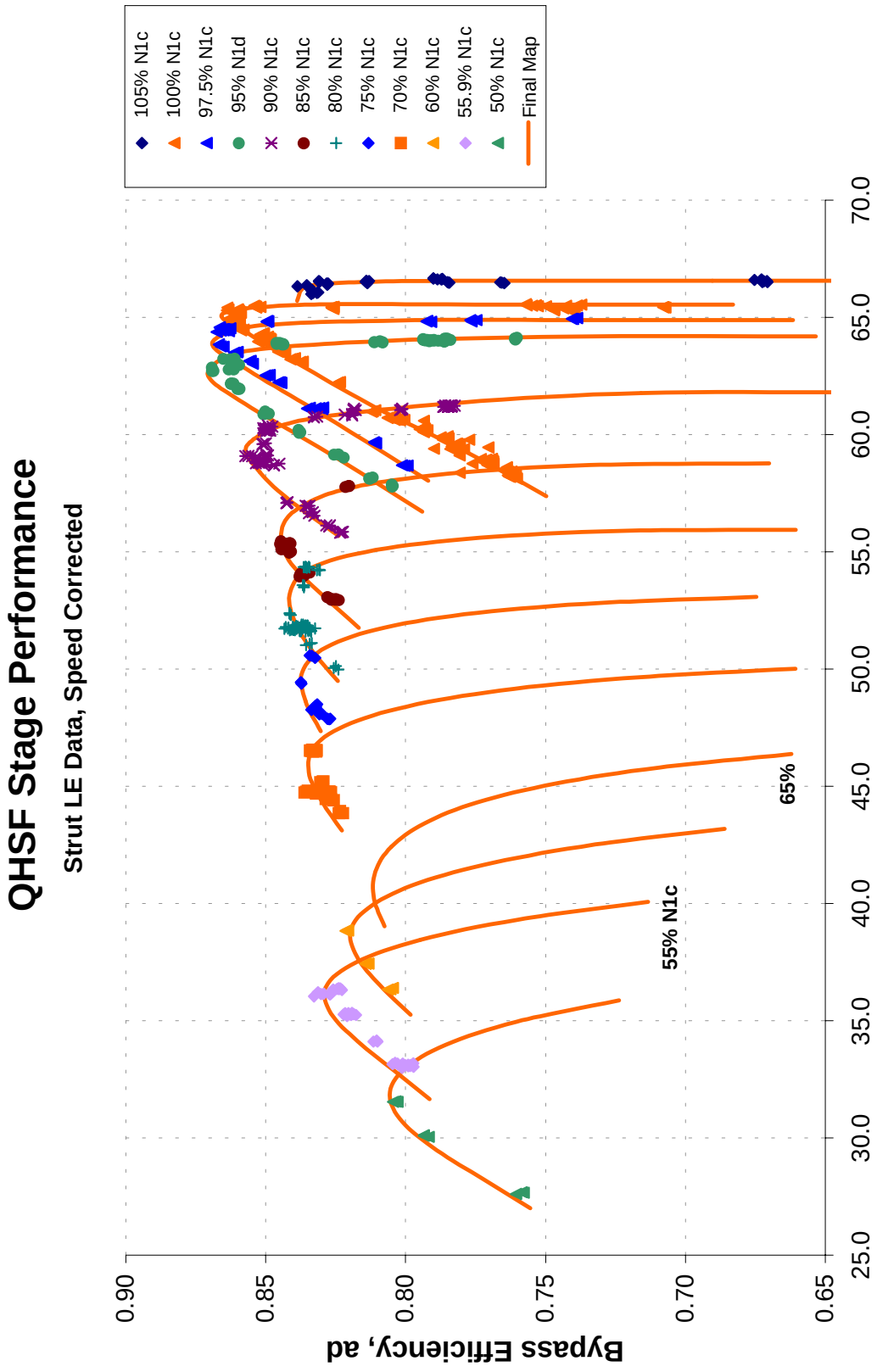

Figure 9-21. Bypass Performance Map (Wc Versus Eff) Overlayed on Level 2 Data.

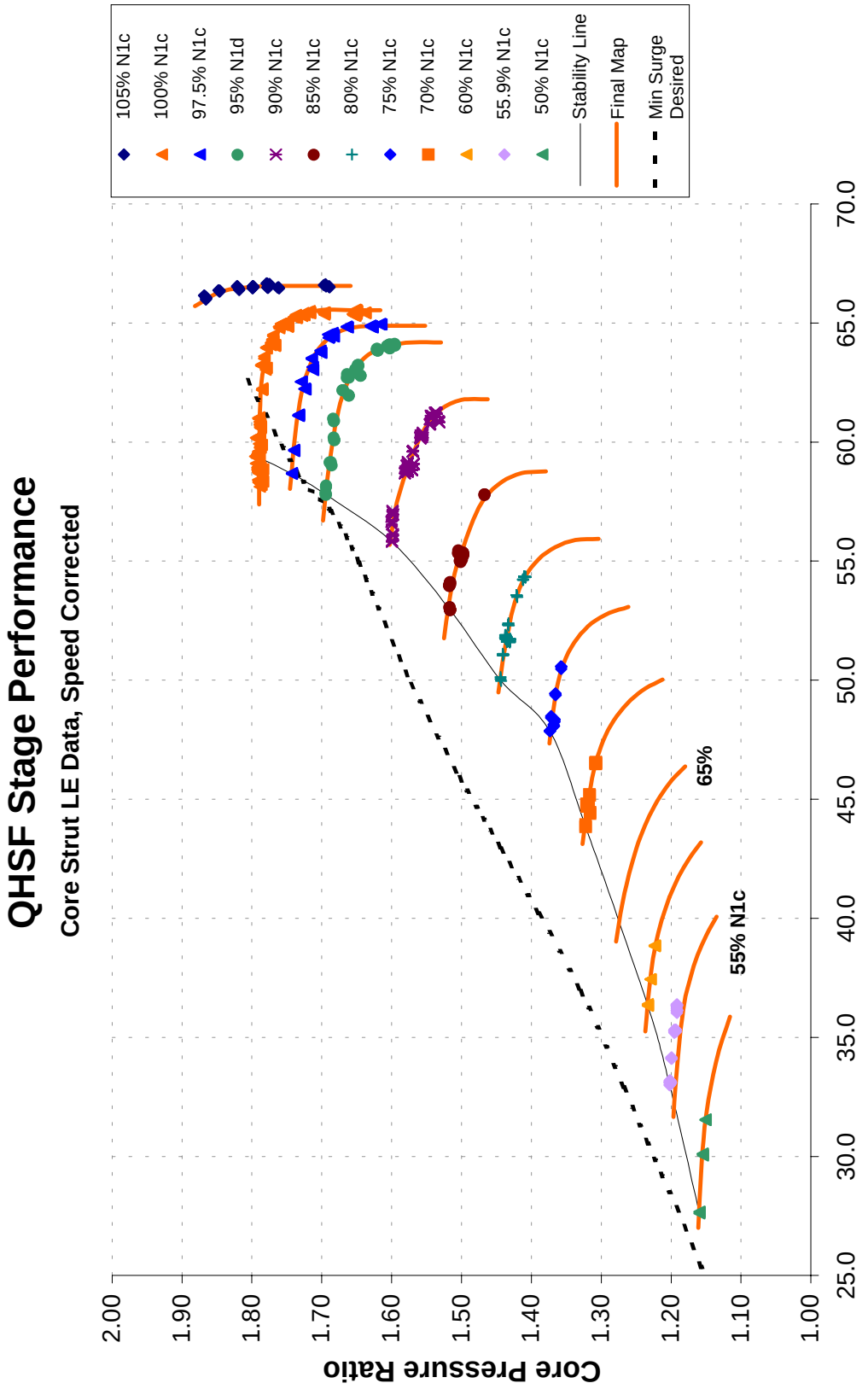

Figure 9-22. Core Performance Map (Wc Versus PR) Overlayed on Level 2 Data.

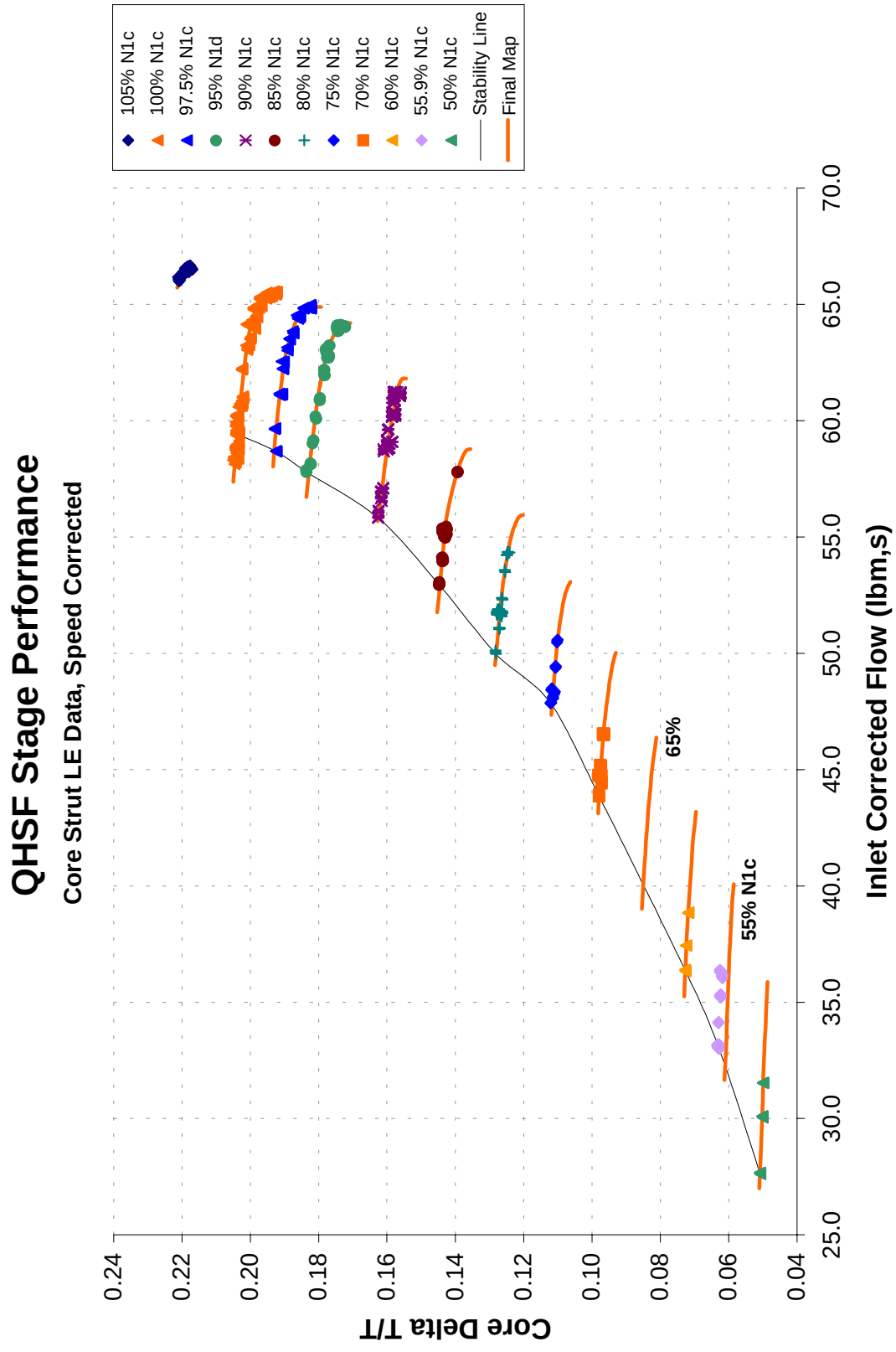

Figure 9-23. Core Performance Map (Wc Versus ΔT/T) Overlayed on Level 2 Data.

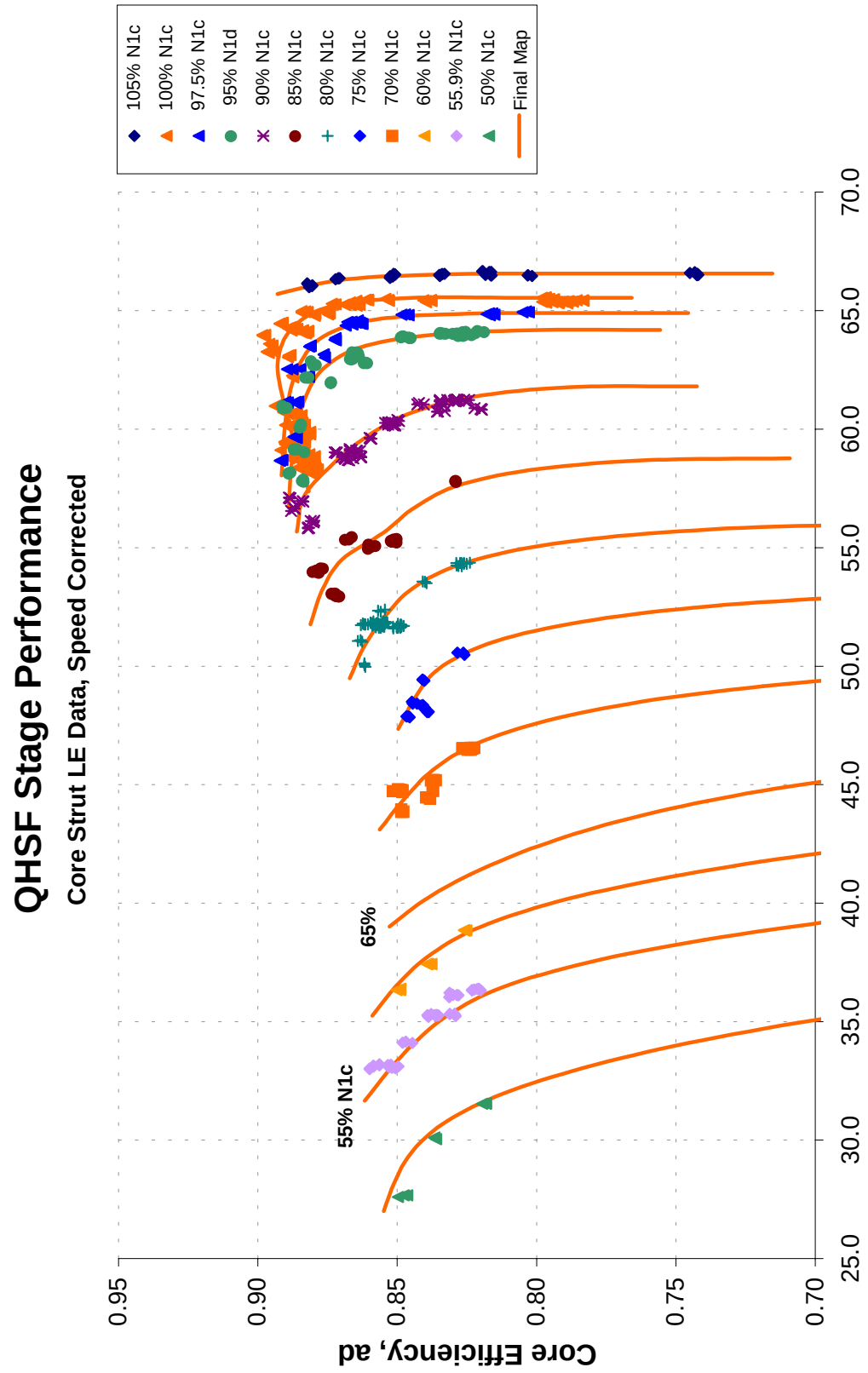

Figure 9-24. Core Performance Map (Wc Versus Eff) Overlayed on Level 2 Data.

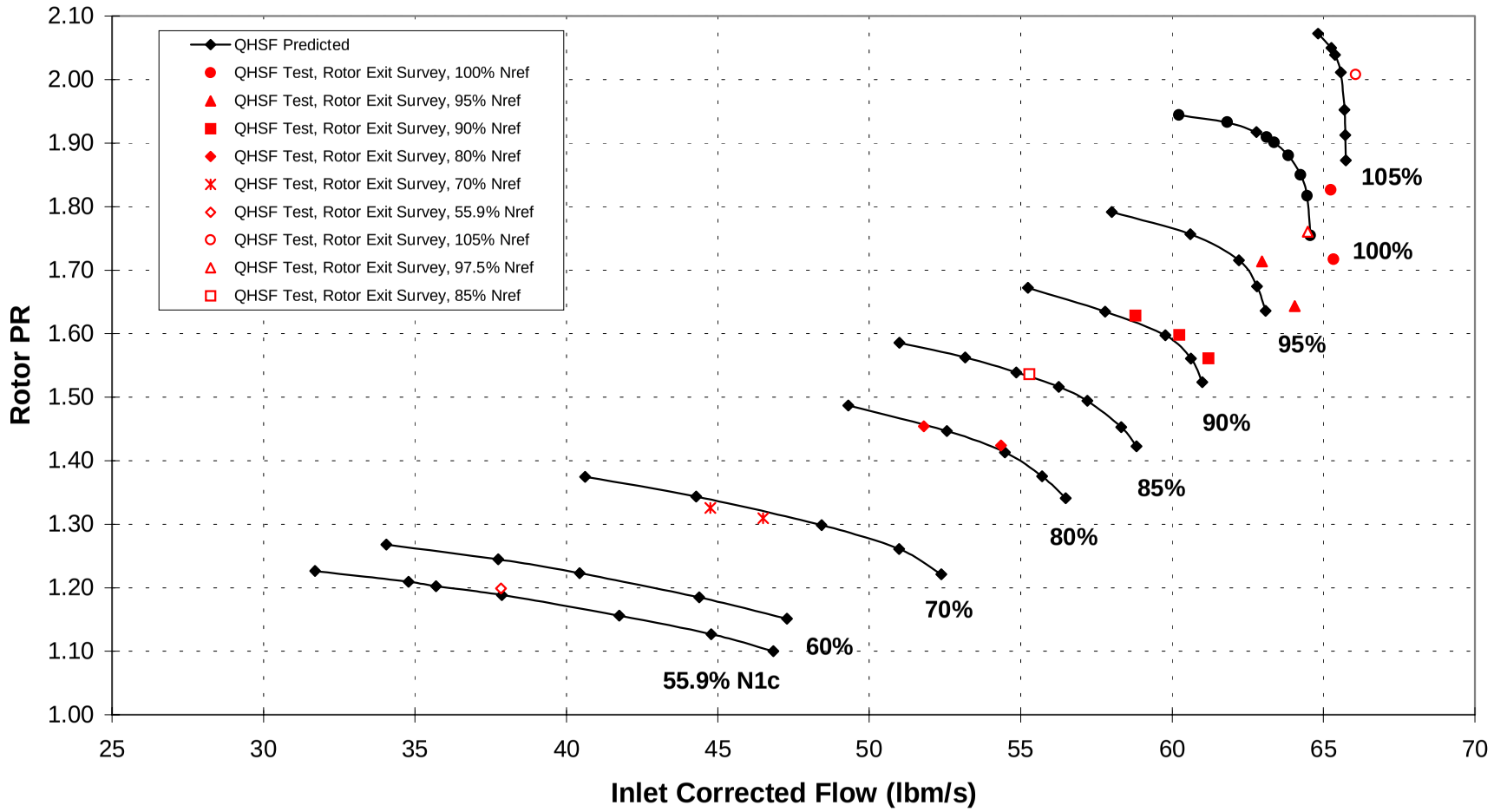

Figure 9-25. QHSF Predicted Map (Wc Versus PR) with Rotor Exit Survey Data.

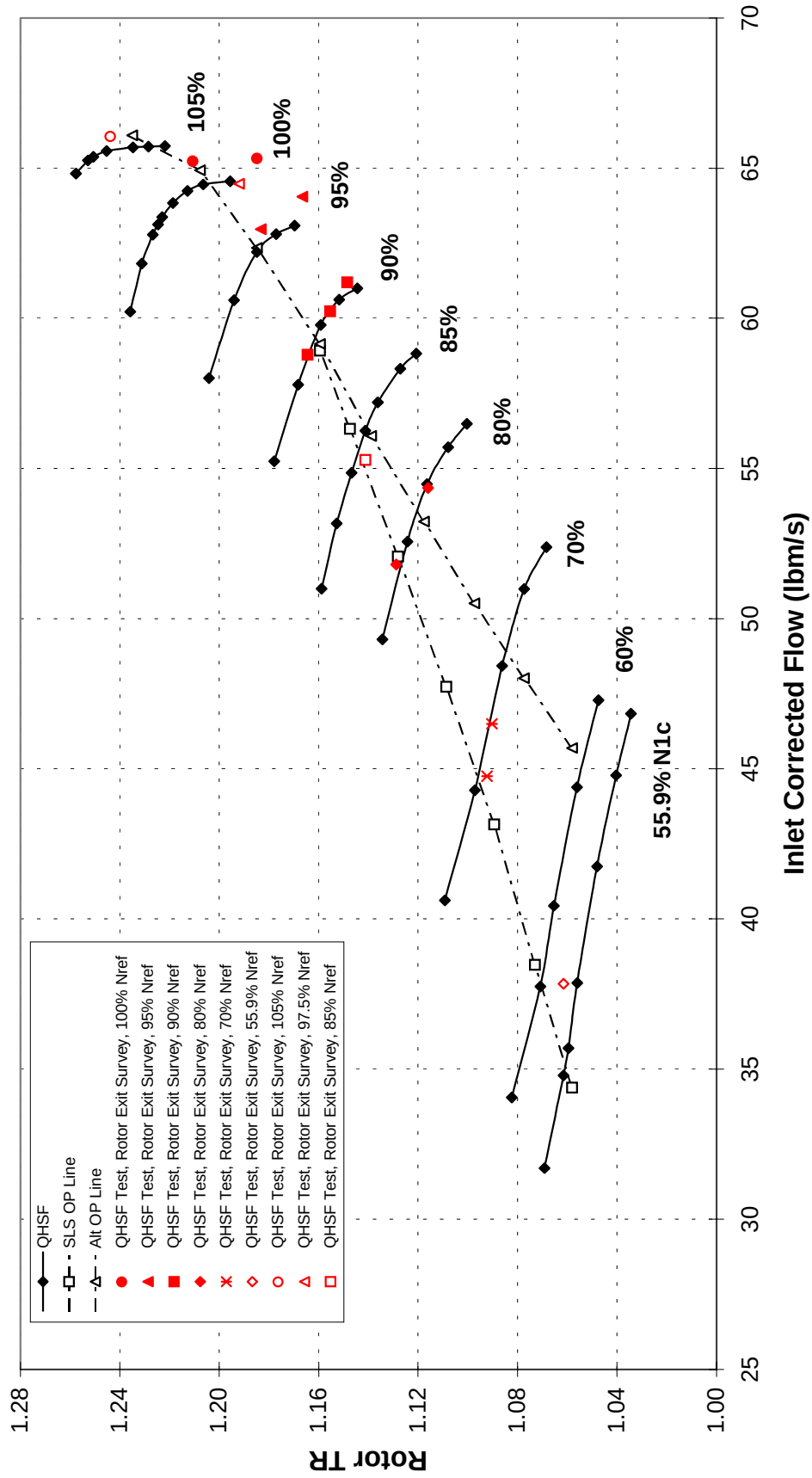

Figure 9-26. QHSF Predicted Map (Wc Versus TR) with Rotor Exit Survey Data.

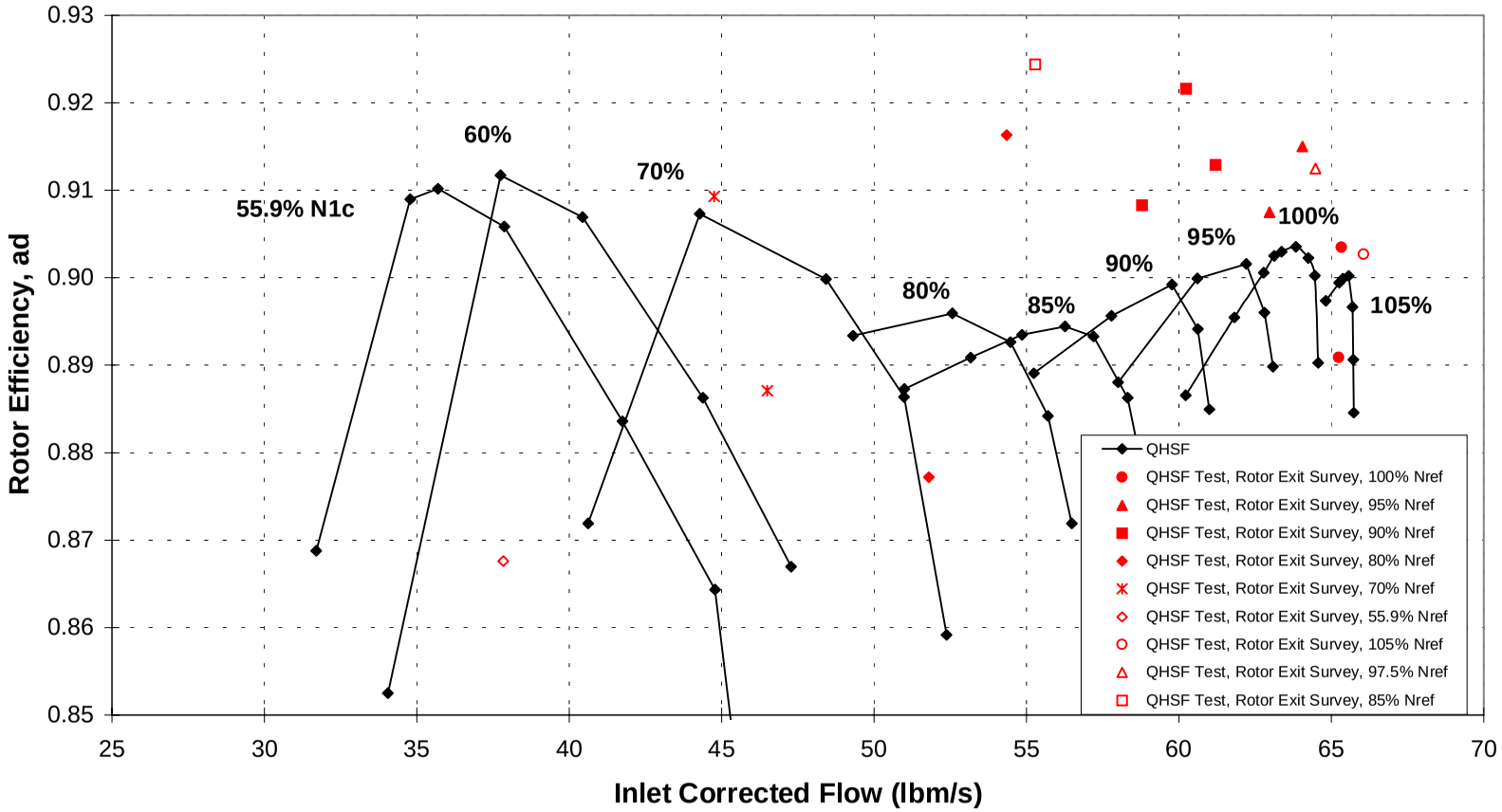

Figure 9-27. QHSF Predicted Map (Wc Versus Eff) with Rotor Exit Survey Data.

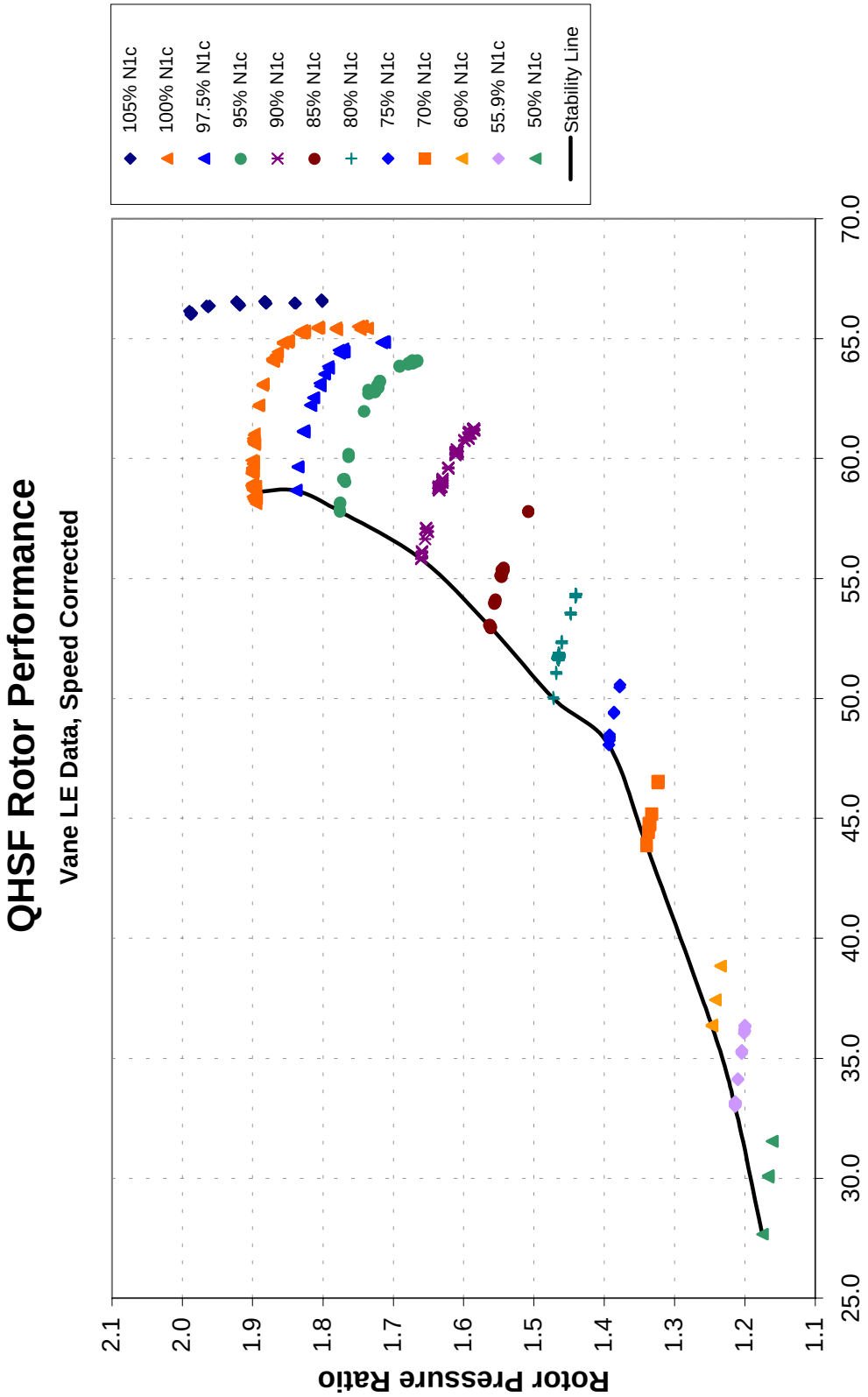

Figure 9-28. QHSF Tested Map (Wc Versus PR) Based on Vane LE Instrumentation.

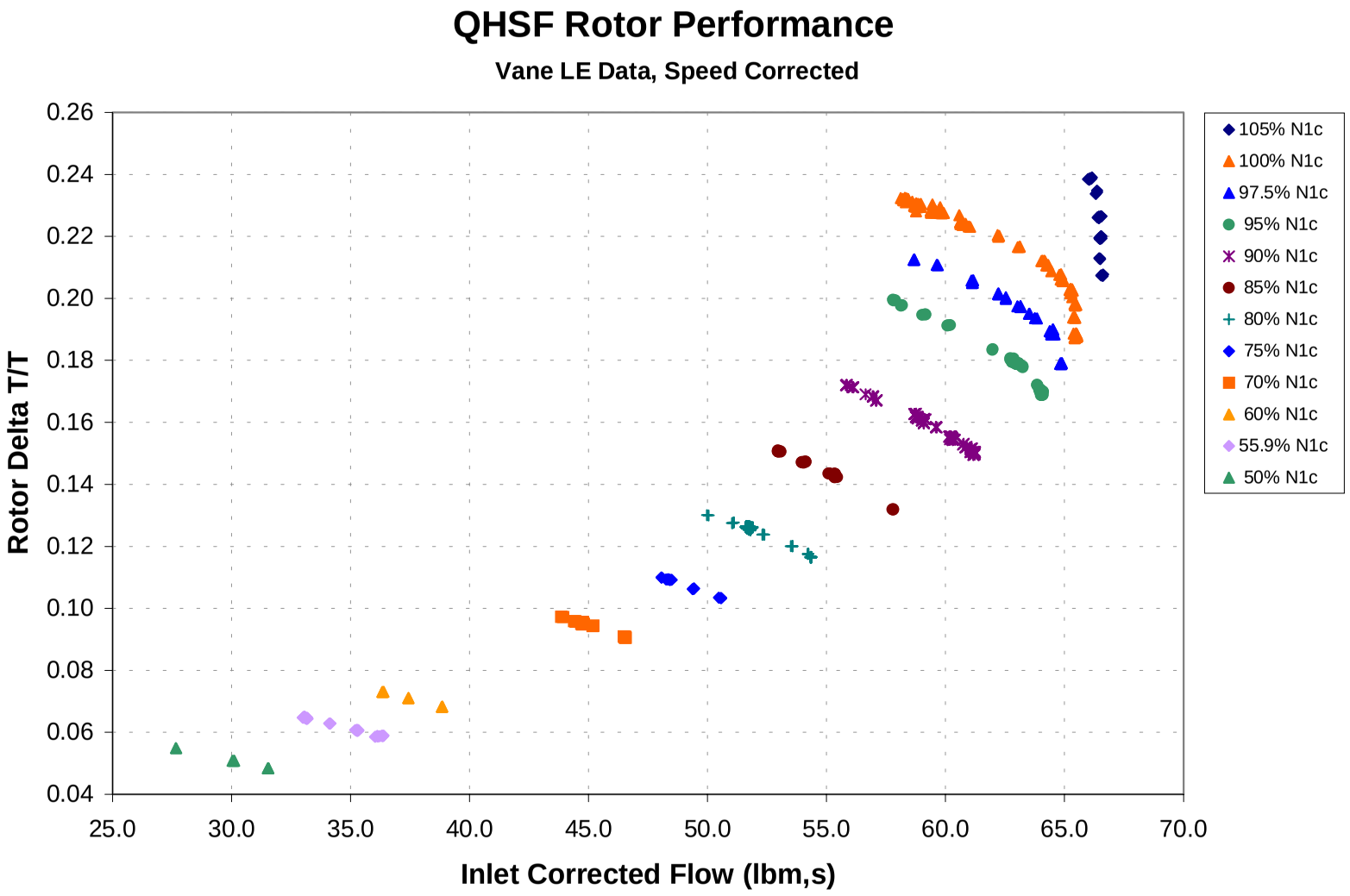

Figure 9-29. QHSF Tested Map (Wc Versus ΔT/T) Based on Vane LE Instrumentation.

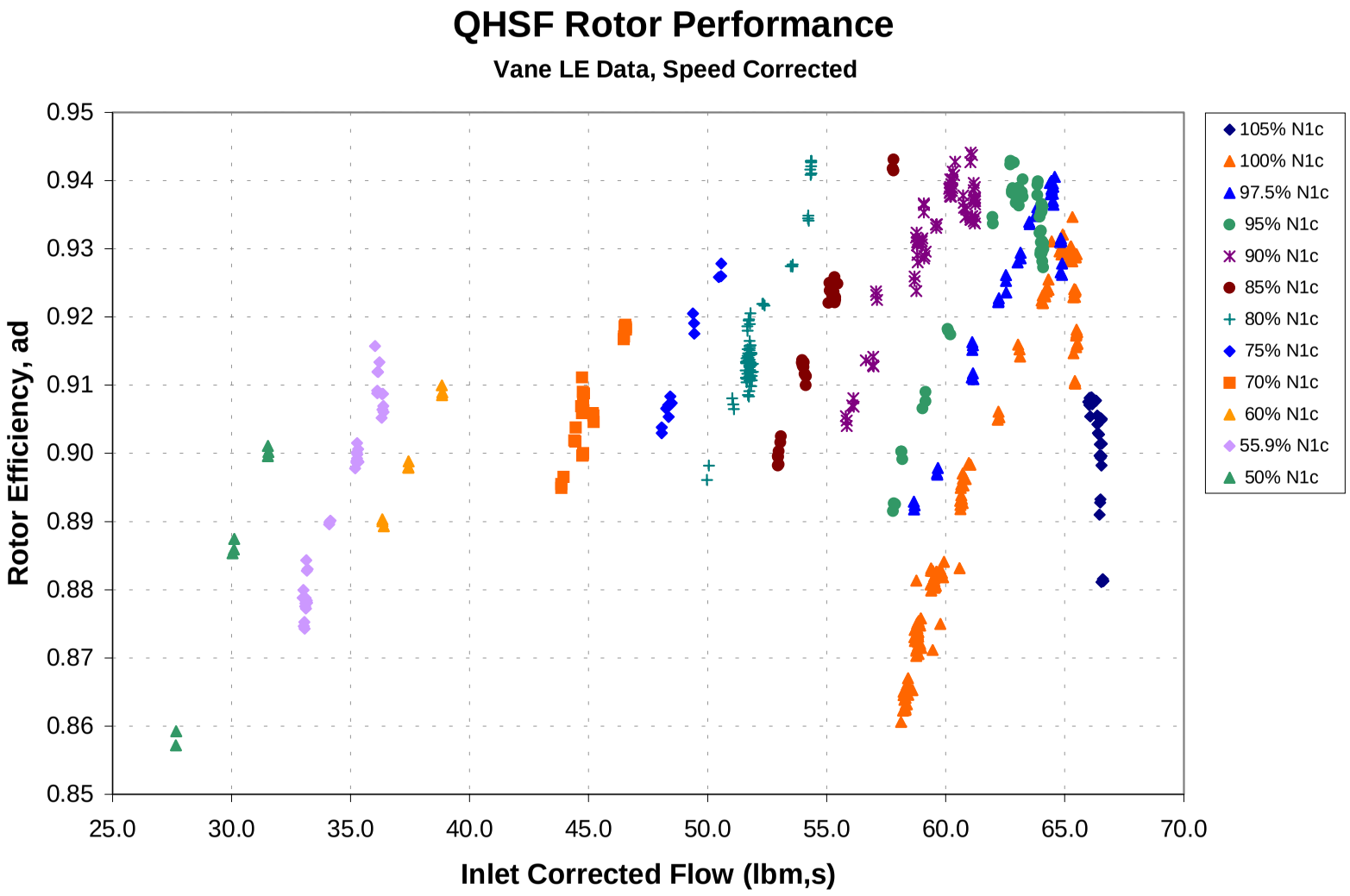

Figure 9-30. QHSF Tested Map (Wc Versus Eff) Based on Vane LE Instrumentation.

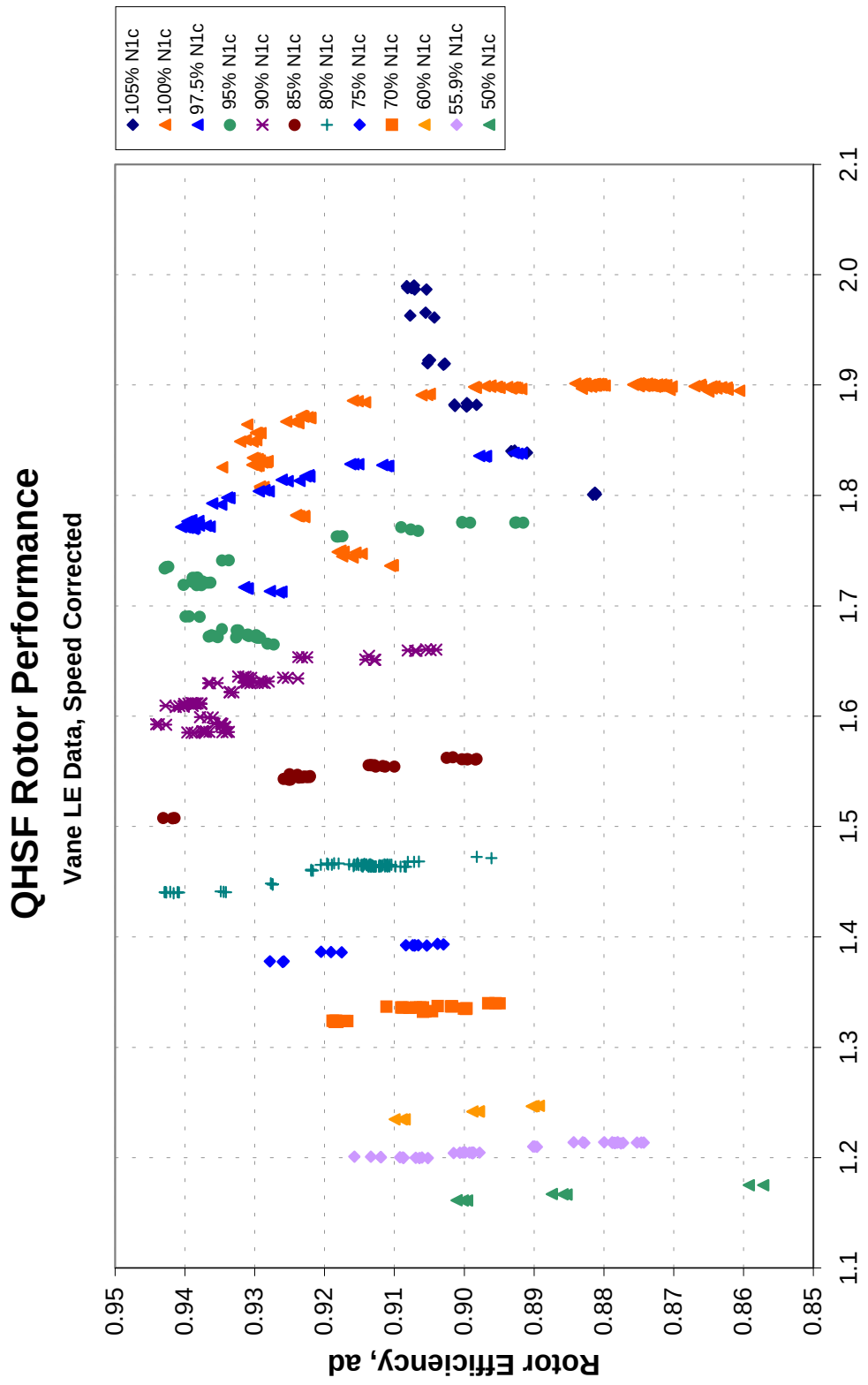

Figure 9-31. QHSF Tested Map (PR Versus Eff) Based on Vane LE Instrumentation.

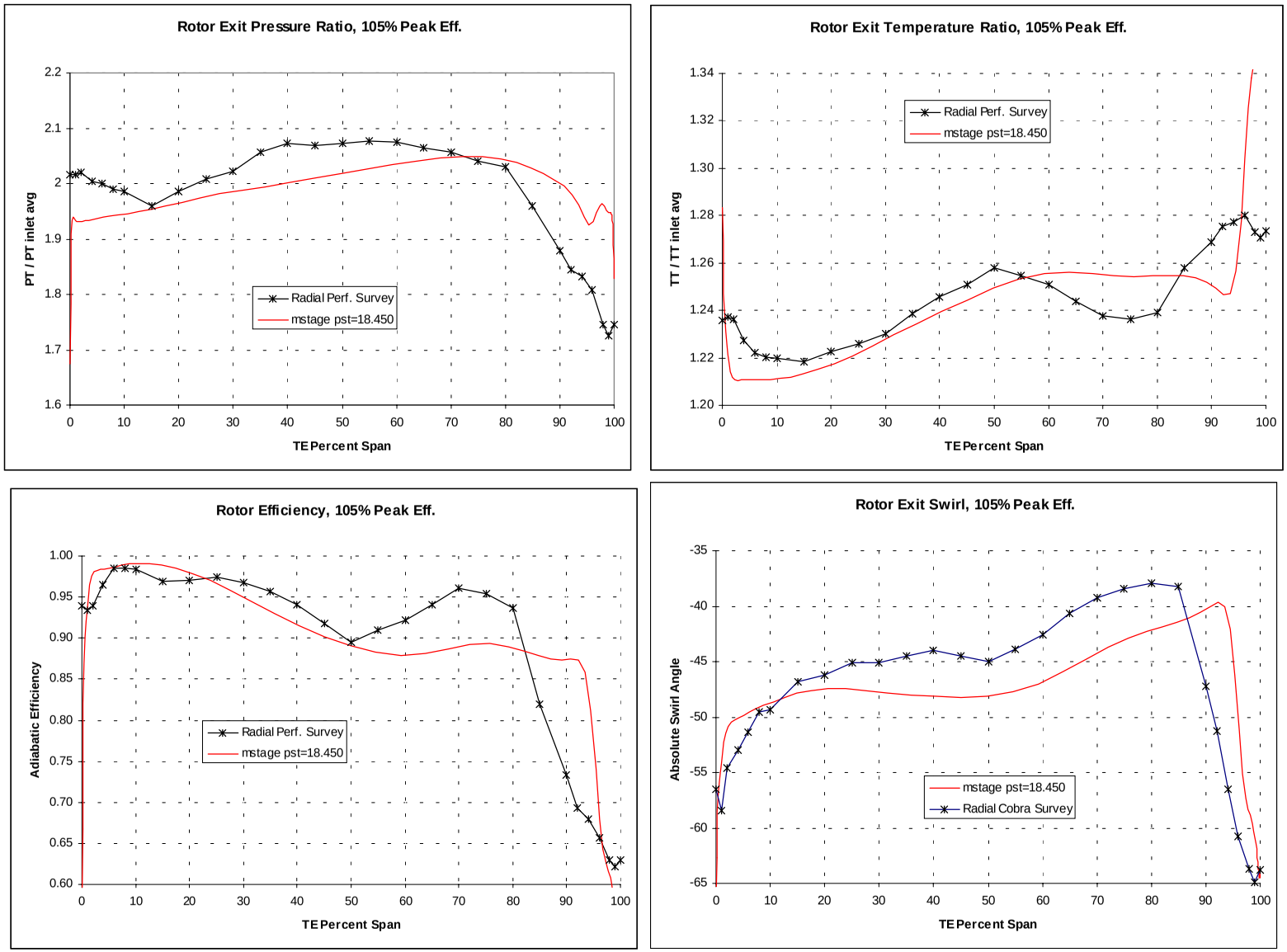

Figure 9-32. Rotor Exit Survey Data Compared to DAWES Analysis at 105% N1c Near Peak Efficiency.

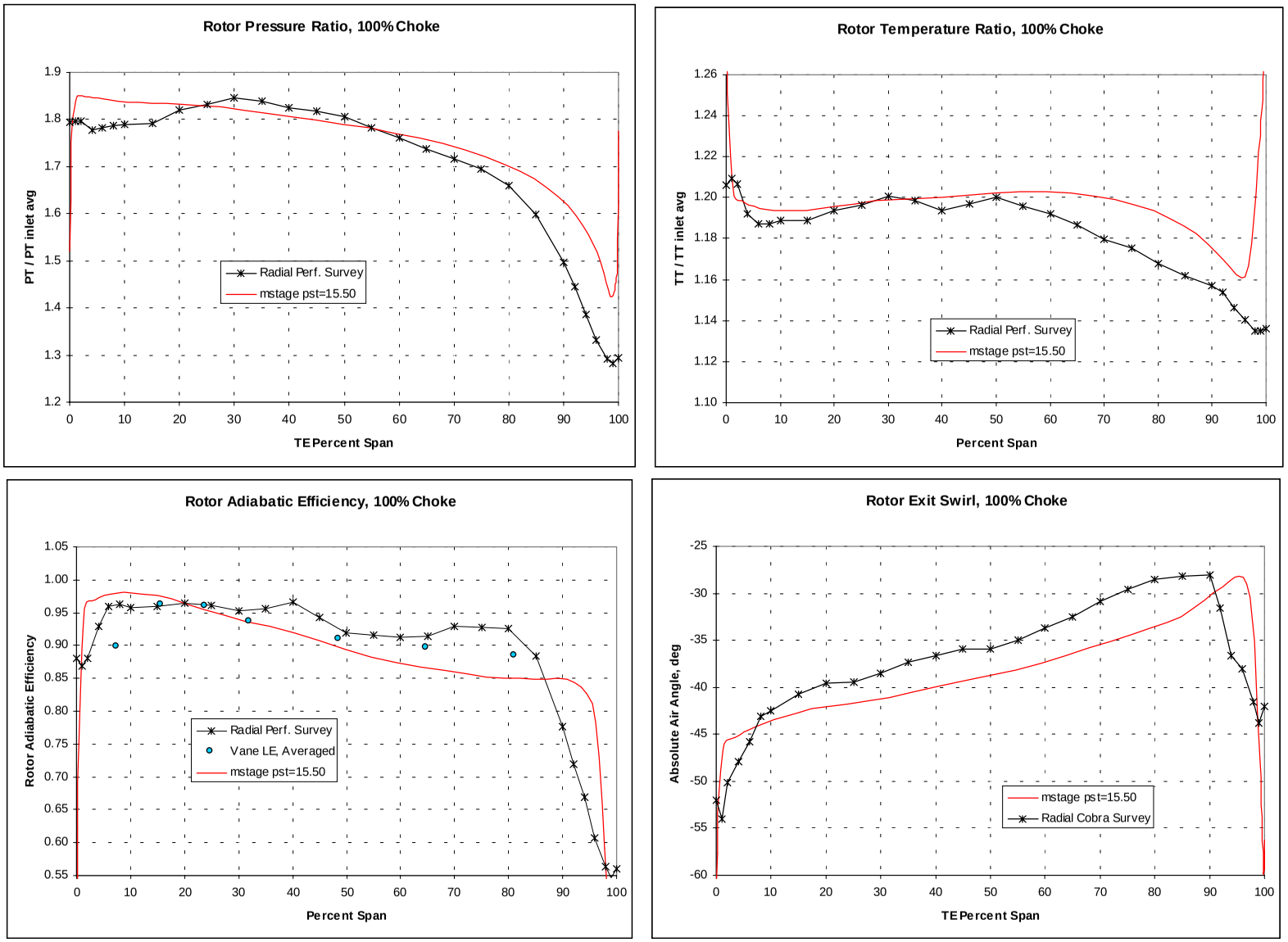

Figure 9-33. Rotor Exit Survey Data Compared to DAWES Analysis at 100% N1c Choke.

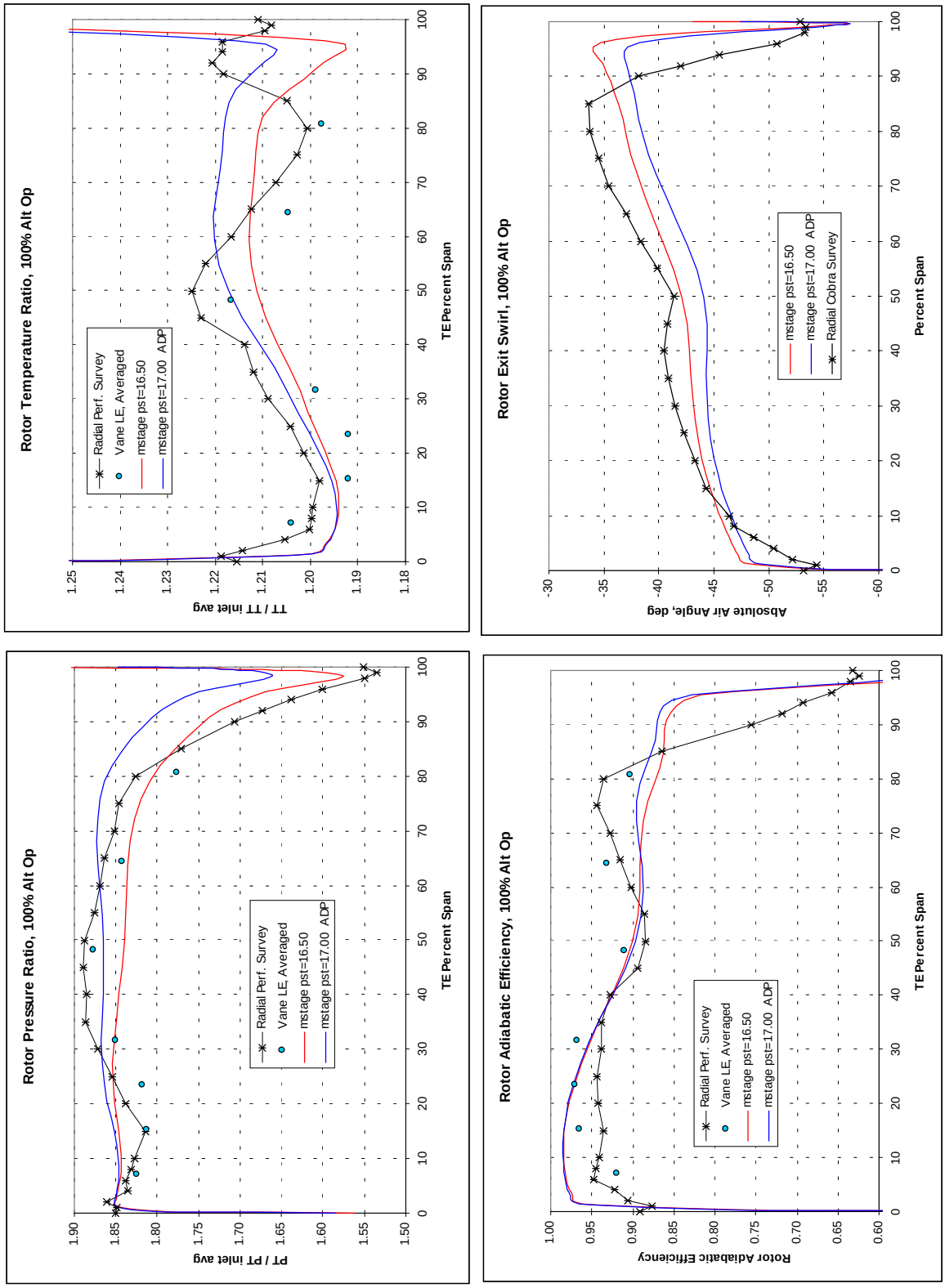

Figure 9-34. Rotor Exit Survey Data Compared to DAWES Analysis at 100% N1c Near Aero Design Point.

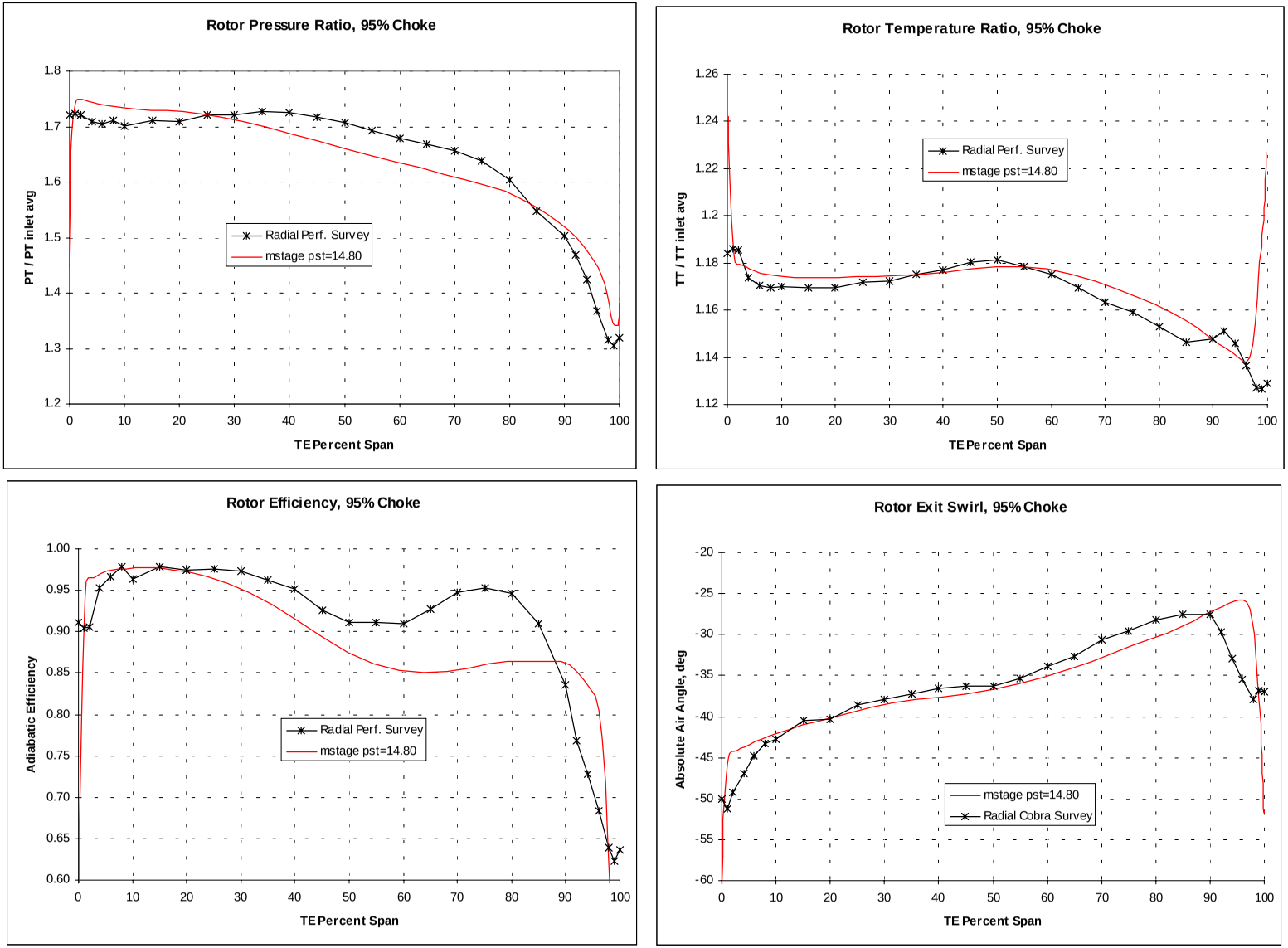

Figure 9-35. Rotor Exit Survey Data Compared to DAWES Analysis at 95% N1c Choke.

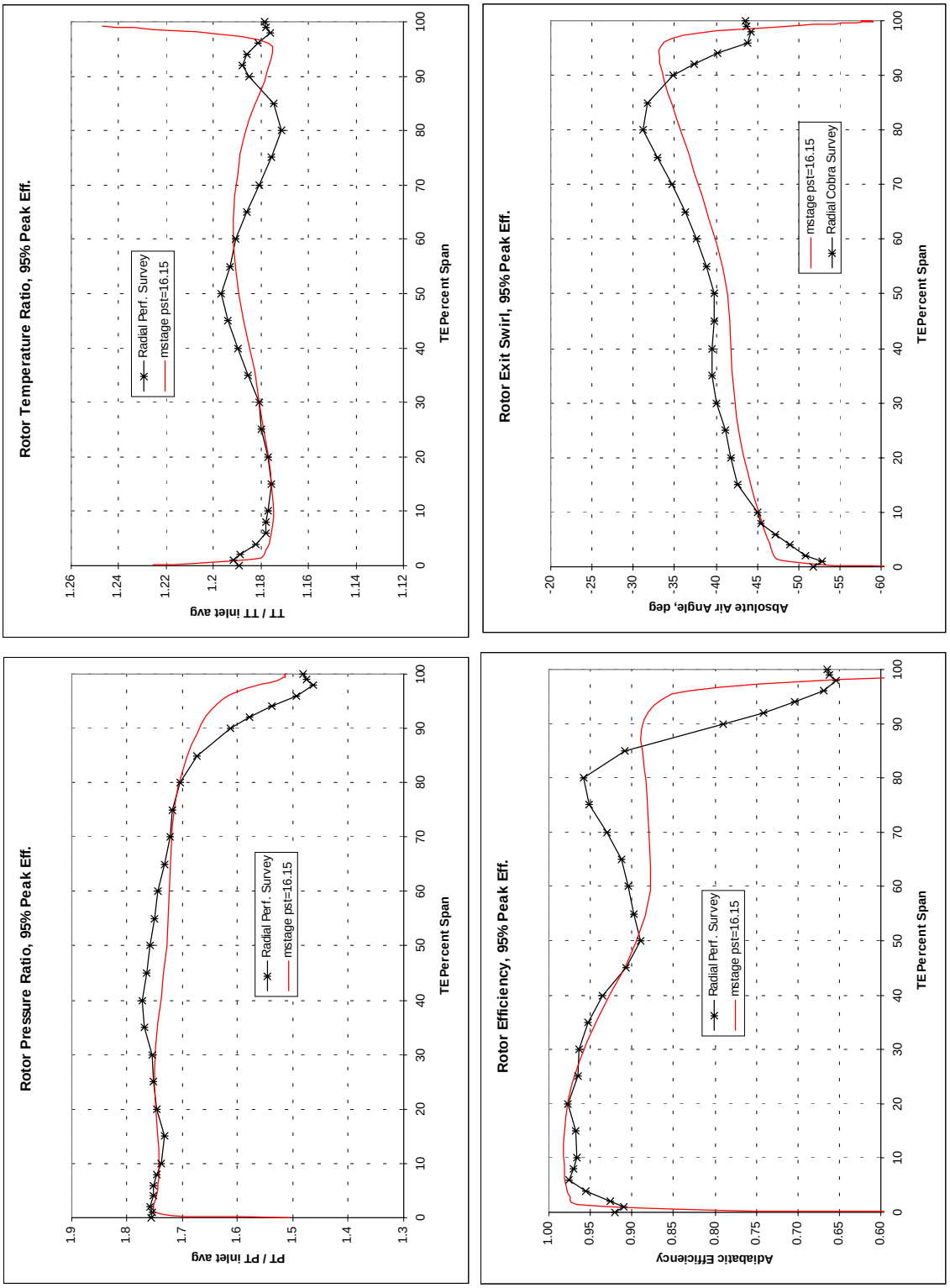

Figure 9-36. Rotor Exit Survey Data Compared to DAWES Analysis at 95% N1c Near Peak Efficiency.

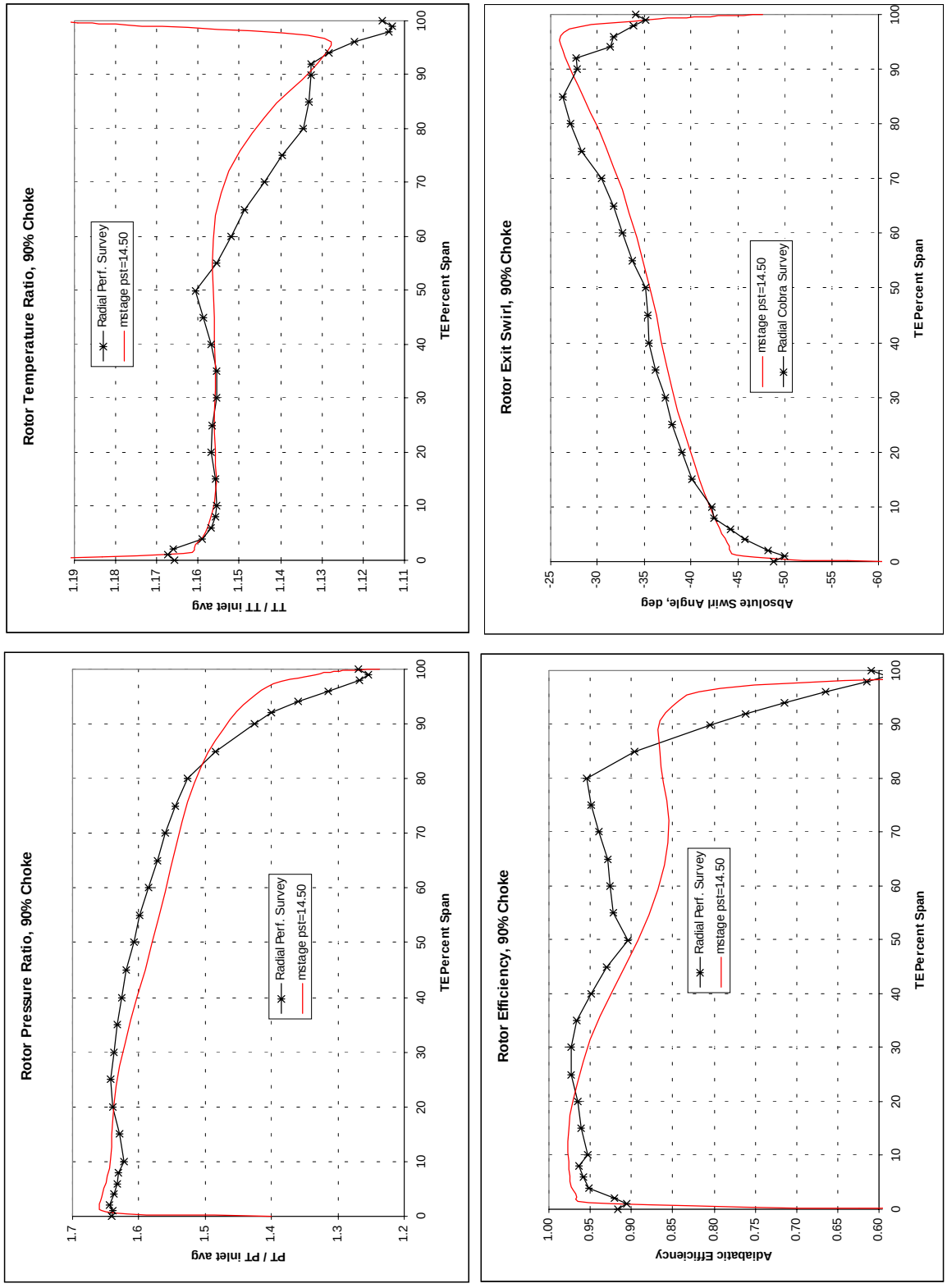

Figure 9-37. Rotor Exit Survey Data Compared to DAWES Analysis at 90% N1c Choke.

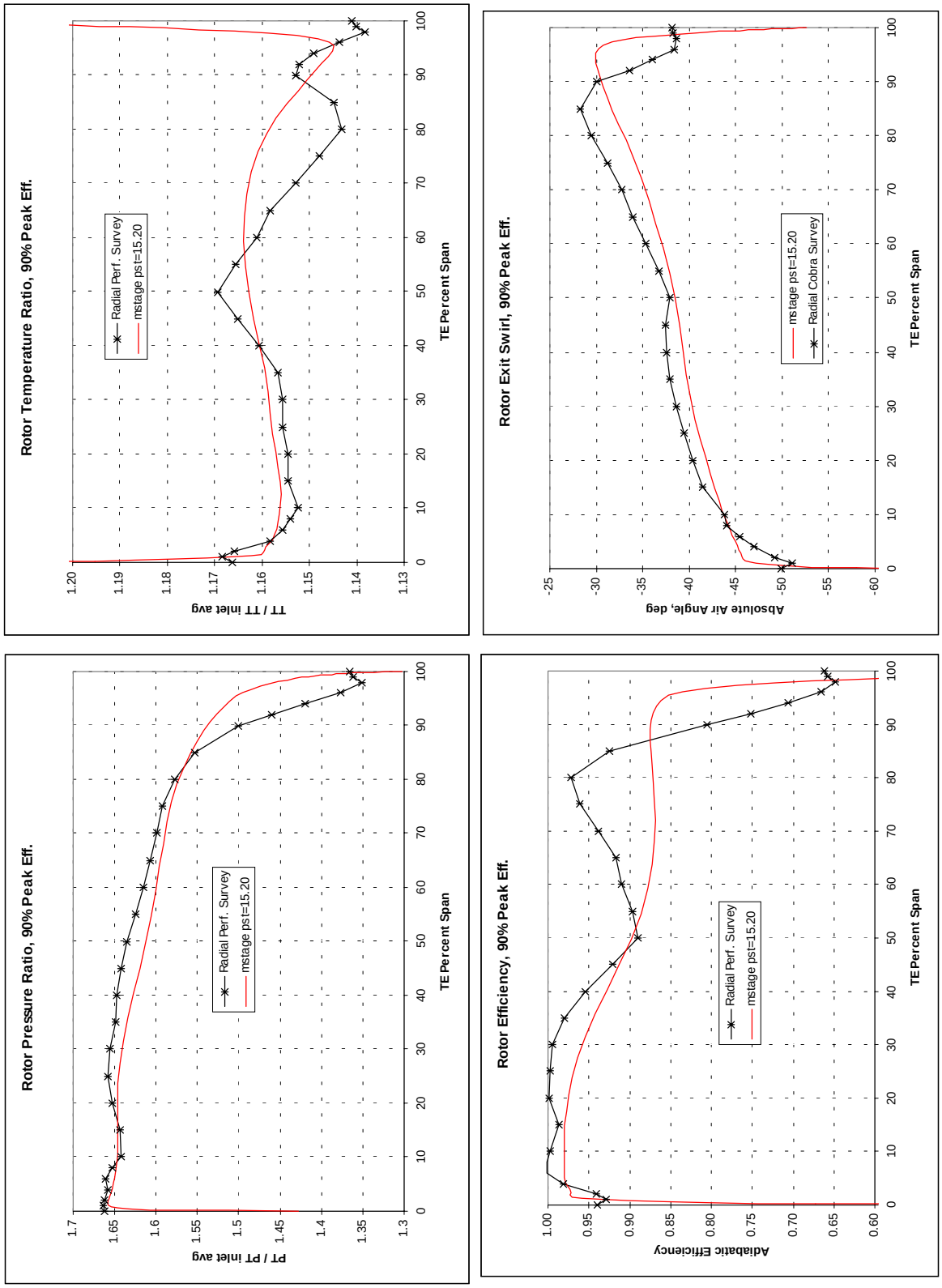

Figure 9-38. Rotor Exit Survey Data Compared to DAWES Analysis at 90% N1c Near Peak Efficiency.

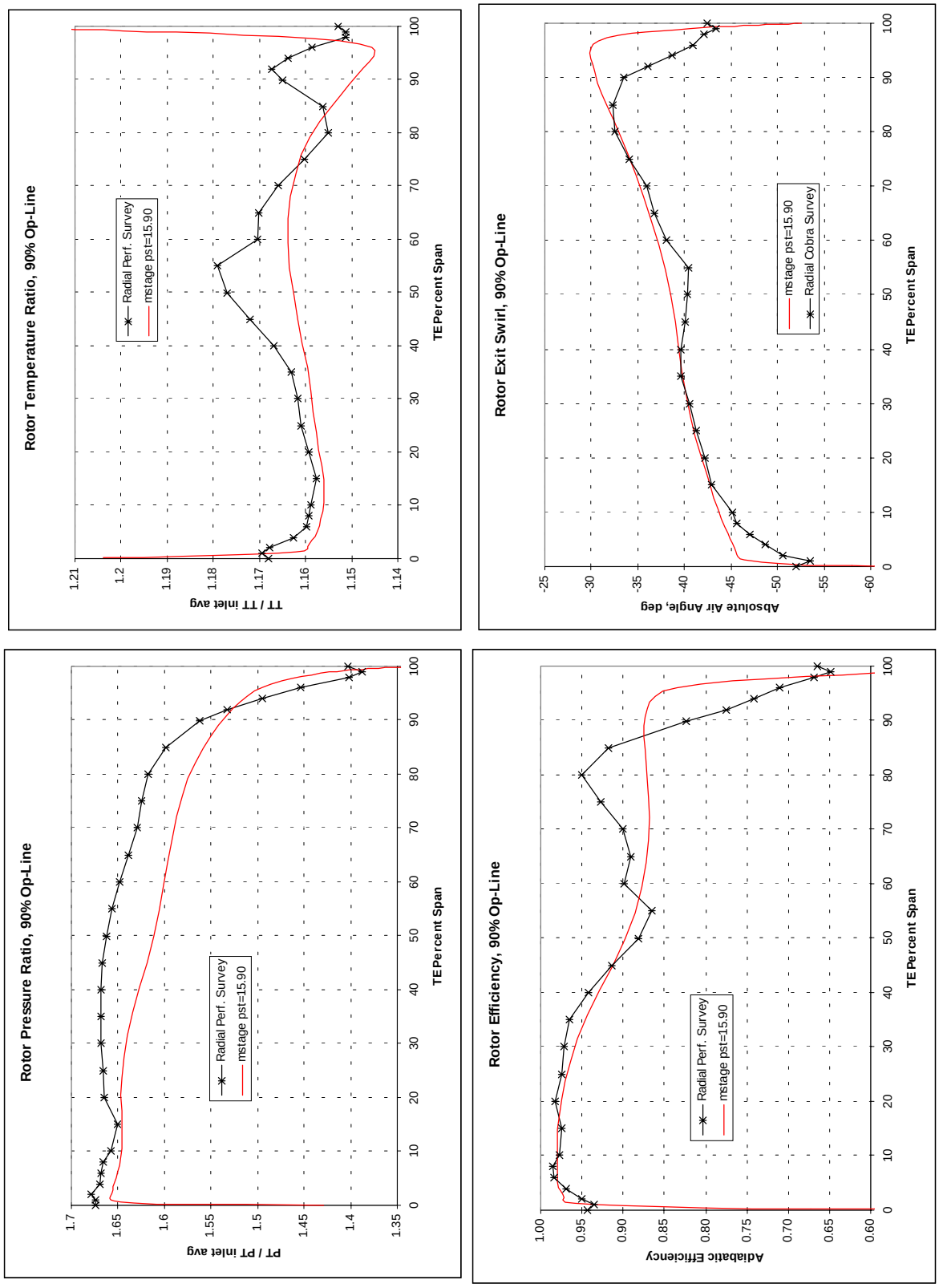

Figure 9-39. Rotor Exit Survey Data Compared to DAWES Analysis at 90% N1c SLS Operating Line.

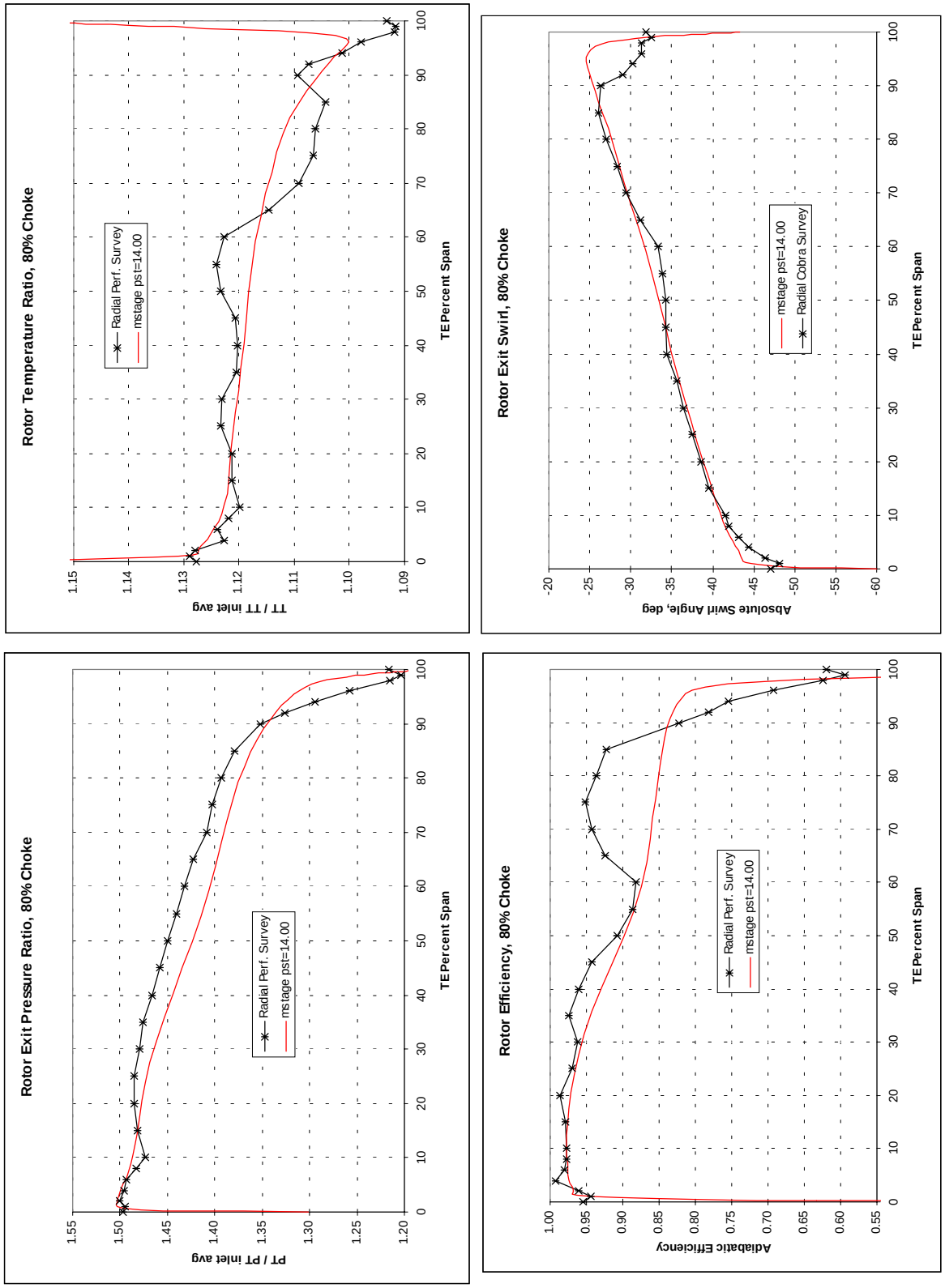

Figure 9-40. Rotor Exit Survey Data Compared to DAWES Analysis at 80% N1c SLS Operating Line.

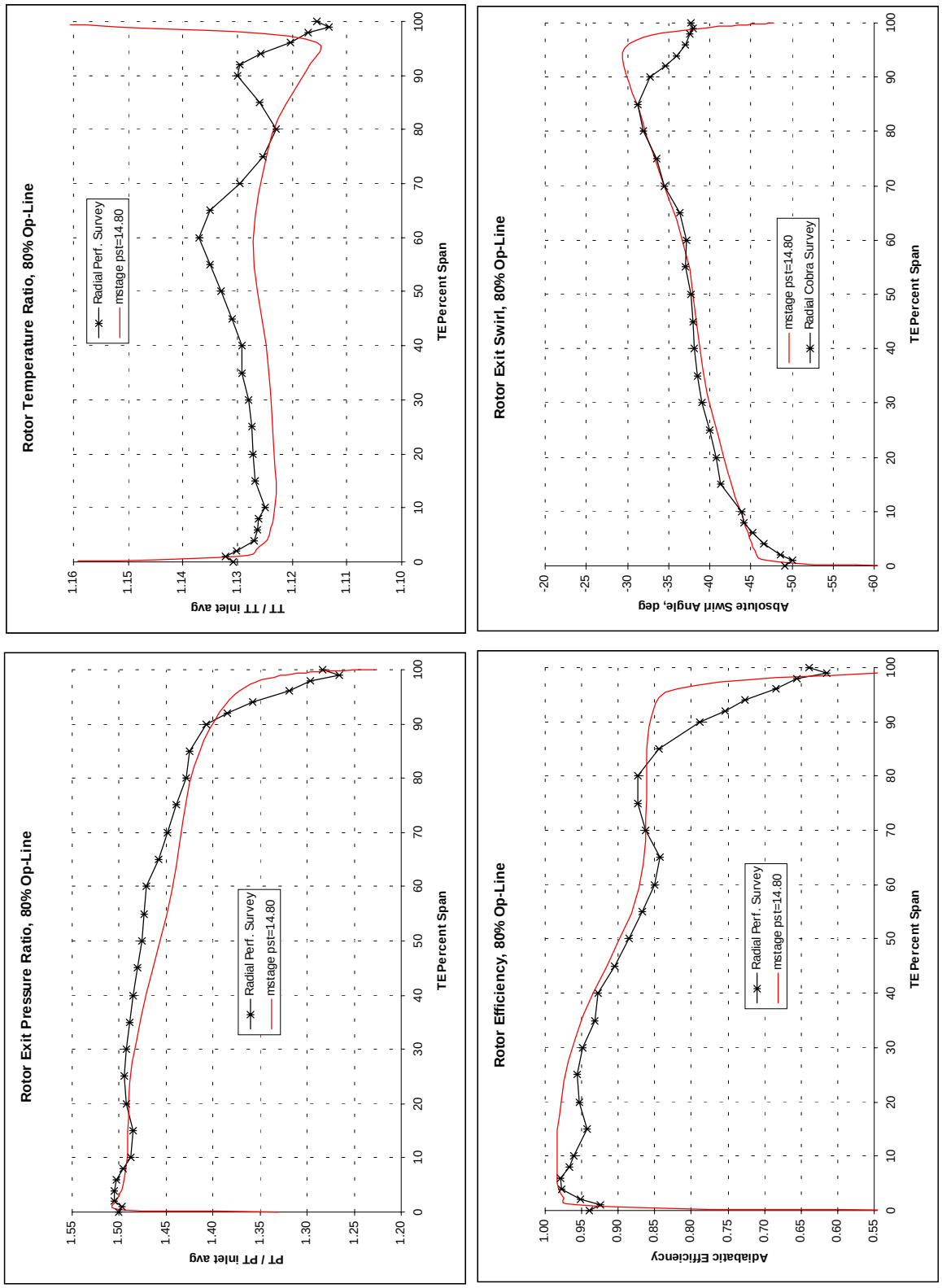

Figure 9-41. Rotor Exit Survey Data Compared to DAWES Analysis at 80% N1c SLS Operating Line.

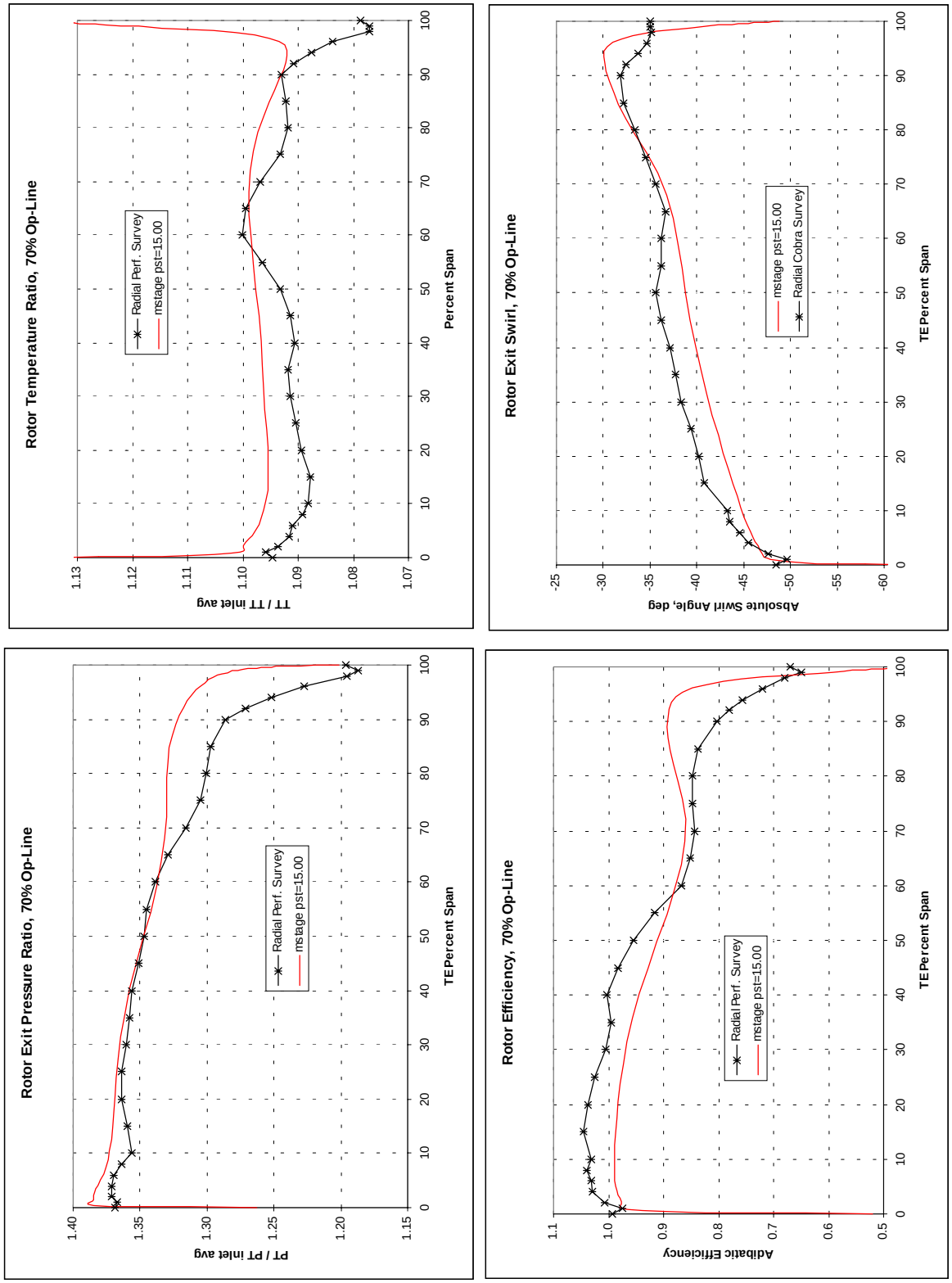

Figure 9-42. Rotor Exit Survey Data Compared to DAWES Analysis at 70% N1c SLS Operating Line.

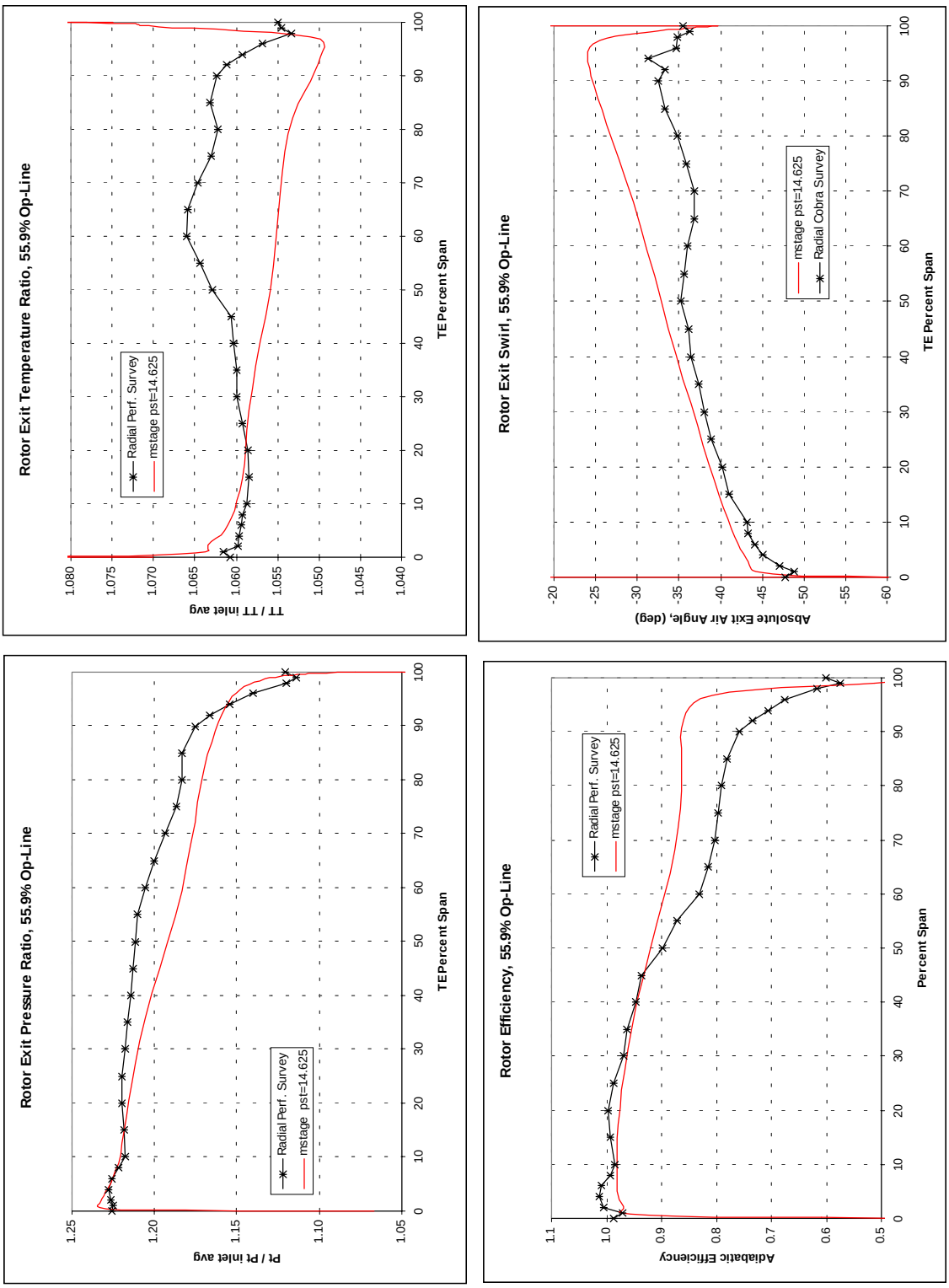

Figure 9-43. Rotor Exit Survey Data Compared to DAWES Analysis at 55.9% N1c SLS Operating Line.

Figures 9-44 through 9-46 show the rotor performance maps compared to the DAWES analyses. Note that at 100 percent N1c there are two predicted lines; the higher-pressure ratio line is based on the use of restart files in the analyses. It was believed during the design that this was acceptable; however, the test data tends to agree more with the analyses that were completed without restart files. The vane leading edge data was adjusted to coincide with the survey data to produce the final rotor maps. However, each speed line was not scaled separately, but the map as a whole was scaled based on all the survey data. This scaling provided smooth maps, but left some question as to the correct level of peak efficiency. Again, this "final rotor map" is a best-fit map to the measured data. For example, at 100 percent N1c near the operating line, survey results produced an efficiency of 0.8910, yet for the same flow, the scaled map estimates an efficiency of 0.9100.

Figures 9-47 through 9-51 show the AXCAPS (mean streamline) data match model for the design point as compared to the AXCAPS model of the design intent. These results were based on using Run numbers 130 for the rotor, 356 for the stator total pressure, and 359 for the stator exit air angle. Run number 356 was a repeat of Run number 130 when the stator x-y did not work; which, to save time, the rotor survey was not repeated. Run 359 was a repeat of this operating point but with a stator exit cobra probe installed. There was some very slight adjusting of the data at the end walls to allow the model to converge.

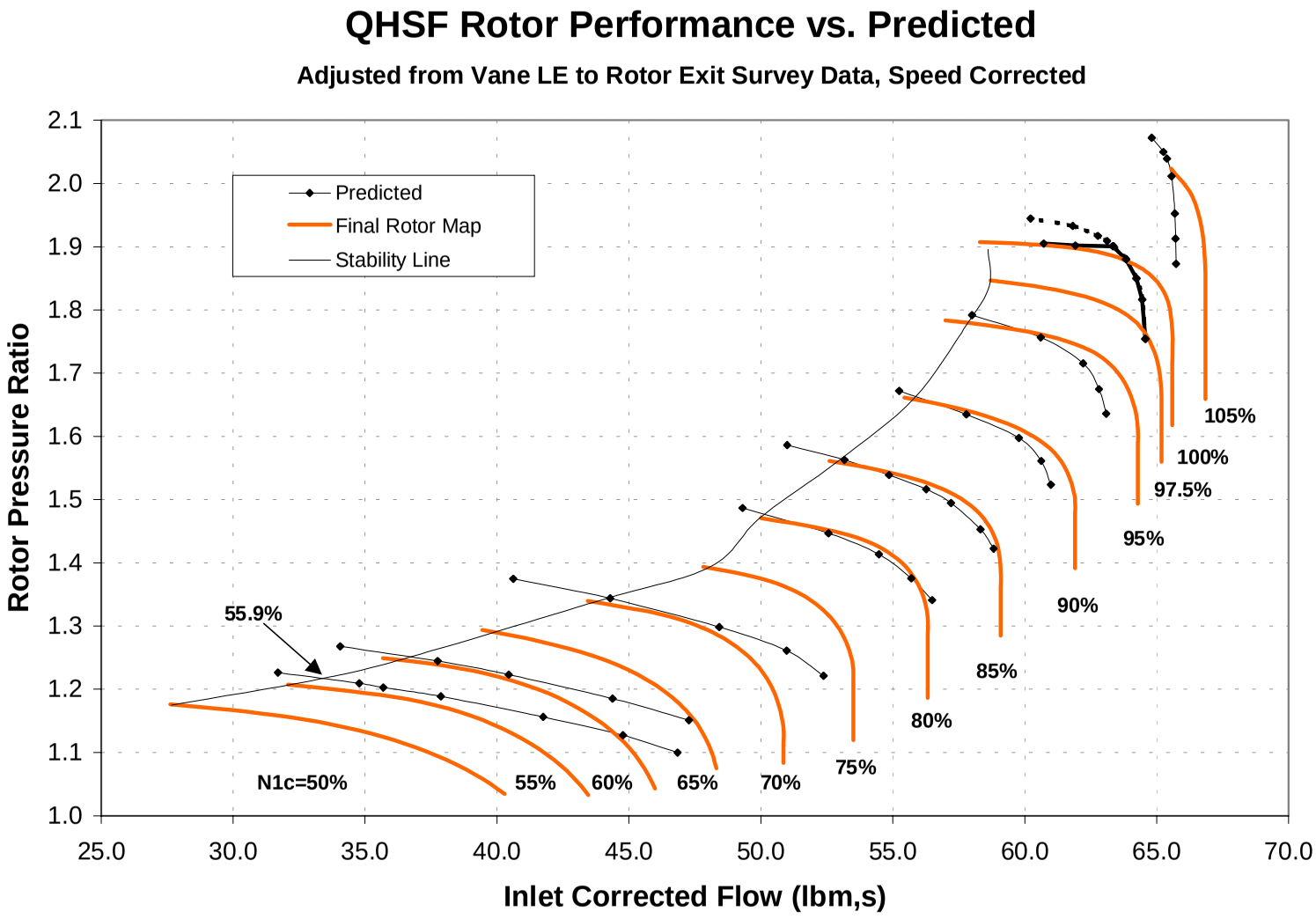

Figure 9-44. QHSF Rotor Map (Wc Versus PR) Compared to DAWES Analyses.

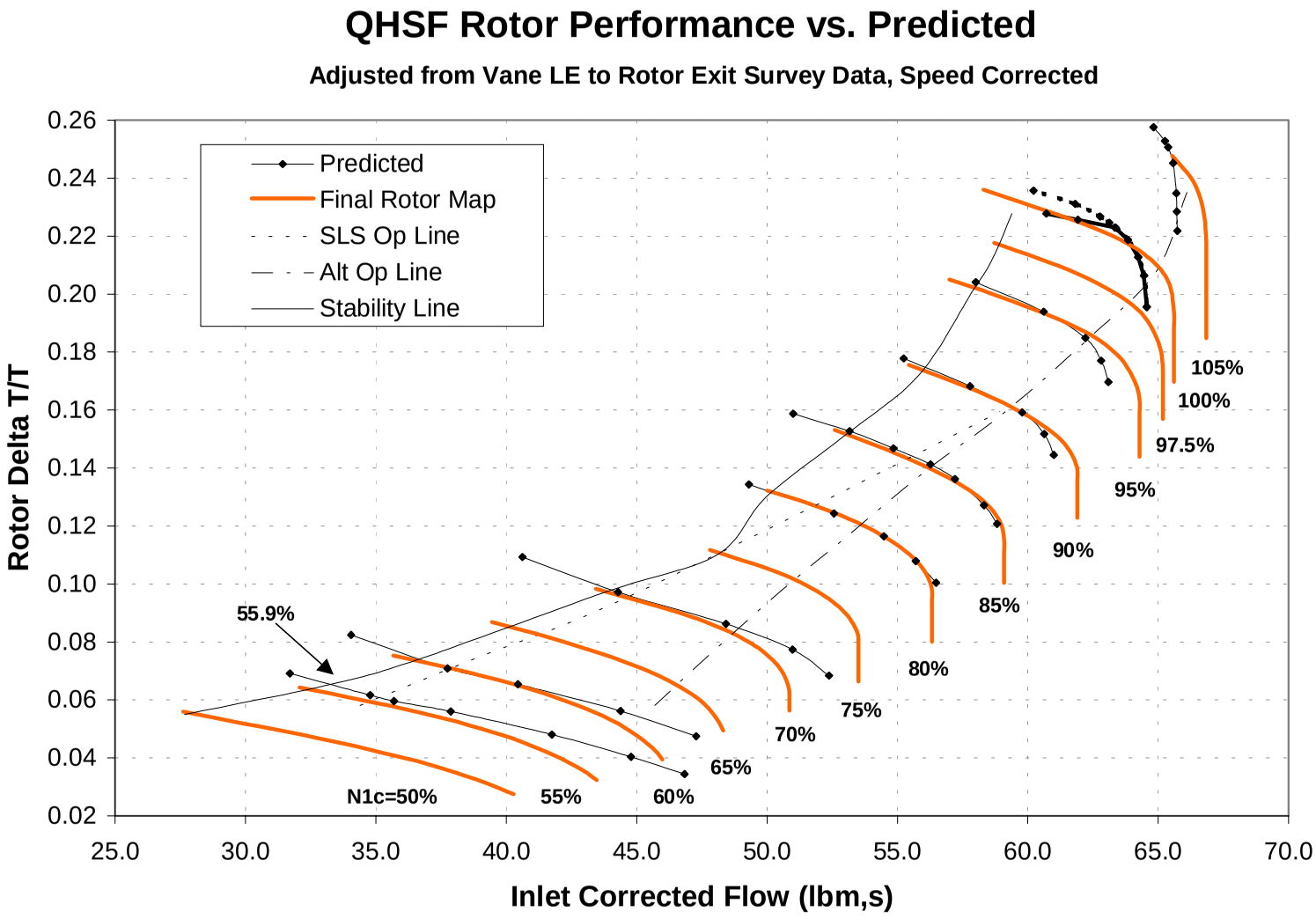

Figure 9-45. QHSF Rotor Map (Wc Versus ΔT/T) Compared to DAWES Analyses.

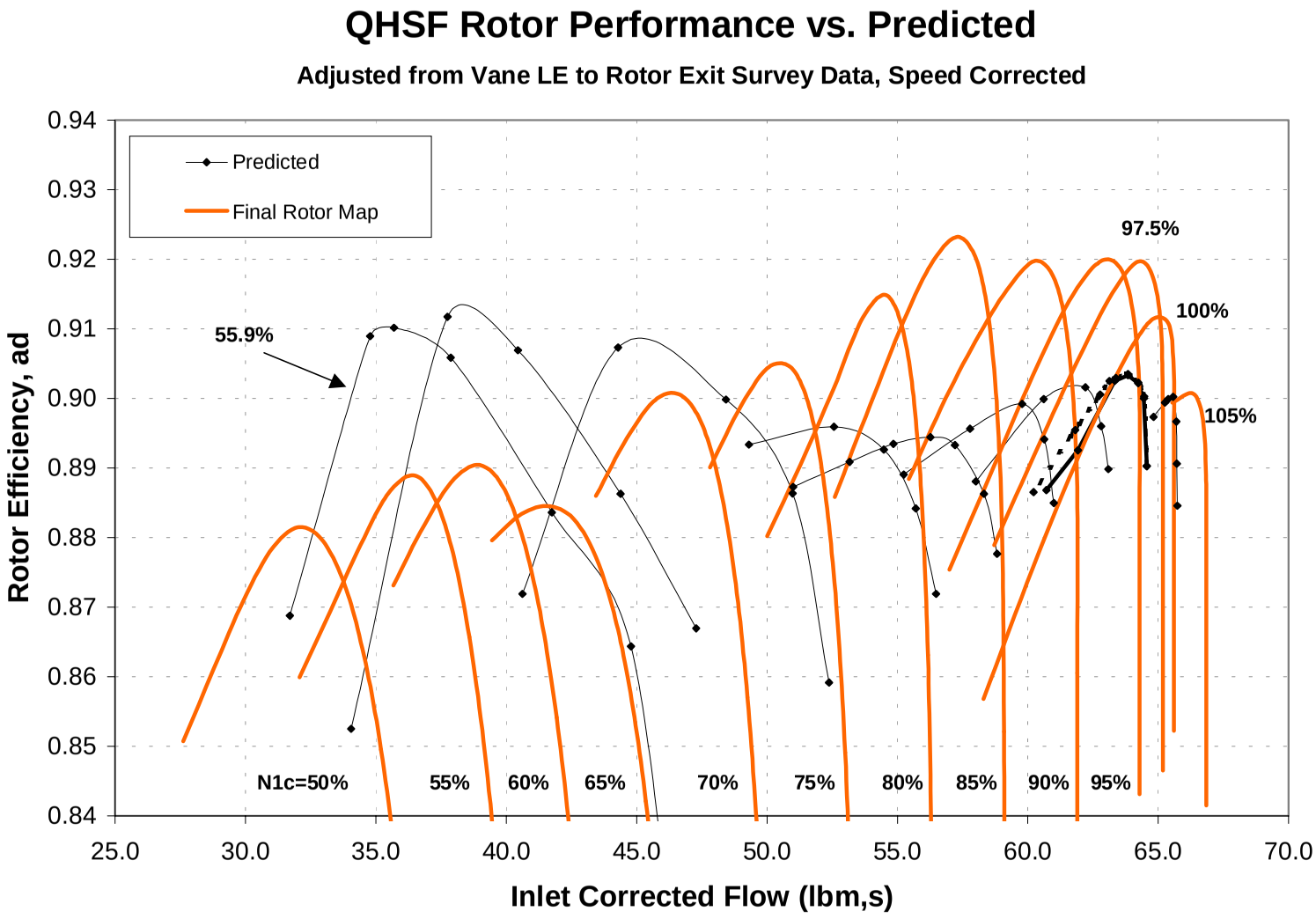

Figure 9-46. QHSF Rotor Map (Wc Versus Eff ad) Compared to DAWES Analyses.

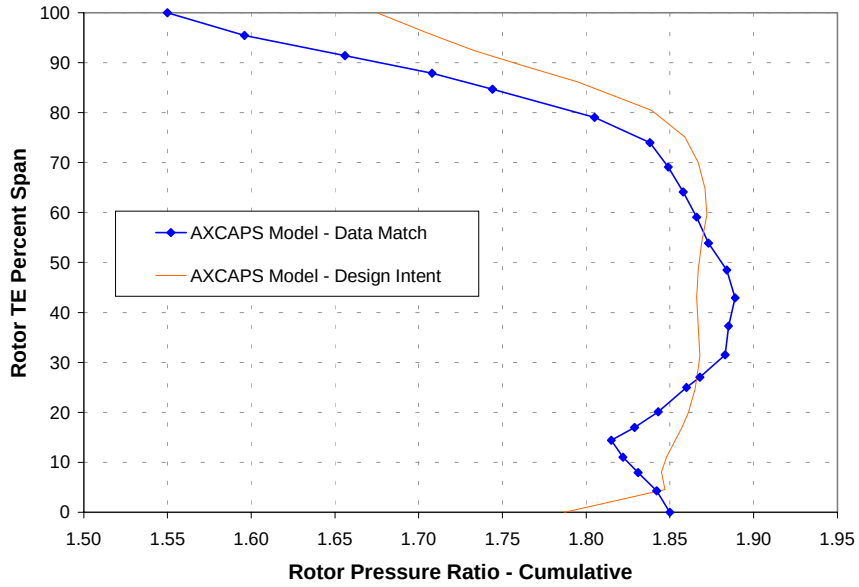

Figure 9-47. Mean Streamline Data Match Analysis for the Rotor Pressure Ratio Radial Distribution.

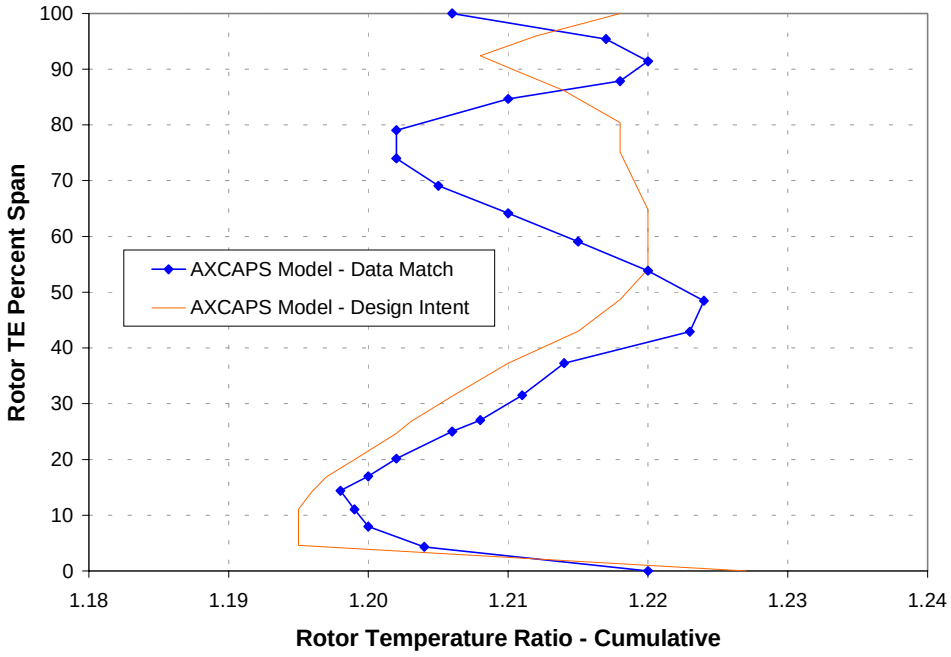

Figure 9-48. Mean Streamline Data Match Analysis for the Rotor Temperature Ratio Radial Distribution.

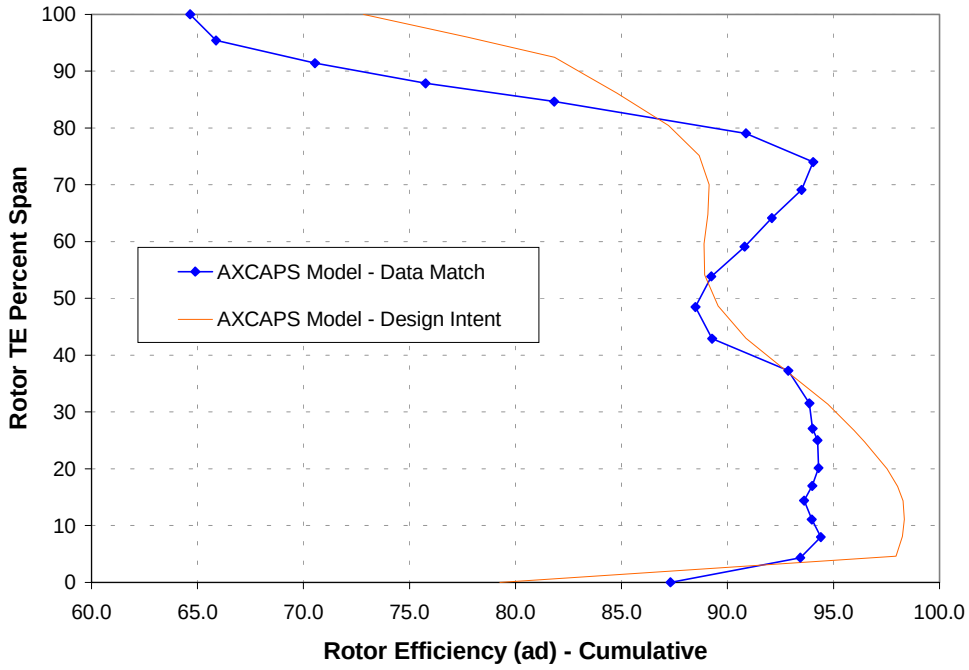

Figure 9-49. Mean Streamline Data Match Analysis for the Rotor Efficiency Radial Distribution.

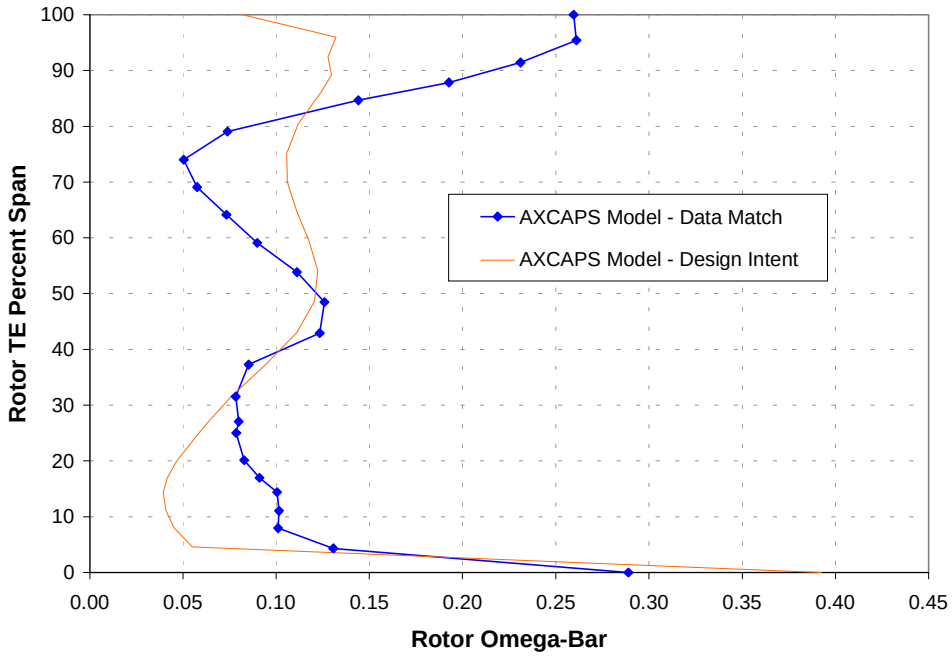

Figure 9-50. Mean Streamline Data Match Analysis for the Rotor Omega-Bar Radial Distribution.

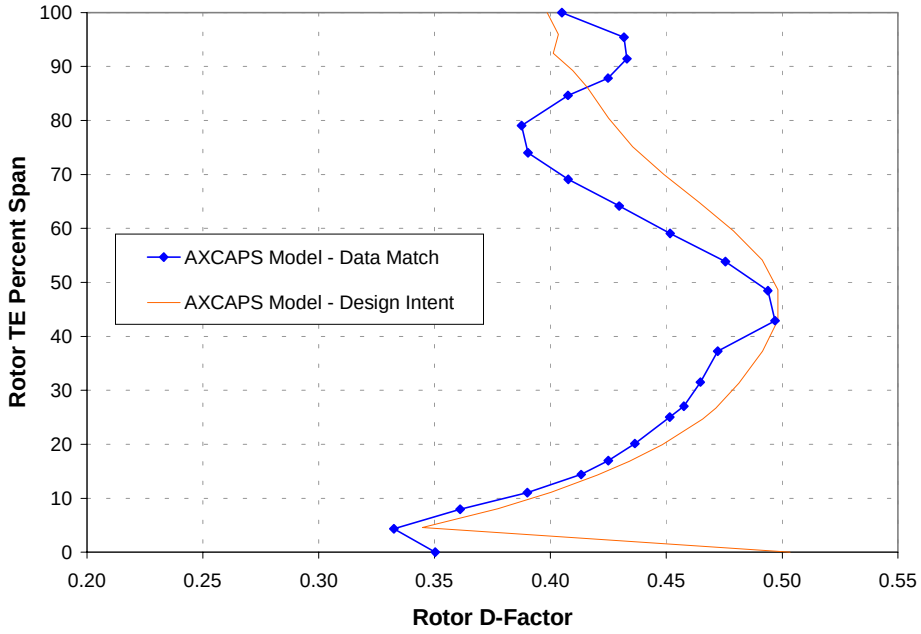

Figure 9-51. Mean Streamline Data Match Analysis for the Rotor D-Factor Radial Distribution.

9.3.5 Stator Performance

Results of the AXCAPS data match model for the stator are shown in Figures 9-53 through 9-58. Stator losses were higher than design intent, especially near the hub. The very high hub losses combined with the large exit flow angle measured by the calibrated, non-nulling cobra probe indicated that the airflow in the hub region may have been severely separated.

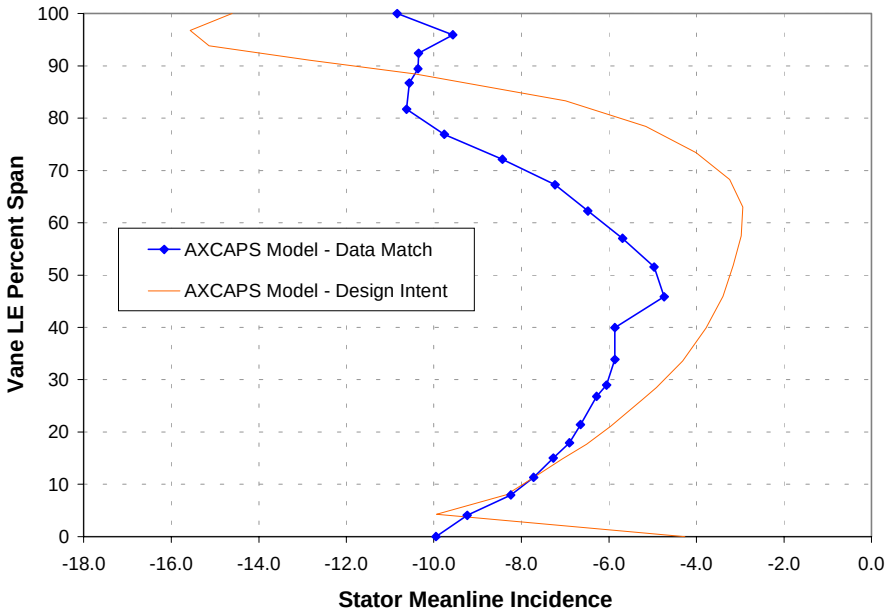

Figure 9-52. Mean Streamline Data Match Analysis for the Stator Mean Line Incidence Radial Distribution.

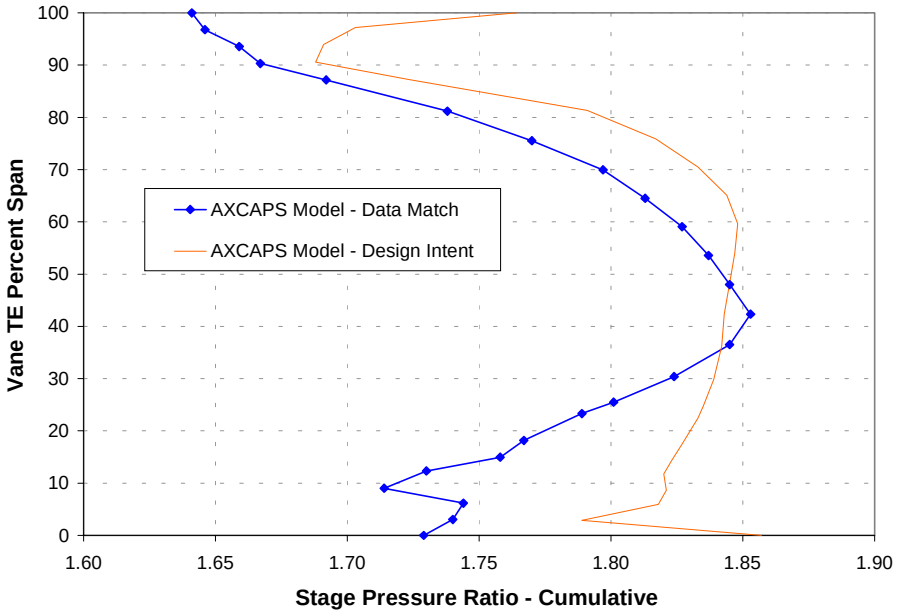

Figure 9-53. Mean Streamline Data Match Analysis for the Stage Pressure Ratio Radial Distribution.

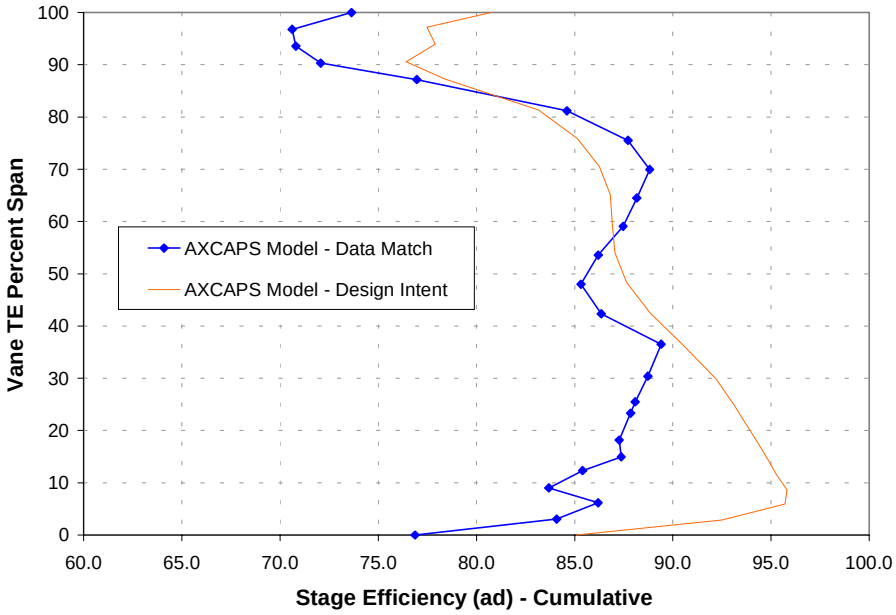

Figure 9-54. Mean Streamline Data Match Analysis for the Stage Efficiency Radial Distribution.

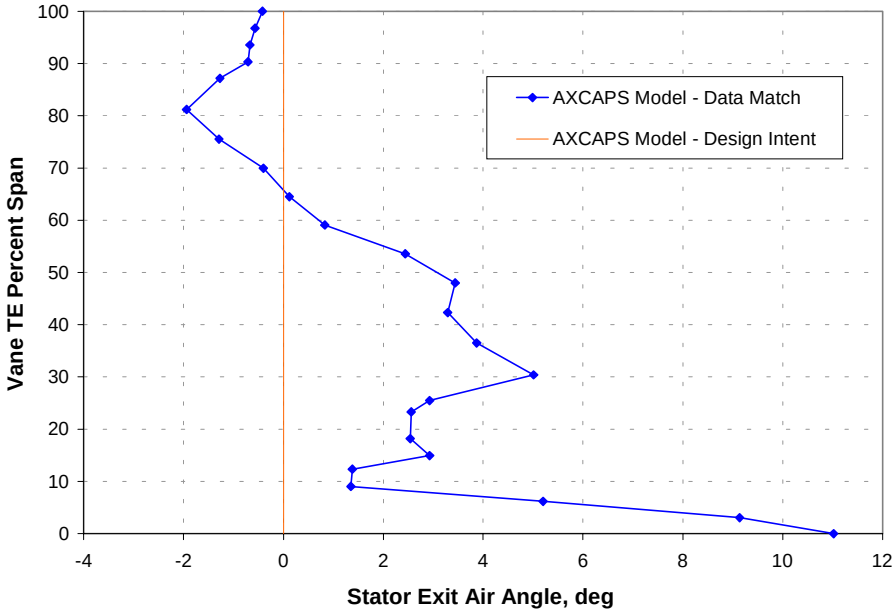

Figure 9-55. Mean Streamline Data Match Analysis for the Stator Exit Air Angle Radial Distribution.

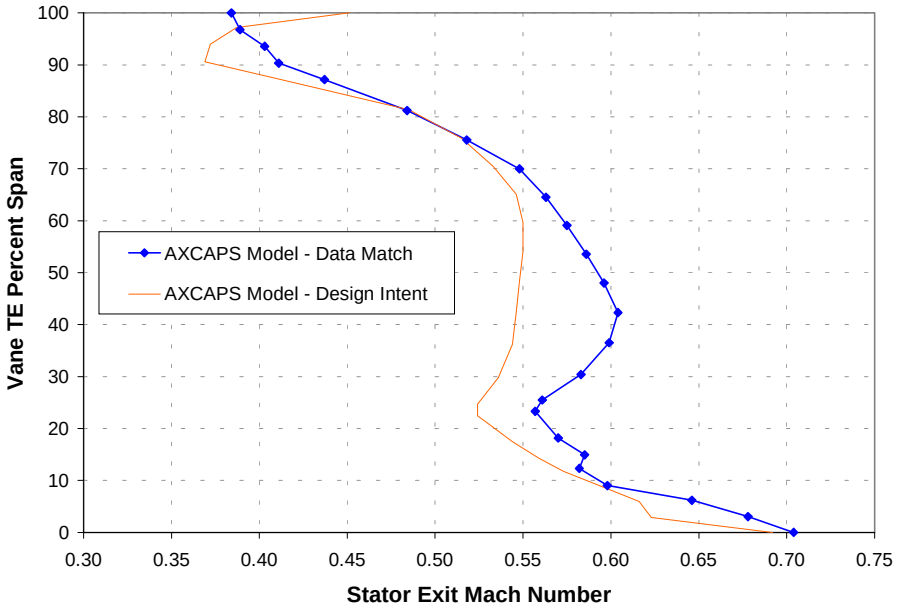

Figure 9-56. Mean Streamline Data Match Analysis for the Stator-Exit Mach Number Radial Distribution.

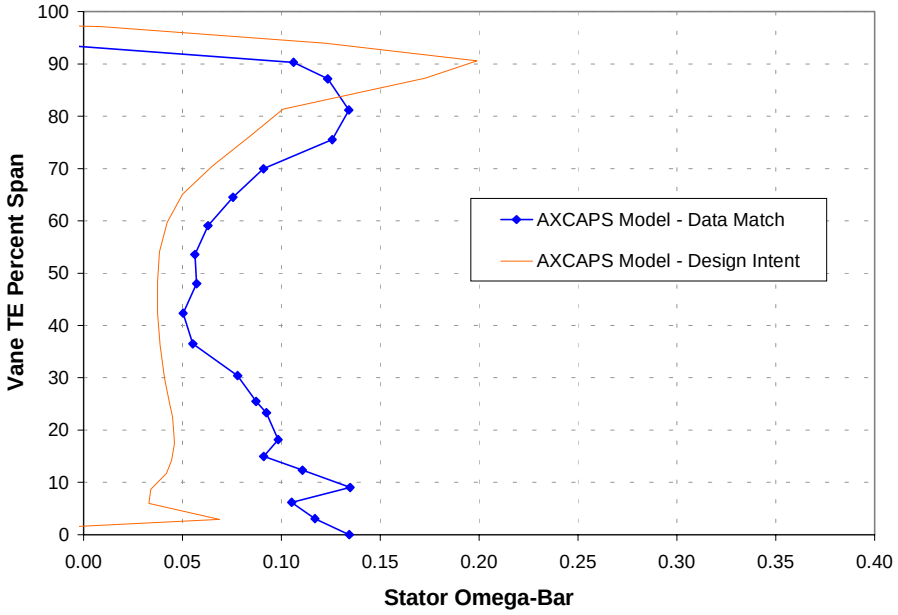

Figure 9-57. Mean Streamline Data Match Analysis for the Stator Omega-Bar Radial Distribution.

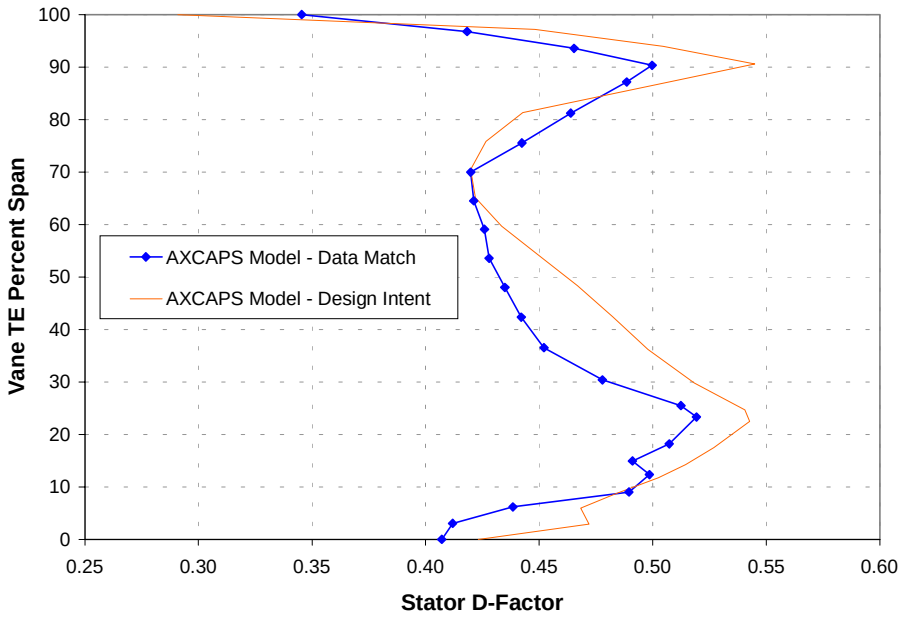

Figure 9-58. Mean Streamline Data Match Analysis for the Stator D-Factor Radial Distribution.

9.4 Mechanical Test Results

A brief mechanical checkout run was first made to verify mechanical integrity of the rig and lubrication systems. The rig was run throughout its operating range, checking vibrations, oil flow, and fan tip clearances. Preliminary aerodynamic data was also taken to verify data quality. At a fan rpm of 2000 (10.5 percent N1c), the clearances were checked and compared to be within a couple of mils of the cold build clearances. The maximum speed obtained with the 0.2-inch shims was 88 percent N1c with the minimum LE clearance at 0.004 inch. The same process was repeated with 0.100 inch shims installed allowing the fan speed to reach 97 percent N1c with minimum LE clearances of 0.004 inch. To allow the fan to run at the design speed, the final configuration had no shims installed. This configuration allowed the fan to run at minimum leading and trailing edge tip clearances of 0.013 and 0.037 inch, respectively, compared to the design intent of a constant 0.014 inch.

Non-synchronous vibration (NSV) was discovered early in the rig test. High vibratory strains were observed along much of the tested speed range above the operating line. Figure 9-59 shows the "stability" line superimposed on the stage map. Operation at pressure ratios above this line would result in a rapid increase in non-synchronous response.

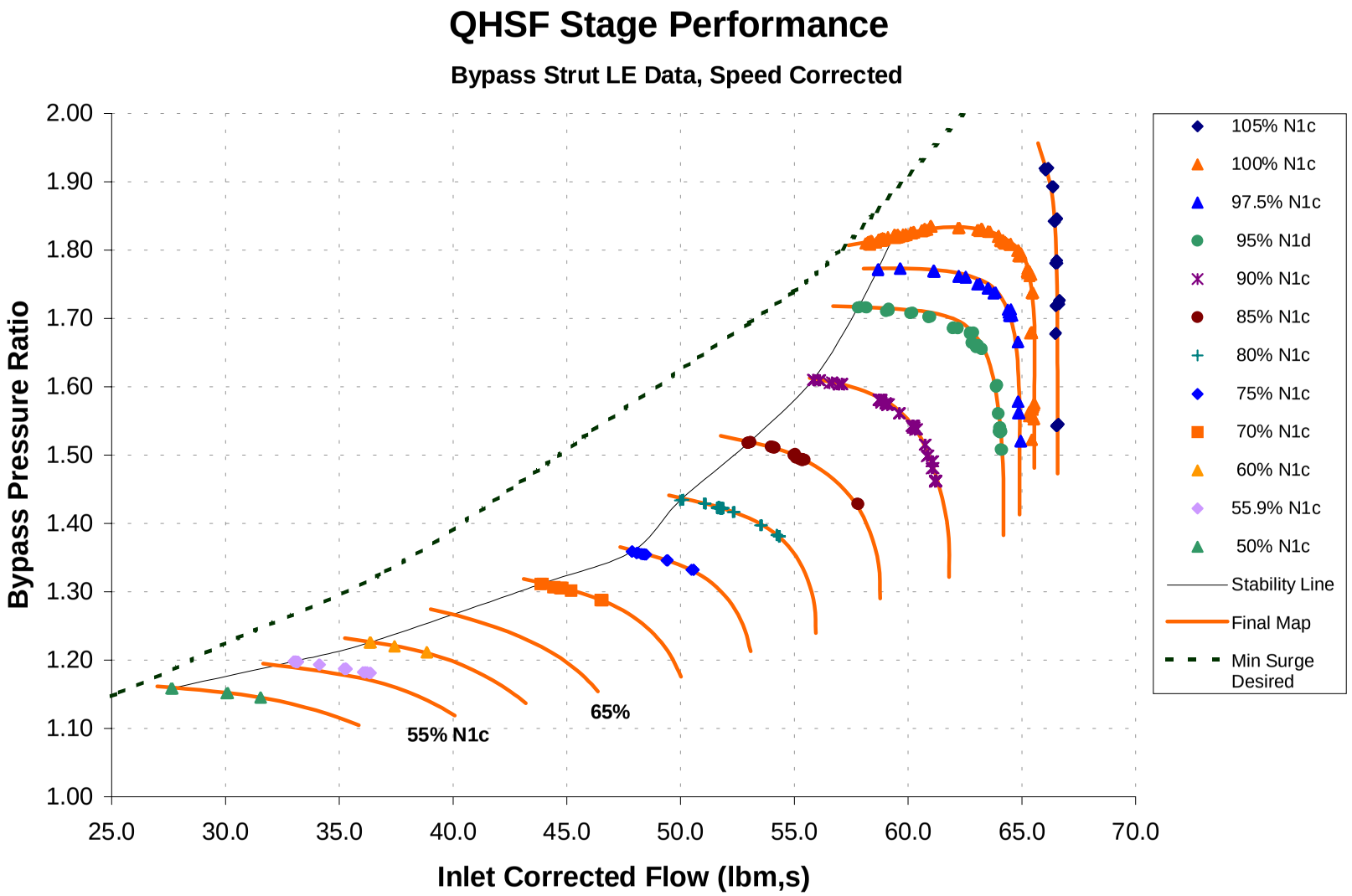

Figure 9-59. Stability Line on the QHSF Stage Performance Map Shows the Region Where High Strains on the Fan Blades Were Measured.

The blade response was measured with both strain gages and light probes. Later portions of the test also included the use of PCB acoustic transducers in the case upstream of the fan. This signal was used to determine the travelling wave nature of the response.

The non-synchronous response on or above the stability line can be categorized into three speed regimes: Low speed (<60 percent speed), part speed between 75 and 95 percent; and high speed (> 95 percent).

At low speed, the dominant response was the 0 nodal diameter umbrella mode at 860 to 900 Hz with strains occasionally exceeding 1000 με. Blade modes 2, 3 and 4 were also observed at lower strain levels. Analysis of the dynamic pressures indicates the rotor was running in a stalled condition at these conditions.

Rotor response in the low-speed region was consistent with a broadband excitation induced by the rotor stall. As the back-pressure was increased, first the 860 Hz umbrella mode would appear and then the various blade modes would begin responding. Spectral analysis of the accompanying acoustic tone revealed the following frequencies, compiled from various data point in this speed regime:

Speed, rpm	Strain gage Freq., Hz	PCB Freq., Hz	Comments
10,890	880	880	0 Nodal Diameter "Umbrella" Mode
11,700	730	1530	4 Nodal Diameter Forward Traveling Wave
10,890	1140	780 and 1505	2 Nodal Diameter Forward Traveling Wave and Backward Traveling Wave

In many cases, several of these modes would respond simultaneously, which is consistent with a broadband excitation spectrum.

Above 75 percent and below 95 percent speed, the significant response was almost exclusively mode 1. This region shows the largest intrusion of the flutter boundary on the stage map. The response increased very rapidly as the fan was back pressured. Maximum strains exceeded 2000 με. Analysis of the dynamic pressures showed that the rotor does not appear to be stalled in this regime but that the response is due to an aeroelastic instability.

As shown in the following table, the PCB signature indicates that the first mode consistently responds in a 2-nodal diameter forward traveling wave with a frequency equal to the blade vibration frequency plus twice the rotational frequency.

Percent Speed	Speed, rpm	Strain gage, Freq., Hz	PCB Freq., Hz	Comment
75	14520	360	842	2-nodal diameter forward traveling wave
85	16560	390	935	"
97.5	18990	420	1055	"

Above 95 percent speed, the rotor is experiencing rotating stall. The response is Mode 1, 2 nodal diameter forward traveling wave with observed strains exceeding 1200 με as the stall line was approached.

Two attempts were made to modify the blades with tip clips to reduce the size of the flutter envelope. The first clip was approximately 10 percent tip chord in length as shown in the sketch below. The clip chord direction was defined to follow the Mode 1 deflection contour.

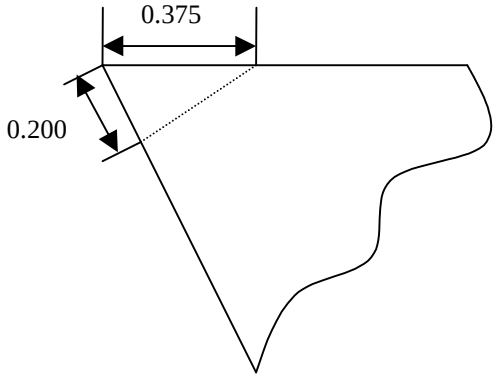

Each blade in the rotor was clipped in an identical manner without removing the blades from the disk to avoid disturbing the strain gage routing. The rotor was re-installed in the rig and selected speed lines were remapped to assess the impact of the clip. The flutter response and its boundary were virtually unchanged with the addition of the clip.

A second tip clip was defined with twice the linear dimensions as the first (0.75 by 0.40 in.). The blades were reworked in an identical manner as before. Testing showed this clip to be ineffective as well.

9.5 Acoustic Results

9.5.1 Summary

The design intent of the NASA Quiet High-Speed Fan (QHSF) is to control the strength and position of the passage shock. Acoustic measurements made on the 18-inch QHSF rig show that this goal has been achieved through a portion of the operating range in which the shock-generated (multiple pure tone or MPT) noise can be prominent in a conventional fan.

Figure 9-60 shows the delayed onset of MPT noise for the QHSF design relative to a non-forward-swept design. Significant MPT noise does not appear to be generated until 86 percent rpm (M_{tr}=1.15), making the quiet high-speed fan design free of shock noise through the equivalent of what is considered to be the “Cutback” in a typical engine operating range.

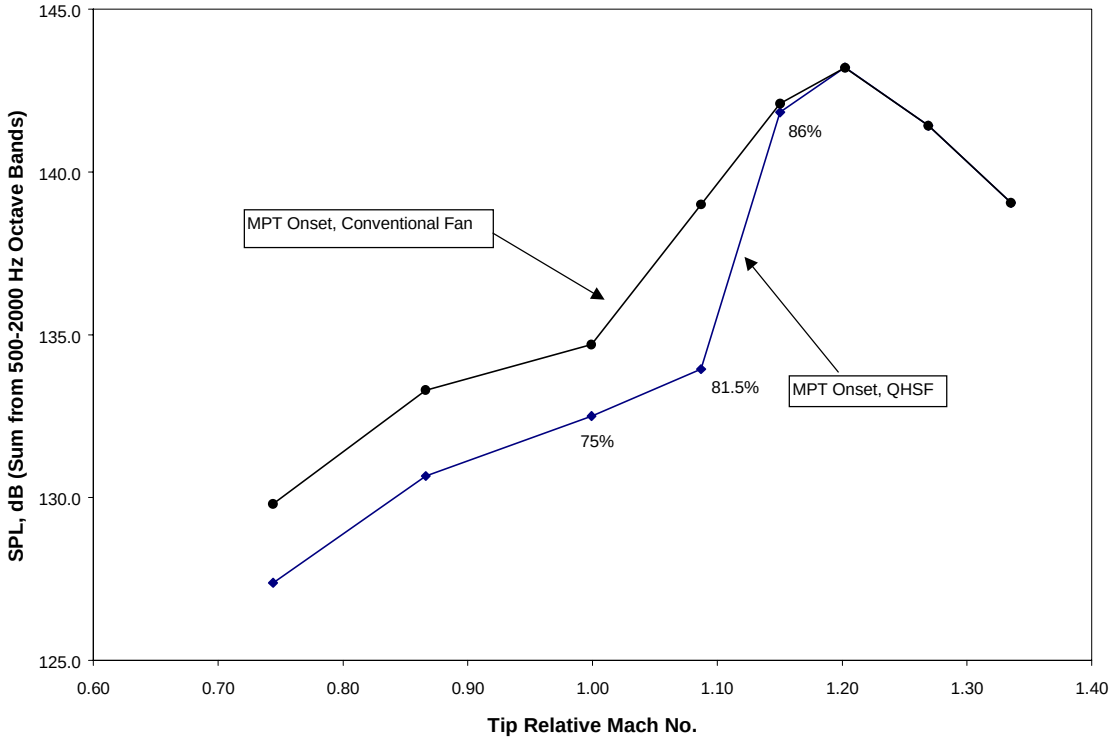

Figure 9-60. The Acoustic Measurements Show Reduced Multiple Pure Tone (MPT) Noise for the QHSF as Compared to the Baseline Design.

9.5.2 Acoustic Test Set-Up

A cross section of the 18-inch QHSF rig is shown in Figure 9-61, with sketched locations of the acoustic sensors shown. A rotating ring of 16 evenly spaced transducers is located in the inlet, approximately 14 inches from the fan blade leading edge. Inlet acoustic measurements were acquired at three ring positions, yielding a total of 48 circumferential measurements (7.5-degree spacing). Kulite sensors in the fan bypass duct were used to acquire aft fan acoustic data at three circumferential locations. Figure 9-62 shows a picture of the 18-inch QHSF rig inlet with the rotating microphone ring installed.

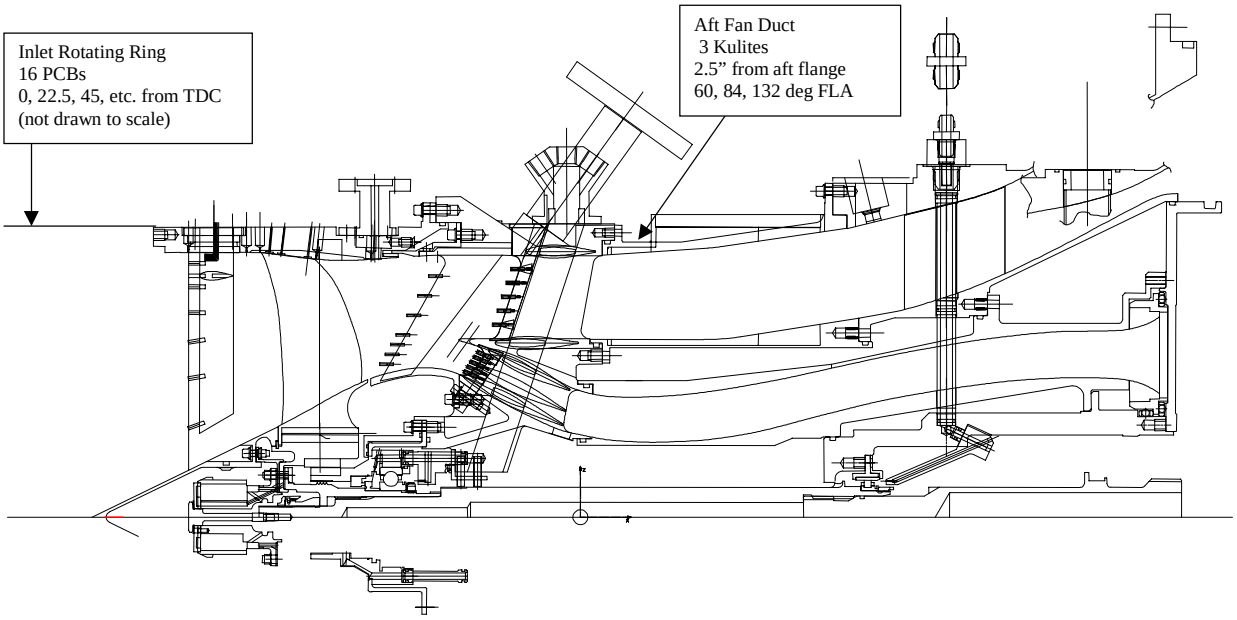

Figure 9-61. Cross Section of the 18-Inch QHSF Rig Showing the Location of the Microphones.

Figure 9-62. Photograph Showing the Inlet Kulite Ring Installed in the 18-Inch QHSF Fan Rig.

Acoustic data at nine different operating conditions were acquired at a range of fan operating corrected speeds of 55 and 100 percent. Additional acoustic data were acquired for the purposes of blade flutter analysis (off the operating line conditions) and also for the clipped fan blade configurations.

Data acquisition was completed using a 24-channel Masscomp digital system, at a sampling rate of 37,500 Hz. Samples were acquired over a 5-second record length.

9.5.3 Fan Inlet Modes

A modal decomposition of the fan blade passing frequency was performed at various operating conditions, using data obtained from the 16-microphone ring. The ring was rotated three times, yielding a total of 48 evenly–spaced circumferential measurements per engine operating condition. These measurements are first synchronized to a 1/rev signal and averaged in time. A discrete Fourier transform applied to the averaged pressure time-history yields a complex spectrum at each microphone location. A spatial Fourier transform at one discrete frequency (blade passing frequency) is applied to determine the dominant circumferential mode orders of that tone.

Data from 48 microphones can resolve mode orders over the range of +/- 24. Mode orders present that fall outside of that range will alias into this range by an integer multiple of 48. Tables 9-2 and 9-3 show the predicted modal structure of the QHSF, including the "aliased" mode where appropriate, for rotor-stator and rotor-strut interactions. Note that not all of these modes are considered to be propagating or "cut-on", but are assumed to be measurable in the duct.

Table 9-2. Circumferential Modes for Rotor-Stator Interaction.

Predicted

Rotor-Stator Interaction m=nB+kV B= 22 V= 52

Predicted Modes

	k=	-5	-4	-3	-2	-1	0	1	2	3	4	5	6
BPF1 n=	1	-238	-186	-134	-82	-30	22	74	126	178	230	282	334
BPF2 n=	2	-216	-164	-112	-60	-8	44	96	148	200	252	304	356

Aliased

Aliased Modes (48 microphones can resolve m=+/- 24)

	k=	-5	-4	-3	-2	-1	0	1	2	3	4	5	6
BPF1 n=	1	2	6	10	14	18	n/a	-22	-18	-14	-10	-6	-2
BPF2 n=	2	-24	-20	-16	-12	n/a	-4	0	4	8	12	16	20

Table 9-3. Circumferential Modes for Rotor-Strut Interaction.

Predicted

Rotor-Strut Interaction m=nB+kS B= 22 S= 10

Predicted Modes

	k=	-10	-9	-8	-7	-6	-5	-4	-3	-2	-1	0	1	2	3	4	5	6	7	8	9	10
BPF1 n=	1	-78	-68	-58	-48	-38	-28	-18	-8	2	12	22	32	42	52	62	72	82	92	102	112	122
BPF2 n=	2	-56	-46	-36	-26	-16	-6	4	14	24	34	44	54	64	74	84	94	104	114	124	134	144

Aliased

Aliased Modes (48 microphones can resolve m=+/- 24)

	k=	-10	-9	-8	-7	-6	-5	-4	-3	-2	-1	0	1	2	3	4	5	6	7	8	9	10
BPF1 n=	1	18	-20	-10	0	10	20	n/a	n/a	n/a	n/a	n/a	-16	-6	4	14	24	-14	-4	6	16	-22
BPF2 n=	2	-8	2	12	22	n/a	n/a	n/a	n/a	n/a	-14	-4	6	16	-22	-12	-2	8	18	-20	-10	0

Figure 9-63 shows the modal structure of the fan inlet-radiated blade passing frequency at the 55.9 percent rpm condition. Strong content from rotor-strut interactions are shown (m= -18, +12,). Similar modes dominate the fan modal pattern at the 65 percent rpm condition, shown in Figure 9-64. However, a strong mode at m= -15 is not attributable to rotor-stator or rotor-strut interactions.

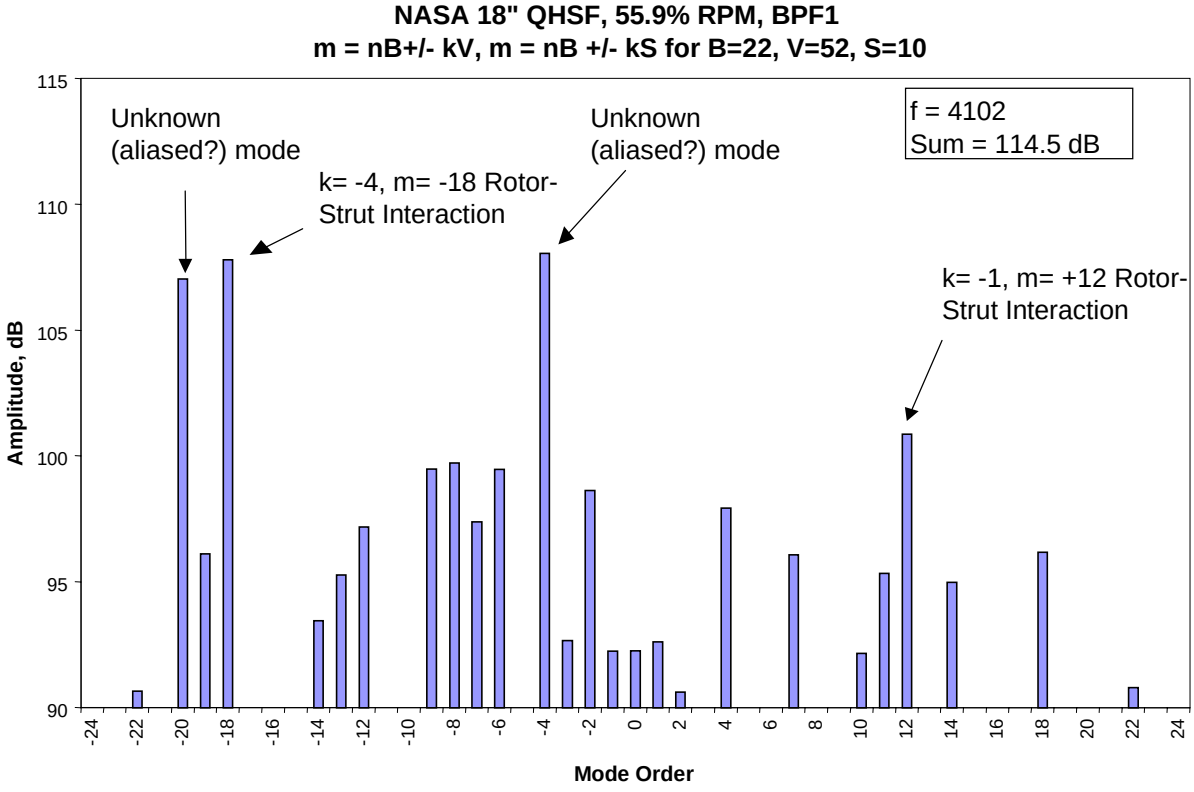

Figure 9-63. Modal Decomposition of Blade Passing Frequency, 55.9% RPM.

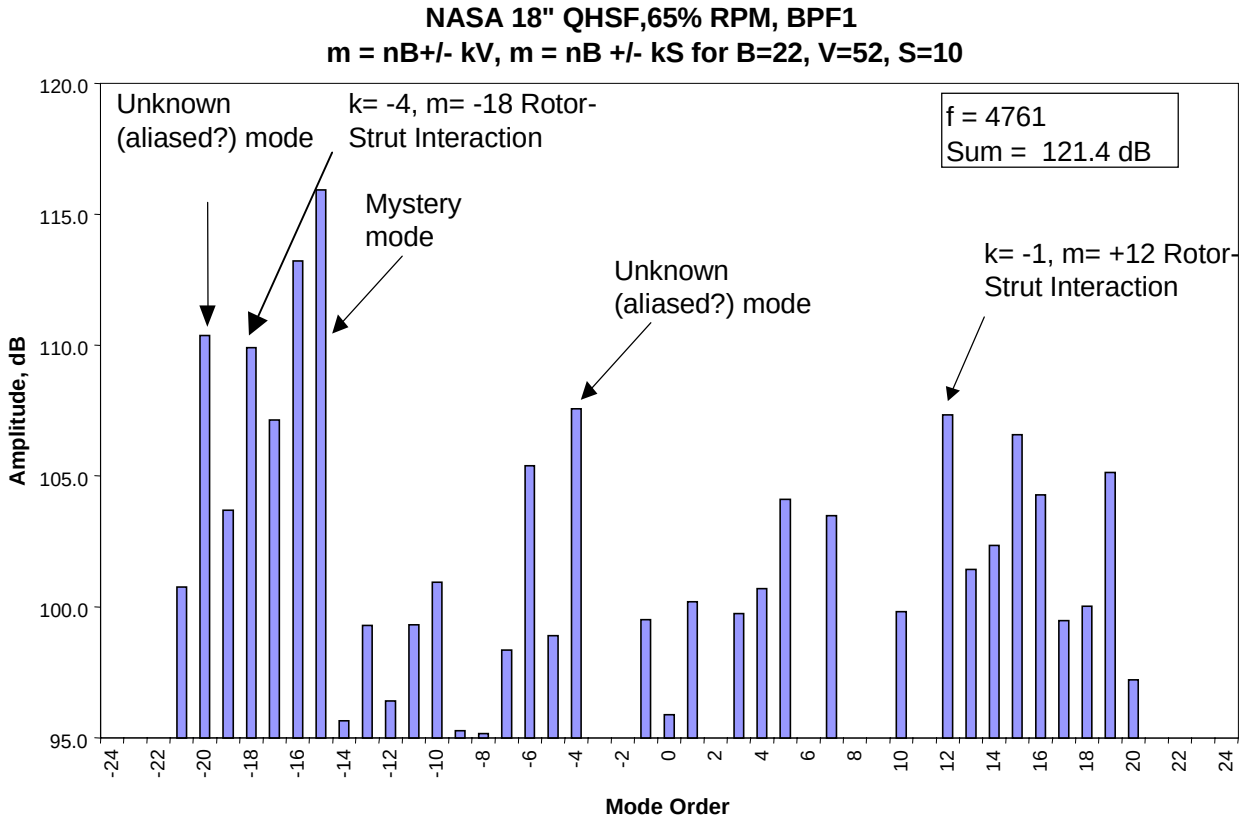

Figure 9-64. Modal Decomposition of Blade Passing Frequency, 65% RPM.

The modal content of the fan blade passing tone changes significantly once the rotor-alone mode becomes "cut-on", as it is for the 81.5% RPM condition shown in Figure 9-65. The rotor-alone m= +22 mode clearly dominates. Several other significant, high-order modes from rotor-stator interactions appear to have been measured in the duct, although these modes should theoretically have decayed prior to the measurement location.

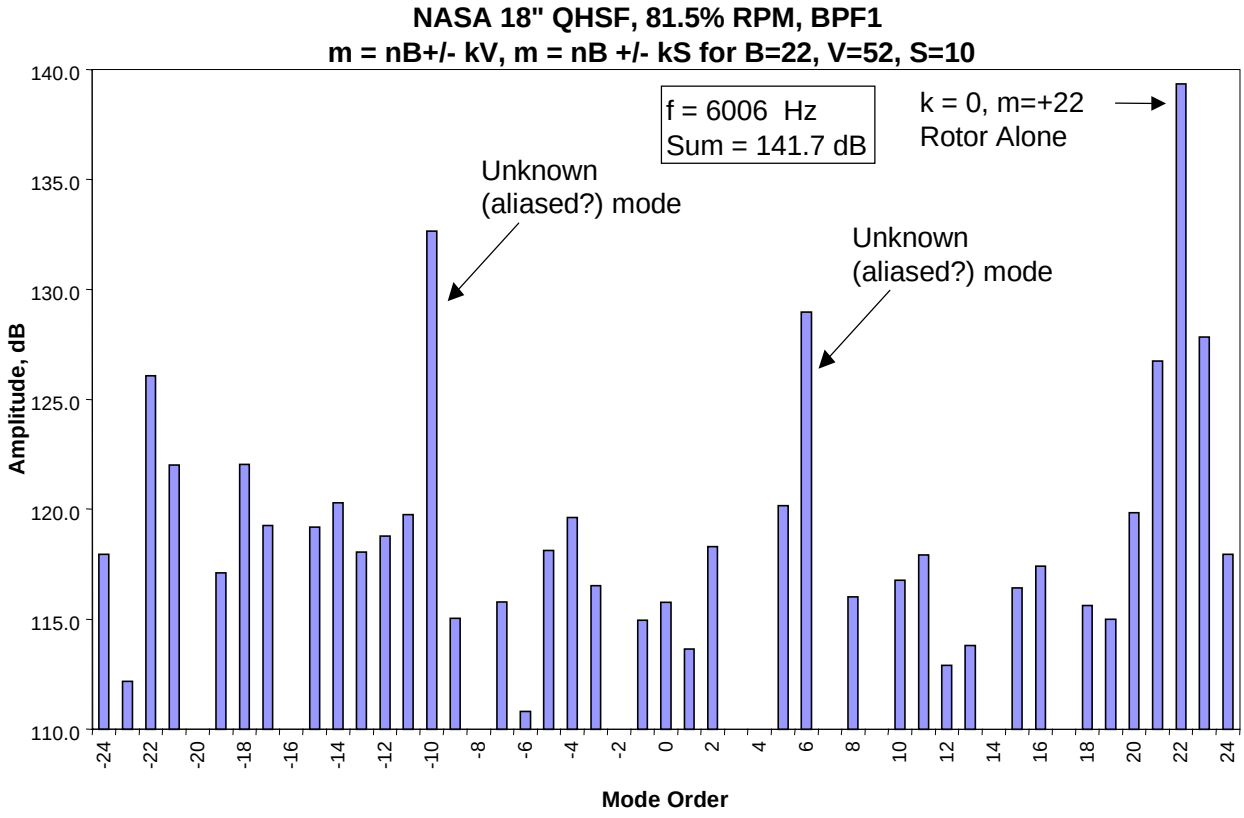

Figure 9-65. Modal Decomposition of Blade Passing Frequency, 81.5% RPM.

Modal decomposition of the first harmonic of the blade passing frequency (2X BPF) is shown in Figures 9-66 and 9-67. At 65 percent rpm, the dominant modes appear to be primarily from high order modes that have aliased into lower-order modes as shown in Figure 9-65.

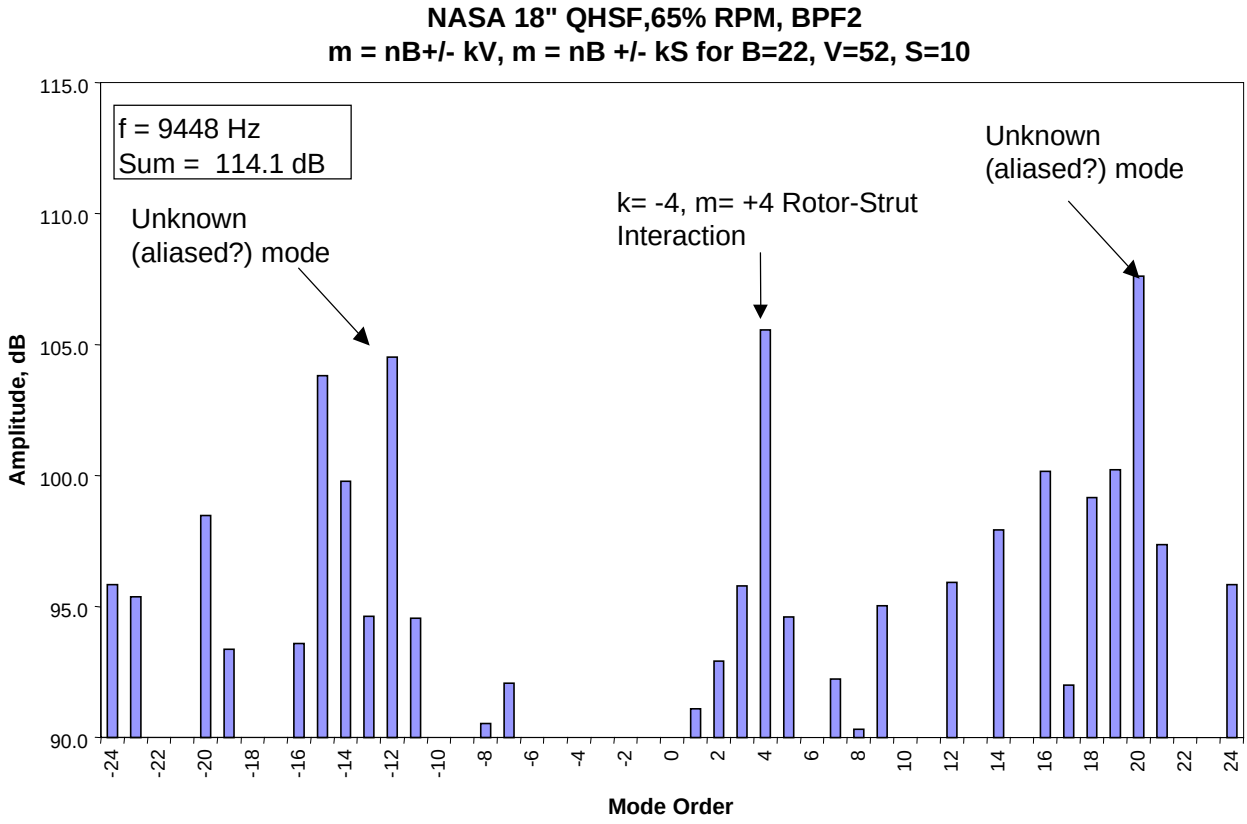

Figure 9-66. Modal Decomposition of 2X Blade Passing Frequency, 65% RPM.

Similarly to the fundamental tone, the rotor-alone mode of the second harmonic (m= +44) dominates once the mode becomes cut-on, as it is at the 81.5 percent rpm condition shown in Figure 9-66. Several other high-order interaction modes have been measured as well.

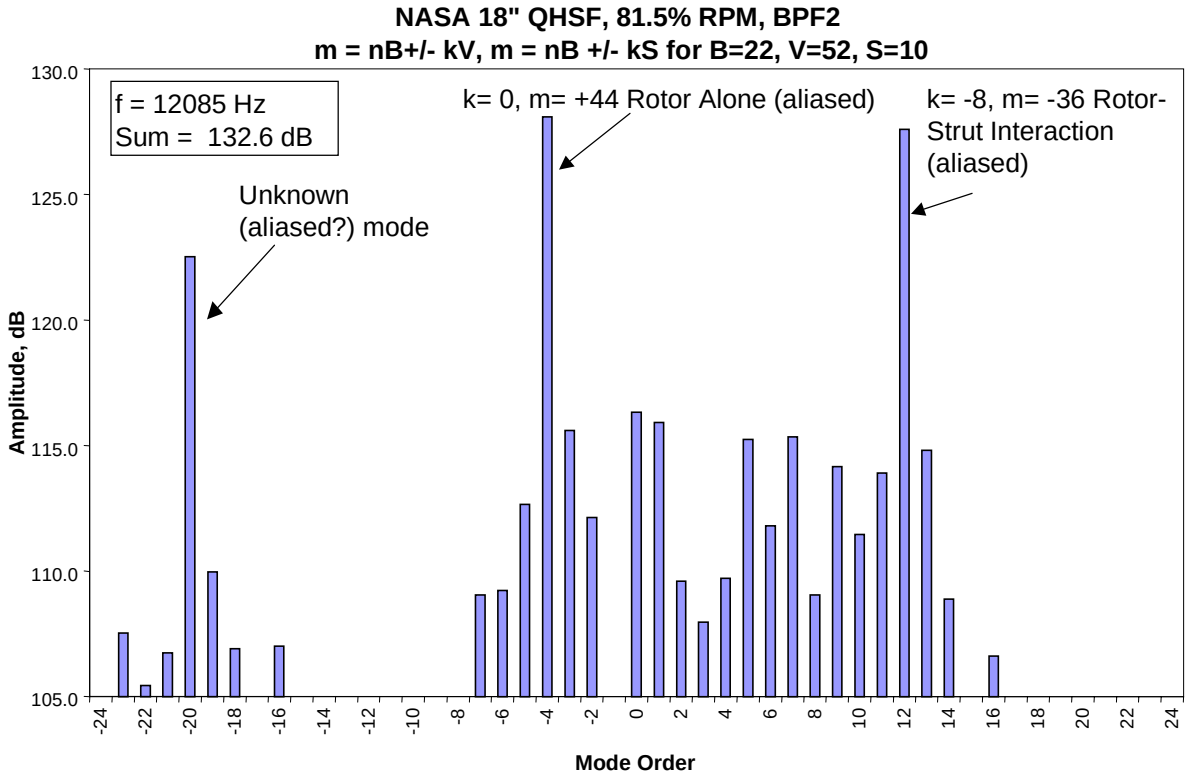

Figure 9-67. Modal Decomposition of 2X Blade Passing Frequency, 81.5% RPM.

9.5.4 Overall Noise Levels

Figure 9-68 shows a summary of the in duct one-third octave band measured noise levels at selected operating conditions. These noise levels are an average of the data from the 16 individual inlet microphones.

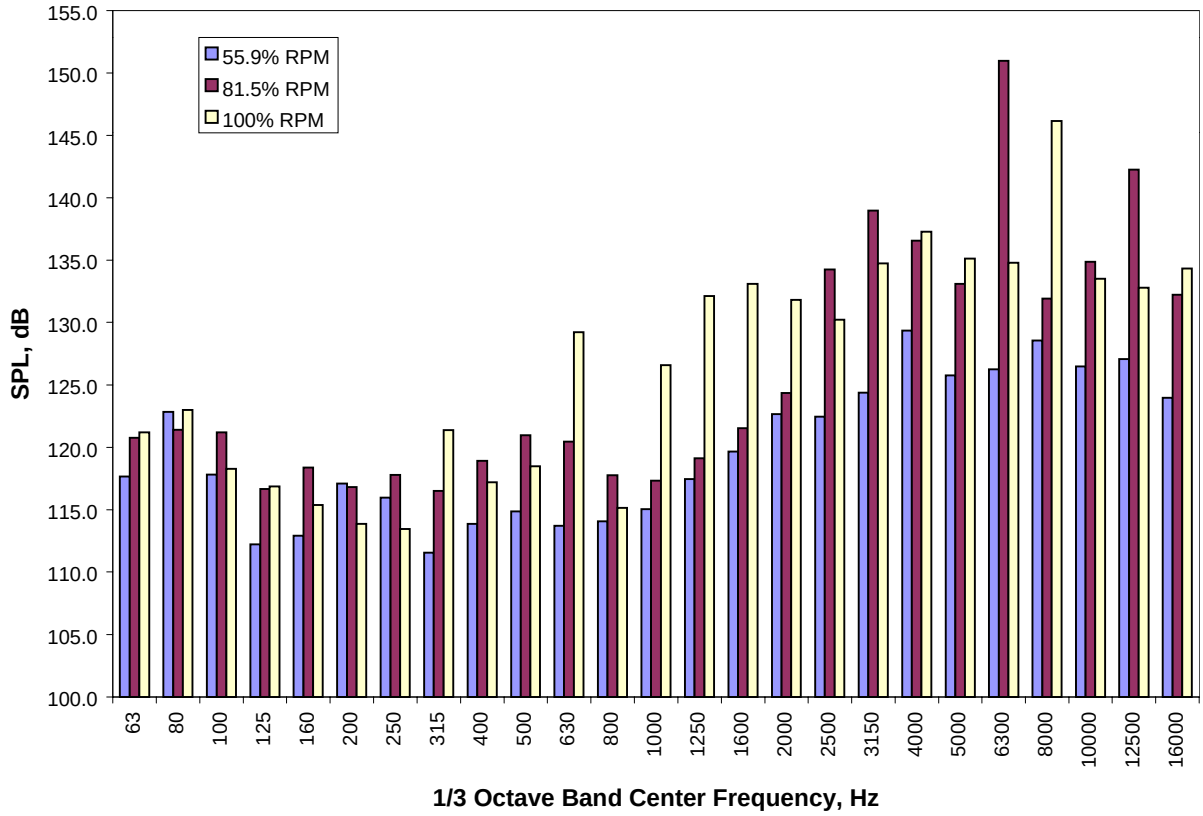

Figure 9-68. One-Third Octave Band Inlet Sound Pressure Levels at Three Operating Speeds.

9.5.5 Baseline QHSF versus "Clipped" Fan Blade

Acoustic testing was repeated for subsequent "clipped" blade configurations. In general, the acoustic results did not appear to be affected. Figure 9-69 shows a typical baseline QHSF versus 10 percent clipped blade comparison.

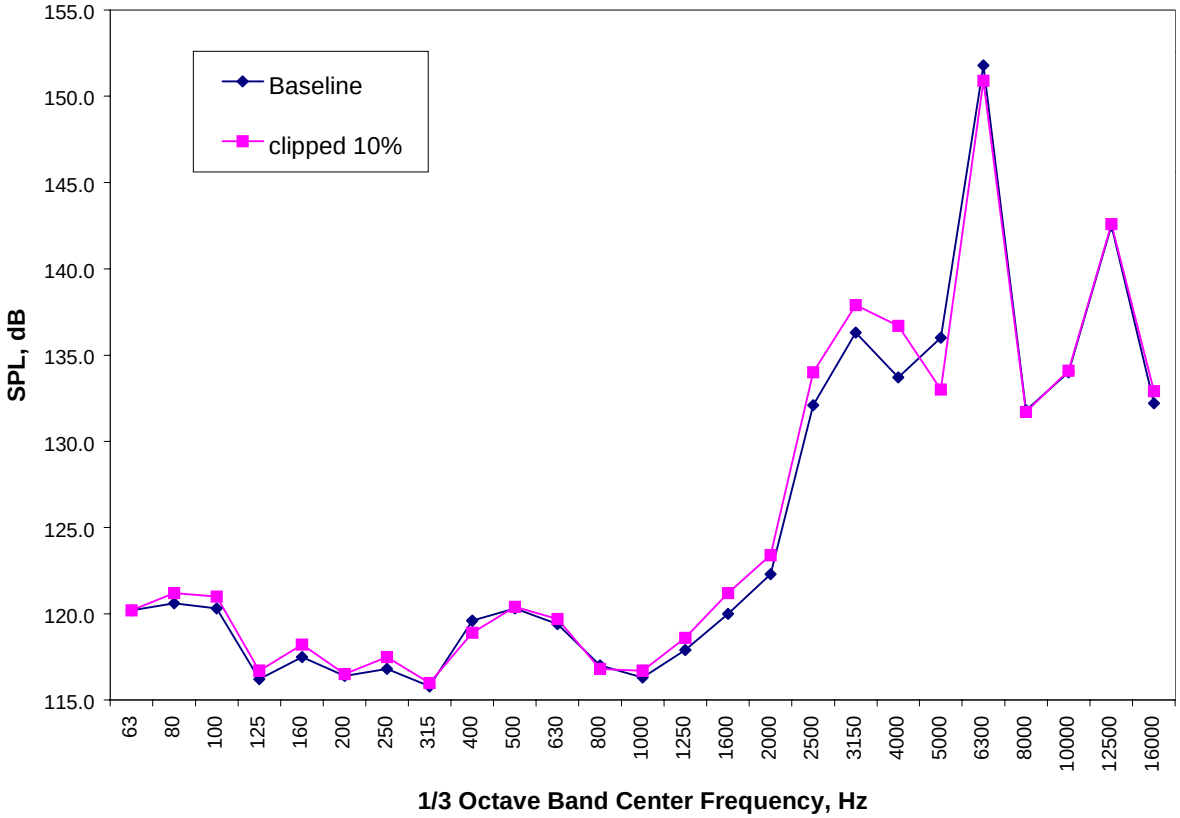

Figure 9-69. Comparison of the Measured Spectra of the Unclipped and Clipped QHSF Fan Blades at 81.5% RPM.

9.5.6 Narrowband Data

Narrow-band data from the 0-degree inlet microphone are shown for the range of operating conditions tested in Figures 9-70 to 9-75. It is interesting to note the noise levels of the MPTs relative to the blade passing frequency tone as the fan speed changes.

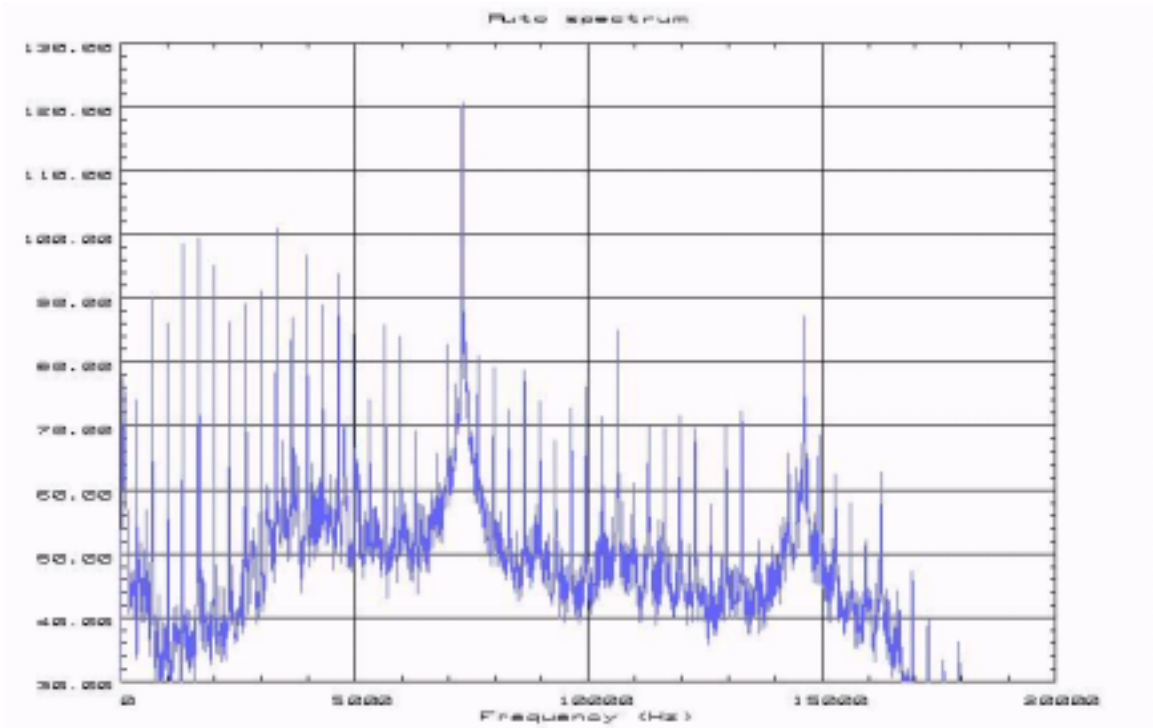

Figure 9-70. Inlet Narrow Band Spectrum at 100% RPM.

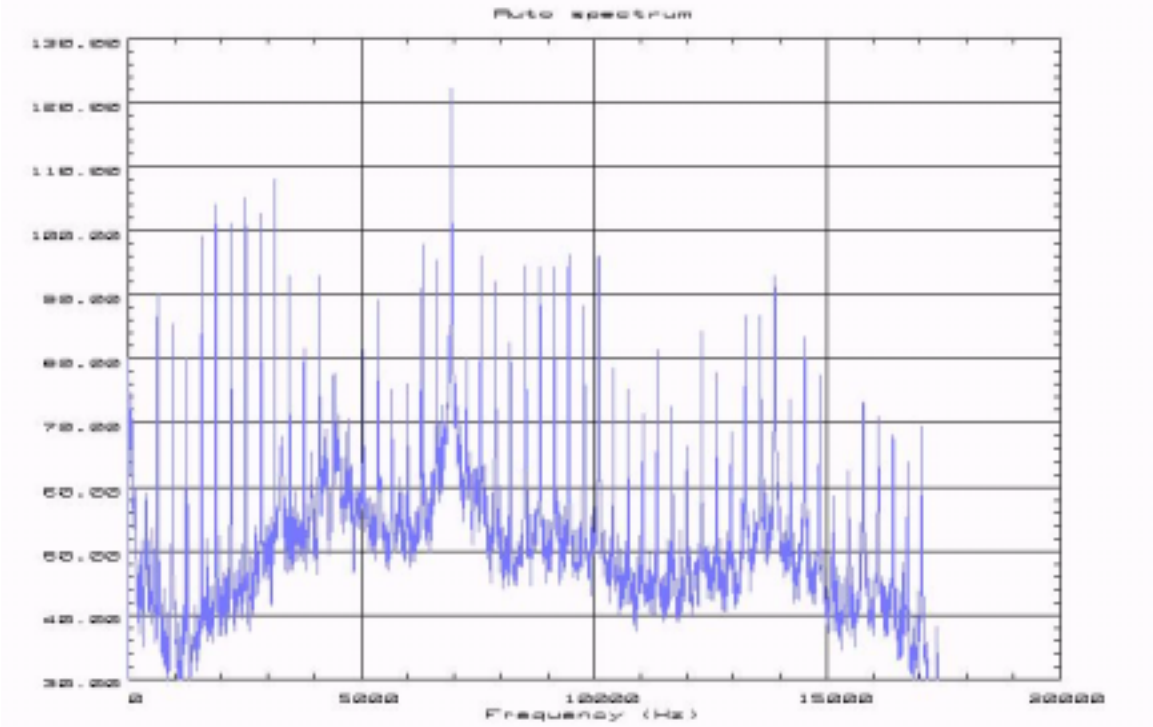

Figure 9-71. Inlet Narrow Band Spectrum at 95% RPM.

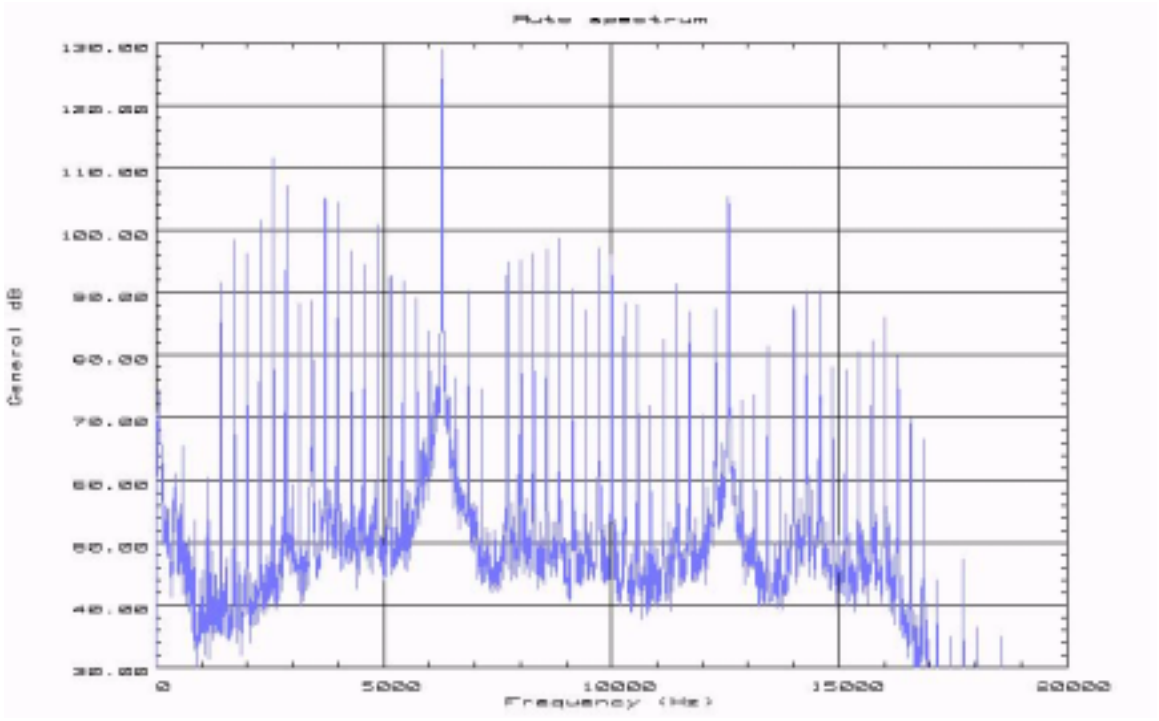

Figure 9-72. Inlet Narrow Band Spectrum at 86% RPM.

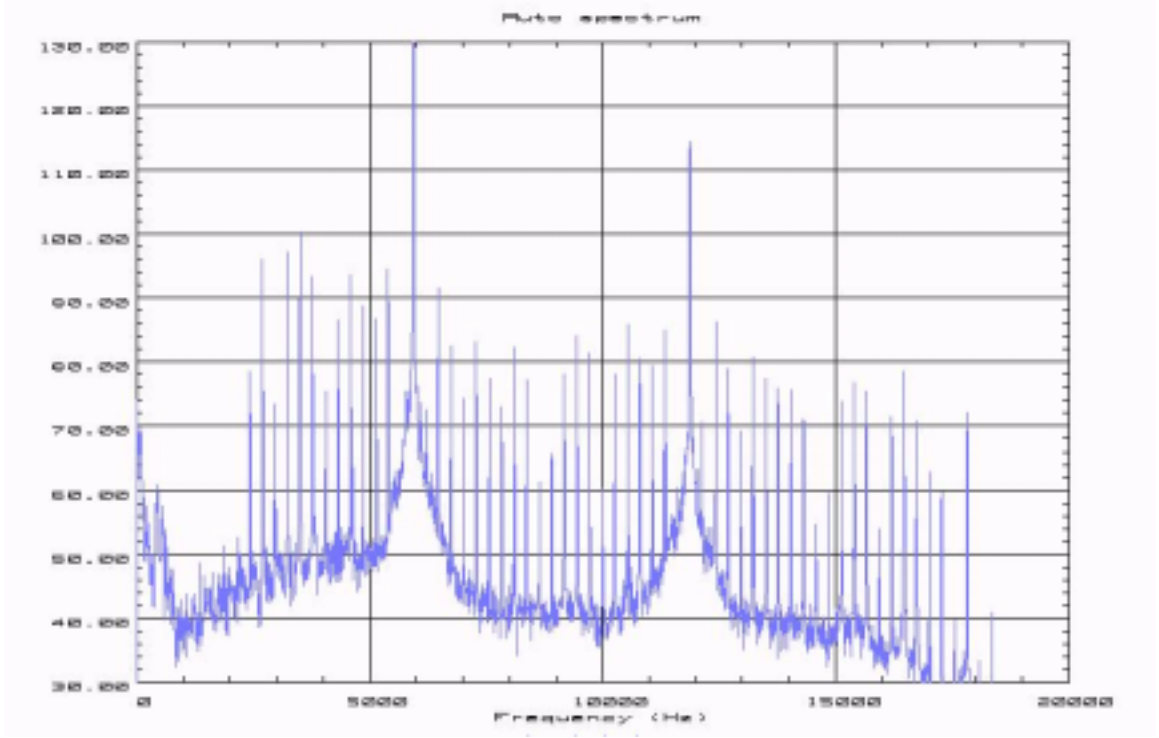

Figure 9-73. Inlet Narrow Band Spectrum at 81.5% RPM.

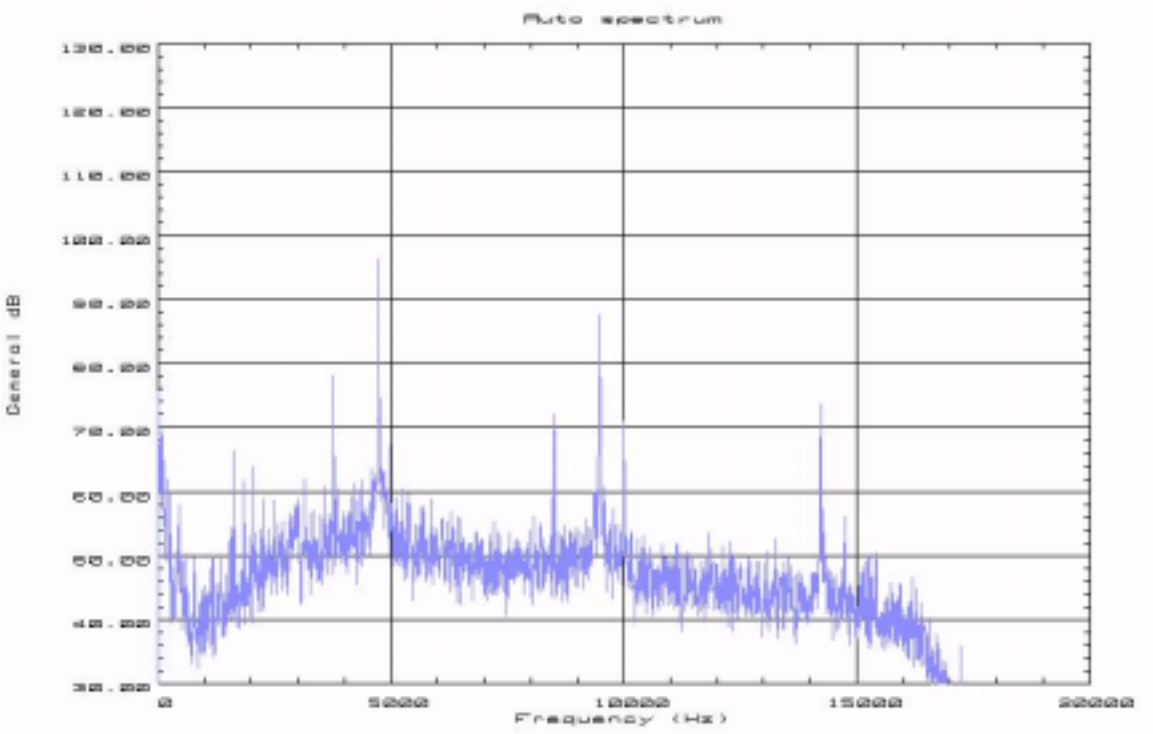

Figure 9-74. Inlet Narrow Band Spectrum at 65% RPM.

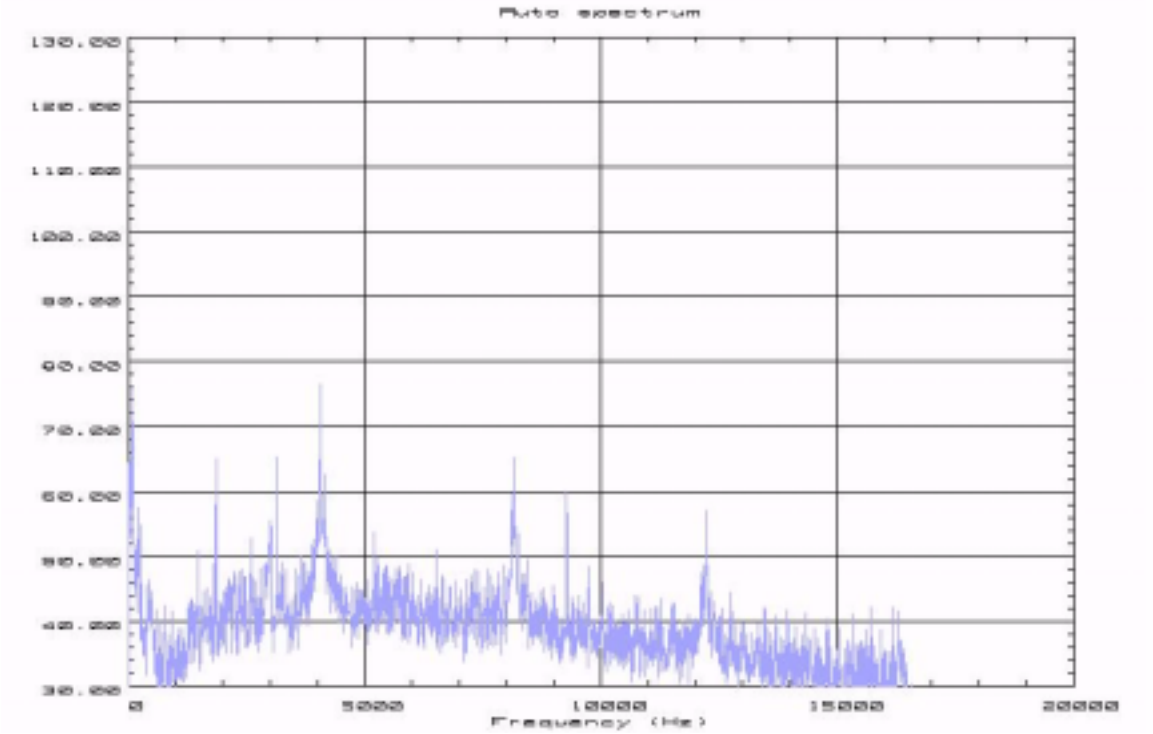

Figure 9-75. Inlet Narrow Band Spectrum at 55.9% RPM.

9.6 Dynamic Analysis

9.6.1 Summary

Tests of the QHSF rig showed both flutter and stalling behavior along the stability limit of the fan. Dynamic analysis of the unsteady flows has shown some unexpected behavior near the stability limit. This includes some high-speed behavior similar to rotating stall, which is typically a low-speed event. The purpose of this section is to present these results and explain the aerodynamics behind what is seen, as compared to classical behavior. Both stall flutter and self-excited flutter (flutter not driven by stall) are observed.

The following are the key findings of the dynamic analysis:

- High-response pressure data at 50 percent corrected speed shows the rotor to be in a part-span, full circumference stalled condition. This is not untypical at this speed, after the collapse of rotating stall into a part-span full-circumference stall.
- High-response data at 90 and 95 percent corrected speed does not show any condition of stalling or surge behavior, but the effect of the blade flutter on the airfoil loading can be seen in the change of the wake structure.
- At 97.5 and 100 percent speed, the fan does not surge (as it would classically do) but goes into a stall mode similar to a rotating stall but with different blade flows (as seen in the wake structure). This will be called a "high-speed sustainable stall," since the nature of it is different than the classical low-speed rotating stall. This condition does not typically exist because the system would precipitate a surge rather than exhibiting this stall behavior.
- Where there is no stall, the rotor blades are in a classical self-excited flutter mode. At 97.5 and 100 percent corrected speed, a stall flutter exists.

9.6.2 Classical Behavior of Compression Systems in Instability

To examine the behavior of the QHSF, it is first necessary to discuss the classical behavior of a stalled compression system stage. Both stall and surge can be viewed on a stage characteristic basis, which shows the distinct differences in stalling behavior that occurs. Figure 9-76 shows the general regions of operation on a typical stage characteristic. The overall pressure rise characteristics of the stage and the volumetric system characteristics determine the system response to operation on the pressure characteristic at the point where normal operation and rotating stall operation intersect. Surge behavior in a compression system is always preceded by stall, which in nature is similar to rotating stall but does not have the time to fully develop (ref. 21).

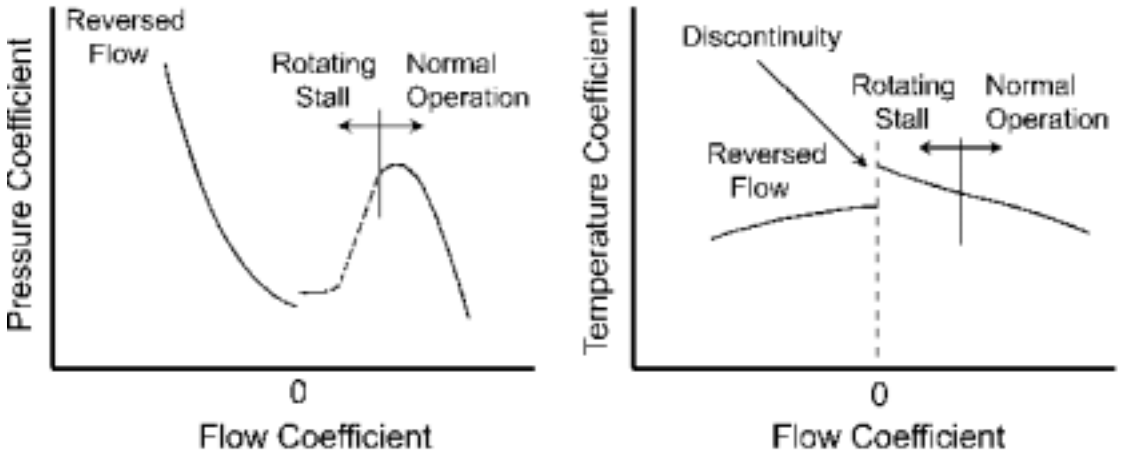

Figure 9-76. General Regions of the Typical Stage Characteristic (Taken from Ref. 21).

Figure 9-77 shows the pressure characteristic with regions of rotating stall operation and a surge cycle. There are several detailed regions to the rotating stall characteristic. From normal operation, increasing the backpressure on the stage moves the operating point up the stage characteristic from normal operation into the incipient stall region (between D and A). The incipient stall region is characterized by blades stalling and recovering in a random manner around the circumference of the rotor. Slight changes in inlet conditions, speed, etc. can cause the operating point of the compression stage to "jump" to the post stall characteristic at a lower flow rate and pressure rise. Initially, several stall cells may be present, but as the backpressure is increased (to Point B), these collapse into a single rotating stall cell. Further increases in backpressure cause the stall cell to grow in the circumferential direction until a full-circumference, part-span stall is achieved. Decreasing the backpressure moves the operating point toward Point D, at which stall recovery occurs and operation resumes on the normal portion of the characteristic.

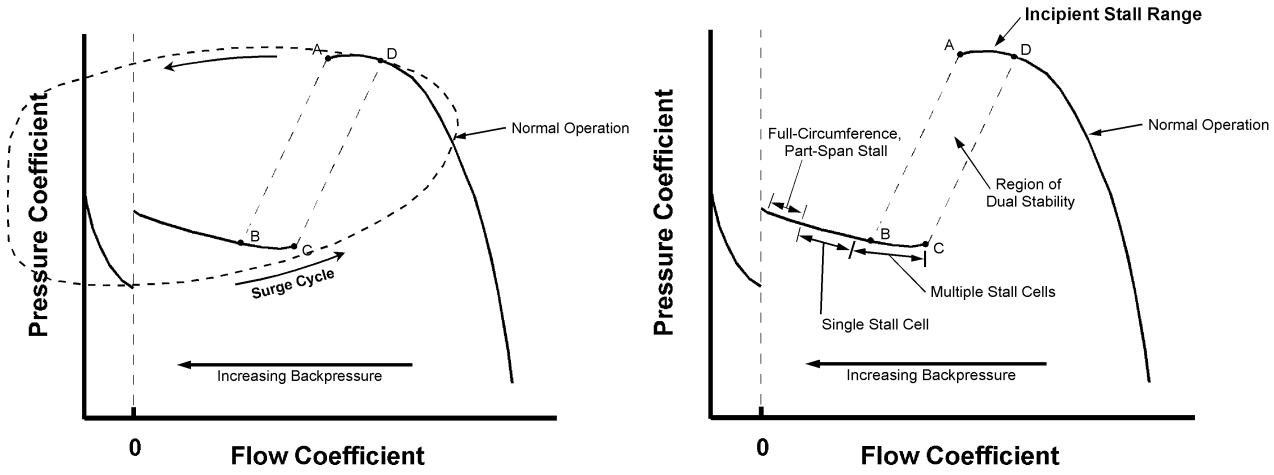

Figure 9-77. Details of Surge and Rotating Stall on the Pressure Characteristic.

Surge occurs when the volume downstream of compression system is large enough to store significant energy relative to what the system can produce. When the system is back-pressured and the operating point moves into the incipient stall region, the lack of pressure rise in the stalled blades provides less resistance to the high-downstream pressure. The system back-flows, tracing the complete surge cycle, often multiple times, until decreasing the back-pressure on the compressor restores system stability.

9.6.3 Unsteady Aerodynamic Characteristics of the QHSF

The QHSF exhibits characteristics in the low-speed region of operation that are quite normal and consistent with the classical rotating stall behavior previously described. At high speed (97.5 percent and above), however, the QHSF exhibits quite a different behavior than the typical fan stage. The system never enters into a full-surge mode, but rather, seems to operate on the post-stall characteristic in what might be called a "high-speed sustainable stall." In doing so, enough pressure rise is generated by the stage to maintain the pressure downstream and not surge. Details of the flow are significantly different while operating on the post-stall characteristic at high speed. This can be seen in the wake structure measured behind the rotor and will be discussed later in this report. It is suggested that the high forward sweep of the blade allows the streamlines to shift downward along the blade surface when the tip area stalls (as they normally do on any stage). The fact that a greater portion of the blade in the chordwise direction is still available to do work on the flow and create pressure rise enhances the pumping of the stage under stalled conditions, thus preventing surge.

9.6.4 Examination of Dynamic Data at 90 Percent Corrected Speed

The dynamic data at 90 percent corrected speed is shown in Figure 9-78. The sudden increase in strain can be seen on strain gauge No.1, starting at about 20 seconds into the trace. Figure 9-79 is a closer examination of the data over a 30 ms time frame starting at 29.60 seconds. The sine wave structure of the strain response can clearly be seen, and also the time associated with one rotor revolution. The two pressure transducers (P30 and P300) do not show any sign of blade stalling behavior. If the blade were stalled, the wake structure would not be as heavily seen in the pressure traces, as it tends to wash out with blade flow separation. The effect on the wake structure due to the moving blade can be seen in the pressure traces. As the blade incidence angle is changed due to the fluttering condition, the boundary layer is thicker over the blade and the pressure defect in the wake becomes smaller in the circumferential direction.

9.6.5 Examination of Dynamic Data at 95 Percent Corrected Speed

The data at 95 percent corrected speed is shown in Figures 9-80 and 9-81. As in the 90 percent corrected speed data, the sinusoidal pattern of blade flutter can be seen in the strain measurements, although not to as large a magnitude. The blade wakes can clearly be seen in the pressure traces (the P30 trace is autoscaled to a noise spike in the data that can be seen in Figure 9-79). With the lower magnitude of strain (and thus lower magnitude of blade movement), the effect on the structure of the wake pressure distribution is significantly less than that seen at 90 percent corrected speed.

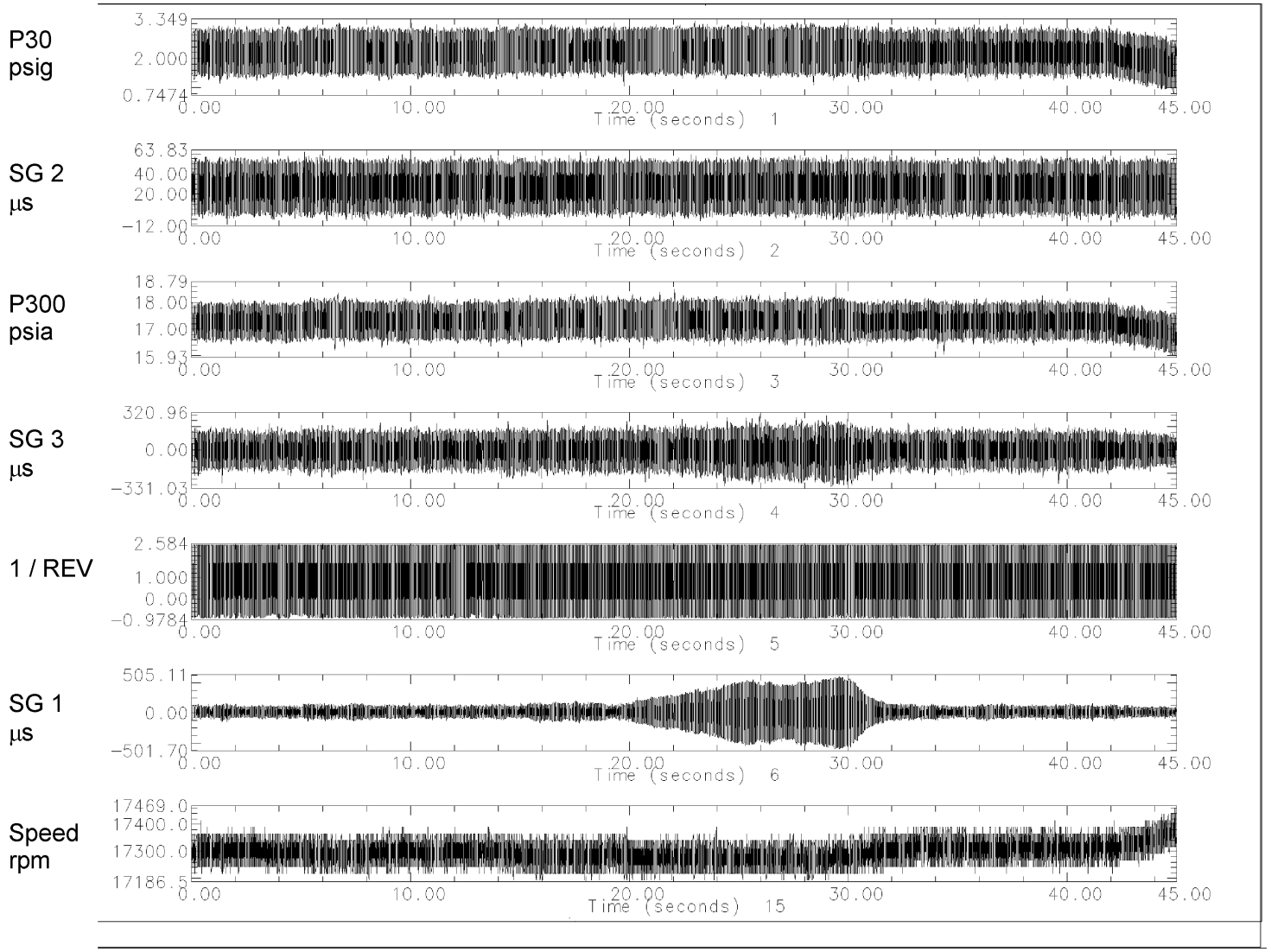

Figure 9-78. Pressure and Strain Measurements at 90% Corrected Speed During Flutter Without Blade Stall.

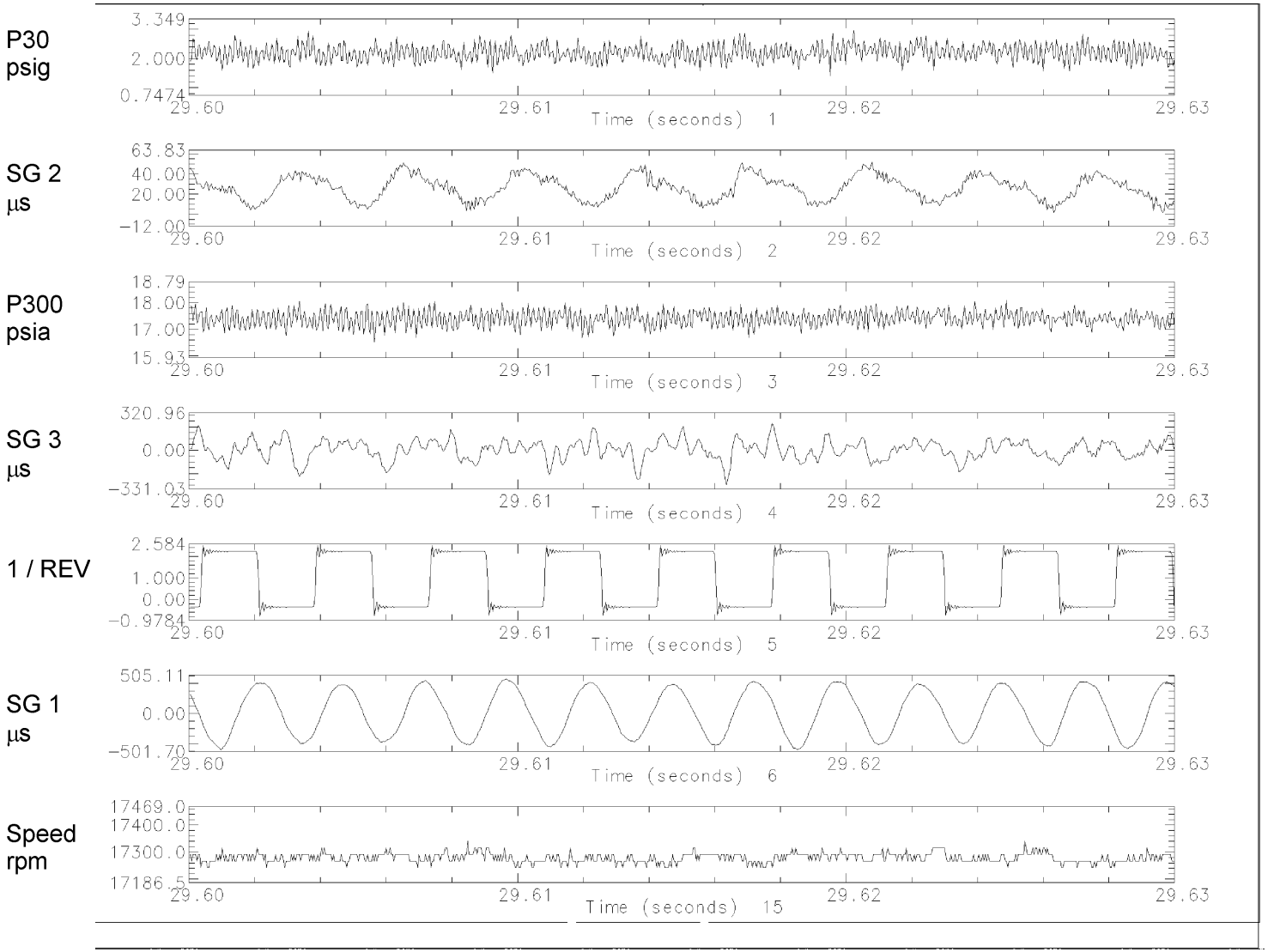

Figure 9-79. 30 ms of Data Showing Pressure and Strain Measurements at 90% Corrected Speed During Flutter Without Blade Stall.

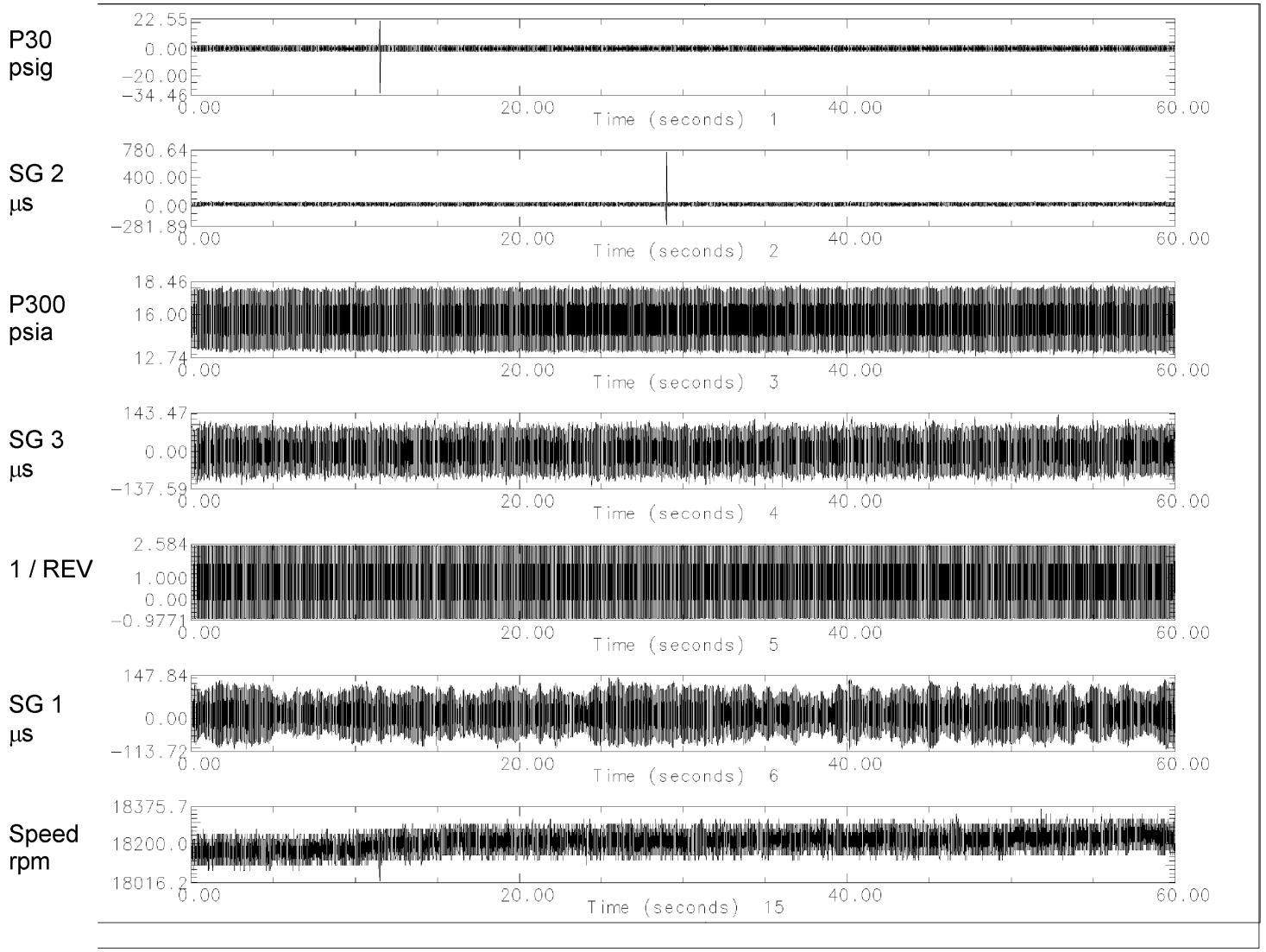

Figure 9-80. Data Showing Pressure and Strain Measurements at 95% Corrected Speed During Flutter Without Blade Stall.

9.6.6 Examination of Dynamic Data at 50% Corrected Speed

At 50 percent corrected speed, there was no flutter present as can be seen in Figure 9-82. There is some noise on the strain gauge signals. To show that this noise was not a high strain measurement, the data was expanded about the noise. Figure 9-83 shows the expansion of the data and the noise (known not to be real strain or it would have the signature of that in Figures 9-78 through 9-81). The pressure distribution of the wake structure is completely destroyed, indicating that all of the blades are in a stalled condition. This is typical when measuring the wake downstream of a rotor with a full-circumference part-span stall. It is known that this is a part-span stall since the rotor still shows some pressure rise as can be seen in the P300 trace. To confirm the lack of a wake structure and any correlation to the strain measurement, a cross-spectrum was performed between the pressure signal and the strain signal. Figure 9-84 shows the result. The broadband frequency distribution inherent with fully stalled airfoils can be clearly seen between 1000 and 2500 Hz. Due to the non-deterministic nature of the separated flow disturbance in the wake, the broadband frequency distribution occurs at a lower frequency than the approximate blade passing frequency (3500 Hz), but at a similar magnitude. The operation of the rotor at this condition is on the post-stall side of the stage characteristic shown in Figure 9-77. At 50 percent speed, the rotor did not seem to maintain a rotating stall (remain on the right-hand side of the characteristic), but rather moved quickly to the part span full-circumference stalled condition.

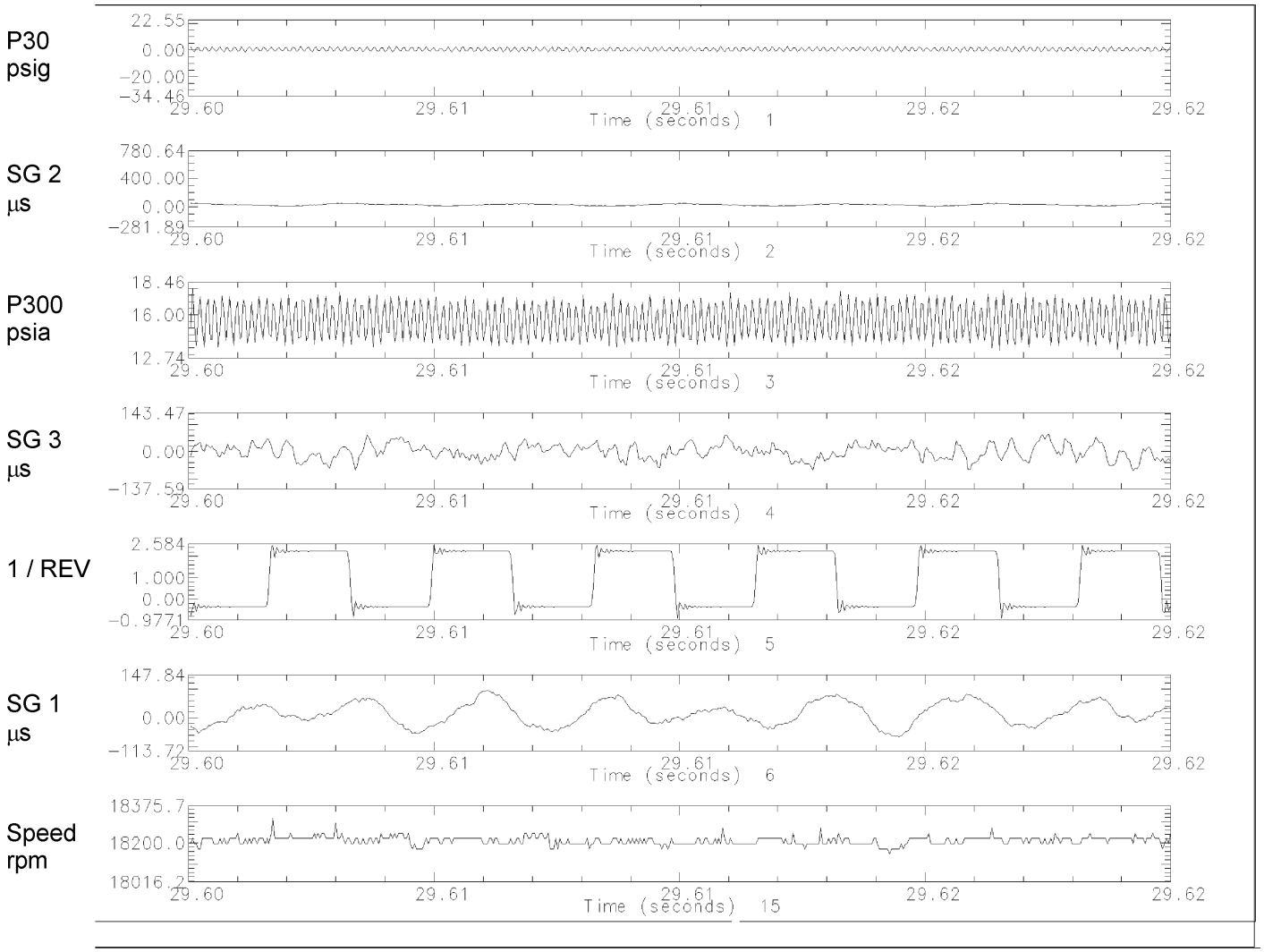

Figure 9-81. 20 ms of Data Showing Pressure and Strain Measurements at 95% Corrected Speed During Flutter Without Blade Stall.

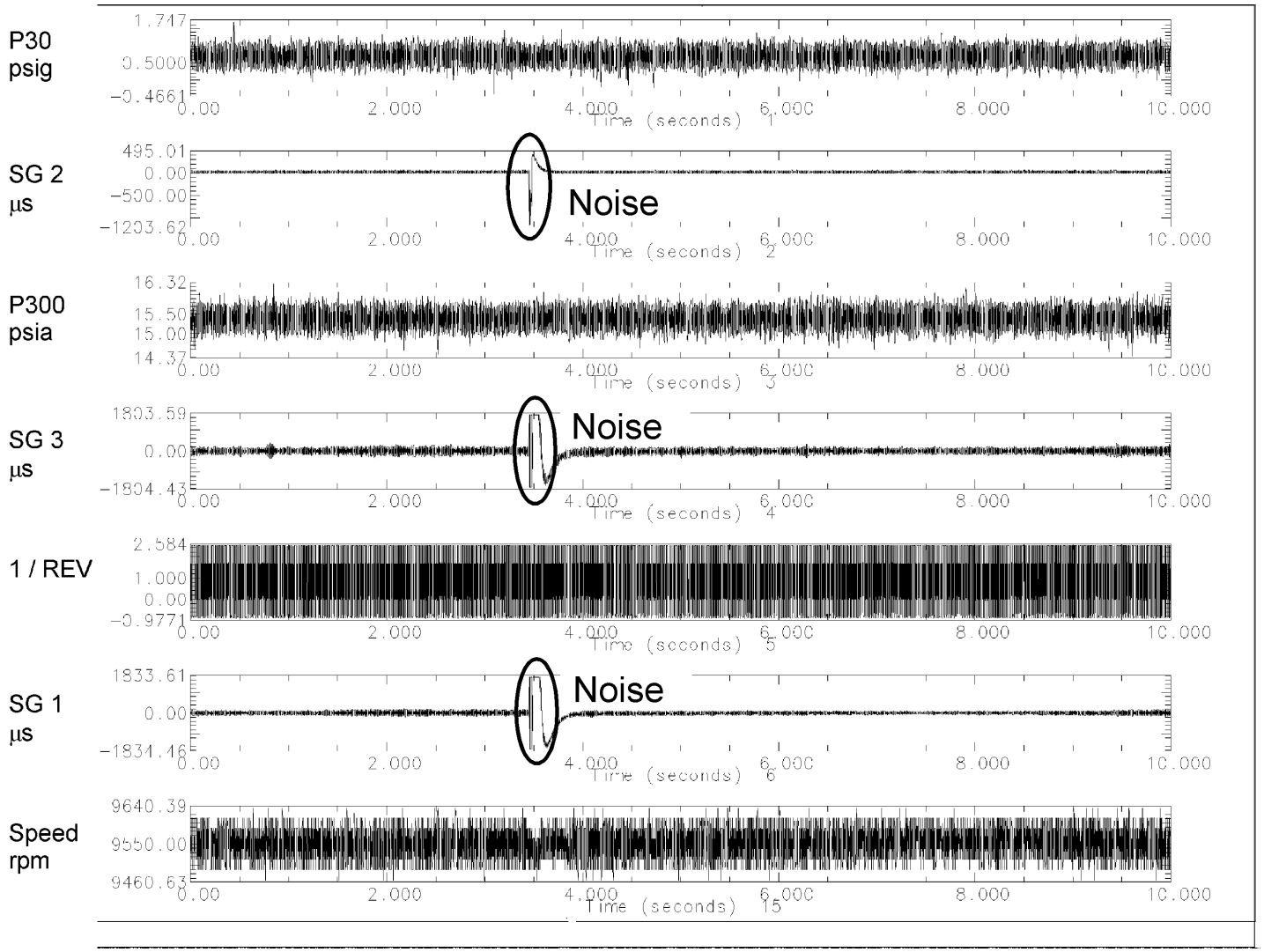

Figure 9-82. Data Showing Pressure and Strain Measurements at 50% Corrected Speed During Full-Circumference Part-Span Stall Without Flutter.

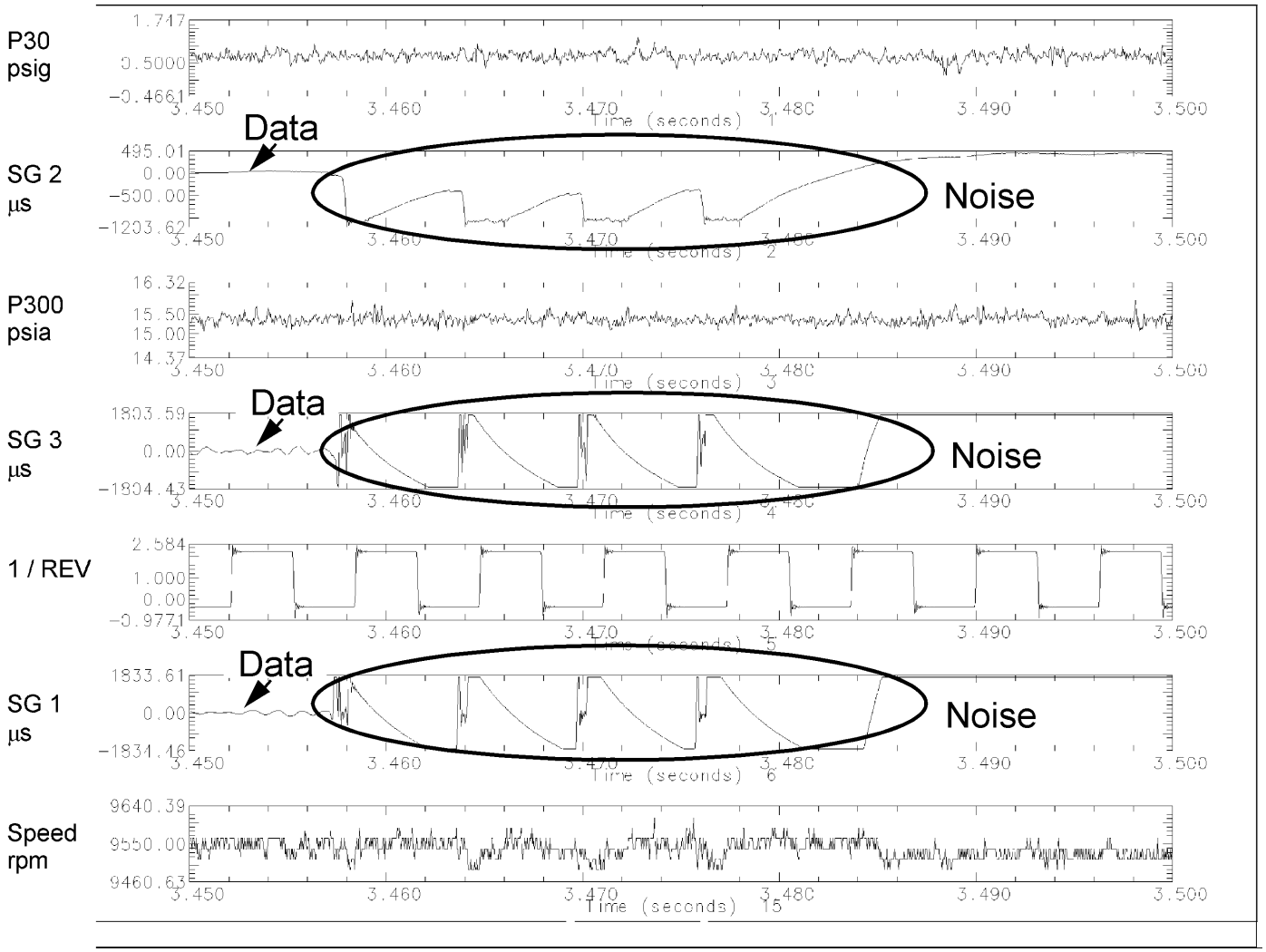

Figure 9-83. 50 ms of Data Showing Pressure and Strain Measurements at 50% Corrected Speed During Full-Circumference Part- Span Stall Without Flutter.

9.6.7 Examination of Dynamic Data at 100% and 97.5% Corrected Speed

Figure 9-85 shows the data obtained at 100 percent corrected speed. It can be clearly seen that the pressure signals show activity prior to the sudden rise in strain in SG 1 due to a flutter condition. However, SG 3 starts to show some activity at the same time as the pressure signals. Examination of this area of the time trace (200 ms starting at 22.00 seconds) is shown in Figure 9-86. It can be clearly seen that there exists a different pressure pattern at this speed than at those previously examined. Performing an auto-spectrum of the P300 trace (Figure 9-87) shows that there is a large frequency component at 20 Hz. This is typical of surge behavior, which occurs at frequencies generally less than 30 Hz, depending upon the downstream system. However, this pressure fluctuation is not surge behavior. True surge behavior has a completely different pressure characteristic than that in Figure 9-86. Figure 9-88 shows a surge characteristic from another compression system. While the system in Figure 9-88 is a three-stage machine, it is important to note that on the blowdown portion of the pressure trace (the lower part of the surge cycle shown in Figure 9-77) the magnitude of the pressure is ambient or nearly so. Clearly, the QHSF behavior in Figure 9-86 is not a surge. What the QHSF is undergoing in Figure 9-86 is what can be called "plenum breathing." Depicted on a stage characteristic (Figure 9-89), plenum breathing is an unstable condition at the stability limit of the compression system. In this case, the compression system is starting to have some airfoils stalled, but still maintains enough pumping capacity to keep a full surge cycle from occurring. For a fan of a more traditional design, surge would occur at this point since the pumping capacity would not occur.

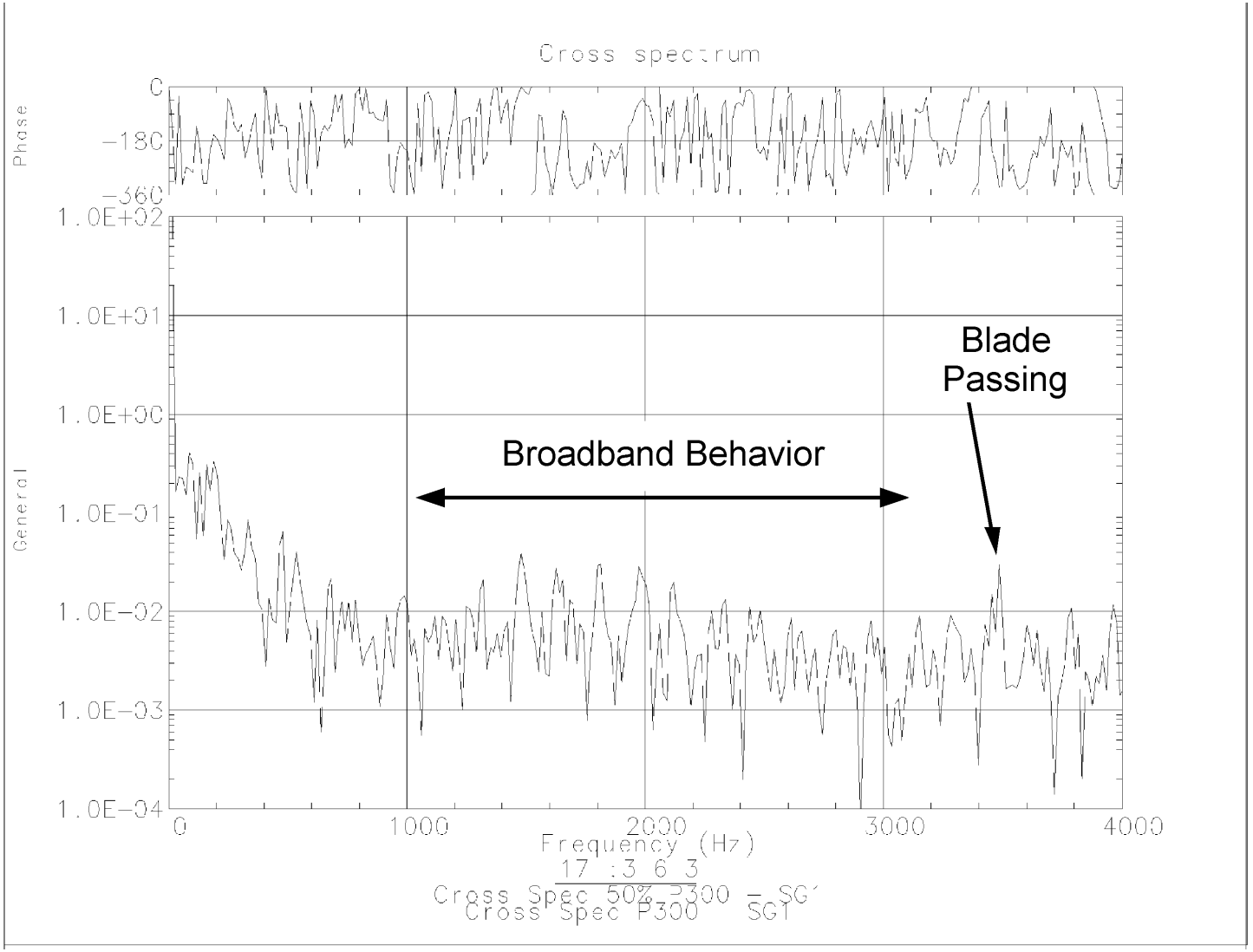

Figure 9-84. Cross Spectrum Between Pressure and Strain Measurements at 50% Corrected Speed During Full-Circumference Part-Span Stall Without Flutter Showing Typical Broadband Frequency Behavior - Approximate Blade Passing Frequency of 3500 Hz.

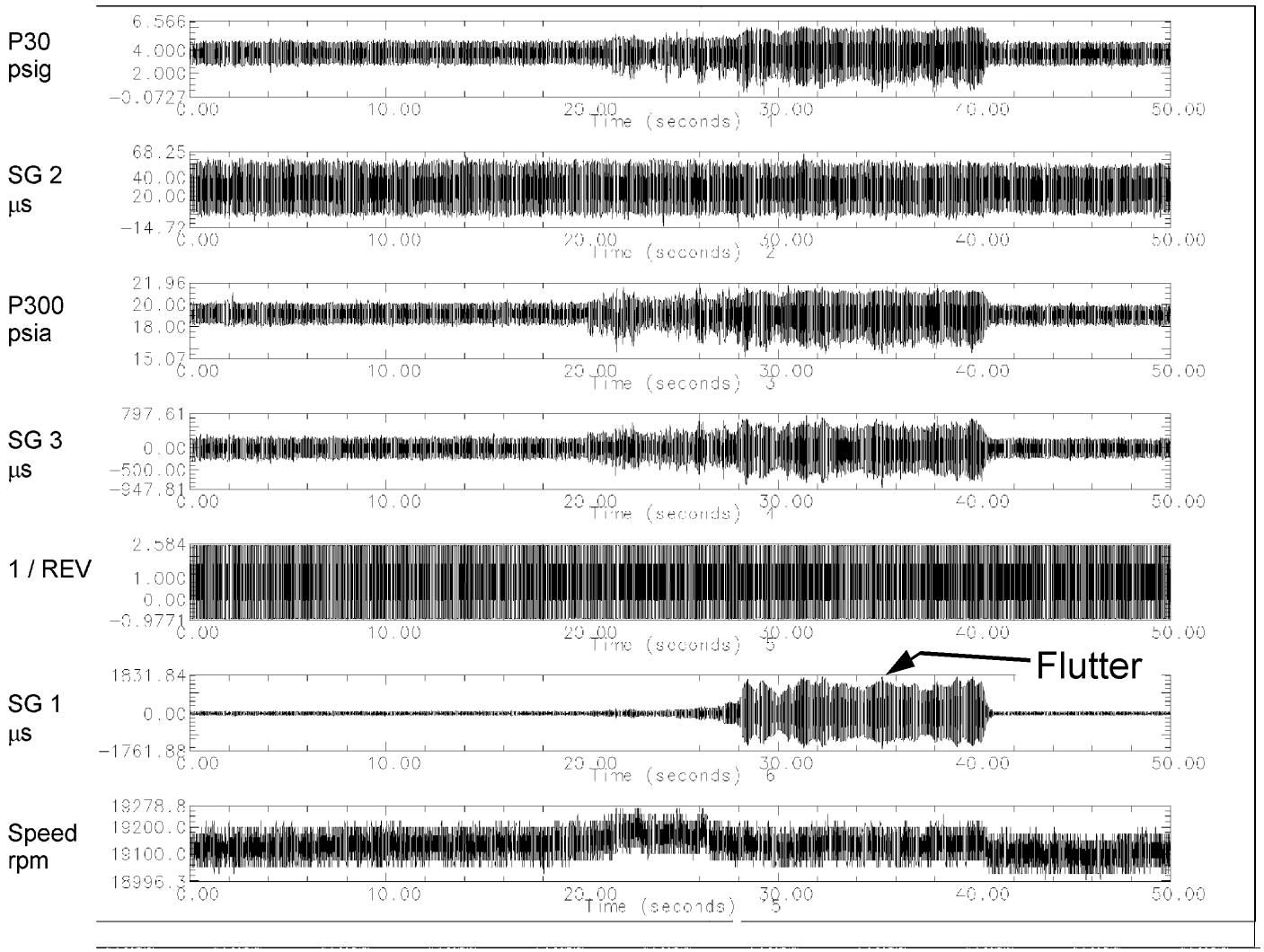

Figure 9-85. Data Obtained at 100% Corrected Speed, Showing the Sudden Increase in Strain Beginning After a Change in Pressure Behavior.

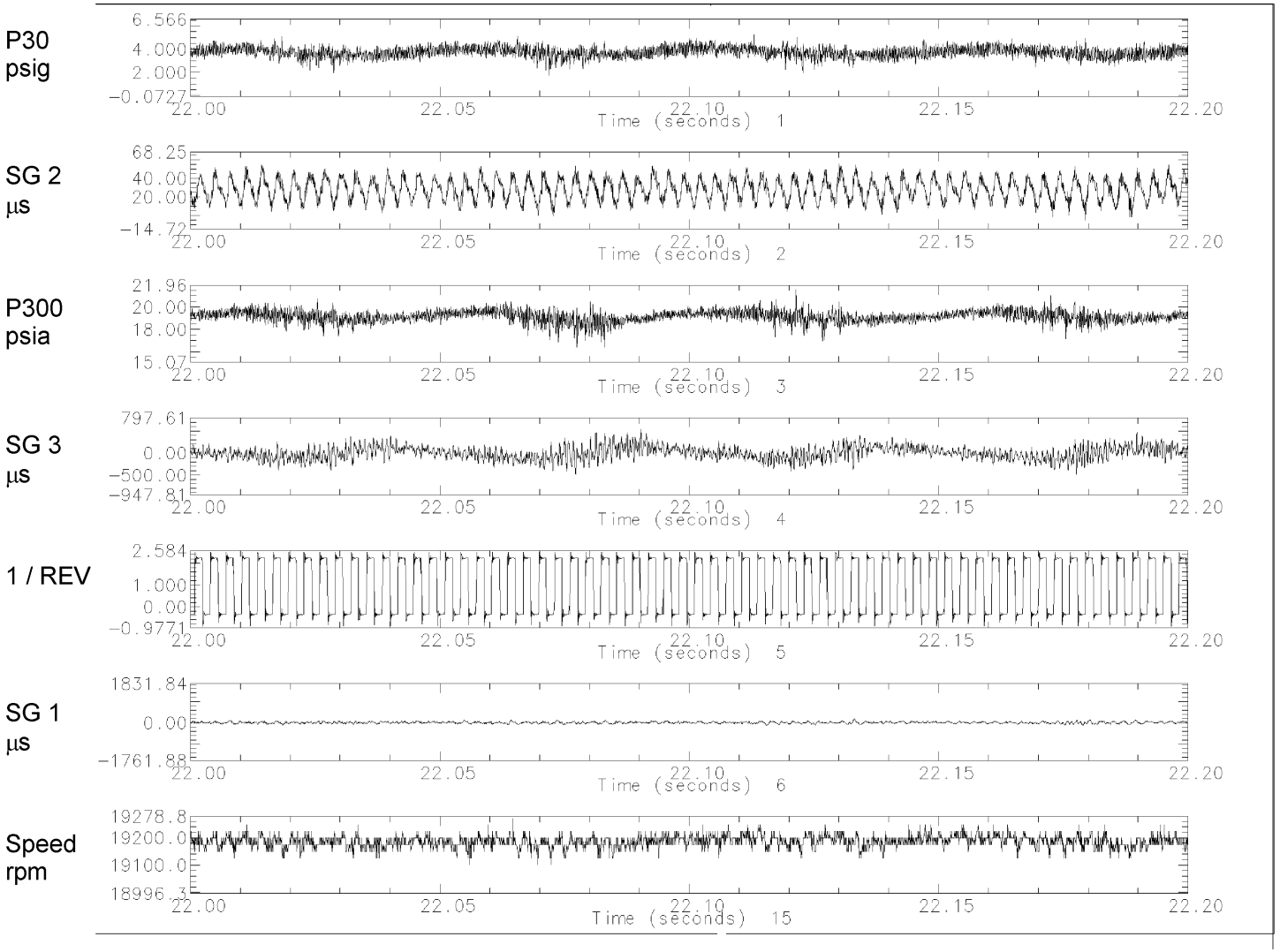

Figure 9-86. 200 ms Expansion of the Data at 22.00 Seconds Showing “Plenum Breathing” But No Flutter.

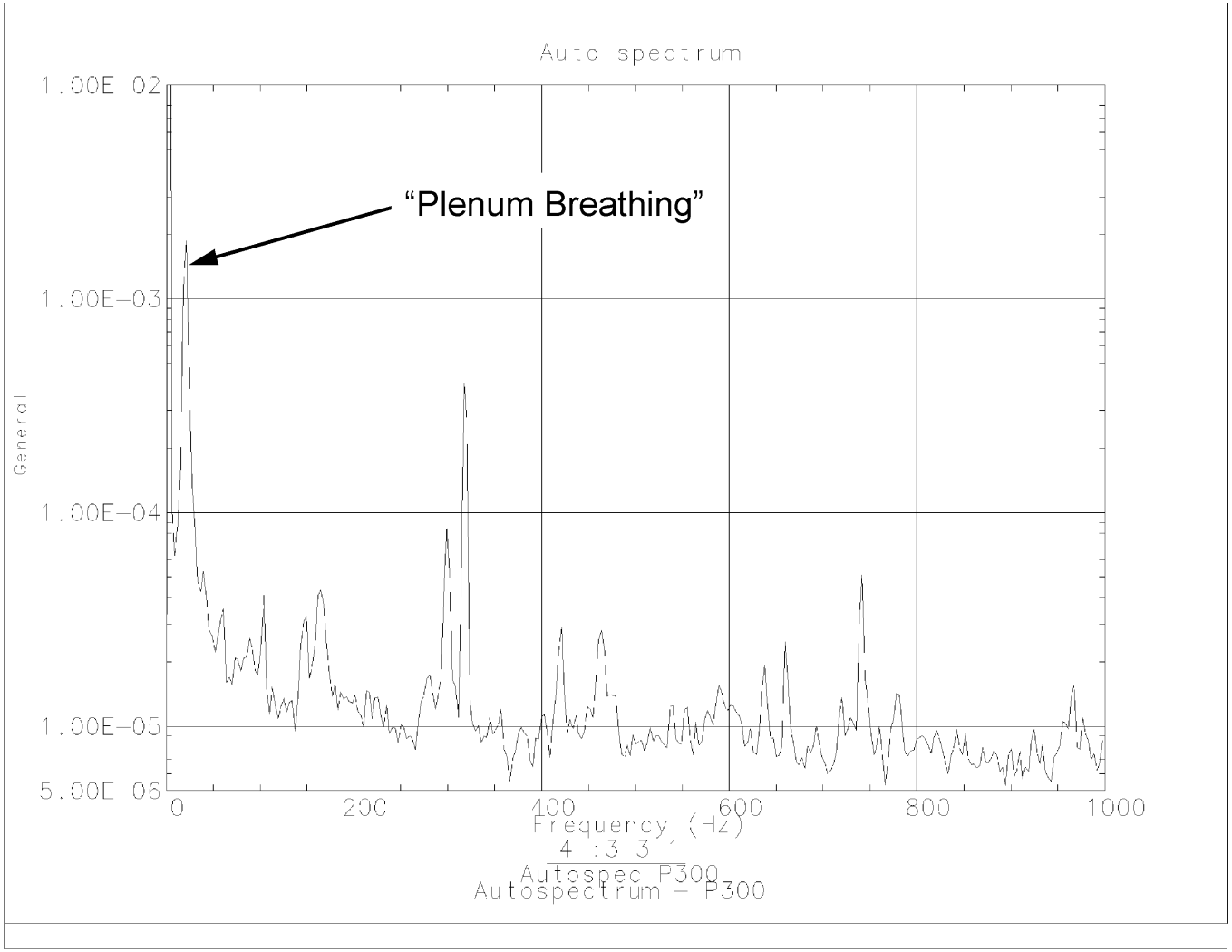

Figure 9-87. Autospectrum of the Data Obtained at 100% Corrected Speed, Showing the "Plenum Breathing" Frequency of About 20 Hz.

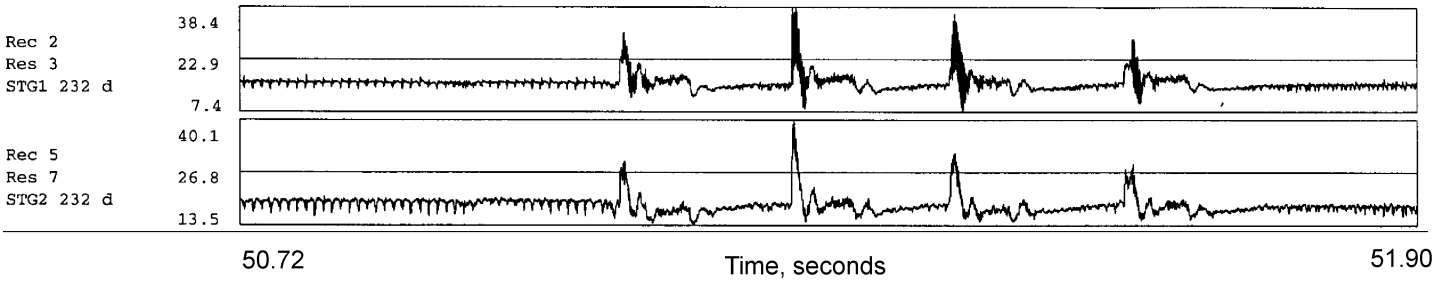

Figure 9-88. Surge Cycles Measured on a Three-Stage Compression System.

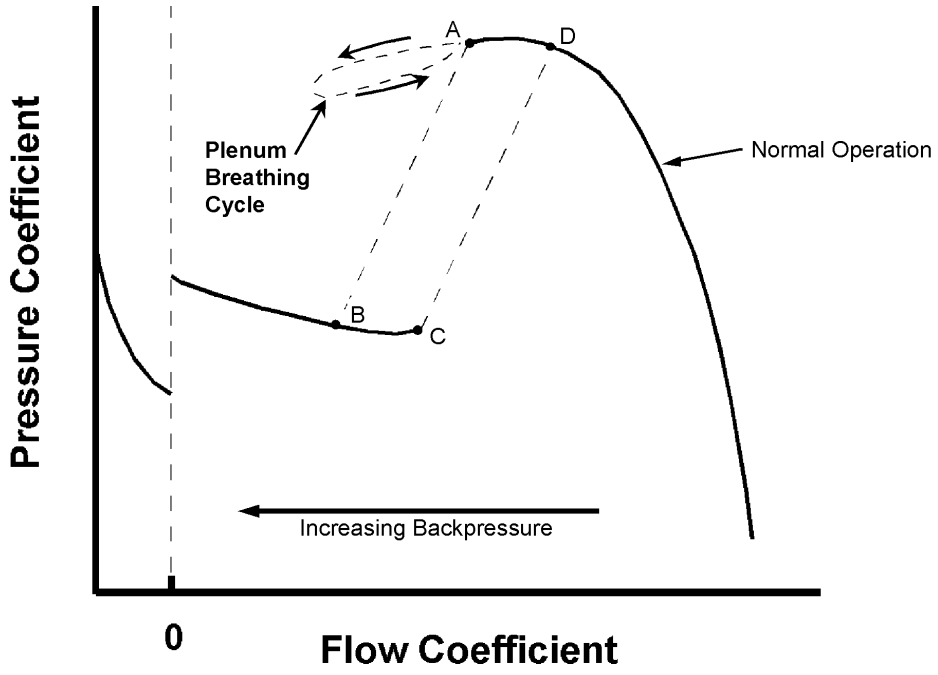

Figure 9-89. Pressure Characteristic Showing the Simulated Path of "Plenum Breathing" Seen at the Stability Limit.

Examination of the data during the time when high strains are observed shows a different behavior, as shown in Figure 9-90. During this time period, the rotor is clearly in flutter, but has been driven there by the pressure forces over the stalled airfoil. Examination of the pressure signal shows that they have a signature similar to that of a low-speed rotating stall, but not exactly the same. Figure 9-91 shows a classical rotating stall signature where there is one stall cell in the rotor. The QHSF shows three pressure disturbances in each revolution, and they have a slightly different character. A classical rotating stall pressure signature is characterized by the disappearance of the resolution of the blade wakes in the stalled sector, just as in the case of the part-span full-circumference stall. The stall in the QHSF does not show this. The blade wakes are seen throughout the pressure field.

In addition, there are three stall disturbances existing in the time of one rotor revolution. Figures 9-92 and 9-93 show the data obtained at 97.5 percent corrected speed. Similar characteristics are seen at 97.5 percent corrected speed and at 100 percent corrected speed. To clarify that the pressure disturbance seen as "high-speed sustainable stall" is in fact rotating, a cross spectrum was performed between the two pressure transducers for the 97.5 percent corrected speed case. Figure 9-94 shows the frequency (1039 Hz) of the rotating of the stall. The phase on the plot is indicative of the rotational spacing between the two transducers. Also indicative of this type of stalling behavior is the speed variation seen in Figure 9-93 as the rotor pressure loading changes.

Under these stalled conditions (found at 97.5 and 100 percent corrected speed), the rotor is operating on the post-stall side of the pressure characteristic in the multiple stall cell region of the characteristic. This makes physical sense when considering the progression into this behavior. It started with increasing the back pressure on the rotor until plenum breathing was reached. Still being able to pump due to the high-forward sweep of the blade and the fact that the particles of fluid in the shifted streamlines are able to progress over more of the chord of the blade (being swept as it is), the stage continues to retard surge behavior. The stall, however, becomes stronger and stronger until the operating point moves to the post-stall characteristic. The fact that blade wakes can still be seen in the data means that a significant portion of the rotor is still producing pressure rise, in fact, more than a conventional rotor in this state which would have surged when the plenum breathing started at high-speed.

If the pressure signal is a sustainable high-speed stall and it is causing the blade to flutter, then the excitation frequencies of the flutter should exist in the pressure trace. Figure 9-95 shows a cross spectrum between the pressure measurement P30 and the strain gauge SG 1. The 400 Hz frequency exists in both the pressure and strain data. The one-per-revolution frequency at about 320 Hz can be seen, as well as the 20 Hz plenum breathing. Examination of the phase information at the 400 Hz flutter frequency shows that the pressure signal leads the strain response (when taking into account the slight distance between the rotor and the pressure transducer). This phase lead indicates stall flutter, rather than self-excited flutter as was seen at 90 and 95 percent corrected speeds. The coherence plot in Figure 9-96 shows the strong association between the pressure and strain signals at the associated frequencies.

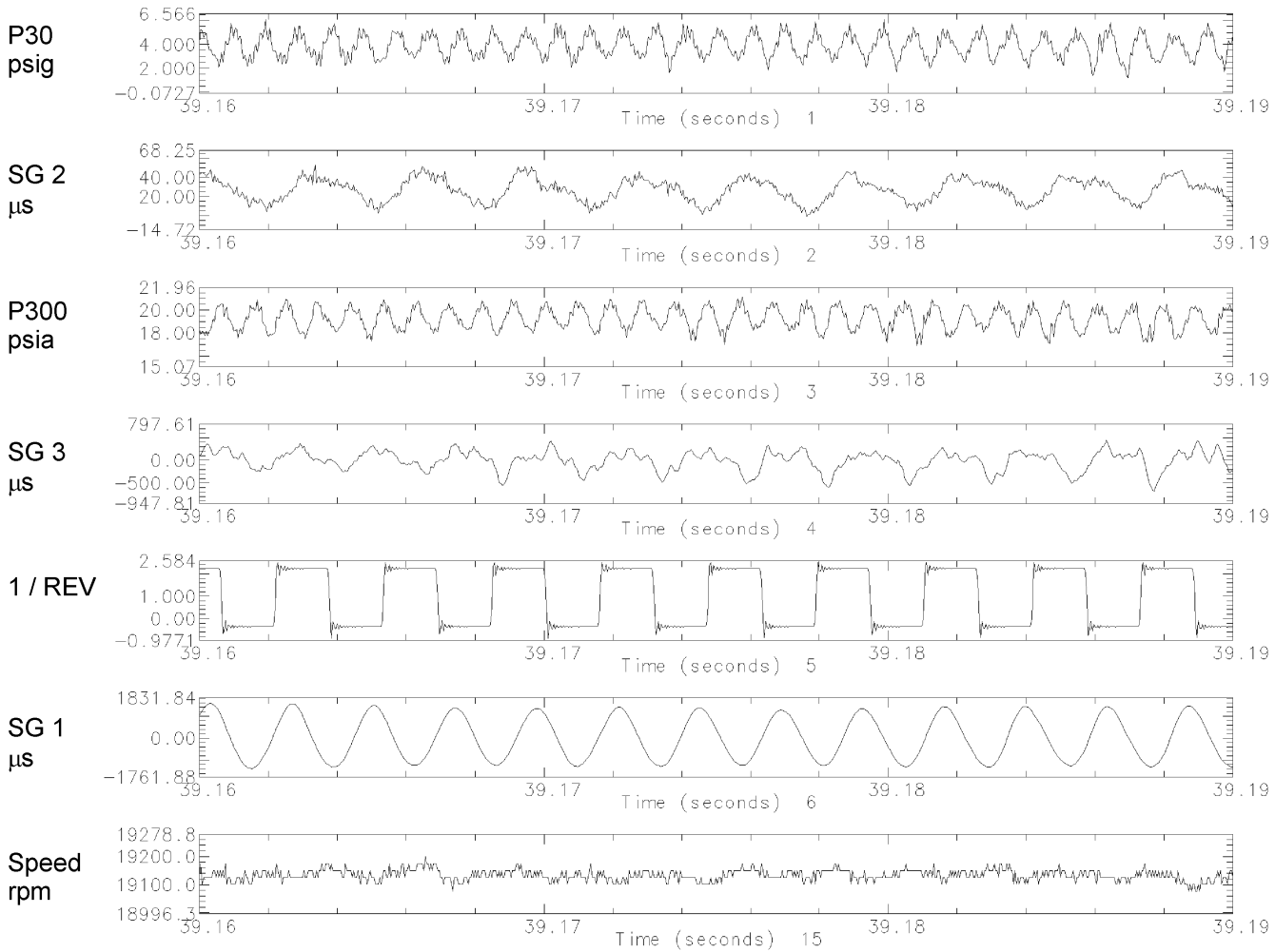

Figure 9-90. 30 ms of Data During the Flutter Event at 100% Corrected Speed "High-Speed Sustainable Stall" Is Present.

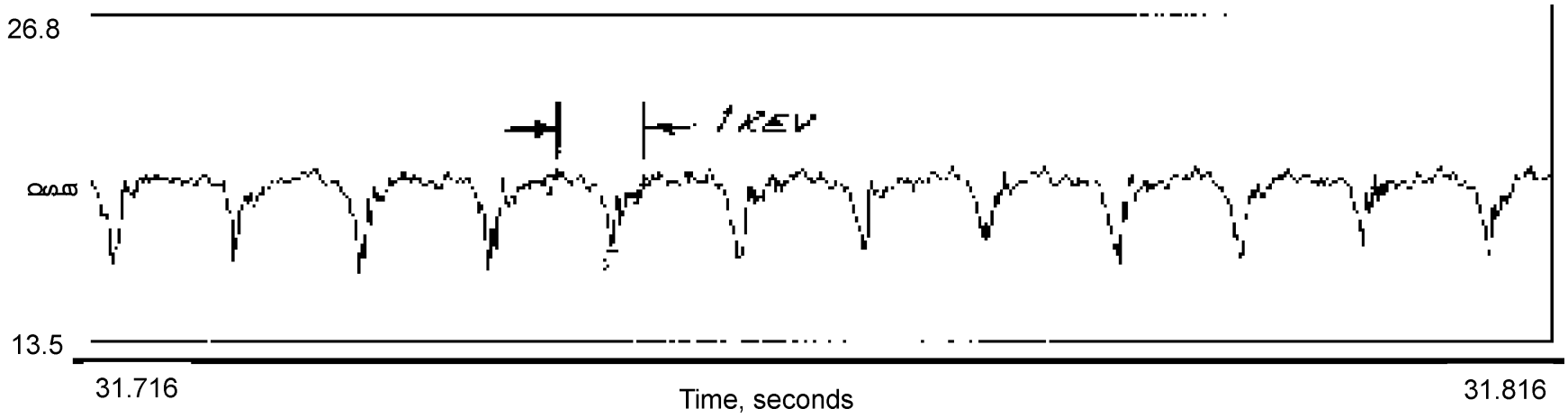

Figure 9-91. Example of Classical Rotating Stall from Another Compression System.

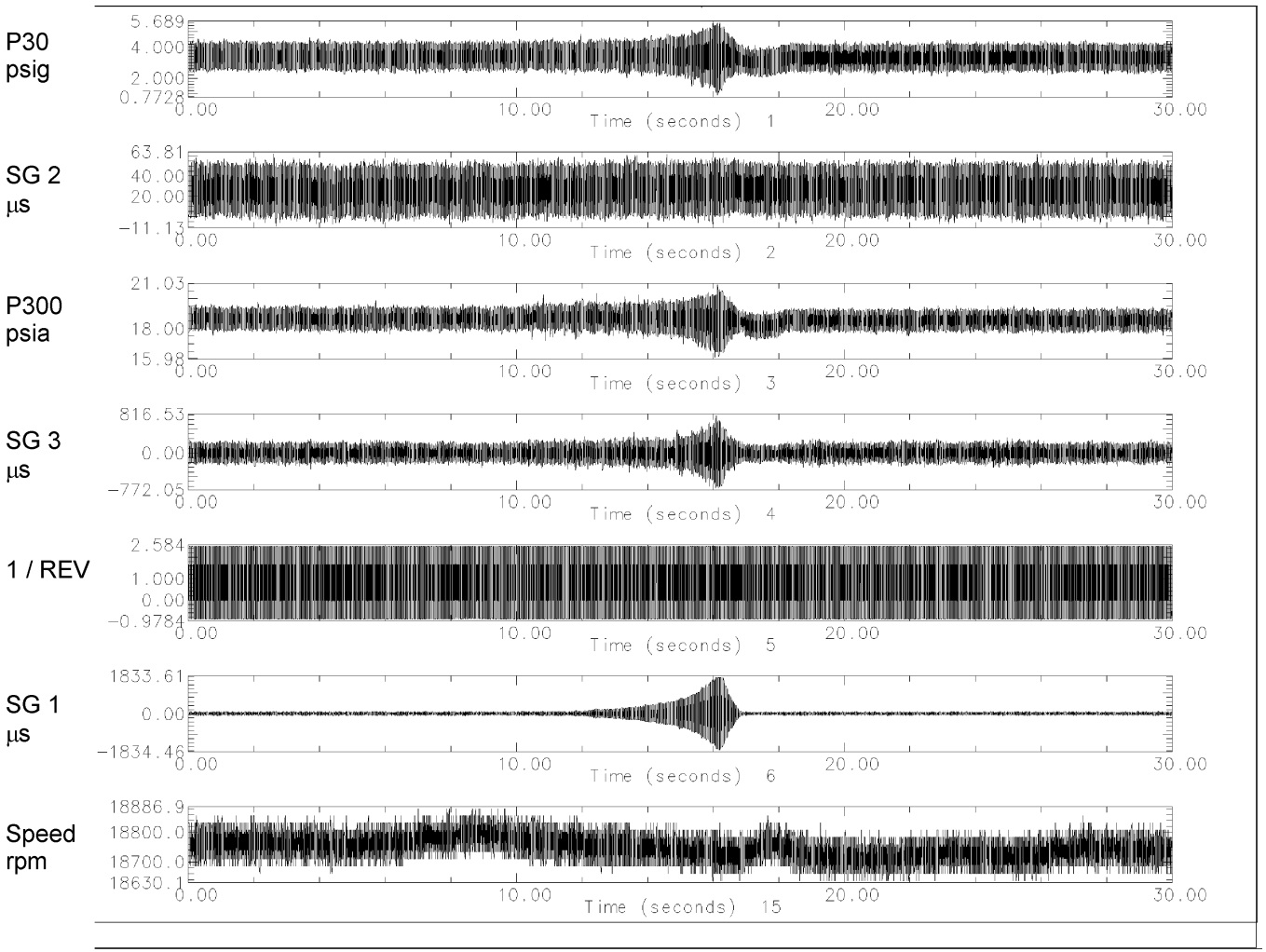

Figure 9-92. Data at 97% Corrected Speed Shows a Similar Characteristic to that at 100% Corrected Speed.

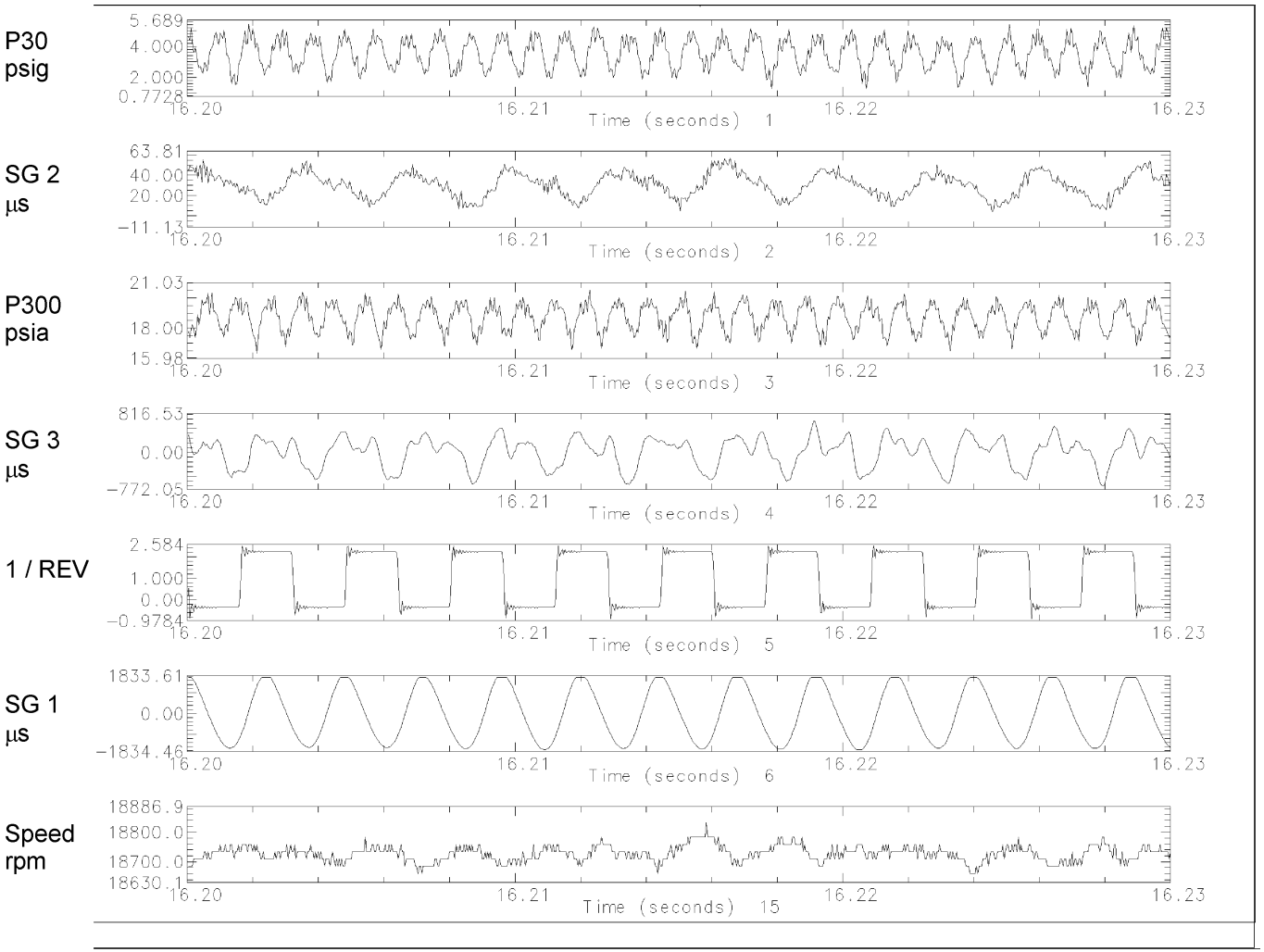

Figure 9-93. 30 ms Expansion of the Data at 97.5% Corrected Speed at 16.2 Seconds Showing "High-Speed Sustainable Stall" to be Similar to that at 100% Corrected Speed.

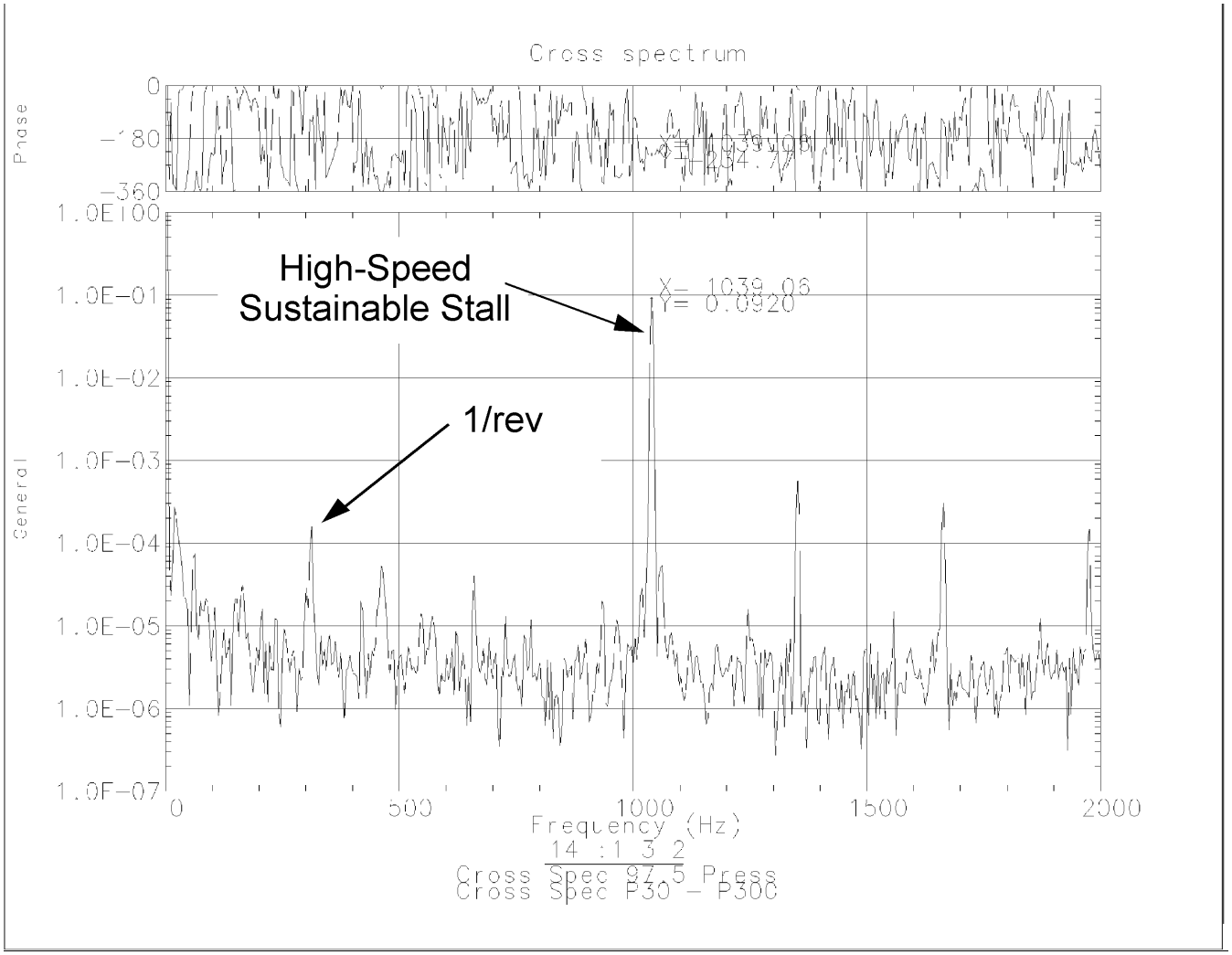

Figure 9-94. Cross-Spectrum Between Pressure Signals showing the Frequency Associated With the "High-Speed Sustainable Stall" at 100% Corrected Speed.

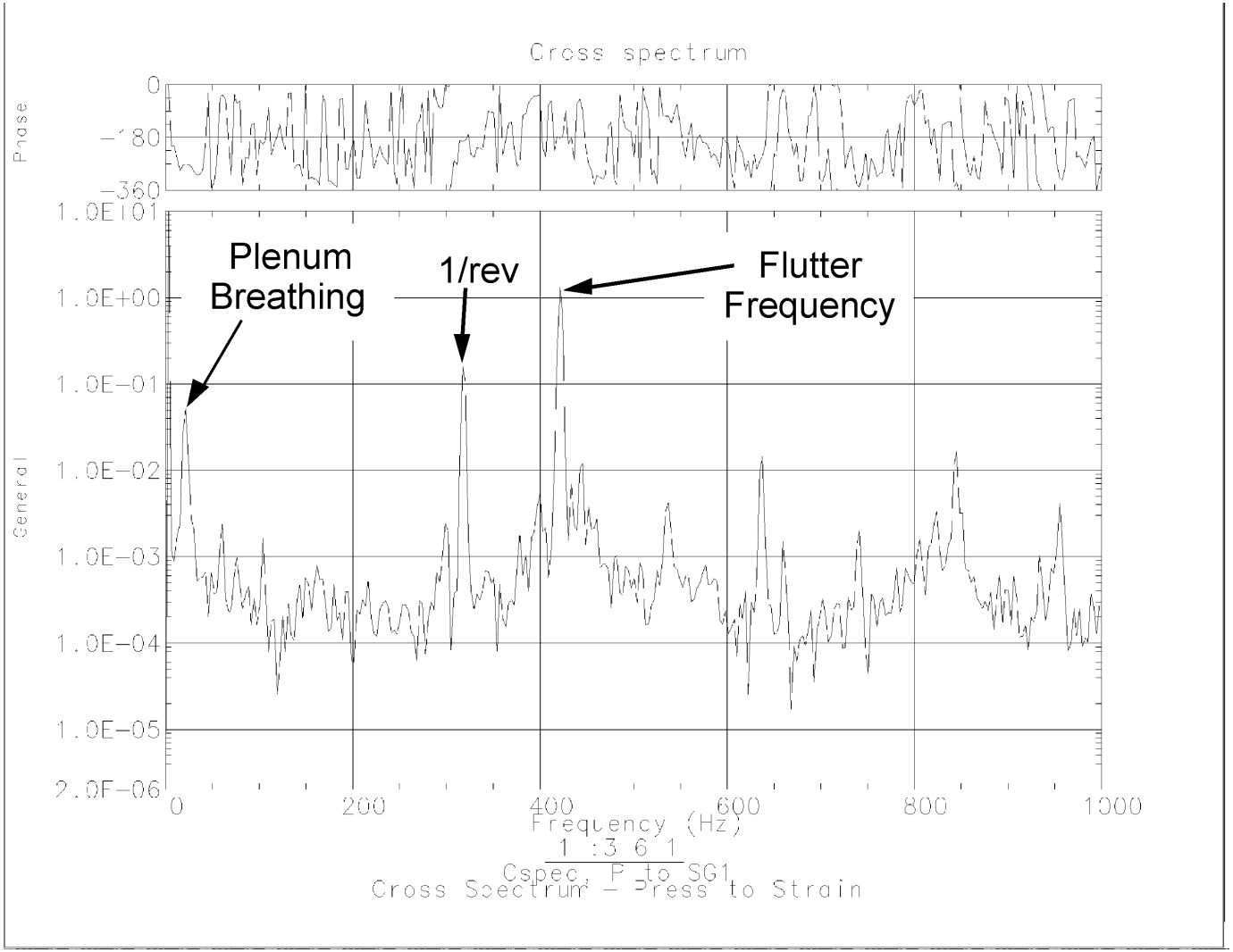

Figure 9-95. Cross-Spectrum Between Pressure Signal P30 and Strain Gauge SG1 Showing the Frequencies Common to Both (100% Corrected Speed).

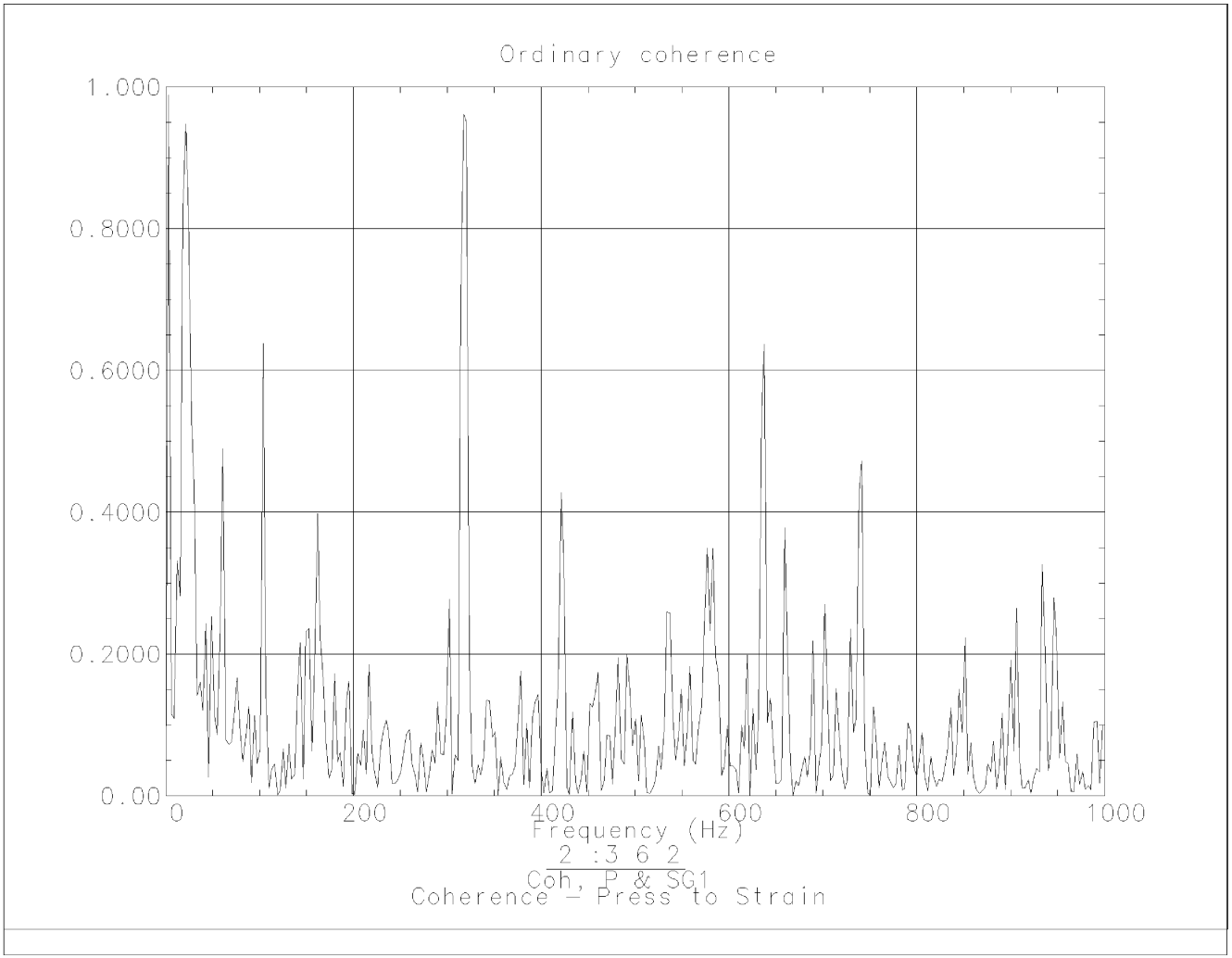

Figure 9-96. Coherence Between Pressure Signal P30 and Strain Gauge SG1 Showing the Strong Association Between the Frequencies Common to Both (100% Corrected Speed).

10. CONCLUSIONS AND RECOMMENDATIONS

The QHSF has been designed to meet aggressive acoustic goals while maintaining performance and mechanical qualities equal to or better than the baseline fan. The design was achieved through innovative use of advanced design techniques and close cooperation between the design disciplines.

The studies of flow physics using the DAWES program showed that the use of a CFD tool is feasible for predicting flow behavior that impacts noise generation. The DAWES program was able to predict inlet shock location, and relate that location to the presence or absence of MPT noise.

The Adamczyk Average-Passage program, SSTAGE, was used to predict flow behavior for both the baseline and QHSF fan rotors, using both the rotor-only and stage analysis models. In general, shock behavior and shape were similar for the rotor-only and stage analyses. However, details of the shock structure were somewhat different.

Acoustic analysis tools from the NASA Advanced Subsonic Technology Noise Reduction program have been successfully applied to design an advanced fan.

Instability through either blade flutter or rotating stall prevented the QHSF from achieving the surge margin required at part speed to be a viable fan for commercial application without a significant redesign effort.

It is recommended for the 22-inch diameter QHSF wind tunnel testing to be completed at NASA Glenn that cold build clearances be obtained prior to testing and the blade tip contour is corrected if necessary in order to run at a constant design clearance of 0.017 inch.

11. REFERENCES

1. Hayden, R.E., Bliss, D.B., Murray, B.S., Chandiramani, K.L,Smullin., J.I., Schwaar, P.G., "Analysis and Design of a High-Speed, Low-Noise Aircraft Fan Incorporating Swept Leading Edge Rotor and Stator Blades", NASA CR-135092, December 1977.

2. Repp, R., Gentile, D., Hanson, D., Chunduru, S., "NAS3-27752, NASA AST - AOI 14, Design and Test of Fan/Nacelle Models, Quiet High-Speed Fan Design Report", AE Report 21-9591, March 31, 1997. CR–2003–212369, July 2003.

3. Storace, A.F., "Foreign Object Damage Criteria", AFAPL -TR-78-81 Volume IV Aero Propulsion Laboratory (AFWAL/POTA), Air Force Wright Aeronautical Laboratories, January, 1985.

4. Dawes, W.N., "A Numerical Analysis of the Three-Dimensional Viscous Flow in a Transonic Compressor Rotor and Comparison With Experiment," *ASME Paper 86-GT-16*, June 1986.

5. User's Guide for FLUENT/UNS and RAMPANT, Release 4.0, Fluent, Inc., April 1996.

6. Adamczyk, J.J., "Model Equations for Simulating Flows in Multistage Turbomachinery," *ASME Paper 85-GT-226*, March 1985.

7. Adamczyk, J.J., Mulac, R.A., Celestina, M.L., "A Model for Closing the Inviscid Form of the Average-Passage Equation System," *ASME Paper 86-GT-227*, June 1986.

8. Kester, J. D., "Generation and Suppression of Combination Tone Noise from Turbofan Engines", *Proceedings AGARD Fluid Dynamics Panel*, Saint-Louis, France, May 1969.

9. Sofrin, T. G., Pickett, G. F., "Multiple Pure Tone Noise Generated by Fans at Supersonic Tip Speeds," *Fluid Mechanics, Acoustics, and Design of Turbomachinery Symposium*, Penn State, 1970.

10. Morfey, C. L., Fisher, M. J., "Shock Wave Radiation from a Supersonic Ducted Rotor," *The Aeronautical Journal of the Royal Aeronautical Society*, 74, July 1970, pp. 579-585.

11. Hawkings, D., "Multiple Tone Generation by Transonic Compressors," *Journal of Sound and Vibration*, Vol. 17 (2), 1971, pp. 241-250.

12. Kurosaka, M., "A Note on Multiple Pure Tone Noise," *Journal of Sound and Vibration*, Vol. 19 (4), 1971, pp. 453-462.

13. Pickett, G. F., "The Prediction of the Spectral Content of Combination Tone Noise," *AIAA Paper 71-730*, 1971.

14. Fink, M. R., "Shock Wave Behavior in Transonic Compressor Noise Generation," *ASME Paper 71-GT-7*, 1971.

15. Kantola, R. A., and Kurosaka, M., "The Theoretical and Experimental Investigations on Multiple Pure Tone Noise," *AIAA Paper 72-127*, 1972.

16. Stratford, B. S., Newby, D. R., A New Look at the Generation of Buzz-Saw Noise, *AIAA Paper 77-1343*, 1977.

17. Cargill, A. M., "Shock Waves Ahead of a Fan With Nonuniform Blades," *AIAA Journal*, Vol. 21, No. 4, April 1983, pp. 572-578.

18. Kantola, R. A., Kurosaka, M., "The Theoretical and Experimental Investigations on Multiple Pure Tone Noise, Part 1," *NASA-CR-1831*, 1971.

19. Goldstein, A. W., Glaser, F. W., Coats, J. W., *Acoustic Properties of a Supersonic Fan*, NASA Lewis Research Center, 1972.

20. Kumasaka, H.A. and Weir, D.S., "Definition of the 1992 Technology Aircraft Noise Levels and the Methodology for Assessing Airplane Noise Impact of Component Noise Reduction Concepts," NASA CR-198298, March 1995.

21. Cousins, W.T., "The Dynamics of Stall and Surge Behavior in Axial-Centrifugal Compressors," Ph.D. Dissertation, Virginia Polytechnic Institute and State University, Blacksburg, VA, 1997.

APPENDIX I

INSTRUMENTATION MASTER NUMBER LIST

(7 pages)

Measurement	Part Number	Instrumentation	Identification Tag	Model Number	Escort Name	Theta Loc. (CWFLA)	Radial Loc.	Axial Loc.
Inlet Pressure	MCP-0004003	Wall Static Pressures	612 / PS20(1)	612	PS20(1)	9	N/A	2.118
			613 / PS20(2)	613	PS20(2)	36	N/A	2.118
			614 / PS20(3)	614	PS20(3)	72	N/A	2.118
			615 / PS20(4)	615	PS20(4)	108	N/A	2.118
			616 / PS20(5)	616	PS20(5)	144	N/A	2.118
			617 / PS20(6)	617	PS20(6)	180	N/A	2.118
			618 / PS20(7)	618	PS20(7)	216	N/A	2.118
			619 / PS20(8)	619	PS20(8)	252	N/A	2.118
			620 / PS20(9)	620	PS20(9)	288	N/A	2.118
			621 / PS20(10)	621	PS20(10)	324	N/A	2.118
Total Pressure	Lab	Inlet Boundary Layer Rakes	1712 / PB20(01)	1712	PB20(1)	18	0.482	N/A
			1713 / PB20(02)	1713	PB20(2)	18	0.517	N/A
			1714 / PB20(03)	1714	PB20(3)	18	0.571	N/A
			1715 / PB20(04)	1715	PB20(4)	18	0.679	N/A
			1716 / PB20(05)	1716	PB20(5)	18	0.822	N/A
			1717 / PB20(06)	1717	PB20(6)	18	0.965	N/A
			1718 / PB20(07)	1718	PB20(7)	18	1.109	N/A
			1719 / PB20(08)	1719	PB20(8)	18	1.252	N/A
			1720 / PB20(09)	1720	PB20(9)	18	1.395	N/A
			1721 / PB20(10)	1721	PB20(10)	18	1.539	N/A
			1722 / PB20(11)	1722	PB20(11)	90	0.482	N/A
			1723 / PB20(12)	1723	PB20(12)	90	0.517	N/A
			1724 / PB20(13)	1724	PB20(13)	90	0.571	N/A
			1725 / PB20(14)	1725	PB20(14)	90	0.679	N/A
			1726 / PB20(15)	1726	PB20(15)	90	0.822	N/A
			1727 / PB20(16)	1727	PB20(16)	90	0.965	N/A
			1728 / PB20(17)	1728	PB20(17)	90	1.109	N/A
			1729 / PB20(18)	1729	PB20(18)	90	1.252	N/A
			1730 / PB20(19)	1730	PB20(19)	90	1.395	N/A
			1731 / PB20(20)	1731	PB20(20)	90	1.539	N/A
			1732 / PB20(21)	1732	PB20(21)	162	0.482	N/A
			1802 / PB20(22)	1802	PB20(22)	162	0.517	N/A

Measurement	Part Number	Instrumentation	Identification Tag	Model Number	Escort Name	Theta Loc. (CWFLA)	Radial Loc.	Axial Loc.
			1803 / PB20(23)	1803	PB20(23)	162	0.571	N/A
			1804 / PB20(24)	1804	PB20(24)	162	0.679	N/A
			1805 / PB20(25)	1805	PB20(25)	162	0.822	N/A
			1806 / PB20(26)	1806	PB20(26)	162	0.965	N/A
			1807 / PB20(27)	1807	PB20(27)	162	1.109	N/A
			1808 / PB20(28)	1808	PB20(28)	162	1.252	N/A
			1809 / PB20(29)	1809	PB20(29)	162	1.395	N/A
			1810 / PB20(30)	1810	PB20(30)	162	1.539	N/A
			1811 / PB20(31)	1811	PB20(31)	234	0.482	N/A
			1812 / PB20(32)	1812	PB20(32)	234	0.517	N/A
			1813 / PB20(33)	1813	PB20(33)	234	0.571	N/A
			1814 / PB20(34)	1814	PB20(34)	234	0.679	N/A
			1815 / PB20(35)	1815	PB20(35)	234	0.822	N/A
			1816 / PB20(36)	1816	PB20(36)	234	0.965	N/A
			1817 / PB20(37)	1817	PB20(37)	234	1.109	N/A
			1818 / PB20(38)	1818	PB20(38)	234	1.252	N/A
			1819 / PB20(39)	1819	PB20(39)	234	1.395	N/A
			1820 / PB20(40)	1820	PB20(40)	234	1.539	N/A
			1821 / PB20(41)	1821	PB20(41)	306	0.482	N/A
			1822 / PB20(42)	1822	PB20(42)	306	0.517	N/A
			1823 / PB20(43)	1823	PB20(43)	306	0.571	N/A
			1824 / PB20(44)	1824	PB20(44)	306	0.679	N/A
			1825 / PB20(45)	1825	PB20(45)	306	0.822	N/A
			1826 / PB20(46)	1826	PB20(46)	306	0.965	N/A
			1827 / PB20(47)	1827	PB20(47)	306	1.109	N/A
			1828 / PB20(48)	1828	PB20(48)	306	1.252	N/A
			1829 / PB20(49)	1829	PB20(49)	306	1.395	N/A
			1830 / PB20(50)	1830	PB20(50)	306	1.539	N/A
Vane exit pressure	MCP-0004042	Strut leading edge probes 10 immersions/ 5 struts	2002 / PT17(01)	2002	PT17(1)	0	8.3% bypass	N/A
			2003 / PT17(02)	2003	PT17(2)	0	25% bypass	N/A
			2004 / PT17(03)	2004	PT17(3)	0	41.7% bypass	N/A
			2005 / PT17(04)	2005	PT17(4)	0	58.3% bypass	N/A
			2006 / PT17(05)	2006	PT17(5)	0	75% bypass	N/A

Measurement	Part Number	Instrumentation	Identification Tag	Model Number	Escort Name	Theta Loc. (CWFLA)	Radial Loc.	Axial Loc.
			2007 / PT17(06)	2007	PT17(6)	0	91.7% bypass	N/A
			2008 / PT17(07)	2008	PT17(7)	72	8.3% bypass	N/A
			2009 / PT17(08)	2009	PT17(8)	72	25% bypass	N/A
			2010 / PT17(09)	2010	PT17(9)	72	41.7% bypass	N/A
			2011 / PT17(10)	2011	PT17(10)	72	58.3% bypass	N/A
			2012 / PT17(11)	2012	PT17(11)	72	75% bypass	N/A
			2013 / PT17(12)	2013	PT17(12)	72	91.7% bypass	N/A
			2014 / PT17(13)	2014	PT17(13)	144	8.3% bypass	N/A
			2015 / PT17(14)	2015	PT17(14)	144	25% bypass	N/A
			2016 / PT17(15)	2016	PT17(15)	144	41.7% bypass	N/A
			2017 / PT17(16)	2017	PT17(16)	144	58.3% bypass	N/A
			2018 / PT17(17)	2018	PT17(17)	144	75% bypass	N/A
			2019 / PT17(18)	2019	PT17(18)	144	91.7% bypass	N/A
			2020 / PT17(19)	2020	PT17(19)	216	8.3% bypass	N/A
			2021 / PT17(20)	2021	PT17(20)	216	25% bypass	N/A
			2022 / PT17(21)	2022	PT17(21)	216	41.7% bypass	N/A
			2023 / PT17(22)	2023	PT17(22)	216	58.3% bypass	N/A
			2024 / PT17(23)	2024	PT17(23)	216	75% bypass	N/A
			2025 / PT17(24)	2025	PT17(24)	216	91.7% bypass	N/A
			2026 / PT17(25)	2026	PT17(25)	288	8.3% bypass	N/A
			2027 / PT17(26)	2027	PT17(26)	288	25% bypass	N/A
			2028 / PT17(27)	2028	PT17(27)	288	41.7% bypass	N/A
			2029 / PT17(28)	2029	PT17(28)	288	58.3% bypass	N/A
			2030 / PT17(29)	2030	PT17(29)	288	75% bypass	N/A
			2031 / PT17(30)	2031	PT17(30)	288	91.7% bypass	N/A
			2202 / PT025(01)	2202	PT025(1)	0	12.5% core	N/A
			2203 / PT025(02)	2203	PT025(2)	0	37.5% core	N/A
			2204 / PT025(03)	2204	PT025(3)	0	62.5% core	N/A
			2205 / PT025(04)	2205	PT025(4)	0	87.5% core	N/A
			2207 / PT025(05)	2207	PT025(5)	72	12.5% core	N/A
			2208 / PT025(06)	2208	PT025(6)	72	37.5% core	N/A
			2209 / PT025(07)	2209	PT025(7)	72	62.5% core	N/A
			2210 / PT025(08)	2210	PT025(8)	72	87.5% core	N/A

Measurement	Part Number	Instrumentation	Identification Tag	Model Number	Escort Name	Theta Loc. (CWFLA)	Radial Loc.	Axial Loc.
			2212 / PT025(09)	2212	PT025(9)	144	12.5% core	N/A
			2213 / PT025(10)	2213	PT025(10)	144	37.5% core	N/A
			2214 / PT025(11)	2214	PT025(11)	144	62.5% core	N/A
			2215 / PT025(12)	2215	PT025(12)	144	87.5% core	N/A
			2217 / PT025(13)	2217	PT025(13)	216	12.5% core	N/A
			2218 / PT025(14)	2218	PT025(14)	216	37.5% core	N/A
			2219 / PT025(15)	2219	PT025(15)	216	62.5% core	N/A
			2220 / PT025(16)	2220	PT025(16)	216	87.5% core	N/A
			2222 / PT025(17)	2222	PT025(17)	288	12.5% core	N/A
			2223 / PT025(18)	2223	PT025(18)	288	37.5% core	N/A
			2224 / PT025(19)	2224	PT025(19)	288	62.5% core	N/A
			2225 / PT025(20)	2225	PT025(20)	288	87.5% core	N/A
Vane Exit Pressure	MCP-0004042	Wall static pressure Pressure taps on inner and outer wall	1512 / PSCII(1)	1512	PSCII(1)	18	5.985	0.805
			1513 / PSCII(2)	1513	PSCII(2)	90	5.985	0.805
			1514 / PSCII(3)	1514	PSCII(3)	162	5.985	0.805
			1515 / PSCII(4)	1515	PSCII(4)	234	5.985	0.805
			1516 / PSCII(5)	1516	PSCII(5)	306	5.985	0.805
			1502 / PSCIO(1)	1502	PSCIO(1)	18	7.125	1.771
			1503 / PSCIO(2)	1503	PSCIO(2)	90	7.125	1.771
			1504 / PSCIO(3)	1504	PSCIO(3)	162	7.125	1.771
			1505 / PSCIO(4)	1505	PSCIO(4)	234	7.125	1.771
			1506 / PSCIO(5)	1506	PSCIO(5)	306	7.125	1.771
			1302 / PS17I(1)	1302	PS17I(1)	18	7.5325	1.932
			1303 / PS17I(2)	1303	PS17I(2)	90	7.5325	1.932
			1304 / PS17I(3)	1304	PS17I(3)	162	7.5325	1.932
			1305 / PS17I(4)	1305	PS17I(4)	234	7.5325	1.932
			1306 / PS17I(5)	1306	PS17I(5)	306	7.5325	1.932
			1223 / PS17O(1)	1223	PS17O(1)	18	10.877	3.542
			1224 / PS17O(2)	1224	PS17O(2)	90	10.877	3.542
			1225 / PS17O(3)	1225	PS17O(3)	162	10.877	3.542
			1226 / PS17O(4)	1226	PS17O(4)	234	10.877	3.542
			1227 / PS17O(5)	1227	PS17O(5)	306	10.877	3.542

Measurement	Part Number	Instrumentation	Identification Tag	Model Number	Escort Name	Theta Loc. (CWFLA)	Radial Loc.	Axial Loc.
Vane exit temperature	MCP-0004042	Strut leading edge probes	6201 / ETT17(01)	6201	ETT17(1)	0	8.3% bypass	N/A
		10 immersions/ 5 struts	6202 / ETT17(02)	6202	ETT17(2)	0	25% bypass	N/A
			6203 / ETT17(03)	6203	ETT17(3)	0	41.7% bypass	N/A
			6204 / ETT17(04)	6204	ETT17(4)	0	58.3% bypass	N/A
			6205 / ETT17(05)	6205	ETT17(5)	0	75% bypass	N/A
			6206 / ETT17(06)	6206	ETT17(6)	0	91.7% bypass	N/A
			6207 / ETT17(07)	6207	ETT17(7)	72	8.3% bypass	N/A
			6208 / ETT17(08)	6208	ETT17(8)	72	25% bypass	N/A
			6209 / ETT17(09)	6209	ETT17(9)	72	41.7% bypass	N/A
			6210 / ETT17(10)	6210	ETT17(10)	72	58.3% bypass	N/A
			6211 / ETT17(11)	6211	ETT17(11)	72	75% bypass	N/A
			6212 / ETT17(12)	6212	ETT17(12)	72	91.7% bypass	N/A
			6213 / ETT17(13)	6213	ETT17(13)	144	8.3% bypass	N/A
			6214 / ETT17(14)	6214	ETT17(14)	144	25% bypass	N/A
			6215 / ETT17(15)	6215	ETT17(15)	144	41.7% bypass	N/A
			6216 / ETT17(16)	6216	ETT17(16)	144	58.3% bypass	N/A
			6217 / ETT17(17)	6217	ETT17(17)	144	75% bypass	N/A
			6218 / ETT17(18)	6218	ETT17(18)	144	91.7% bypass	N/A
			6219 / ETT17(19)	6219	ETT17(19)	216	8.3% bypass	N/A
			6220 / ETT17(20)	6220	ETT17(20)	216	25% bypass	N/A
			6221 / ETT17(21)	6221	ETT17(21)	216	41.7% bypass	N/A
			6222 / ETT17(22)	6222	ETT17(22)	216	58.3% bypass	N/A
			6223 / ETT17(23)	6223	ETT17(23)	216	75% bypass	N/A
			6224 / ETT17(24)	6224	ETT17(24)	216	91.7% bypass	N/A
			6225 / ETT17(25)	6225	ETT17(25)	288	8.3% bypass	N/A
			6226 / ETT17(26)	6226	ETT17(26)	288	25% bypass	N/A
			6227 / ETT17(27)	6227	ETT17(27)	288	41.7% bypass	N/A
			6228 / ETT17(28)	6228	ETT17(28)	288	58.3% bypass	N/A
			6229 / ETT17(29)	6229	ETT17(29)	288	75% bypass	N/A
			6230 / ETT17(30)	6230	ETT17(30)	288	91.7% bypass	N/A
			6304 / ETT025(01)	6304	ETT025(1)	0	12.5% core	N/A

Measurement	Part Number	Instrumentation	Identification Tag	Model Number	Escort Name	Theta Loc. (CWFLA)	Radial Loc.	Axial Loc.
			6305 / ETT025(02)	6305	ETT025(2)	0	37.5% core	N/A
			6306 / ETT025(03)	6306	ETT025(3)	0	62.5% core	N/A
			6307 / ETT025(04)	6307	ETT025(4)	0	87.5% core	N/A
			6308 / ETT025(05)	6308	ETT025(5)	72	12.5% core	N/A
			6309 / ETT025(06)	6309	ETT025(6)	72	37.5% core	N/A
			6310 / ETT025(07)	6310	ETT025(7)	72	62.5% core	N/A
			6311 / ETT025(08)	6311	ETT025(8)	72	87.5% core	N/A
			6312 / ETT025(09)	6312	ETT025(9)	144	12.5% core	N/A
			6313 / ETT025(10)	6313	ETT025(10)	144	37.5% core	N/A
			6314 / ETT025(11)	6314	ETT025(11)	144	62.5% core	N/A
			6315 / ETT025(12)	6315	ETT025(12)	144	87.5% core	N/A
			6316 / ETT025(13)	6316	ETT025(13)	216	12.5% core	N/A
			6317 / ETT025(14)	6317	ETT025(14)	216	37.5% core	N/A
			6318 / ETT025(15)	6318	ETT025(15)	216	62.5% core	N/A
			6319 / ETT025(16)	6319	ETT025(16)	216	87.5% core	N/A
			6320 / ETT025(17)	6320	ETT025(17)	288	12.5% core	N/A
			6321 / ETT025(18)	6321	ETT025(18)	288	37.5% core	N/A
			6322 / ETT025(19)	6322	ETT025(19)	288	62.5% core	N/A
			6323 / ETT025(20)	6323	ETT025(20)	288	87.5% core	N/A
Rotor blade strain	R3559462-1	Strain gauges	defined by AE			TBD	4.362	1.112
		Critical modes/	defined by AE			TBD	10.829	1.523
		15 gages	defined by AE			TBD	10.87	1.805
			defined by AE			TBD	10.87	1.955
			defined by AE			TBD	3.549	0.81
			defined by AE			TBD	4.362	1.112
			defined by AE			TBD	10.829	1.523
			defined by AE			TBD	10.87	1.805
			defined by AE			TBD	10.87	1.955
			defined by AE			TBD	3.549	0.81
			defined by AE			TBD	4.362	1.112
			defined by AE			TBD	10.829	1.523
			defined by AE			TBD	10.87	1.805
			defined by AE			TBD	10.87	1.955

Measurement	Part Number	Instrumentation	Identification Tag	Model Number	Escort Name	Theta Loc. (CWFLA)	Radial Loc.	Axial Loc.
			defined by AE			TBD	3.549	0.81
			defined by AE			TBD	4.362	1.112
			defined by AE			TBD	10.829	1.523
			defined by AE			TBD	10.87	1.805
			defined by AE			TBD	10.87	1.955
			defined by AE			TBD	3.549	0.81
			defined by AE			TBD	4.362	1.112
			defined by AE			TBD	10.829	1.523
			defined by AE			TBD	10.87	1.805
			defined by AE			TBD	10.87	1.955
			defined by AE			TBD	3.549	0.81
Static Pressures in core	MCP-0004044	Wall static taps	1523 / PSCWO(1)	1523	PSCWO(1)	18	N/A	1.618
		10 locations on shroud	1524 / PSCWO(2)	1524	PSCWO(2)	18	N/A	2.758
			1525 / PSCWO(3)	1525	PSCWO(3)	18	N/A	3.898
			1526 / PSCWO(4)	1526	PSCWO(4)	18	N/A	5.038
			1527 / PSCWO(5)	1527	PSCWO(5)	18	N/A	6.178
			1528 / PSCWO(6)	1528	PSCWO(6)	18	N/A	7.318
			1529 / PSCWO(7)	1529	PSCWO(7)	18	N/A	8.458
			1530 / PSCWO(8)	1530	PSCWO(8)	18	N/A	9.598
			1531 / PSCWO(9)	1531	PSCWO(9)	18	N/A	10.738
			1532 / PSCWO(10)	1532	PSCWO(10)	18	N/A	11.878
Pressure/ Area Measurements		Wall static taps	228 / PSRS(1)	228	PSRS(1)	45	5.5445	N/A
			229 / PSRS(2)	229	PSRS(2)	135	5.5445	N/A
			230 / PSRS(3)	230	PSRS(3)	225	5.5445	N/A
			231 / PSRS(4)	231	PSRS(4)	315	5.5445	N/A

REPORT DOCUMENTATION PAGE

Form Approved
OMB No. 0704-0188

1. AGENCY USE ONLY (*Leave blank*)	2. REPORT DATE	3. REPORT TYPE AND DATES COVERED
	July 2003	Final Contractor Report

4. TITLE AND SUBTITLE

Design and Test of Fan/Nacelle Models Quiet High-Speed Fan

5. FUNDING NUMBERS

WU–781–30–11–00
NAS3–27752

6. AUTHOR(S)

Donald Weir

7. PERFORMING ORGANIZATION NAME(S) AND ADDRESS(ES)

Honeywell Engines & Systems
Phoenix, Arizona

8. PERFORMING ORGANIZATION REPORT NUMBER

E–13946

9. SPONSORING/MONITORING AGENCY NAME(S) AND ADDRESS(ES)

National Aeronautics and Space Administration
Washington, DC 20546–0001

10. SPONSORING/MONITORING AGENCY REPORT NUMBER

NASA CR—2003-212370

11. SUPPLEMENTARY NOTES

Project Manager, Christopher J. Miller, Structures and Acoustics Division, NASA Glenn Research Center, organization code 5940, 216–433–6179.

12a. DISTRIBUTION/AVAILABILITY STATEMENT

Unclassified - Unlimited
Subject Category: 07 Distribution: Nonstandard

Available electronically at http://gltrs.grc.nasa.gov

This publication is available from the NASA Center for AeroSpace Information, 301–621–0390.

12b. DISTRIBUTION CODE

13. ABSTRACT ***(Maximum 200 words)***

The Quiet High-Speed Fan program is a cooperative effort between Honeywell Engines & Systems (formerly AlliedSignal Engines & Systems) and the NASA Glenn Research Center. Engines & Systems has designed an advanced high-speed fan that will be tested on the Ultra High Bypass Propulsion Simulator in the NASA Glenn 9- by 15-foot wind tunnel, currently scheduled for the second quarter of 2000. An Engines & Systems modern fan design will be used as a baseline. A nacelle model is provided that is characteristic of a typical, modern regional aircraft nacelle and meets all of the program test objectives.

14. SUBJECT TERMS

Jet aircraft noise; Compressor blades; Turbofans; Turbomachinery

15. NUMBER OF PAGES

266

16. PRICE CODE

17. SECURITY CLASSIFICATION OF REPORT	18. SECURITY CLASSIFICATION OF THIS PAGE	19. SECURITY CLASSIFICATION OF ABSTRACT	20. LIMITATION OF ABSTRACT
Unclassified	Unclassified	Unclassified	